FUNCTIONALIZED GOLD NANOPARTICLES FOR CELLULAR UPTAKE

Emma Harrison BSc (Hons)

Faculty of Computing & Engineering of

Ulster University

This dissertation is submitted for the degree of Doctor of Philosophy

April 2018

(I confirm that the word count of this thesis is less than 100,000 words)

Acknowledgements

This Thesis would not have been possible without the help and support of my friends, both inside and outside of NIBEC. I honestly could not thank them enough.

Primarily I would like to thank my supervisor and mentor, Dorian Dixon. Without him I would never have explored the field of nanotechnology. Dorian has provided endless support, he has forced me to push myself and thrown me so far out of my comfort zone more times than I can recall, and as such has made me 100 times more confident both academically and personally in the past 4 years. Alongside Dorian I wish to extend my thanks to Jeremy Hamilton for listening and preventing borderline chemistry related breakdowns, and for keeping me entertained throughout my final year. To Adrian for always being more than happy to help and to Paddy Dunlop and George Burke for lending their expertise and support whenever it has been needed.

A large number of collaborators have been involved throughout my PhD; my thanks are owed to Jonathan Coulter and his students, James Nicol, Shannon O' Neill and Natalie Owen. James Nicol broke up many a dull morning with comical genius and very dramatic emails – and the occasional bit of science.

I wish to thank the students and my now friends here at NIBEC and NIACE. For those that have finished and have inspired me that there is a light at the end of the tunnel, I wish to thank Aidan O'Neill, Robert McLister, Leanne Robinson, Naomi Lowry, Aaron McConville, Ruairi McGlynn and Katie-Jo Harwood. My thanks to Kate goes so far beyond this PhD, she has been my accomplice and the devil on my shoulder in many a late night in NIBEC and I can't wait for our next trip abroad; that thanks also extends to Chelsea for bringing River and Sokka into my life. Also to the newer PhD students, who have provided me with entertainment for the past year – a bit too much of that at the research awards dinner – Joanna Ward, Christopher Dooley, Kieran O'Donnell, Shannon Wilson and Stephen McKillop.

For those that are still there, I want to thank you for not letting me quit or make excuses (that means you Fiona) and for listening to my endless rants and taking up several mornings with great coffee gossips. Miss Fiona Rogan, or 'MaMa Rogan' (among other names) thank you so much for being so helpful and compassionate in

absolutely everything you do. I also extend my thanks to everyone else in NIBEC, Damian, Ann and Brian and the research staff over in the main building.

The most important thanks must go to those who have not been involved academically, but have been there for me personally, that means you Liah Luke and Samantha Spiers (there - you finally got named on a publication of mine). Liah, I couldn't thank you enough for everything, not just over the past 3 years, but the past 26. Let's never break that Wednesday routine.

My friends mean the world to me and I would not be here if it was not for them. Thank you for putting up with my sub-par friendship levels for the past year, and especially the past few months, and thanks for being so understanding of my 'PhD brain' as I put it. An extra thanks goes to my extended family, primarily Anita Finn, for so much enthusiasm and encouragement throughout my entire academic lifetime.

Last but most definitely not least, I wish to thank Alfie, Roxy, John Benson, and his wonderful family, Lue, Jay, June and Johnny. John, thanks for showing me the centrifuge 4 years ago, without your patience there, we would not be where we are today. Thank you for showing me unconditional support both inside and outside of work, and for whisking me away every few months to save me from the all-consuming PhD. The one sad thing about finishing my research is that I won't be working with you every day. Thanks to my partner in crime.

Contents

ABSTRACT

Nanoparticles attract vast international research interest for medical applications due to their ability to be manipulated via the incorporation of various ligands and ligands. These ligands enable the regulation of a diverse range of biomedical processes which take place at a nanometer scale. Two approaches are commonly used to co-functionalize AuNPs, these methods include synthesizing either a mixed monolayer or by using a bifunctional Polyethylene glycol (PEG) linker. This Thesis directly compares the two approaches by incorporating the use of an internalization and endosomal escape peptide to compare the two arrangements for stability, cell viability, internalization and radio sensitization. An extensive research effort employed to confirm peptide arrangement has revealed that difficulties arise due to the higher binding affinity of thiolated ligands to gold in comparison to amine terminated ligands which are commonly used to synthesize a linker surface arrangement. It is shown that the successful synthesis using a bifunctional linker is heavily dependent on the method of attachment coupled with the solvents used. Inductively coupled plasma mass spectrometry (ICP-MS) has indicated a statistical difference for internalization, demonstrating that the linker has elicited a higher internalization response for both cell lines with an overall F value of 181.8 and a P value of 0.0095 ($P < 0.05$ statistically significant) for the DU145 cell lines resulting in over 3 times the amount of gold within the cells. Stability studies and cell viability studies have also indicated enhanced stability for the linker samples and preliminary data obtained from a clonogenic survival assay has indicated enhanced radiosensitivity, with an SER 1.36 for the linker, which represents a 36% increase in radiosensitivity for the samples in comparison to the untreated control. Concurrent attachment studies have identified that cysteine binding efficiency can be optimized by altering the pH of an AuNP suspension to ~ 8, while extensive collaboration efforts have established that the solvents used to attach the peptide and/or ligands is paramount to a successful, stable covalent attachment, and an essential criteria for successful synthesis using a linker using a pre-synthesized NHS ester.

Abbreviations

AAS	Atomic absorption spectroscopy
AIF	Apoptosis-inducing factor
AUC	Area under the curve
AuNPs	Gold nanoparticles
BCA	Bicinchoninic acid
BSA	Bovine serum albumin
C11PC	Photosensitizer
CCC	Critical coagulation concentration
CTAB	Cetyl trimethylammonium bromide
CYT-6091	Aurimune Clinical Trial
d.nm	Diameter of nanoparticle
DDS	Drug delivery systems
DLS	Dynamic Light Scattering
DLVO	Derjarguin-Laudau-Verwey-Overbeck
DMEM	Dulbecco's Modified Eagle Medium
DMF	Dimethylformamide
DMSO	Dimethyl sulfoxide
DRIFTS	Diffuse Reflectance Infrared Fourier Transform Spectroscopy
DTDC	3,3′-diethylthiadicarbocyanine iodide
DU145	Epithelial cell line, homosapien prostate
EDC	(1-ethyl-3-(3-dimethylaminopropyl) carbodiimide hydrochloride)
EGCg	epigallocatechin-gallate
EMEM	Eagle's Minimum Essential Medium
EPR	Enhanced Permeability and Retention factor
FBS	Fetal bovine serum
FT-IR	Fourier Transform – Infra Red Spectroscopy
GCPII	Glutamate carboxypeptidase II
Gy	The gray: unit of ionizing radiation dose
H5	H5WYG Endosomal escape peptide
HEPES	Zwitterionic biological buffer

ICP-Ms	Inductively coupled mass spectrometry
keV	Unit of energy, Electronvolt
LDH	Lactate dehydrogenase
MBS	3-maleimido benzoic acid N-hydroxysuccinimide ester
MID	Mean inactivation dose
MTT	3-[4, 5-dimethylthiazol-2-yl]-2,5-diphenyl tetrazolium bromide
MUAPEG	Mercaptoundecyl-tetraethylene glycol
MUDA	11-mercaptoundecanoic acid
NF-kB	Nuclear factor kappa-B
NHS	N-Hydroxysuccinimide
NLS	Nuclear localization signal
NP	Nanoparticle
NS	Nanostar
OEG	Oligo(ethylene glycol)
PAMA	poly(dimethylaminoethyl methacrylate)
PARP	Poly-(ADP-ribose)-polymerase
PC3	Epithelial cell line, homosapien prostate
PDI	Poly Dispersity Index
PEG	Polyethylene Glycol
PEI	poly(ethyleneimine)
pI	Isoelectric point
Pk	Dissociation constant
pL	Photoluminescence
PLA	poly(L-lysine)
PpIX	Protoporphyrin IX
PSMA	Prostate Specific Membrane Antigen
QD	Quantum dot
RCF	Relative centrifugal force
RES	Reticular Endothelial System
RGD	Nrp-1 Targeting peptide
RME	Receptor mediated endocytosis
ROS	Reactive oxygen species

RPM	Revolutions per minute
SDS	sodium dodecyl sulfate
SER	Sensitizer enhancement ratio
SERRS	Surface-enhanced resonance Raman scattering
SF	Survival Fraction
SH-PEG	Methoxyl PEG Thiol
SH-PEG-SGA	Thiol PEG Succinimidyl Glutaramide
SPR	Surface Plasmon Resonance
TAT	Cell penetrating peptide
TBE	Tris/Borate/EDTA
TEM	Transmission Electron Microscopy
TGA	Thermo Gravimetric Analysis
THF	Tetrahydrofuran
TiO_2	Ttitanium oxide
TNF	Recombinant human tumor necrosis factor alpha
TUNEL	Terminal deoxynucleotidyl transferase dUTP nick end labelling
UV/Vis	Ultraviolet/visible light
XPS	X-ray photoelectron spectroscopy

DECLARATION

"I hereby declare that with effect from the date on which the thesis is deposited in Research Student Administration of Ulster University, I permit

1. The Librarian of the University to allow the thesis to be copied in whole or in part without reference to me on the understanding that such authority applies to the provision of single copies made for study purposes or for inclusion within the stock of another library.
2. The Thesis to be made available through the Ulster Institutional Repository and/or EThOS under the terms of the Ulster eTheses Deposit Agreement which I have signed.*

IT IS A CONDITION OF USE OF THIS THESIS THAT ANYONE WHO CONSULTS IT MUST RECOGNISE THAT THE COPYRIGHT RESTS WITH THE AUTHOR AND THAT NO QUOTATION FROM THE THESIS AND NO INFORMATION DERIVED FROM IT MAY BE PUBLISHED UNLESS THE SOURCE IS PROPERLY ACKNOWLEDGED".

LIST OF PUBLICATIONS RESULTING FROM THIS THESIS

Journal Publications

[1] E. Harrison, J. W. J. Hamilton, M. Macias-Montero, D. Dixon, Nanotechnology 2017, 28, 295602.

[2] E. Harrison, J. A. Coulter, D. Dixon, Nanomedicine 2016, 11, 851.

[3] E. Harrison, J. R. Nicol, M. Macias-Montero, G. A. Burke, J. A. Coulter, B. J. Meenan, D. Dixon, Mater. Sci. Eng. C 2016, 62, 710.

[4] J. R. Nicol, E. Harrison, D. Dixon, H. O. McCarthy, J. A. Coulter Nanomedicine: Nanotechnology, Biology, and Medicine 2017 - *submitted*

[5] E. Harrison, N. Owen, F. Rogan, G. A. Burke, K. J. Harwood, J. Callan, J. A. Coulter, R. McGlynn, D Dixon; Small – *to be submitted*

Abstract Publications from Conferences

[6] H. Emma, N. James, C. Jonathan, D. Dorian, Front. Bioeng. Biotechnol. 2016, 4, DOI 10.3389/conf.FBIOE.2016.01.00631.

[7] D. Dixon, J. Nicol, J. A. Coulter, E. Harrison, in World Acad. Sci. Eng. Technol. Int. J. Bioeng. Life Sci., 2015.

Conferences

1. Research Student Conference 2015
2. NIBES Annual Symposium June 2015

"Gold Nanoparticles co-functionalized with Polyethylene Glycol and Receptor Mediated Endocytosis Peptide"

3. UK Society for Biomaterials Annual Conference and Postgraduate Day June 2015

"Gold Nanoparticle Comparative Study of Cellular Uptake and Stability using Mixed Monolayer and Hetero-Bifunctional PEG Linker Methodologies for Surface Co-functionalization"

4. Britain's Early – Career Researchers October 2015

"Gold Nanoparticle Surface Functionalization: The Influence of a Bi-functional Linker on Cellular Uptake"

5. Advanced Functional Polymers in Medicine October 2015

"Gold Nanoparticles Co-functionalized with PEG and RME peptide using Mixed Monolayer and Linker Approaches"

6. 10th World Biomaterials Congress 2016

"Gold Nanoparticles co-functionalized with polyethylene glycol and receptor mediated endocytosis peptide for cellular uptake"

7. Research Student Conference January 2016

"Gold nanoparticles co-functionalized with Polyethylene Glycol and Receptor Mediated Endocytosis peptide for cellular targeting"

8. RSC Biomaterials Chemistry Special Interest Group Conference January 2017

"Gold nanoparticles co-functionalized with Polyethylene Glycol and Receptor Mediated Endocytosis peptide for cellular targeting"

9. British Society for Nanomedicine 2017

"The Influence of pH on AuNP and Peptide Binding Efficiency"

AWARDS

- SET for Britain House of Commons early researcher competition - finalist
- UK Society for Biomaterials Annual Conference – RSC best chemistry poster 1st place
- RSC Biomaterials Chemistry Special Interest Group Conference – best student poster 1st place

1. INTRODUCTION

1.1 Introduction

Nanotechnology has vast opportunities for advancing medical science and disease treatment. Gold nanoparticles, in particular, have become of significant clinical interest due to their unique optical, chemical and biological properties; with cancer research becoming one of the most predominant areas of interest. Gold nanoparticles are non-toxic, and thermally stable; these properties can be manipulated 'to provide an effective and selective platform to obtain a targeted intracellular release' of a therapeutic drug, dye or other payload. [1] This is of particular interest to biomedical engineering as the surface functionalization with different peptides, ligands and/or other ligands has the potential to allow for the synthesis of a 'golden bullet' which may target and destroy cancer cells as a result of external irradiation via a range of methods (some of which are illustrated in Figure 1-1). AuNPs offer the sensitization of tumors to radiation through utilization of their high atomic number (Gold (Z = 79)). This approach can maximize the differential response between tumors and normal tissue known as the therapeutic ratio through the introduction of the high-atomic number (Z) material into the target tissue. The mass energy of the coefficient of gold is 100-150 times greater than that of soft tissue in the keV energy range. This may overcome current issues with selectivity for radiotherapy, as both cancerous and healthy tissue have similar mass energy absorption profiles. Due to the high Z-average of the AuNPs, introduction of the AuNPs to cancerous tissue offers a stark contrast between the tissue types for enhanced selectivity improving tumor control, reducing side effects and increasing survival when compared to radiotherapy alone. [2]

Another approach of using AuNP properties to aid the treatment of cancerous tissue is by utilization of the Surface Plasmon Resonance (SPR) properties of AuNPs at nanoscale. Photo thermal therapy (PTT) involves the conversion of photon energy into thermal energy to kill cancer cells. Due to the SPR of AuNPs, AuNPs absorb light strongly in the visible range, and convert light into heat upon irradiation. Upon irradiation to electromagnetic radiation, surface electrons are excited resulting in

strong surface fields. The relaxation of these electrons result in strong localized heat emission. In noble metal nanoparticles, adsorption and scattering efficiencies are strongly enhanced due to the SPR, the absorption and scattering are at least 1000 times stronger than other organic dye molecules otherwise used in PTT. Changing the shape of these nanoparticles can allow for fine tuning of these properties to near infrared (NIR) region, where light penetration for tissue is optimal. For this reason, NIR-absorbing gold-based nanoparticles have received considerable attention in plasmonic photo thermal therapy, with gold nanoshells, gold nanorods and gold nanocages leading the literature, with silica based gold nanoshells experimented by Halas and co-workers in 1988, Au nanorods investigated due to their precise and readily controllable NIR properties by Wang, Murphy and El-Sayed groups and Au nanocages being developed as a NIR-absorbing structure by the Xia group. [3–11]

To further enhance the therapeutic abilities of AuNPs, various ligands can be tethered to the AuNP surface to elicit a biological response. Multi functionality is the key feature of nanoparticle-based agents. Production via the Turkevich method permits the synthesis of citrate capped particles with a zeta potential of approximately -20 - -40 mV. The citrate capping is loosely bound on the AuNP enabling it to be easily displaced with other functional groups. Targeting ligands, thiol linkers and other functionalities can all be integrated to allow for targeted cancer therapy. The interaction of AuNP with thiols in particular; is of specific interest as this can provide an effective and selective means of controlled intracellular release via an external stimulus, release of the payload at the required

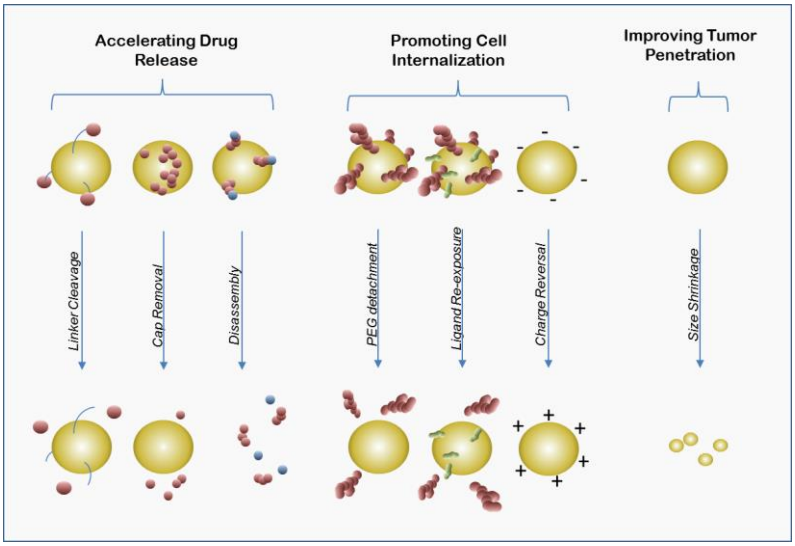

Figure 1-1 Schematic of the potential applications of gold nanoparticles

site can be achieved using photoexcitation or by means of intracellular glutathione levels. The intracellular concentration of glutathione is 1–10 mM, whereas extracellular levels are 2 μM, which can be used to break the thiol linker, releasing the payload inside the cell. [12,13] The main focus of this research is AuNP functionalization as it could potentially allow for a drug delivery system that can target a specific tumor cell and overcome natural physiological barriers that manifest in several distinct ways. For intravascular delivery of NPs, the barrier manifests in the form of: (i) immune clearance in the liver and spleen, (ii) permeation across the endothelium into target tissues, (iii) penetration through the tissue interstitium, (iv) endocytosis in target cells, (v) diffusion through cytoplasm and (vi) eventually entry into the nucleus, if required. [14] The thiol-terminated polyethylene glycol (PEG) is commonly used to functionalize the surface of the AuNP as PEG improves colloidal stability *in vivo* and prevents uptake by the reticular endothelial system, however it limits the overall uptake into the target cancer cell. As illustrated in Figure 1-2, the goal of this Thesis is to firstly identify the surface arrangement to be used, which gives the best biological response, then optimize the attachment of the ligands to the AuNPs which will be chosen based on their potential to enhance radiosensitization.

1.2 Aims and Objectives

1.2.1 Aims

The ultimate aim of this Thesis is to determine whether the method of co-functionalization would directly affect the colloidal stability, and biological response of a gold nanoparticle conjugate. To achieve this, this research effort involved the synthesis and characterization of both a mixed monolayer surface arrangement, and compared the conjugate to a AuNP co-functionalized using a bifunctional PEG linker. A range of comparative colloidal stability and biological studies were performed, with the outcome to be the identification of whether one method of co-functionalization would initiate cellular internalization and enhanced radiosensitivity to a higher degree than the latter. To achieve an ideal complex, the scope also involved the optimization of peptide attachment to the AuNP surface through pH and the application of this optimized model in a range of *in vitro* studies.

1.2.2 Objectives

1. To synthesize AuNPs and PEGylate their surface for enhanced colloidal stability, followed by co-functionalization of the AuNP surface with various peptides
2. To co-functionalize the AuNPs using peptides to synthesize a mixed monolayer and utilize a PEG linker, then conduct an in-depth characterization profile of the conjugates
3. Conduct a range of comparative studies, including, but not limited to, a range of in depth characterizations (using spectroscopy and dynamic light scattering) followed by *in vitro* colloidal stability studies and non-specific protein adsorption studies to determine if one co-functionalization methodology can enhance colloidal stability over the other
4. Complete a range of cellular internalization and radiosensitization studies to identify if one arrangement offers an increase in intracellular concentration – and consequently an improved radiotherapy response - in comparison to the other
5. Identify novel agents for AuNP functionalization
6. Optimize AuNP and peptide binding efficiency through alteration of pH

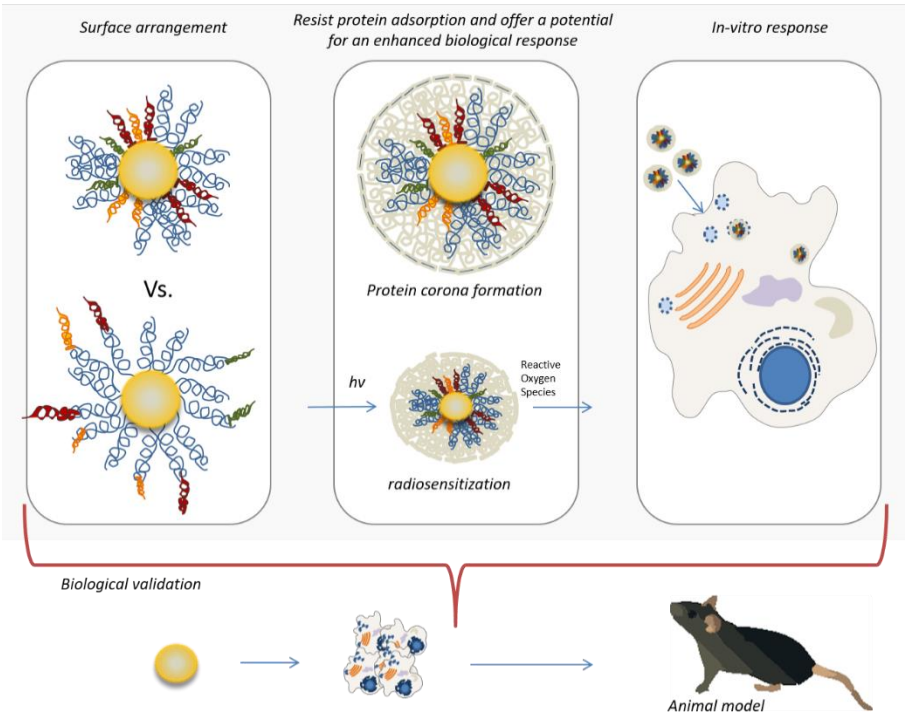

Figure 1-2 Illustration of the Thesis aims and objectives

2. LITERATURE REVIEW

2.1 Cancer Origin, Significance, Outcome and Current Diagnostics/Therapeutics

Cancer is a term used for diseases in which abnormal cells undergo uncontrolled growth as a result of gene malfunctions and are subsequently able to invade their surrounding tissues. In this state, the imbalance of cell division leads to the formation of a malignant tumor (Figure 2-1) where cells can spread to other parts of the body via utilization of the blood and lymphatic systems. [15]

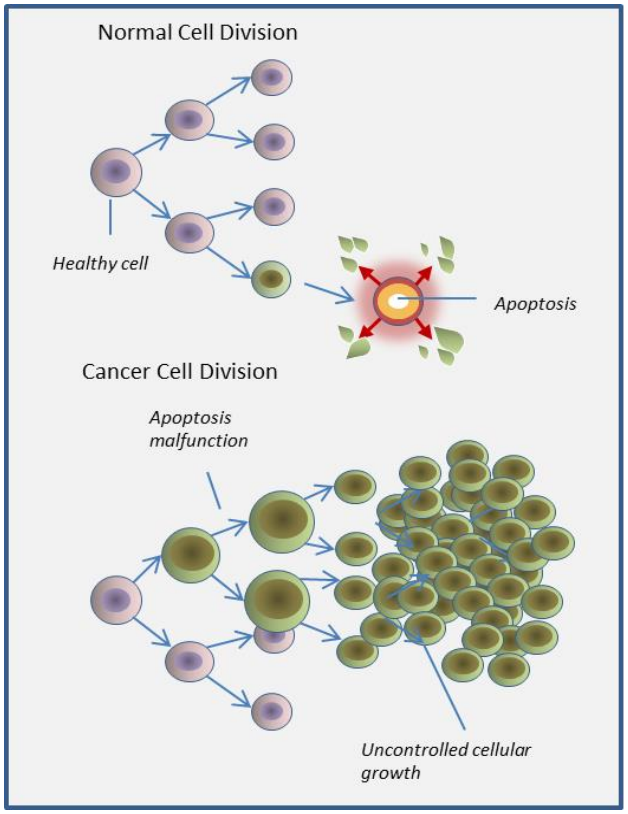

Figure 2-1 Schematic of tumor formation

The overall health of the human body is maintained by the constant division of cells, occasionally the genetic material DNA of these cells may become damaged, thus producing mutations which affect the healthy cell growth process. Consequently,

these mutations result in the cessation of cell apoptosis, ensuing in the continuation of cell generation when they are not required. A tumor is therefore an abundance of these cells. [15]

In 2014 the National Cancer Institute estimated 233,000 new cases and 29,480 deaths from prostate cancer in the United States (U.S) alone. Approximately 15% of men will be diagnosed with prostate cancer during their lifetime and in 2016 there was an estimated 3.3million with a history of prostate cancer living in the U.S. and an estimated additional 180,890 men which will be diagnosed in 2016. [16–18] Cancer is currently being diagnosed with pathological testing such as blood and biopsy. Treatment usually follows the mechanism of surgery, radiation therapies, chemotherapy, immunotherapy and the utilization of anti-cancer drugs. These drugs are commonly injected directly into the tumor site, administered intravenously for general systematic distribution via anti-cancer therapy drug implants or electro chemotherapy. The drugs used are predominantly dependent on both the tumor location and severity and are currently only administered in order to induce a period of partial or complete remission (remission for 5+ years without reoccurrence) or for palliative purposes. [19]

Cancer mortality is still primarily linked with the development of metastatic disease. Current curative treatment schedules are typically limited to localized/primary disease within clearly defined tumor boundaries; therefore, effective treatment options remain limited for disseminated disease. Therapeutic drugs are administered intravenously leading to general systemic distribution, this results in detrimental side-effects as the drugs attack healthy tissues in addition to tumor cells. As the drugs also impact healthy cells, treatment doses must be bound within established margins to avoid the risk of drug induced adverse effects. Targeting technologies utilizing suitable tumor specific antigens can therefore be applied to help reduce systemic toxicity by conferring more selective targeting. [20–23]

It should be noted that other routes of administration are available, however they too have their limitations. Oral ingestion, for example, is lacking due to the inability to overcome the acidity of the stomach. [24] Research is therefore focused on the development of a method to selectively target the tumor cell to elicit controlled drug

delivery with sustained release over a specific time period while avoiding non-specific interactions with plasma proteins (opsonization), remain stable in physiological conditions in a wide array of pH and evade uptake via the reticuloendothelial system.[24]

2.2 Nanoparticles

Nanoparticles are particles between 1 and 100 nanometers in size with a surrounding interfacial layer. The interfacial layer is an integral part of nanoscale matter, fundamentally affecting all of its properties.[25] Nanotechnology is linked to Richard Feynman in 1959 whom first described the concept of being able to arrange atoms 'one by one, just as we want them' and has since attracted vast international interest over the past several decades resulting in the development of various potential biomedical applications. Biological applications range from drug, protein or peptide delivery, imaging, tumor targeting - with the biggest areas of growth revolving around detection of molecules associated with diseases such as diabetes, mellitus neurodegenerative diseases and cancer. [26–28]

2.3 Nanomaterials for Drug Delivery

Metal nanoparticles have long been considered to exhibit unique physical and chemical properties which are different from those in their bulk state. The unusual property of small crystals that arise from confinement of electrons to small regions of space designates the quantum size effect. The quantum size effect describes the physics of electron properties in solids with a great reduction in size. It can dominate the comportment of matter at nanoscale affecting the optical, electrical and magnetic behavior. Examples of such behaviors include the rendering of gold nanoparticles as ruby red at room temperature, and optical electric-field enhancement at a metal surface arising from surface-plasmon excitation. The reduction of the bulk gold to nanoscale results in the a conduction band of electrons which oscillate due to the interaction with the electromagnetic field which can be used to trigger payload release or induce localized heating. [21,29,30] This phenomena is known as the surface plasmon resonance effect which arises due to the drastic change in electronic properties as a result of the vast reduction in size and when they are exposed to

external optical fields, plasmonic coupling causes electric field enhancement, which originates from the charge separation in the AuNP during the plasmon resonance and can occur at small, sub-micron sizes. [31,32]

Noble metallic nanoparticles can be attached to single strands of DNA non-destructively; furthermore they can navigate through vasculature and localize targets. As a result they offer the opportunity for a wide array of *in vivo* medical diagnostic, therapeutic, imaging and biomedical applications. [33]

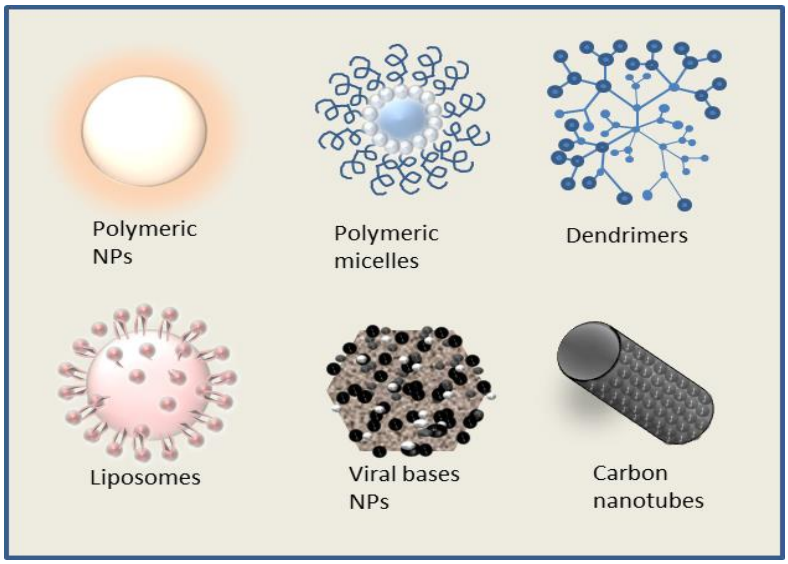

Figure 2-2 The various types of nanoparticles for biomedical applications

Some of the most well studied nanoparticles are illustrated in Figure 2-2; they include quantum dots, carbon nanotubes, Nano shells, magnetic nanoparticles and dendrimers. Nanocarriers comprise mainly polymer therapeutics (polymer–protein and polymer–drug conjugates), where the drug is covalently bound or conjugated to a polymeric structure, and particulate drug nanocarriers, where the drug is physically entrapped within molecular assemblies with different structures made from different materials, such as polymers (polymeric micelles, dendrimers and polymeric nanoparticles), lipids (liposomes), or organometallic compounds (carbon nanotubes). The first generation of anticancer nanocarriers to be approved by FDA included both liposomal drugs and polymeric conjugates. [23,34,35]

Covalently conjugating anticancer proteins to polymers can reduce immunogenicity and increases its circulation time in blood. [36] Drugs commonly result in cytotoxic affects, therefore a polymer-drug conjugate offers the cytotoxic drug an increased circulation time in blood, an improved aqueous solubility, a passively targeted delivery to tumors, and a reduced toxicity, improving the therapeutic value of the anticancer drug. [37–39]

Liposomes are self-assembled colloidal vesicles with a characteristic lipid bilayer membrane composed of amphiphilic phospholipids. [23] Hydrophilic anticancer drugs can be encapsulated in their aqueous core, and hydrophobic cytotoxic agents in its hydrophobic membrane. A major limitation with liposomes however is the low drug loading capacity, due to the small membrane space; they are also prone to instability when drugs are loaded onto the membrane. [40,41]

Carbon nanotubes are tubular hydrophobic networks of carbon atoms with a diameter of approximately 1–4 nm (depending on the number of graphene layers), 1–100 lm in length and unique structural, electronic, optical and mechanical properties. [42][43] Carbon nanotubes can contain a range of anticarrier drugs within their hallow inner cavity, or on their surface, they overcome the limited space apparent from the liposomes, however they are insoluble in all solvents, which results in an array of toxic problems. Theses carriers have the ability to cross the plasma membrane and enter into the cancerous cells by endocytosis. [43–45]

Dendrimers are highly branched three-dimensional synthetic polymeric macromolecules. One of their major advantages is that they allow a high level of control over their properties, such as the ability to adjust biocompatibility by tuning the chemical synthesis of the dendrimer. They have good water solubility and high drug loading capacity, while there is an abundance of literature available for the application of dendrimers for oncology; their slow translation form preclinical to clinical trials is most likely due to the toxicity of the dendrimers as a result of their multiple functional groups found on their surface. [23,46–51]

2.4 Properties and Applications of Gold nanoparticles

Extensive research has been focused on the area of gold nanoparticles (AuNPs) as drug delivery systems (DDS). The current goal is to synthesize non-toxic particles capable of delivering high doses of a payload to a target cell without triggering a undesired immune response with minimal side effects to the surrounding tissue. In a sense it is the ideal of improving chemotherapy via selectivity. [52] AuNPs have a range of unique properties, namely ease of synthesis, inert nature, ease of functionality and the potential to act as a radio sensitizing agent or for photothermal therapy (PTT). As a high Z material, AuNPs have shown great promise at increasing the effectiveness of conventional radiotherapy. [53] Hainfeld *et al.* has shown that radiotherapy is enhanced from a 20% survival rate for tumor bearing mice to an 86% 1-year survival rate when used in conjunction with a 1.9 nm AuNP/PBS suspensions. While this experimental design was unlikely to represent a clinically feasible option due to the prohibitive AuNP concentrations used and the high single fraction radiation dose, the study demonstrated clear proof-of-concept that AuNPs can significantly augment the efficacy of radiotherapy. [21,54] Using a mouse model seeded with melanoma cells, Chang *et al.* reported a survival time of 20 days for a control group receiving radiation alone compared to 65 days for those treated with AuNP and irradiation. [55] This radio sensitization effect is driven by an increased yield of low energy secondary electrons following photoelectric adsorption events. Differential photoelectric adsorption is most prominent at kV energies that are closest to those of the binding energies of the lower shelled electrons of the gold. [24,25] A potential issue is that the kV energies used, have an inherently shallow penetration, therefore limiting the exploitation of this physical effect for non-superficial tumors, Mesbahi *et al.* have shown that monoenergetic kilovoltage beams demonstrated a dose enhancement factor of 1.4 to 3.7, whereas the dose enhancement factors for megavoltage beams were negligible and less than 3% for all AuNP sizes and concentrations. [21,53,56,57]

AuNPs can be functionalized by attaching various ligands by means of thiol groups. This elicits the appending of a high density of ligands for targeting or therapeutics among others. [58] Drugs can be covalently bonded via cleavable linkers, or bound non-covalently to be released upon external stimulation. Therefore they can be

exploited for various treatment modalities including photothermal ablation therapy, radio sensitization, imaging and drug delivery.

Table 2-1 and Table 2-2 adapted from Harrison *et al. (2016)* outlines clinical trial results to date for AuNP based treatments, and overviews the preclinical (animal studies) results for the use of AuNPs in cancer therapy. Promising results have been obtained across a range of applications, using a wide variety of AuNP formulations. The results highlight both the potential of AuNP treatments and their inherent complexity.

Table 2-1 Clinical applications of AuNPs adapted from Harrison et al. 2016

Particle	**Application**	**Functionalization**	**Model**	**Result**	**Ref**
Clinical Trials					
Particle	Application	Functionalization	Model	Result	Ref
AuNPs (CYT-6091: Cyt-immune)	Advanced solid tumors	Human tumor necrosis factor alpha & SH-PEG	30 advanced-stage cancer patients	Phase I and Pharmacokinetic Studies of CYT-6091 (NCT00356980, NCT00436410). CYT-6091 may be administered systemically at doses of rhTNF that were previously shown to be toxic and that CYT-6091 may target to tumors	[59–63]
Silica-AuNPs: NANOM FIM	Treatment of coronary athero - sclerosis	Silica-AuNP & silica-AuNP iron bearing	180 patients with CAD and angiographic SYNTAX score ≤22	NANOM FIM- a completed phase I\II clinical trial (NCT01270139)12.6% reduction in the percentage atheroma volume (PAV) post procedure. The plasmonic resonance therapy using silica-gold NP proved efficient regression of coronary atherosclerosis in both approaches	[64]
Silica-gold nanoshells (AuroShells: AuroLase®)	Photothermal therapy for the treatment of advanced lung tumors resulting from either primary lung cancer or metastatic tumors in the lung			FDA-approved pilot study (NCT00848042, NCT01679470). Human trials were on-going as of 2014, the trials are complete, the results have not yet been disseminated	[65]

Table 2-2 Preclinical studies of AuNPs adapted from Harrison et al. 2016

Preclinical/Animal Studies					
Particle	Application	Functionalization	Model	Result	Ref
AuNP	Glioma targeting & accumulation efficiency	Gelatin (G) nanoparticles, doxorubicin (DOX), Cy5.5 and RRGD, a tandem peptide of RGD and octarginine	C6 cells xenograft-bearing mice	G-AuNPs-DC-RRGD displayed the best glioma targeting and accumulation efficiency, with good colocalization with neovessels. Cy5.5 also showed good colocalization with DOX, indicating the Cy5.5 could be used for imaging of the DOX delivery.	[66]
AuNRs	Targeted photothermal (PT) therapy and chemotherapy of triple negative breast cancer (TNBC)	Cisplatin–polypeptide poly (L-glutamic acid) (PGA), wrapping and folic acid (FA) functionalization (FA-GNR@Pt)	4T1 tumor bearing mice	The Folic acid gold nanorod hybrid nanoparticles significantly inhibited the growth of the TNBC tumor and extensively suppressed the dissemination of TNBC cells from the primary tumor to the lung	[67]
Hollow AuNS (DOX@ HAuNS)	Photothermal ablation (PTA)	Multifunctional doxorubicin (DOX)-loaded hollow gold Nanospheres DOX@HAuNS)	Hey tumors bearing mice (5.0×106 cells/mouse)	Tumors in six of the eight mice treated with laser & T-DOX@HAuNS regressed completely with only residual scar tissue by 22 days following injection	[68]
AuNP	Chemotherapy and radiation head and neck squamous cell carcinoma (HNSCC)	Epidermal growth factor receptor (EGFR), C225 antibody, liposomal green fluorescent dye & 2C5 antibody conjugate	Pretreated HN31 cells subcutaneously into the flanks of mice	Improved the efficacy of standard chemo and radiation treatment in resistant and aggressive head and neck cancer by 100-fold *in vitro* and 17-fold *in vivo*, reduced the effective entry doses of drugs and X-rays to 2–6% of their clinical doses	[69]
Uniform gold nano-stars	Integration of targeting tumors, chemotherapy and photo-thermotherapy into a single system	Cyclic RGD (cRGD) and near infrared (NIR) fluorescence probe (MPA) (Au-cRGD-MPA) or anti-cancer drug (DOX) (Au-cRGD-DOX)	S180 tumor-bearing mouse models	Viability of MDA-MB-231 cells was only 40 % after incubation with Au-cRGD-DOX and irradiation with NIR light. Both tail vein and intratumoral injections showed Au-cRGD-DOX treated mice exhibiting the slowest tumor volume increase	[70]
AuNP	radiotherapy	N/A	B16F10 melanoma tumor-bearing mice	Tumor volume in the combination therapy group was significantly smaller compared with that in radiation alone group ($P < 0.05$), whereas administration of AuNP or PBS alone did not exert any antitumor effect on tumor bearing mice	[55]
AuNP	radiotherapy	N/A	Mice bearing subcutaneous EMT-6 mammary carcinomas	Those receiving injections of 1.35 or 2.7 g Au/kg before radiation showed 50% and 86% long-term (>1 year) survival compared to 20% for the control group.	[54]

2.5 The Concept of the ‘Magic Bullet’

Paul Ehrich gave the preliminary description of drug delivery as a ‘magic bullet’ in 1891. Most drugs are administered orally or intravenously, the ‘magic bullet’, or now commonly known as ‘the magic gold bullet’ is a fictional description of a drug delivery system which would be able to administer drugs to a specific cell. It is considered fictional as it is the perception of forming a perfect DDS to administer therapeutic drugs with minimal side effects and ease of access. This ideal would be extremely difficult to achieve, due to sheer complexity, and as such, has not yet been realized. It is this concept on which this research is based. [71] If AuNPs can successfully overcome the natural barriers of biocompatibility, targeting and toxicity then they have the potential to revolutionize cancer treatment. For this, the AuNPs would have to carry specific peptides, payloads and polymers with quantities sufficient enough to target the cell, resist a biological response, initiate uptake and deliver a therapeutic. [27]

2.6 Biocompatibility of Gold Nanoparticles

AuNPs have been widely reported as being non-toxic in a range of *in vitro* and animal studies. [72,73] However, it is recognized that the published literature on AuNP toxicity varies both in methodology and conclusions, with several publications reporting toxic effects [2,48,47]. For example it has been reported that citrate capped AuNPs of 8-37 nm diameter were toxic in animal studies resulting in fatigue, loss of appetite, change in fur color, and weight loss. [76] Mironava *et al.* reports that 45 nm AuNPs display greater toxicity than 13 nm particles and are internalized via a different clathrin mediated pathways; they penetrate the cell membrane and accumulate in large vacuoles. [77]

Several studies have also reported toxic effects with various types of functionalized AuNPs; Pan *et al.* reported toxic effects (cell death) of triphenylphosphine functionalized 1.4 nm particles in four cell lines. [78] It is generally understood that functionalized AuNPs have greater toxicity. This poses a potential obstacle for the application of AuNPs *in vivo* as functionalization is paramount to synthesize a clinically useful AuNP treatment. Cho *et al.* also reported toxic effects in the case of

exposure to PEG functionalized AuNPs in animal studies, observing liver inflammation and apoptosis, with gene expression profiles showing alterations in apoptosis, cell cycle and inflammation mediators. [79] Goodman reported that cationic surface modification of AuNPs induced greater toxicity than anionically functionalized particles. [80] While Alkilany *et al.* also found greater toxicity in AuNPs with a cationic coating compared to uncharged particles. [81] Several studies have suggested that such toxic effects arise from the presence of unreacted chemicals left over from the synthesis process, such as sodium citrate or cetyltrimethylsmmonium bromine (CTAB). [82] This can be studied by determining the functional impact of the supernatant following centrifugation.

N. Chanda *et al.* overcame toxicity issues by functionalizing Au-198 nanoparticles (^{198}AuNPs) with gum arabic glycoprotein (GA) plant extract; by the end of the 30-day study, all control mice (30 μL of DPBS intratumorally) were sacrificed due to deteriorating health, whereas the treatment group (intratumoral injections of GA-198AuNPs (408 μCi) in DPBS (30 μL)) showed no cause for termination. It was also noted that the therapeutic payload had remained within the tumor site throughout the 30-day treatment regimen, as the therapeutic payload found within non-target organs was insignificant, with 2% to 5% of the injected dose being released from the tumor and cleared through renal pathways. The paper reports an impressive 82% reduction in tumor volume. [83] The influence of the method of attachment on toxicity is not fully understood and due to the complexity of clinically relevant AuNP preparations, it is necessary to conduct extensive cytotoxicity analysis prior to animal studies. It should be noted that the amount of *in vivo* toxicity data is limited and that the translation of cell studies to *in vivo* behavior is problematic. [84,85]

2.7 Synthesis of Gold Nanoparticles

The reduction of tetrachloroaurate solution by phosphorous in carbon disulphide is one which ignited the interest in gold nano formation in 1857. [86] After the seminal report by Faraday in 1857 of the reduction of a tetrachloroaurate solution by phosphorus in carbon disulfide, the preparation of AuNPs with controlled sizes and shapes received considerable attention, leading to the breakthroughs by Turkevich, Frens and Schmid in 1951, 1973 and 1981 respectively. [87] Although the work of

Turkevich and his co-workers is a landmark for AuNP synthesis, the synthesis is actually traceable back to Ernst A. Hauser and J. Edward Lynn who published their research in 1940 reporting the formation of gold colloids using $HAuCl_4$ and trisodium citrate (Na_3Ct) solution. [88,89] Further sophistication of the synthesis technique led to the stabilization of AuNPs with thiol groups by Mulvaney and Giersing (1993) and finally the Schiffrin group in 1994 whom devised a more efficient thiol stabilization methodology. [87]

AuNPs were produced at an approximate size of 20nm; Frens obtained a broad size range (15 – 150nm) by controlling the amount of trisodium citrate added which has been widely adopted by research groups such as Kimling *et al.* whom concluded that low sodium citrate levels results in larger molecules. [90,91] Another example of chemical AuNP synthesis, via the reduction of $HAuCl_4$ is the Brust-Schiffrin method. This two-step method allows the synthesis of AuNPs in sizes of 5 nm or less. The relative ease of synthesis coupled with the high thermal and air colloidal stability of the AuNPs have resulted in the wide spread adoption of this technique. A limitation is that the AuNPs are typically stabilized using a separate thiol terminated group such as an alkanethiol, which can be difficult to subsequently replace with other functional groups. [30,92–96]

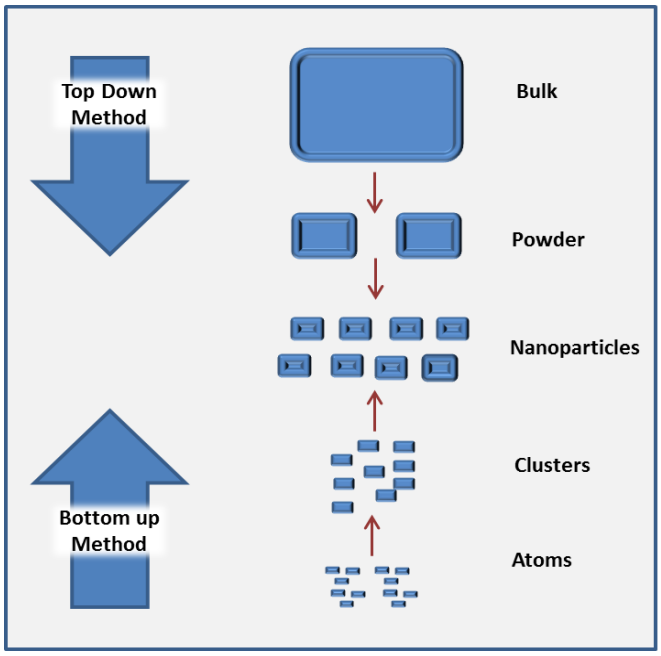

Figure 2-4 Schematic dictation of both the "Top Down" and "Bottom Up" methods

Nanoparticles can be prepared by either “top down” or “bottom up” approaches. A schematic of both these approaches is illustrated in Figure 2-4. For “top down” procedures a bulk state is systematically broken down in steps for the synthesis of the nanomaterial. In this case particle formation is generally controlled by a pattern or matrix and is considered limited concerning the control of the size and shape of particles as well as further functionalization. [30,97]

“Bottom up” approach is one in which the material is synthesized from individual molecules utilizing reduction. This reduction method involves two steps, nucleation and successive growth. When both these progressions are completed in the same process it is known as *in situ* synthesis. Seed-growth enlarges the nanoparticles step by step, initially small seeds are prepared, those seeds are then added to a growth solution, Natan *et al.* pioneered gold nano seeds by utilizing citrate as the reducing and capping agent of spherical seeds. In this procedure, AuNPs between 20 nm and 100 nm were prepared by adding citrate-capped, $NaBH_4$-reduced seeds into a “growth” solution containing a mild reducing agent such as citrate. [98,99] The newly reduced Au^0 then grows on the Au seed to develop the nanoparticles. [30,100]

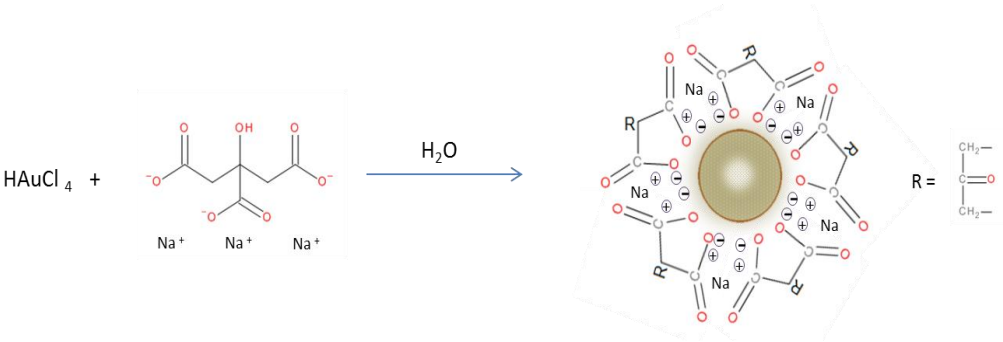

Figure 2-5 AuNP synthesis using the Turkevich method adapted from Zhao et al. and taken from Harrison et al. 2016 [30]

The synthesis of AuNPs using chemical in situ synthesis by means of the Turkevich method (Figure 2-5) is elegant as it utilizes citrate as both the stabilizing and reducing agent. Citrate capping results in a distinct advantage as the citrate ions (which display a surface potential of -20 - -40 mV as observed by DLS) are loosely

bound on the nanoparticle surface and can therefore be easily replaced by external groups. In the approach $HAuCl_4$ solution is brought to the boil and whilst undergoing vigorous stirring, an aliquot of trisodium citrate (Na_3Ct) solution is added. The process is generally accepted as nucleation and growth, however there are various discrepancies in the literature, with the number of proposed growth mechanisms almost being the same as the number of publications on this topic; ranging from nucleation and growth, an 'organizer' model, Ostwald ripening and a Finke-Watzky growth mechanism. [90,101–107]

Upon the addition of sodium citrate, a color change will occur from clear yellow to blue. It has generally been accepted that this color change indicates the formation of the nuclei and the following change from blue to red indicates the formation of the nanoparticle itself. However this topic is controversial in the literature. Nucleation events are thought to be induced by the production of dicarboxy acetone (DCA) which is a product of the oxidation of sodium citrate. The auric salt is then reduced to aurous salt and Au^0; the aurous salt is then assembled onto the Au^0 atoms to form AuNPs. Thus reflecting that the actual stabilizer in the Turkevich/Frens method is dicarboxy acetone as a result of oxidation and not the citrate itself. [108]

Studies in 1994 attributed the blue color to the reversible aggregation of primary particles; this was only to be later redefined as the formation of 2D nanowire networks or the formation of linear assemblies from clusters. Mikhlin *et al.* hypothesized the growth mechanism as being the formation of liquid domains from Au clusters and the formation of aggregates. [109] The uncertainty in this area is further empathized by the publication by Wuithschick *et al.* in 2015 that highlights the work of Polte *et al.*.. Polte *et al.* combined X-Ray scattering (SAXS) and X-Ray absorption near edge spectroscopy (XANES) to allow real time measurements of the reduction of Au^{3+} and monitoring of the particle growth in situ. [110,111] Instead it was declared that the *in situ* process is comprised of four steps, the partial reduction of the precursor and the formation of small clusters from Au monomers. The formation of nano seeds (radii >1.5nm) from these clusters and the attraction of the remaining gold ions to the seeded particles and the subsequent attachment of the ions as co-ions in the electronic double layer (EDL) . The final step involves the reduction of ionic gold and the growth of the gold monomers on the seed particle surfaces until the

precursor is expanded. [110,111] Therefore, it was concluded that the origin of the blue color during the initial phase is misinterpreted, that there are no aggregates formed during the Turkevich method, and the bluish color is most likely caused by the attachment of gold ions in the EDL and the subsequent change of their electronic properties. [90,101–107]

2.8 Surface Functionalization

Au-citrate bonds are very weak (Au-O_{COOH} (~2 kcal/mol)), this results in the Au-citrate bonds being easily substituted with stronger bonds, such as thiolate bonds (Au-S (~40 kcal/mol)). [30] [112] This reaction can be carried out with relative ease under ambient conditions, for example, this replacement reaction has previously allowed the successful conjugation of gold with thiolate DNA and Polyethylene Glycol (PEG), in the form of a mixed monolayer. [30,113,114] Throughout this Thesis, unless otherwise stated, conjugation refers to the functionalization of the AuNP with the respective ligand and/or peptide via covalent bonding. While the Au-thiolate reaction is commonly used throughout the literature, there are a range of limitations associated with utilizing the Au-thiolate bonds. The main limitations associated with this method of surface functionalization include the potential for irreversible aggregation, minimal control over the arrangements of the groups on the surface and potential issues with the biological availability of shorter ligands when used in conjunction with longer ligands such as high molecular weight PEG.

PEGylation is the most common way of reducing uptake by the Reticular Endothelial System (RES), thus enhancing circulation time *in vivo*. Referring to Table 2-3 and the later Table 2-5 it is apparent that PEG or the lower molecular weight Oligo Ethylene Glycol (OEG) variety are the most widely adopted anti-fouling agents, with a limited number of studies adopting alternative agents such as BSA. PEG produces a steric barrier which hinders the attachment of phagocytes by preventing non-specific protein adsorption. [115,116] It has been widely reported in the literature that ‘as synthesized’ AuNPs are readily recognized as foreign *in vivo* and consequently a protein corona is formed, encapsulating the AuNP for removal. PEG reduces non-specific protein adsorption of serum proteins thus increasing circulation time while rendering AuNPs stable at *in vivo* salt concentrations. [73,117,118]

PEGylated gold nano shells were one of the first models to successfully harness the potential of metallic nanoparticles for use in photothermal ablation therapy. [119] AuNPs capped with both PEG and targeting ligands hold great promise. For example, AuNPs functionalized with both PEG and tumor necrosis factor alpha resulted in a significant reduction in tumor volume and enhanced survival in MC-38 tumor-burdened C57/BL6 mice. [60–62] A snapshot of various functionalization ligands are highlighted in Table 2-3.

Table 2-3 Summary of ligands used for AuNP functionalization and their intended application

d.nm	Ligand	Application of functionalization ligand	End nanoparticle application	notes	ref
5	Cetuximab & Gemcitabine	Cetuximab is targeting, gemcitabine is therapeutic	DDS for pancreatic cancer	in phase 2 of clinical trial	[120]
2-100	Trastuzumab, antibodies	Targeting	drug delivery, SK-BR3 breast cancer	internalized into cytoplasm by cross linking with HER-231	[121]
110	PEG	Enhanced circulation time	PC3 human prostate cancer xenografts	complete resolution of tumor in 93% of mice	[122]
2	Tetra ethylene glycol, TTMA ligand and BODIPY	The dye molecule doped into the particle monolayer provides an analogue for hydrophobic drugs and allows facile detection of payload release.	Payload release		[13]
2	Trimethylammonium and DNA clusters (MMPCs)	Inhibition of DNA transcription of T7 RNA polymerase.	DNA release	Release caused by intracellular concentrations of glutathione	[123]
4	Polyethyleneimine and β-gal DNA	Delivery of plasmid DNA into monkey kidney cells (COS-7)	Gene therapy		[124]
10	PEG, thioctic acid and folic acid	Targeting	Uptake by folate receptor positive (FR+) cancer cells via receptor-mediated endocytosis	Solubility over a broad range of pH and ionic strength values	[125]

2.9 Targeting

Nanoparticles can enhance the intracellular concentration of drugs in cancer cells while avoiding toxicity in normal cells. [126] There has been considerable debate about the mode of entry of the AuNPs into cells, with the most likely being non-specific receptor mediated endocytosis (RME). [127]

Before AuNPs can internalize into the desired cancerous cell, the AuNPs must accumulate at the desired tumor site. This can be achieved via both passive and/or active targeting strategies. *In vivo* AuNPs can accumulate at the tumor sites passively due to a phenomenon known as the Enhanced Permeability and Retention factor (EPR). This phenomenon is a result of leaky vasculature with wider fenestrations than normal vasculature which allows the nanoparticles to pass through (Figure 2-6).

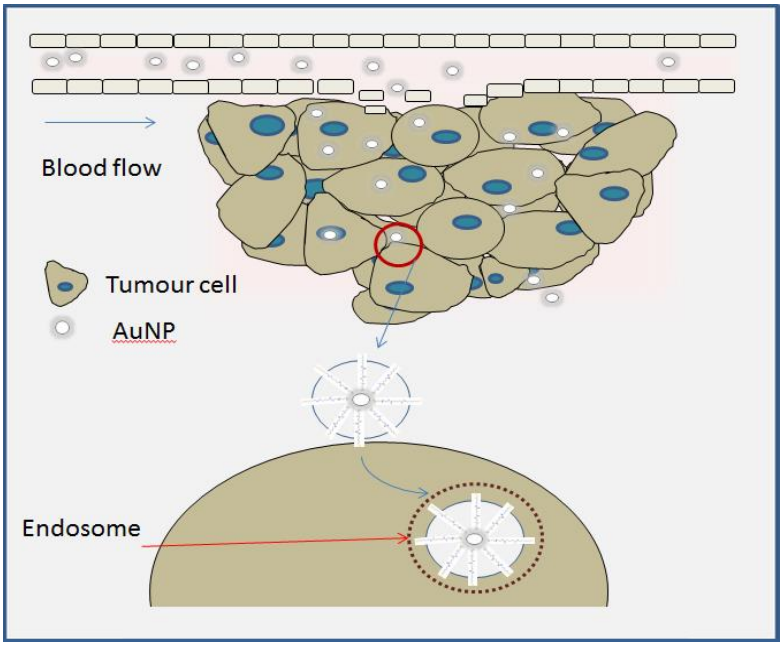

Figure 2-6 Schematic of the Enhanced Permeability and Retention Factor

Previous experimental data which utilized plasma proteins and synthetic polymers and various conjugates showed that macromolecules accumulate in solid tumors and are retained there for longer periods of times, thus lending the name, enhanced permeability and retention. [128] Molecular substances of a lower weight are not

retained, and are therefore returned to circulation at a greater rate. [129] Tumors also have a unique blood flow. Studies conducted in 1981 discovered that tumor blood flow could be increased through inducing hypertension by infusing angiotensin II; whereas blood flow in the normal organs remained constant irrespective of pressure. [130] This led to the conclusion that the tumor tissue was unable to auto regulate the homeostatic control of the blood flow. Therefore, manipulation of the blood pressure may lead to enhanced AuNP accumulation and consequently enhanced drug delivery.

The EPR effect is a result of tumor vasculature which is limited at poorly differentiated cancers, it also allows the possibility of detection and uptake by the RES. [115] A major challenge for improving anticancer treatments is to direct the therapeutic agent specifically to the tumor cells or tumor blood vessels, thus enhancing the efficacy of the treatment and decreasing these undesirable side effects. Therefore the application of a targeted drug delivery system is significant for reducing the undesirable side effects of anticancer drugs in healthy cells/organs.

Active targeting is the functionalization of the AuNP surface with ligands for specific recognition by cell receptor surfaces (Figure 2-7). These can be in the form of antibodies, peptides or small molecules which can be used to recognize specific receptors on the tumor surface; which can then be followed by receptor mediated endocytosis and nanoparticle internalization. [131]

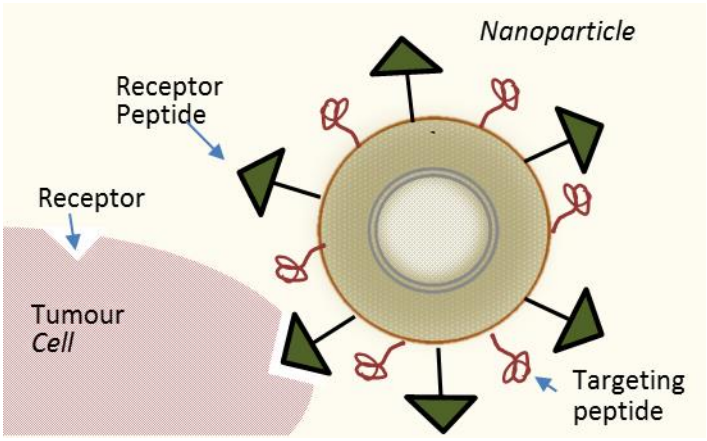

Figure 2-7 Schematic of active targeting using specific receptor sites found on the cells

The idea of tumor targeting is one which is currently contentious, recent work has shown that targeting ligands do not increase the total accumulation in the tumor but instead functions to increase the receptor mediated internalization. [132–135] Therefore it is argued through the literature whether targeting has any influence on internalization, or if they are two separate entities. Quantitative pharmacokinetic and biodistribution data has previously shown that targeting ligands only marginally improve the total gold accumulation in xenograft tumor models for AuNRs in comparison with non-targeted controls. However targeting could greatly alter the intracellular and extracellular nanoparticle distributions. When the AuNRs were administered via intravenous injection, it was found that the active molecular targeting of the tumor microenvironments (e.g., fibroblasts, macrophages, and vasculatures) did not significantly influence the tumor nanoparticle uptake. [131] There is also a considerable amount of opposing data showing that the use of tumor targeting ligands is effective in delivering imaging and therapeutic agents into solid tumors. [136–141] For example, Fluorescent studies have successfully identified that by conjugating the nanoparticles with labelled antibodies that there is a higher tumor uptake (measured on the basis of per gram of tumor mass) compared to that of the unconjugated species. [136] [138] [135] [132]

It has also been shown that PEGylated liposomes co-functionalized with HER2 antibodies have previously been used for targeting and cellular internalization. While it was found that they were successfully internalized into the tumor cells, the total volume was not different from the unconjugated nanoparticles [134]. This concluded that while not adversely affecting the internalization, there was no obvious benefit to targeting the nanoparticles with HER2. This conclusion has since been complemented by the work by the Davis group whom used transferrin to target the tumor cells, it was found that it improved the cellular internalization but did not increase the total tumor uptake. [132,133]

Adding yet another variable is the concerns that using a targeting ligand may in fact hinder the nanoparticle potential by initiating opsonization at a higher rate. PSMA is a Prostate Specific Membrane Antigen that is found in abundance on the membrane of prostate cancers. It is also commonly referred to as glutamate carboxypeptidase II (GCPII) and is a classic type – II membrane glycol protein and acts as an enzyme

biomarker target due to its expression in both primary and metastatic prostate cancer cells. [142–146] PSMA can be induced for internalization by bound antibodies or inhibitors. The Liu group developed a novel approach by the synthesizing of phosphoramidate peptidomimetic inhibitors of PSMA. [142] Biotinylated PSMA inhibitor, CTT54 was found to have an exceptionally high affinity and rate of uptake and internalization. It worked based on a biotin – streptavidin coupling system, where the inhibitor would target and bind to the PSMA, concurrently using the biotin to attract cy5-streptavidin for drug delivery or imaging. [142,143]

Another method of targeting the prostate specific membrane antigen PSMA is by using an A10 RNA aptamer that binds to the extracellular domain of the PSMA. This methodology was investigated in LNCaP cells injected subcutaneously into the right flank of mice [144].

PSMA is only one of a few receptors for active targeting, both the Nrp-1 receptor and the laminin receptor Lam67R have been successfully targeted in PC3 cell lines by the Kumar *et al.* and Payton *et al.* respectively. [147,148] Although both displayed successful targeting, both groups used very different methods to do so. Kumar *et al.* sought to deliver the current anti-cancer drugs cisplatin, oxaliplatin and carboplatin by developing a glutathione stabilized AuNP. A lethal dose was administered to the cells by co-functionalizing the AuNP with a Nrp-1 targeting RGD peptide (CRGDK). [147] Payton *et al.* instead conjugated AuNPs with epigallocatechin-gallate (EGCg) which reduces tumor volume and targets the Lam67R receptors. Platinum based anti-cancer drug research holds great promise, high anticancer activity is displayed by the upregulation of nuclear factor kappa-B (NF-kB) protein expression and activation of NF-kB-DNA binding activity. [147,149]

Once targeted, the AuNPs must initiate internalization, while functionalizing the AuNP surface with PEG increases colloidal stability *in vivo*, it greatly reduces cellular uptake in comparison to citrate capped AuNPs. [73] This problem can be overcome by co-functionalizing the AuNP surface with ligands to initiate cellular uptake, such as a receptor mediated endocytosis peptide (RME) which operates effectively for nanoparticles. [150,151] Macromolecules and particles are internalized by phagocytosis, pinocytosis and receptor mediated endocytosis pathways such as

caveolae-mediated, clathrin-mediated and caveolae/clathrin independent endocytosis. [151,152] All these different pathways operate by using different cellular receptors, some of which would be unsuitable for AuNPs, such as phagocytosis. Therefore the most common way to obtain cellular internalization is by utilizing the receptors on the cell for receptor mediated endocytosis [150,151]. Cells absorb molecules (endocytosis) by the inward budding of plasma membrane vesicles containing proteins with receptor sites specific to the molecules being absorbed.

Various research groups such as Lui *et al. (2007)* utilized an RME peptide sequence CKKKKKKSEDEYPYVPN to enhance internalization into the cell. [153,154] It is also worthy of note that RME is dependent upon temperature and previous studies investigated the uptake of gold nanoparticles at 37 versus 4 °C. These results are in agreement with previous RME studies, where ligands did not enter cells at 4 °C but were only bound to the cell membrane. [127,155,156] A significant benefit of this approach is that it bypasses recognition of P-glycoprotein which is one of the main drug resistance mechanisms encountered by the AuNPs as they are enveloped by endosomes upon entrance into the cells. [126,157–159]

H5WYG, sometimes referred to as H5 is an endosomal escape pathway. Once internalized the problem emerges that it will be entrapped by endosomes for degradation, therefore with reference to Tkachenko *et al. (2003)* the identification of an endosomal escape pathway is crucial for nuclear targeting. [157]

There are a range of viral and bacterial proteins and synthetic peptides and polymers that have been synthesized to achieve endosomal escape, there are also various routes which can be taken, such as pH buffering and lipid bilayer fusion. A few of the proteins and synthetic peptides are outlined in the Table 2-4 which is adapted from Varkouhi *et al. (2010).*

Table 2-4 Commonly used endosomal escape pathways identified from the literature

Agent	Mechanism of escape	Ref
hemagglutinin (HA2)	fusion	[160–162]
dilNF-7	fusion	[163–167]
TAT	unclear	[168–171]
L2 from Papillomavirus	fusion	[172]
Pneumococcal pneumolysin (PLO)	pore	[173]
streptococcal streptolysin O	pore	[173]
KALA	fusion	[174]
bovine prion protein (bPrPp)	pore	[175,176]
SAP peptide	fusion	[177]

Literature has shown that endosomal escape can be achieved by the incorporation of analogues of viral proteins such as H5WYG which is taken from the N-terminal segment of the HA-2 subunit of the influenza virus hemagglutinin. [178] It is proposed that unprotonated amines would exhibit a proton 'sponge' effect, in which the unprotonated amines found on the H5WYG would absorb protons as they are pumped into a lysosome. This would result in more protons being pumped in and an increased influx of Cl- ions and water, ultimately causing osmotic swelling and rupture of the lysosomal membrane. [179]

H5WYG permeabilized the cell membrane at a slightly acidic pH but not at neutral pH, therefore as the pH drops towards degradation the peptide undergoes a conformational change which correlates with the protonation of the histidyl residues. [180]

The Midoux group showed great cell permeabilization at pH 6.4 that was not present at a pH of 7 and consequently increased the expression of genes transferred to cells as glycosylated polylysine-DNA complexes. Therefore, it was concluded the several

histidines become positively charged when the pH decreases which is induced by acidification of endosomes.

2.10 Optimizing Attachment

It is generally assumed that the higher binding energy of the covalent Au-S bond surface relative to the loosely bound citrate results in functionalization via ligand exchange. [21,181–185] However, in a detailed study using FTIR and XPS, Park and Schumaker-Parry found that a proportion of the citrate oxidizes into acetoacetate on the AuNP surface, and that it is largely this acetoacetate that is replaced by the thiol bound ligands. They also reported that much of the citrate capping remains after ligand attachment, with the citrate and thiol bound ligands forming a regular structure on the AuNP surface. This co-absorption, results in a lower ligand packing density on citrate capped AuNPs compared to that which has previously been observed with self-assembled monolayers of PEG on planar gold.

Whilst citrate capped AuNPs form stable colloidal suspensions, they aggregate under physiological salt concentrations and a protein corona is quickly formed in the body which leads to their removal. Aggregation is usually prevented by the repulsive force between particles due to electrostatic repulsion, steric exclusion or the synthesis of a hydration layer on the nanoparticle surface. [117,186–188] Thiol and disulfide containing ligands bind irreversibly to gold substrates, therefore the thiol containing amino acid groups cysteine and cystine (the oxidized dimer of cysteine) readily form self-assembled monolayers at these surfaces. [189–191] The adsorption of thiol bound ligands onto planar flat gold (111) surfaces has demonstrated that sulfur adsorption is influenced by the rate of oxidation of the gold and that many lattice structures are feasible and can be manipulated via the control of external factors such as pH. L-cysteine forms ($\sqrt{3}$x $\sqrt{3}$)R30° adlayers consistent with hexagonal packing, under neutral (H_2O) and slightly acidic (0.1 M $KClO_4$ +1 mM $HClO_4$) conditions. [189,192–195] The relationship of pH on binding proteins and peptides to gold is not very well understood, it has been previously reported that functionalization can be achieved by, ‘non-specific’ adsorption through altering the pH close to that of the pI of the protein or the nanoparticle so that the electrostatic repulsion is reduced. [196] It has also been suggested that AuNP – ligand surface binding can be initiated by

introducing an opposite charge on the desired ligand which is to be attached by van der Waals forces, hydrogen bridges, gold–thiol bonds (from cysteine residues) or by hydrophobic interaction. [186] 'As synthesized' citrate capped AuNPs have a zeta potential of approximately -30mV. Goldman *et al. (2002)* synthesized electrostatic interactions between negatively charged dihydro- lipoic acid (DHLA)-capped CdSe-ZnS core-shell QDs and a positively charged leucine zipper affixed onto the C-terminus of engineered recombinant proteins. It was reported that proteins absorbed onto the nanoparticles by electrostatic attraction if both partners are oppositely charged. [197–200] Adjustment of the pH to below the pI value (isoelectric point 10 - 10.5) has previously been used to bind avidin to AuNPs. [197,201]

As zwitterionic molecules, peptides can display both negative and positive charges on different functional groups simultaneously depending on pH. However, the ratio of functional groups bearing a charge changes with pH, resulting in peptides being predominantly positively charged at pH values below the peptides isoelectric point and negatively charged above. At the isoelectric point the overall net charge is zero. This offers the possibility to attract peptides electrostatically to negatively charged nanoparticles. [186]

2.11 Mixed Monolayer and PEG Linker Approaches to Co-Functionalization

Functional groups are typically designed to overcome specific barriers that limit therapeutic efficacy. These include ligands to promote the endocytotic and targeting potential of the nanoparticle whilst reducing undesirable nanoparticle agglomeration. This typically requires the development of multi-functional particles. Peptides are only an example of ligands which can be used to target tumors, increase cellular uptake, and target the nucleus. [24,136,147,153,157,158,202] Nuclear targeting is challenging due to four principles that must be satisfied for success. The nuclear probe has to enter the cell, escape endosomal/lysosomal pathways, and possess a nuclear localization signal (NLS) for nuclear interaction, while remaining small enough to cross the nuclear membrane. [157]

Three common methods are used for co-functionalization. The first uses a thiol terminated mono-functional PEG is used to partially cap the AuNP surface; the surface is then co-functionalized with additional ligands to form a mixed monolayer (Figure 2-8a). [158,184] The second method uses a hetero-bifunctional linker, typically in the form of BSA or PEG. One end is usually thiol terminated, which again binds to the AuNP surface while a second active functional group on the opposite end of the linker offers the potential to bind with a peptide or other functional ligand (Figure 2-8b). The linker approach can potentially offer complete surface saturation and offers the promise of improved biological availability as the peptide is on the end of the PEG as opposed to being on the AuNP surface. The third method of surface functionalization is a combination of both the mixed monolayer and linker approaches. First the nanoparticle surface is functionalized with both mono-functional and bifunctional PEG forming a mixed monolayer/linker complex, then a second ligand is used to co-functionalize the surface by fastening onto the end of the PEG linker. [203,204] Studies involving thiol bound PEG on planar gold, have confirmed that when saturated with PEG that the ligands adopt a monolayer arrangement of the surface [205,206] It has also been reported that 5000Mw thiolate PEG forms a monolayer on the surface of ~19 nm AuNPs with the ligands adopting an extended random coil confirmation. [12]

All three approaches have been widely employed in the synthesis of co-functionalized AuNPs for applications in cancer therapeutics. [182] While the use of PEG renders the AuNP stable under *in vitro* conditions it greatly reduces biological activity and cellular uptake. It can be seen from Table 2-5 that all three methods for co-functionalization have been successfully employed to enhance cellular uptake. Nanoparticles based on both the mixed monolayer and linker methodologies have also been used for sensing and monitoring biological events and Photodynamic Therapy (PDT). [58,204,207–209] Inconsistencies in the literature include the effect on colloidal stability, the resulting opsonization and the effect each methodology has on cellular internalization. Currently there is little consensus regarding which approach should be applied in a situation. However, from analyzing the literature which is summarized in Table 2-5, it is apparent that the greatest *in vivo* significance has been achieved by using the mixed monolayer arrangement, such as that reported by Paciotti *et al.* (42,44,53,54)

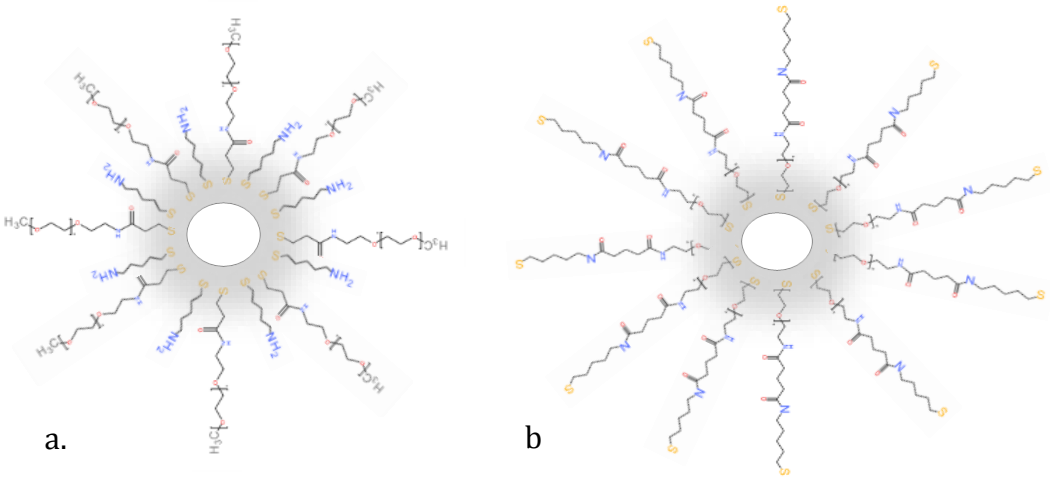

a. b

Figure 2-8 schematic illustrating a) mixed monolayer and b) bifunctional linker

*Table 2-5 Mixed monolayer versus hetero bifunctional linker (*NI – not included)*

d. nm	PEG M_W	Arrange-ment	Attached ligands	Internalization\ colloidal stability	Notes	Ref
10	900, 1500, and 5000	Mixed Monolayer	PEG, an adenoviral NLS, an adenoviral RME,	Entered HeLa cells in 6h, Found in cytoplasm or nucleus	5000 M_W PEG was internalized as efficiently as 900 Mw	[153]
17	5000	Mixed Monolayer	PEG, Bodipy Dye	Controlled release of dye	Inhibiting the initial burst release of payloads as well as preventing particle aggregation	[182]
14	NI	Mixed Monolayer	PEG & TAT peptide	Freely roam the cell including crossing the nuclear membrane in HeLa lines		[210]
NI	NI	Mixed Monolayer	Nanostars, TAT Peptide and Thiol PEG	Bound to the membrane or were found outside the vesicles in the cytoplasm	TAT Peptide enhanced BT549 breast cancer cell uptake	[211]
26	NI	Mixed Monolayer	PEG-Thiol & Tumor Necrosis Factor	7-10-fold increase was seen in the amount of TNF that is delivered to the tumor	In a small animal study, 15 µg-native TNF resulted in a 60% survival compared to the 100% survival after treatment with15 µg–PT–Au-TNF	[59–63]
80-290 Å	N/A	Linker	BSA Linker, SV40 large T NLS peptide	nucleus of HepG2 cells		[158,212–215]
25	N/A	Linker	BSA, SV40 large T NLS, adenoviral NLS, adenoviral RME adenoviral fiber protein	Found in cytoplasm/trapped in endosomes and/or nucleus		[157]
20-30	N/A	Linker	Acetal-PEG-PLA co-polymers	PEG linker allowed colloidal stability in what was considered 'harsh environment' [216]	Protein adsorption reduced with increasing the number of micelle coating	[217]
10-15	1500	Linker	Coumarin-PEG-thiol	Large dose found in endosomes OF MDS-MB-231 cells in culture	Flexible enough in the attached fluorescent ligand without compromising cellular uptake.	[218]
30	2080	Linker	PEG, Oxaliplatin	Unusual ability to penetrate the nucleus in the A549 lung cancer cells	Extensively cytotoxic	[149]
13	NI	Mixed Monolayer &linker Complex	OEG and cyanine 5 alkyl thiol terminated spacer	>99% uptake in cytoplasm	Cyanine 5 used for fluorescent tracking with confocal microscopy	[219]
4	3000	Mixed Monolayer &Linker Complex	HER2, PEG and C11PC photosensitizer	Readily seen in cell interior in SK-BR-3 and MDS-MB-231 cells		[203]

In the early 1990's the work of Feldherr *et al.* and Tkachenko *et al.* marks an early discrepancy in the literature regarding surface arrangement. Feldherr *et al.* investigated a "Trojan horse" using a BSA linker and an NLS sequence derived from the SV40 large T antigen. [157,158,212–215,220] The "Trojan horse" efficiently facilitated nuclear delivery to translocate into the nucleus of both HepG2 and HSC oral cancer cells respectively. This was challenged by Tkachenko *et al.* in 2003 who found a number of limitations when applying this BSA model in practice including colloidal stability inconsistencies and conjugates being found in the cytoplasm. [157,220] Thus authors such as Oyelere *et al.* adopted the use of a thioalkyl-triazole linker to efficiently facilitate nuclear delivery of AuNPs to HSC oral cancer cells and noncancerous human HaCaT cells. [220,221]

Consequently, however the frequent colloidal instability of peptide-BSA-AuNP conjugates prompted the exploration of PEG based alternative formulation strategies for cell-targeting nanoparticles. As a result, from 2007 onwards it was felt that a new approach for Feldherr's model may be more beneficial, resulting in the synthesis of a mixed monolayer using 10nm citrate coated AuNPs modified with mono functional PEG, an adenoviral NLS Sequence (CGGFSTSLRARKA) and/or an adenoviral RME sequence (CKKKKKKSEDEYPYVPN). [153] The mixed monolayer approach overcame the stability issues identified by Tkachenko *et al.*, thus igniting the hypothesis that a linker may compromise nanoparticle colloidal stability. However, it is difficult to make direct comparisons due to differences in cell lines, peptides used and/or the synthesis technique. [157,221]

Another apparent inconsistency in the published literature is the role of peptide length in relation to biological availability. Initially it was believed that when functionalizing a nanoparticle with several biologically active ligands such as peptides that these should all be of a similar length. [157] It has been suggested that if the stabilizing agent, such as PEG, exceeds that of the peptide then it may sterically hinder the peptide's function. [153] However, in contrast to that, it is possible that if the PEG length is shorter than that of the peptide, that the AuNP could instead have an 'anti-PEG' effect. This is a key issue identified through this Thesis, as it has been reported that the PEG length has to exceed that of the peptide to shield the nanoparticle from opsonization for maximum circulation. [217,222] Therefore it is

plausible that attaching the peptide onto the end of the PEG chain would result in an anti-shielding (‘anti-PEG’) effect, making the AuNP susceptible to non-specific protein attachment and potential removal by the immune system. [131,153,222]

This ignites the hypothesis that it may be crucial to have the length of the stabilizing agent exceeding that of the functional peptide, thus shielding the nanoparticle from opsonization and maximizing circulation time *in vivo* and preventing an ‘anti-PEG’ effect. [131]

It is apparent that a simple consideration of ligand length does not fully predict the biological availability of functions allocated to the AuNP surface. Indeed some of the biological results have been obtained using AuNP functionalized with PEG and short biological groups in a mixed monolayer arrangement. In a recent uptake study by Liu *et al.* using HeLa cells, PEG5000/RME nanoparticle conjugates were shown to have a four-fold higher endocytotic potential over PEG900/RME conjugates. This finding supports the mixed monolayer configuration, indicating that steric hindrance conferred by PEG chain length is not a critical factor-affecting uptake. [153] In support of these findings are various studies which have observed excellent biological performance for mixed monolayer functionalized AuNPs. [56,61,63,223]

In 2011 and 2012 using a TAT peptide both Krpetic *et al.* and Yuan *et al.* respectively formulated a mixed monolayer comprising of PEG and functional peptides (CALNN-based peptides, TAT, Pntn, and NLS which were all oligopeptide sequences derived from elongations of the standard stabilizing pentapeptide CALNN). The authors reported that particles were found roaming freely in the cytosol and able to negotiate intracellular membrane barriers freely. [210] Using nanostars in BT549 breast cancer cells Yuan *et al.* concluded that attaching a TAT peptide in a mixed monolayer arrangement enhanced uptake. [211] Furthermore, Kumar *et al*. utilized the mixed monolayer configuration to allow the controlled release of dye over a period of 2 h, inhibiting the initial burst release of payloads as well as preventing particle aggregation by using a PEG array. [182]

A more clinically significant development was made in 2006 with the development of CYT-6091. In this preparation, TNF was assembled onto a 26 nm AuNP with PEG-Thiol forming a mixed monolayer. A 7-10-fold increase was seen in the

amount of TNF that was delivered to the tumor in comparison to native TNF. It was also found that a 7.5 µg/ml injection of CYT-6091 was as effective as 15 µg/ml native TNF, and that the 15-µg native TNF dose resulted in a 60% survival compared to the 100% survival after treatment with 15 µg PEGylated Au-TNF. This data led to the development of CYT-6091 by CytImmune with subsequent progression into clinical trial. [59–63]

Despite the reported success of the mixed monolayer approach, there are potentially significant benefits of attaching ligands using a bifunctional PEG linker. The ability to develop a method of attaching active groups to the end of the PEG rather than directly to the AuNP surface may allow for enhanced colloidal stability and bioavailability. [217] Otsuka *et al.* utilized a hetero bifunctional PEG obtaining acetal-PEG-PLA on aminated polypropylene surfaces. The aldehyde group was then further reacted with ligand molecules and saccharide ligands for the development of a non-viral delivery system. It was found that the PEG linker allowed colloidal stability in what was considered a 'harsh environment'. [216] Furthermore, it was concluded that protein adsorption was reduced with increasing density of the PEG coating. [217]

A benefit of using a bifunctional linker would be to allow the AuNP surface to be completely saturated with PEG and the remaining active end groups could then to be used to anchor a biologically active group. This would have a two-fold benefit as firstly, it would allow direct contact with the receptors on the tumor cell, and secondly it would allow more of the required therapeutic, targeting or other payloads to be attached in comparison to a mixed monolayer arrangement.

Even when fully saturated with PEG the nature of the packing may allow further interaction with the gold surface. Shi *et al.* investigated gold nanoparticles functionalized with 11-mercaptoundecanoic acid (Au-MUDA) and found that even in excess surfactants, a closely packed 100% coverage could not be achieved. Polystyrene was added to AuNPs that were completely saturated with MUDA, if the AuNP surface was successfully saturated, then binding the polystyrene would not have been possible, however it was found that even in excess of bifunctional ligands, polystyrene particles were successfully conjugated to the surface. [202] Understanding the packing of PEG on the AuNP surface is critical to any subsequent

co-functionalization. It has been reported that 5000 M_W PEG adopts a somewhat extended random coil when fully saturating the surface of a ~17nm AuNP. [184] This packing density was originally thought to be higher than that reported for PEG coated planar gold due to the highly curved AuNP surface resulting in less confinement at the free end of the PEG. However more recent publications have since argued that citrate is not displaced by the thiol groups, and as such the co-absorption of these molecules on the AuNP surface could consequently result in as lower packing density in comparison to planar gold, which would too explain how even after an excess of bifunctional ligands was added to the Au surface by Shi *et al.* that polystyrene could still be added to the surface. [188,224]

Kumar *et al.* and Sanz *et al.* both achieved surface saturation in 2011 and 2012 respectively. Using a mono-functional PEG and the combination of UV/Vis analysis and TGA, Kumar *et al*. was able to show the point at which the AuNP surface was saturated by analysis of the PEG concentration in the supernatant determining an approximation of 1,140 thiol terminated PEG molecules per 17nm AuNP. [184] Sanz *et al.* developed a 14.47 nm AuNP two-step mixed monolayer and PEG linker complex, a schematic of which is illustrated in Figure 2-9. Initially the AuNP was functionalized with mono functional PEG and then an EDC coupling reaction was used to couple the carboxyl groups forming a bifunctional PEG which was subsequently used to bind to the primary amines of the TAT peptide. Both the

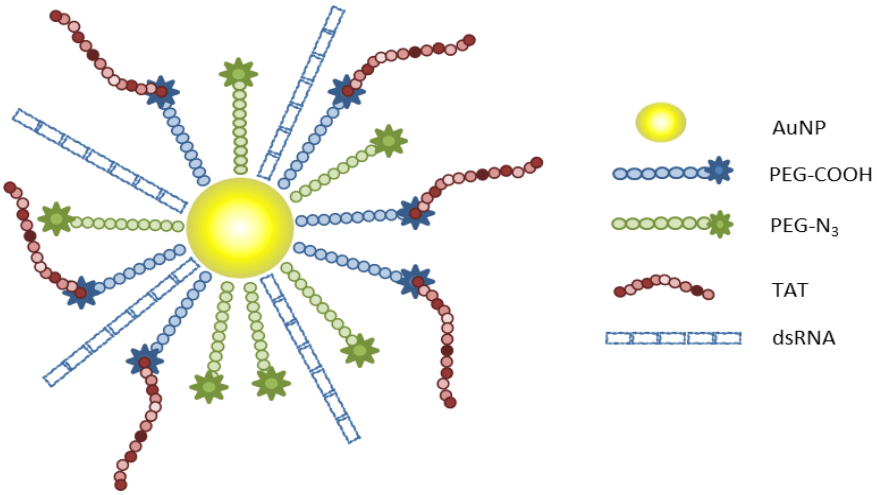

Figure 2-9 Schematic of Bio conjugation of the surface-modified gold nanoparticles with different thiol-PEG layer compositions

bifunctional complex and a mono functional PEG were then anchored to the AuNP surface formulating a mixed monolayer of bifunctional ligands. [225] It was concluded that approximately 5000 thiolate chains would cause complete saturation, and the degree of coverage was controllable. Furthermore, the groups reported that the degree of binding was stronger for the linker and that the spacer played an important role in the loading yield of thiolate oligonucleotide. [225]

It is apparent from the literature that any advantages from the use of a bifunctional linker are not fully understood. It is possible that any benefits lie solely in enhanced colloidal stability [216,217,226]; however there has been a wide array of cellular studies showing successful internalization utilizing the linker surface arrangement but very few preparations have been evaluated *in vivo*.

Feldherr *et al.* synthesized a polyvalent RNA-nanoparticle conjugate (RNA-Au NPs) using RNase-free inorganic gold nanoparticles with a PEG linker and alkylthiol; analytical flow cytometry confirmed uptake of the RNA-Au NPs in >99% of the cell population. [203,219] Another positive outcome involved the synthesis of a combined chemo-AuNP conjugate. Oxaliplatin was grafted onto AuNPs via a PEG linker for the treatment of A549 lung adenocarcinoma cells. Nanoparticle uptake as determined by TEM indicated intracellular accumulation of the chemo-AuNP conjugate, while simultaneously exhibiting a high cytotoxic profile. While this may benefit the final goal of promoting tumor cell death without external stimulation, the passive targeting of the molecule to the cancer site poses a major limitation likely resulting in high level systemic toxicity. This therefore highlights the necessity of active targeting and indicates that the use of a linker may be particularly appropriate for targeting as the loading yield may be increased relative to a mixed monolayer arrangement allowing for more specific targeting and the conjugation of a therapeutic ligand. [149] These studies proved that the linker was stable without compromising cellular uptake. [203,218,219]

2.12 Conclusions

AuNPs have widely been shown to have excellent advances both *in vitro* and *in vivo*. A vast amount of work has been conducted using gold nanoparticles co-

functionalized in either a mixed monolayer or bifunctional arrangement, and while some excellent results have been reported for multifunctional AuNPs produced using PEG linkers, the arrangement of the groups onto the surface is not well understood. There is also a niche which remains to be exploited regarding which surface arrangement may result in improved *in vitro* and *in vivo* colloidal stability, or if literature is correct in predicting an 'anti-PEG' effect if the attached ligand exceeds the length of the stabilizing ligand. The niche also requires an in-depth characterization profile of each surface arrangement and investigations into the biological response regarding non-specific protein adsorption, cellular toxicity and cellular uptake. In addition, the studies which have adopted the approaches mentioned previously do not present evidence to support the arrangement of ligands on the surface. Indeed, given the problems discussed in achieving a tightly packed PEG layer on the AuNPs it may be that when using PEG linkers that some or all of the subsequently added ligands attach directly onto the AuNP surface instead of onto the end of the PEG linker. This however remains to be confirmed. Several methods have been identified in the literature which should help in concluding the AuNP surface arrangement, such as FTIR, UV/Vis and DLS analysis.

3. MATERIALS AND METHODS

3.1 Introduction

This chapter details both the materials and methods employed to synthesize the various AuNP systems. It describes the techniques and methodologies used for the synthesis of gold nanoparticles and the functionalization with PEG and other ligands.

The chapter will finish with a description of the protocols and techniques used to investigate the colloidal stability and opsonization of each of the conjugates and the characterization methods employed throughout this Thesis.

3.2 Experimental Overview

The aim of this research is to determine whether the method of co-functionalization would directly affect the colloidal stability, and biological response of a gold nanoparticle conjugate for prostate cancer therapeutics. To synthesize a stable colloidal complex, extensive characterization and *in vitro* analysis must be carried out and understood. Thus, the research can be sub divided into various sections, namely, the synthesis and characterization of the AuNPs, the modification with PEG followed by co-functionalization with peptides. The synthesis of a mixed monolayer or linker system. Investigations into the arrangement of peptides on the AuNP surface. This will also detail the methods applied to optimize the attachment of the peptides via investigating the role of pH.

3.3 Materials

Materials used for the synthesis and characterization of gold include Gold (III) chloride hydrate, Sodium Citrate $Na_3C_6H_5O_7$ molecular weight 294.1g/mol and potassium bromide (KBr) were all purchased from Sigma Aldrich UK. PEGylation was carried out by using either Methoxyl PEG Thiol mPEG-SH MW 5000 or Thiol PEG Succinimidyl Glutaramide SH-PEG-SGA MW3500 which were both purchased form Jenkem; and co-functionalization was achieved by using a combination of CKKKKKKSEDEYPYVPN Receptor Mediated Endocytosis peptide (RME),

GCGLFHAIAHFIHGGWHGLIHGWYG & GLFHAIAHFIHGGWHGLIHGWYG Endosomal escape pathway peptide (H5WYG) or the targeted Nrp-1 receptor peptide both with and without FITC fluorescent labeling (CRGDK and FITC-Ahx-CRGDK) purchased from BIOMATIK (UK). All peptides investigated were synthesized with a minimum of 99 % purity measured by HPLC, apart from the H5WYG peptide which did not contain a thiol containing cysteine residue. TBE running buffer, MTT (3-[4, 5-dimethylthiazol-2-yl]-2, 5- diphenyl tetrazolium bromide; thiazolyl blue), DMEM media sodium dodecyl sulfate (SDS) (ThermoFisher) and Dimethylformamide (DMF) and Dimethyl sulfoxide (DMSO) were purchased from Sigma Aldrich.

The Glassware involved two 500 ml neck parallel round bottom flask, one 1000 ml neck parallel round bottom flask, water condenser magnetic flea and round bottom and flat bottom heaters. 50 ml polyethylene plastic containers were used for storage as well as 50 ml plastic centrifuge vials and 500/1000 ml glass jars. Biological samples were kept refrigerated while all other samples were stored at room temperature. Prior to use, all glassware was rinsed with aqua regia (1:3 nitric acid : hydrochloric acid) and then rinsed with distilled water and dried at 100 °C in a vacuum oven.

The instrumentation involved included Perkin Elmer Lambda 35, 1.4 ml glass spectrometer cuvettes, Varian 640-IR FTIR Spectrometer, Malvern ZetaSizer Nano ZS Series. Disposable 2 ml cuvettes type DTS0012.

3.4 Methods

3.4.1 Synthesis of Gold Nanoparticles by the Turkevich Method

Gold nanoparticles were synthesized by an adaptation of the Turkevich/Frens method. [30,100] 0.01 wt% solution of chloroauric acid ($HAuCl_4$) was prepared by diluting 0.01 wt% of Gold (III) Chloride Hydrate in 1L of distilled water. The working solution was brought to the boil under reflux whilst undergoing vigorous stirring via a magnetic flea. 22.5 ml of 1 wt% sodium citrate solution was added. The solution changed from transparent to blue, indicating the formation of the nuclei, then blue to wine red, indicating the formation of the nanoparticle itself. The solution was left to boil under reflux for a period of 2 hours and the applied heat was switched off and left to stir vigorously for a minimum period of 8 hours. [12,91,108] All the samples were kept refrigerated after synthesis and all glassware was cleaned with aqua regia before each use.

3.4.2 Functionalization of PEG Modified Gold Nanoparticles

The AuNPs synthesized by the Turkevich method were functionalized with either mono functional or hetero bifunctional Polyethylene Glycol for enhanced colloidal stability and circulation time *in vivo*. A pre-calculated weight of PEG was measured and dissolved in 1 ml of distilled water and added to the required mount of gold stirring by a magnetic flea under ambient conditions. [184] Both PEGs were terminated with a thiol group for ease of surface functionalization. The loosely bound citrate capping the AuNPs because of the synthesis method could therefore be easily displaced by the stronger thiolate ligands. Both structures can be seen in Figure 3-1.

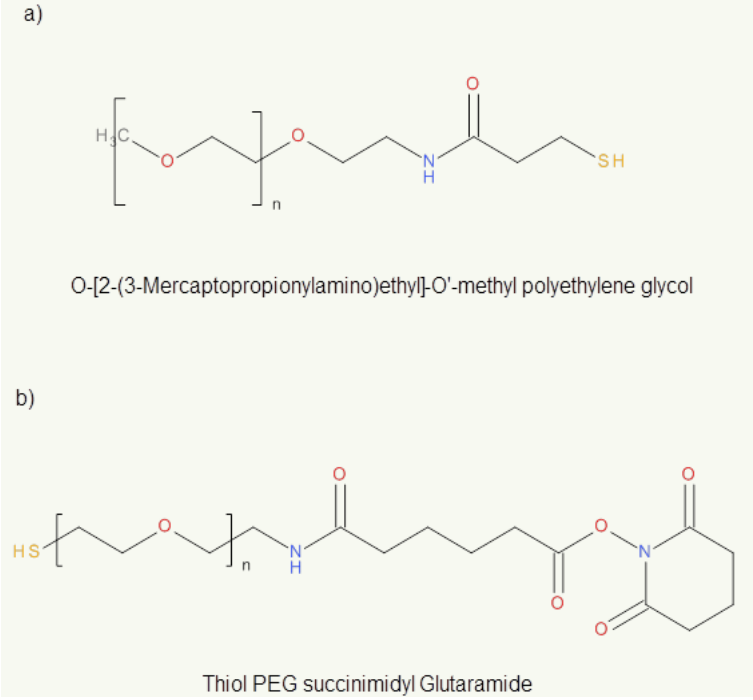

Figure 3-1 Chemical structure for a) mono functional PEG and b) hetero bifunctional PEG

A previous publication from this research group synthesized AuNPs with increasing weights of SH-PEG (5000Mw) and combined UV/Vis analysis with Thermogravimetric analysis of the supernatant of the AuNP conjugate to produce Figure 3-2. The relationship between the concentration of PEG used during synthesis, the amount bound to AuNPs surface after washing and that remaining in the supernatant is illustrated in At low concentrations, all the PEG added adheres to the AuNPs, with increasing amounts remaining in the supernatant at higher addition rates as the AuNP surface becomes saturated. It was observed that saturation of the AuNP surface with tethered PEG occurs at a PEG loading level of ~14 wt.% and that saturation occurs for PEG 5000Mw at approximately 25 µg/ml. Therefore to saturate the AuNP surface with 5000Mw PEG, a minimum of 25 µg/ml should be added, whereas to partially cap the AuNP surface, an estimate of 10.7 µg/ml of 5000 Mw PEG should be added. Partially capping the AuNP surface allows room for further functionalizing the surface with other peptides, drugs or other ligands. This relationship can therefore be used to estimate the µg/ml required to achieve partial capping to varying degrees.

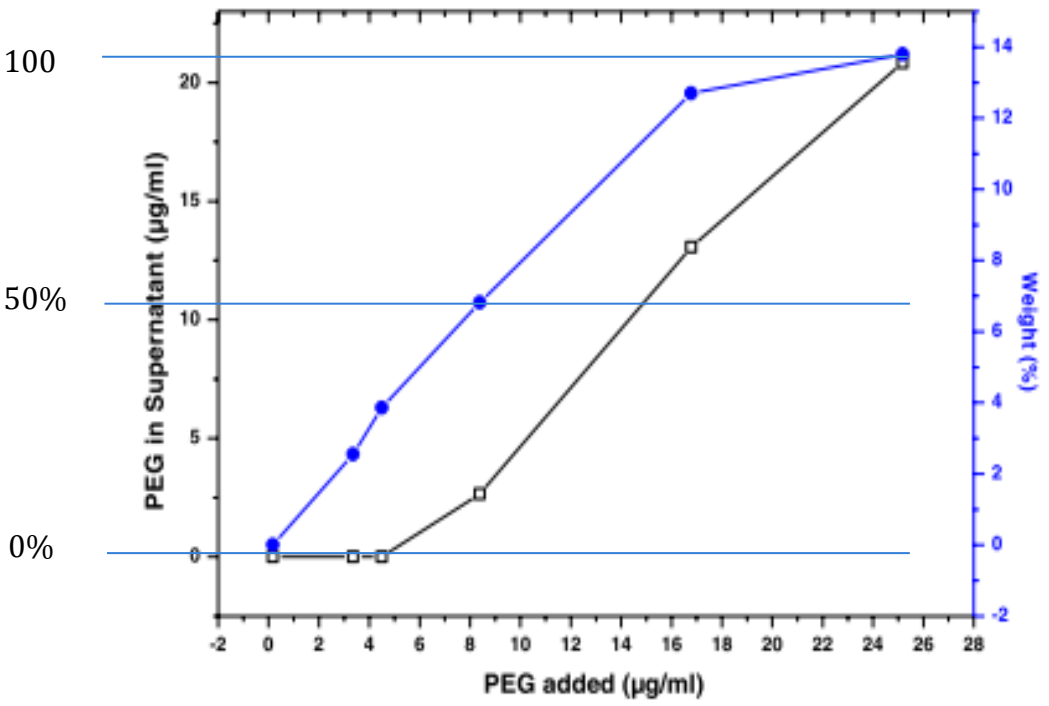

Figure 3-2 PEG concentration remaining in supernatant after first centrifugation and bound to the AuNP surface measured by UV–Vis (black) and TGA (blue) taken from Manson et al. [184]

An interpretation of this relationship using the molecular weights can therefore be implemented to identify the required weight of bifunctional PEG of a different molecular weight to achieve the same level of surface saturation.

Equation 3-1

$$\text{degree of saturation} = \text{desired saturation based of Figure } 3-2(\mu g/ml) * \left(\frac{\text{desired Mw}}{5000\ \text{Mw}}\right)$$

Therefore, implementing Equation 3-1 above, for the bifunctional PEG SH-PEG-SGA (3500Mw), the point of complete saturation should theoretically be calculated by: 25 μg/ml *((3500 Mw)/ (5000 Mw)) = 17.5 μg/ml of PEG 3500Mw. An example of the calculations drawn from this equation can been seen in Table 3-1.

Table 3-1 Calculated concentrations required for desired surface saturation of each ligand based upon the study of PEG 5000M_W using TGA and UV/Vis analysis of the supernatant [184]

Surface Coverage (%)	Sample (μg/ml)			
	SH-PEG	SH-PEG-SGA	RME (mixed monolayer)	RME (hetero bifunctional linker)
12.5	2.67	1.86	1.115	1.47
25	5.34	3.73	2.23	2.93
50	10.68	7.47	4.45	5.86
75	16.02	11.2	6.69	8.79
100	21.36	14.95	8.9	11.7
125	26.7	18.68	11.13	14.63

3.4.3 Washing and Calculating the Concentration of Gold Nanoparticles

Both the 'as synthesized' and functionalized AuNPs were collected and aliquoted evenly into 50 ml centrifuge tubes and centrifuged for 90 min at 13,500 RCF. 90 % of the supernatant was then decanted and discarded leaving the remaining 10 % of the AuNP as a pellet in the bottom of the centrifuge tube. The gold was then made back up to the starting volume and re-dispersed. The sample concentration was measured by Atomic Absorption Spectroscopy detailed in section 3.5.7 and sterilized by a mild heat treatment at ~ 65 - 75°C for 24 hours, as recommended by the World Health Organization (2015).[227] Sterility checks were performed using agar plates

and broth, visually inspected for contamination and compared to a positive and negative control.

3.4.4 Co-functionalized Gold Nanoparticles

Co-functionalization was achieved by returning the re-dispersed AuNP-PEG samples to a 500 ml round bottom flask. While continually stirring, 4.45 µg/ ml (calculated from Equation 3-1) of free RME peptide (dissolved in 1 ml of distilled water) was added. The samples were left for 8 h at room temperature to allow for complete reaction. The process of centrifugal washing was then repeated to remove any unattached reactants. The Receptor Mediated Endocytosis peptide and the targeting peptides were both cysteine terminated leaving a free thiol group at the N-Terminus for attaching to the AuNPs, while the H5WYG endosomal escape peptide had a Glycine group which contains an amine (NH_2) which also facilitates nanoparticle functionalization by displacing the citrate ions on the surface. Both amino groups are illustrated in Figure 3-3 and the peptides used throughout this Thesis are detailed in Table 3-2.

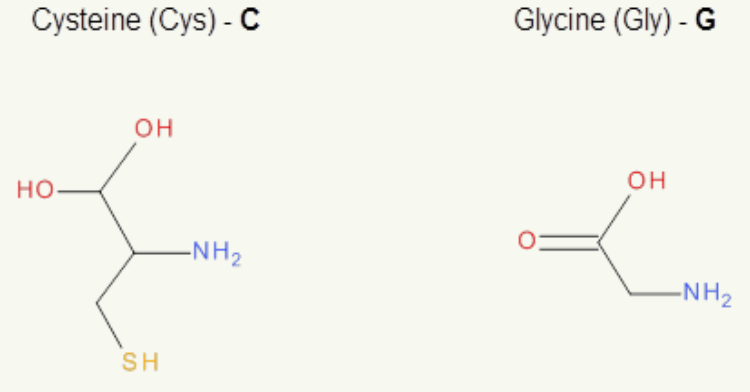

Figure 3-3 Chemical Structures for Cysteine and Glycine

Table 3-2 List of Ligands for AuNP co-functionalization

	Moiety Information			
NAME	H5WYG	RME	RGD	FITC- RGD
Peptide Sequence (if applicable)	GCGLFHAIAHFIHGGWHGLIHGWYG	CKKKKKKSEDEYPYVPN	CRGDK	FITC-Ahx-RGD
Modifications	None	None	None	FITC tag
Chemical Formula	$C_{132}H_{175}N_{37}O_{27}S_1$	$C_{93}H_{150}N_{24}0_{28}S_1$	$C_{12}H_{39}N_9O_8S$	$C_{48}H_{61}N_{11}O_{14}S_2$
Molecular Weight	2744.11g/mol	2084.41g/mol	577.66 g/mol	577.66 g/mol
Isoelectric point (pI) calculated via PepDraw [197]	7.5	9.6	8.6	8.6
Net charge at pH7	+0.4	+2.9	+0.9	+0.9

3.4.5 Colloidal Stability of Co-functionalized Gold Nanoparticles

The colloidal stability (ability of the AuNP to resist aggregation under physiological conditions) of the citrate capped AuNP, PEG capped and the peptide co-functionalized AuNPs were examined using UV/Vis in chapters 4 & 6. A PBS tablet was crushed and vortexed with the AuNP to induce physiological NaCl molarity and monitored for a period of 24 h, the concentrations were then increased to 1M NaCl at intervals of 0.1M NaCl and the SPR patterns were monitored by UV/Vis for any indication of instability (agglomeration). [30]

The PBS tablet was used to prepare a salt concentration of 0.137 M in 100 ml, each tablet was crushed and weighed prior to use. The required weight of PBS tablet required to obtain a AuNP solution of 0.137 M was calculated as follows:

Equation 3-2

$$\text{weight of PBS tablet (g)} \times \frac{\text{Volume of AuNP solution (ml)}}{\text{Required total volume for the PBS tablet (ml)}}$$

The molarity can be increased by adding the required amount of NaCl. The following equation was used to calculate the amount required.

Equation 3-3

$$\text{No. of moles} \times \frac{\text{Volume of AuNP (ml)}}{\text{Required volume of solution for the moles (ml)}}$$

This equation is similar to Equation 3-2, however the number of moles of NaCl (58.54) is used instead of weight (g), and the required volume is 1 liter (1000 ml) as NaCl is 58.54 moles in 1 liter. The resulting value is then simply multiplied by the desired molarity, e.g. 0.05 M, 0.1 M, and 0.2 M as required.

3.4.6 Rate of Opsonization of Gold Nanoparticles

The ability of each conjugate to resist non-specific protein attachment was investigated by aliquoting each sample into a 1.5 ml Eppendorf and micro

centrifuging at 10,000 RCF for 30 minutes. The supernatant was decanted and the sample was re-dispersed in DMEM FCS (10%) then incubated for a period of 2 h at 37 °C 5% CO_2 and characterized using gel electrophoresis and/or DLS.

3.4.7 Optimizing Binding based on pH

AuNPs were functionalized with either mono functional or hetero bifunctional PEG and centrifuged as outlined above. The pellet was then re-dispersed in a pH buffer solution and the samples were characterized with DLS and UV/Vis. A pre-calculated weight of the required peptide was then dissolved in 1 ml of the respective pH buffer and added to the PEG capped AuNPs under ambient conditions undergoing vigorous stirring. The reaction was monitored for a period of 24h with UV/Vis reading being recorded at the following time intervals: 30 minutes, 1 hour, 2 hour, 3 hours, 4 hours, 5 hours, 6 hours, 7 hours & 24 hours. UV/Vis analysis was conducted in the range of 400nm-600nm with intervals of 0.8nm step with a 360-scanning speed. DLS was used to measure both size and zeta potential, prior to and after peptide addition.

3.4.8 Cell Culture

Human epithelial breast cancer cell line MDA-MB-231 was cultured in Dulbecco's modified eagle's medium (DMEM) supplemented with 10% fetal bovine serum. Human epithelial normal breast cell's MCF-10A were cultured in DMEM/F 12 supplemented with 5 % horse serum, 1 % penicillin-streptomycin, 20 ng/ml epidermal growth factor, 0.5 mg/ml hydrocortisone, 100 ng/ml cholera toxin and 10 µg/ml insulin. All cells were purchased from the American Type Culture Collection. Cells were maintained in monolayers in a tissue culture incubator at 37°C with 5 % CO_2 and sub-cultured every 3-4 days to maintain exponential growth. These conditions were used throughout the thesis unless otherwise stated.

3.4.9 MTT Assay/Cell Viability

MTT is a cell viability assay known as MTT (3-[4, 5-dimethylthiazol-2-yl]-2, 5-diphenyl tetrazolium bromide; thiazolyl blue), it is a water soluble tetrazolium salt which yields a yellow solution when lacking phenol red indicator and when prepared using media or salt solutions. Active mitochondrial dehydrogenase enzymes of living cells convert the dissolved MTT into an insoluble purple formazan by cleavage of

the tetrazolium ring. Dead cells will not have this effect. The purple formazan can then be solubilized by the use of a solvent; the dissolved material can then be measured spectrophotometrically in the result of absorbance in relation to concentration by measuring the converted dye hereby reflecting the viability of cells. The amount of formazan produced is directly proportional to the number of viable cells.

The MTT assay was carried out over a range of concentrations. Each sample was centrifuged and the supernatant decanted until concentrations of 1800 µg/ml, 900 µg/ml and 225 µg/ml were attained. 200 µl containing 1.3 x 10^4 cells were seeded into each well of a 96 well polystyrene coated plate and incubated for 24 hours at 37°C 5% CO_2 to adhere. Each AuNP sample was then aliquoted into the wells containing 200 µL of DMEM media, thereby having a 1 in 9 dilution factor, resulting in the overall concentrations of 25 µg/ml, 100 µg/ml and 200 µg/ml respectively. The study was conducted over 7 days with 3 time points for a range of cell lines (chapter 4 & 6) and H_2O_2 was used as a positive control.

MTT (5 mg/ml in phenol free DMEM) was added to the wells in amounts equivalent to 10 % of the cell culture medium. The plates were then incubated for 3 hours at 37°C, 5 % CO_2, after which the liquid was aspirated and the intracellular formazan product was solubilized with acidified (0.1 N HCL) 20 % SDS sodium dodecyl sulfate DMF in double distilled deionized water and incubated for a period of 30 min.

3.4.10 Uptake into Target Cells

All the AuNP uptake studies were conducted in concurrence with our collaborators in Queens University Belfast. Queens University were responsible for the experimental procedure while the author was responsible for the data analysis and interpretation. 4.5 x10^4 cells were plated out and left to adhere for 24 h then exposed to 25 µg/ml gold nanoparticles for 24 h. The nanoparticles were then aspirated off, the cells washed twice with phosphate-buffered saline (PBS), trypsinized and reconstituted in 0.5 ml 18Ω deionized water to a total of 1 ml and counted using a Beckman Coulter counter. 1 ml aqua regia was added to the remaining cells (3:1 hydrochloric: nitric acid), left for 2 hours to digest before the addition of 3 ml of

18Ω deionized water. Samples were analyzed via atomic absorption spectroscopy (AAS).

3.4.11 Clonogenic Survival Assay

The clonogenic assay (colony formation assay) is the gold standard assay for radiation studies *in vitro*. The clonogenic survival assays were also performed by our collaborators in Queens University, Belfast however analysed by the author. A total of 2 x 10^5 cells were plated in 6 well plates (Nunc, UK) and incubated overnight before being pre-incubated in the presence of AuNPs for 24 h in complete medium at 37°C in 5 % CO_2 / 95 % air. Excess AuNPs were removed, cells washed with PBS and incubated in complete media prior to irradiation. Cells were exposed to 0-6 gray (Gy) X-rays, which is a derived unit of ionizing radiation dose in the International System of Units (SI). It is defined as the absorption of one joule of radiation energy per kilogram of matter. [228] Following radiation cells were washed with PBS, trypsinised, diluted 1:2 with fresh medium and vortexed to ensure a homogenous solution before being counted using a coulter counter (Beckman-Coulter, ROI). Cells were then plated at pre-determined cell densities in 6 well plates. After 12 days, colonies were fixed with 0.4 % crystal violet in 70 % methanol and counted using the 50-cell exclusion criterion. The plating efficiency was calculated as the ratio of colonies to cells seeded. The surviving fraction (SF) could then be calculated as the plating efficiency of the treated groups divided by the plating efficiency of untreated cells. The area under the curve (AUC), which represents the mean inactivation dose (MID), was calculated using Prism 6.0 (GraphPad software) and the sensitizer enhancement ratio (SER) calculated by dividing the MID of untreated cells with AuNP treated cells. Statistical analysis was performed using a two-way ANOVA comparing the different AuNP preparations to the untreated control.

Mean plating efficiency values for 0 Gy were used to determine the long term toxicity of the AuNPs.

3.4.12 BCA Assay

Peptide concentrations were calculated using a Micro Bicinchoninic acid (BCA) kit (Thermo Scientific Micro BCA Protein Assay Kit, Pierce Biotechnology). This assay

is used to colorimetrically detect and quantify protein concentrations. Standard protocols in the kits were used in this study and serial dilutions were used to dilute the stock bovine serum albumin (BSA) in accordance with the BCA kit manufacturer's instructions to produce the calibration curve standard. This standard was used across all three peptide types. The experiments were performed in 96-well microplates were N > 4. After incubating the assays for 4 h, the absorbance was measured at 562 nm using an absorbance plate reader (TECAN Sunrise, TECAN Austria). The concentrations quoted were calculated using the calibration curve.

3.5 Characterization Techniques

3.5.1 Dynamic Light Scattering

3.5.2 Particle Size Analysis

Dynamic Light Scattering (DLS) detectors enable the particle size and zeta potential measurements of small amounts of proteins, biomaterials and particles suspended in solutions in the size range of 0.3 nm to 8 µm. Particle size measurement is important as it can act as a valuable indicator of quality; most commonly for powders, suspensions, emulsions and aerosols. [229,230] Many nanotechnologies require the tracking of changes in particles size; such as filtration, functionalization/growth and washing, DLS makes this possible by enabling the monitoring of size both prior to and after each technique.

DLS size measurement is dependent on the shape of the particle to be measured. It is of note that it is in fact the hydrodynamic diameter (D_h) which is recorded. This is a value that refers to how a particle diffuses within a fluid. Non-spherical particles can be described by a combination of multiple length and width measurements which provide greater accuracy, the reported value is typically an equivalent spherical diameter – this means that the diameter which is acquired refers to the diameter of a sphere which would have the same translational diffusion coefficient as the particle; essentially taking the physical measured value and determining the size and shape of a particle that would produce that data. [230] Spherical particles can be described by the diameter alone, because each dimension is equal.

DLS is a measure of Brownian motion, which is the random motion of particles, and relates that to the size of the particles; the larger the particle, the slower the motion. Particles in suspension are constantly undergoing Brownian Motion due to the subatomic molecules, the distance between the scatterers in solution are constantly changing and is dependent on size; the larger the molecules then the slower the Brownian motion will be.

The temperature and concentration must be kept constant as temperature will affect the viscosity, and to stabilize the convection currents which will cause non-random movements, and the ions in the medium can change the thickness of the electric double layer. A low conductivity medium will produce an extended double layer of ions around the particle reducing diffusion speed, resulting in a longer hydrodynamic diameter (D_h). The hydrodynamic diameter (D_h) refers to how a particle diffuses within a fluid. DLS is sensitive to the coating on the AuNP. An adsorbed polymer projecting out into the medium will change the speed; therefore as the AuNPs are functionalized, the particle becomes slower, thus resulting in a larger AuNP size output. [230] Scattering is caused by an incident light inducing electronic distortion. The incident light induces an oscillating dipole in the electron cloud. As the dipole changes, energy is radiated, or scattered in all directions. This phenomenon is known as Rayleigh Scattering. The intensity of light scattered is dependent on the size of the particle and the angle of refraction and the detector. Dynamic Light Scattering (DLS) refers to the measurement and interpretation of light scattering data on a microsecond time scale. The particle motion is measured from determining fluctuations in intensity of the scattered light; this is performed by a digital signal processor known as a correlator, which characterizes that noise in real time. The correlator is a signal comparer, the correlation function compares the intensity of the delay time and the intensity of the reference time. It measures the degree of similarity between two signals or one signal with itself at varying time points. DLS interprets this scattering data on a time scale to determine particle size via particle motion, the longer the time, the weaker the relationship due to diffusion. Therefore for a correlogram, the longer it takes to decay, the larger the particle due to the slower motion, and the steeper the gradient, then the more mono-disperse the solution.

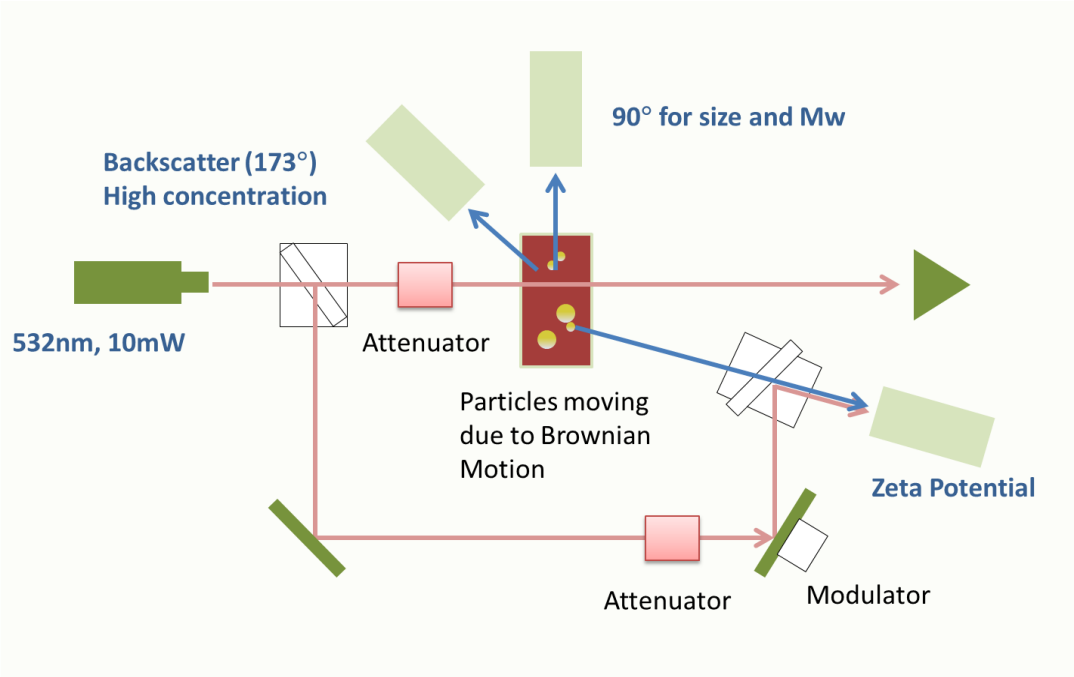

Figure 3-4 Experimental set-up schematic for DLS particle size detection

Light from the laser light source illuminates the sample in the cell; the scattered light undergoes either constructive or destructive interference by the surrounding particles and within this fluctuation, information is contained about the time scale of movement of the scatterers. The scattered light signal is collected with one of two detectors either at a 90° right angle or 173° back scattering angle. The obtained optical signal shows random changes due to the randomly changing relative position of the particles.

DLS then uses the correlator to characterize that noise in real time to give an exponential decay with delay constant gamma using

Equation 3-4 to give the autocorrelation function expressed in Figure 3-5. C is simply an exponential decay of the autocorrelation function, the decay constant is proportional to the diffusion coefficient.

Equation 3-4

$$C(\tau) = \exp(-\Gamma\tau)$$

C – Exponential decay of the autocorrelation function

Γ – Gamma calculated from the delay function

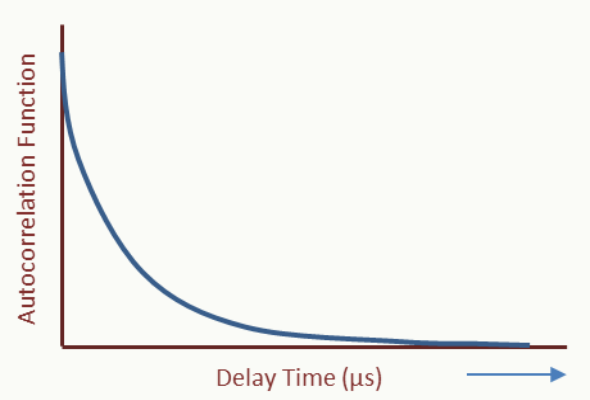

Figure 3-5 Autocorrelation function showing exponential decay

The decay of this function is used to extract particle size. Faster decays correspond to smaller particles. This means that after a long period has elapsed, there is no correlation between the scattered intensity of the initial and final states. The delay function below gives gamma and gamma can then be used to calculation the size. The diffusion coefficient is the proportionality factor 'D' in Fick's Law, it is a physical constant dependent on molecule size and other properties of the diffusing substance as well as on temperature and pressure and is obtained from the relationship expressed in Equation 3-5 where q is the scattering vector derived from Equation 3-6.

Equation 3-5

$$\Gamma = D_t\, q^2$$

Γ – Gamma

D – Diffusion coefficient ($m^2\ s^{-1}$)

q – Scattering vector

Equation 3-6

$$q = \frac{4\pi n}{\lambda} \sin\left(\frac{\theta}{2}\right)$$

n = refractive index

λ = wavelength of laser light (nm)

θ = scattering angle

q = scattering vector

Finally, inserting the diffusion coefficient into the stokes Einstein relationship then solves for the particle size.

Equation 3-7

$$D_h = \frac{K_B T}{3\,\pi_\eta D_t}$$

D_h - Hydrodynamic diameter (d.nm)

K_B - Boltzmann's constant ($1.38064852 \times 10^{-23}\ m^2\ kg\ s^{-2}\ K^{-1}$)

T - Temperature (°C)

ŋ - Dynamic viscosity (Pa s)

D_t - Translational diffusion coefficient (m^2 s^{-1})

DLS average size can be reported in several ways, Z-avg size, Number or Volume. Z-average size is not the intensity width size, instead it is the intensity width of a harmonic.

Z-avg has more confidence than PDI as it is a first order term so there is minimal range for error, the PDI however is extremely important as it informs us about the width of the size distribution. The calculations for PDI are defined under ISO13321:1996E and ISO22412. PDI describes the polydispersity index of the solution, which defines the degree of non-uniformity. For size distribution, a perfectly uniform solution would have a PDI of zero, this would tell the user that the particles in solution are completely monodisperse, whereas if the PDI came back with a value of 0.7, it would indicate to the user that the solution is extremely poly disperse. DLS also facilitates the conversion of 'Intensity' to a 'Number' or 'Volume' mean calculation.

To run the equipment the power source must be turned on, two beeps will sound when the default temperature of 25°C is met, then the equipment must be left for a minimum time of 30 minutes to allow for the stabilization of the laser; this is necessary to prevent any thermal equilibrium problems that may produces errors or inconsistencies in the results. For this thesis, the DLS size measurements were all obtained by using the same SOP. This SOP detailed 15 measurements per one run with a total of 9 runs per sample which were averaged and used to calculate the statistics. Throughout this thesis, unless otherwise stated, Number average was reported when comparing results to minimize any errors and measurements have been carried out on each sample a minimum of 3 times, the mean calculated and standard deviation and COV (standard deviation / mean) as per ISO13320.

Standard deviation and variance are the most common descriptions of dispersion. Throughout this Thesis, all error bars were calculated using Equation 3-8 and

Equation 3-9 respectively. Statistics were all calculated either using either a t-test, One-way ANOVA or Two-way ANOVA with Tukey or Dunnett post-test (as stated) with * p-value <0.05, ** p-value <-0.01, *** p-value <0.001.

Equation 3-8

$$\sigma = \sum \sqrt{\frac{\sum(x - \bar{x})^2}{n}}$$

Equation 3-9

$$s^2 = \frac{\sum(x - \bar{x})^2}{n - 1}$$

x - Mean value of the sample,

Σ - Summation

n-1 - Number of values in the sample minus 1

S - Standard deviation

Σ - Variance

1.1.1.1 Zeta Potential Measurement

DLS can also be utilized to measure the zeta potential which is a measure of the magnitude of the electrostatic or charge repulsion/attraction between particles, and is one of the fundamental parameters known to affect colloidal stability. The value of this knowledge stems for the potential understanding of interactions between particles, and changes in the zeta potential can be used to confirm AuNP attachment. It is measured by electrophoretic light scattering where particle motion is detected in an applied electric field.

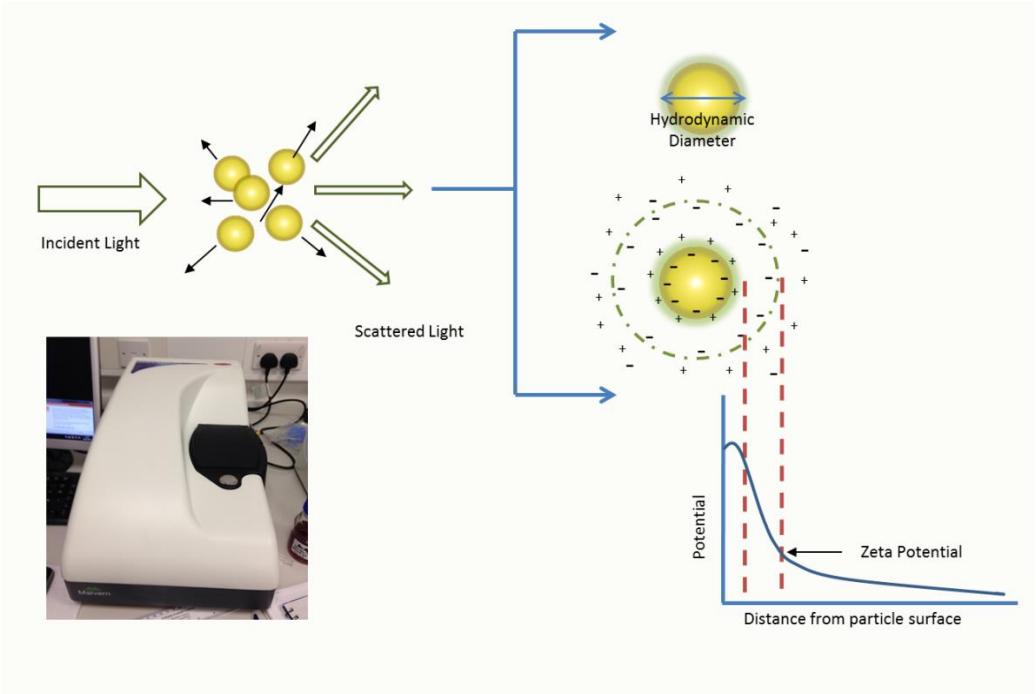

Figure 3-6 Schematic illustrating DLS size and zeta analysis

Zeta potential is the value measured from a double electric layer surrounding a nanoparticle having some surface charge using Dynamic Light Scattaring technique at the present conditions: pH, ionic strength, temperature, etc. of a nanoparticle medium, therefore it can be used to define the charge on the surface of a particle in a specific medium. The zeta-potential is a (relative) indicator for the surface potential of the particle. The more positive or negative the zeta-potential, then the more stable the particles are (due to electrical repulsion). At a value of zero aggregation would occur. The zeta-potential of a particle arises from its surface charge density (i.e. the

greater the number of charged ligands on the particle per unit surface area, the greater the magnitude of the particle's zeta-potential).

Zeta potential measurements work based of the stern layer and diffuse layer of the particles as the charge on the particle surface can affect the ionic environment of the suspension solution (Figure 3-6). The environment is described as being a ‘double layer’ which consists of:

1. The Stern layer of ions which are firmly attached adjacent to the particle surface.
2. A diffuse layer which is located further away from the particle surface but is still attracted to the particle and moves in sync with said particle.

There is an invisible boundary between this layer and the remaining ions in solution, which is called ‘the slipping plane’ and the zeta potential measurement is the measurement in mV at the slipping plane (Figure 3-6).

Zeta potential is measured using a capillary cell which consists of two electrodes. These electrodes formulate an electric field which when applied causes the particles to move towards the anode or the cathode depending on the charge. The speed of this motion is used to calculate the magnitude of the charge and is affected by the viscosity, size, dielectric constant and surface charge. When the particles are illuminated with the laser light, a reference beam mixes with the scattered beam to extract the frequency shift in the scattered light; the magnitude of this frequency shift allows the calculation of the particle velocity. Equation 3-10 therefore calculates the electrophoretic mobility (μ) using the measured frequency shift.

Equation 3-10

$$\mu = \frac{\Delta\omega\lambda_0}{4\pi n E \sin\left(\frac{\theta'}{2}\right)}$$

μ = electrophoretic mobility (V/cm)
ω = measured frequency shift (Hz)

λ = laser wavelength (nm)

n = refractive index of medium

θ’ = contains the angular light scattering information

The zeta potential can therefore be calculated based on the electrophoretic mobility by using the Henry’s equation which is outlines in Equation 3-11.

Equation 3-11

$$\mu = \frac{2\text{ב}\varepsilon\, f(\kappa r)}{3\eta_0}$$

μ= electrophoretic mobility (V/cm)

ζ = zeta potential (mV)

ε = the dielectric permittivity of the medium (F/m)

η_0 = the viscosity (Pa. s)

f= (κr) = a function describing the ratio of the particle radius to the double layer

The testing in this Thesis was conducted using the Malvern Zetasizer Nano ZS Series. Using disposable 2 ml cuvettes (type DTS0012). The samples were analyzed 9 times at 25°C, meeting the requirements of ISO13320 where each analysis consisted of 15 measurements. The system parameters were as follows:

Refractive Index: 1.33

Absorption: 1.00 (max)

Measurement Angle: 173° (standard)

Cell Type: DTS0012

Dispersant: Water

3.5.3 UV-Visible Spectroscopy

UV/Vis belongs to a class of instruments known as spectrophotometers; a spectrophotometer measures the transmittance of light which passes through a cell containing a sample to be analyzed. This light is collected and converted into an electrical current via a photodiode; the current is directly proportional to the amount of light hitting the photodiode. The current is then converted into voltage which corresponds to absorbance. This basis of the theory of operation is initially based on the principle discovered by Bouger and Lambert which determines that when light was passed through a material, a portion of the light's energy was absorbed while the remaining light passes through. The transmittance of this light is proportional to the path length of the material and is dependent on both the material and the wavelength of the light. Thus, identifying a linear relationship between thickness of the material and the transmitted light. Beer later developed this this principle to include solutions, and demonstrated that the transmission of light is directly proportional to the concentration of the solute and the path length at which it travels. [231]

The Beer Lambert Law therefore states that the absorbance of light by a chemical in solution is directly proportional to:

1. The concentration of the solute in solution
2. The path length of the cell
3. The molar absorptivity of the solute

Equation 3-12

$$\text{Absorbance} = \log\left(\frac{I_0}{I}\right) = abc$$

Beers Law is expressed in Equation 3-12 where:

I_0 = Intensity of light beam at entrance of flow cell

I = Intensity of light at exit of flow cell

a = Molar Absorptivity (L mol^{-1} cm^{-1})

b = Cell path length (cm)

c = Solute strength ($molL^{-1}$)

When both the cell path length and the molar absorptivity are held constant, the absorbance measured should be directly proportional to the concentration of the sample. This relationship is only true for monochromatic light and low absorbance.

In UV/Vis, the major energy levels are determined primarily by spatial distributions of electrons known as electronic energy levels, and to a lesser extent, vibrational energy levels which include stretching and bending of covalent bonds.

Elements or molecules which contain sigma (σ), pi (π) or non-bonding (n) electrons can absorb energy from ultraviolet or visible light to excite these valence electrons to higher antibonding (*) molecular orbitals. The lower the energy gap between the highest occupied molecular orbital (HOMO) and the lowest unoccupied molecular orbital (LUMO) the easier the excitation of the electron, and thus the longer the wavelength of light which can be absorbed. There are four types of transitions obeyed, σ - σ* > n - σ* > π - π* > n - π*, where the energy required for each, increase respectively. [232,233]

The energy and wavelength of absorption is defined by the difference in energy levels of an electronic transition, E1 being the energy level of the molecule before absorption and E2 the energy level reached by absorption. This relationship is expressed in Equation 3-13.

Equation 3-13

$$\lambda = hc/(E2 - E1)$$

λ – Wavelength (nm)

h – Planck's constant ($6.62607004 \times 10^{-34}$ m2 kg /s)

c - speed of light (299 792 458 m/s)

E2 – energy of higher state (eV)

E1 – energy of lower state (eV)

If an electron receives more or less than that energy calculated from Equation 3-13, then it cannot jump to a higher energy state. However, photons of light which are of that exact energy will be absorbed by the electron in state E1 and will jump to state E2. Orbital energies are described by vibrations, so each orbital has a range of possible vibrations, therefore the transition from one electronic level to the next can occur between many vibrational levels. When we excite the electron, it has both the potential to be excited to a range of vibrational modes, and the potential to be excited from a range of various vibrational modes; this results in differences in the width of the spectra obtained. If all transitions were between only the lowest vibrational levels of ground and first excited state, then the absorption peak would be narrow and discrete. [234]

UV/Vis spectroscopy is a very common characterization technique used for gold nanoparticle analysis. Literature would demonstrate that AuNPs exhibit an absorption peak at approximately 520 nm for nanoparticles of ~15 – 20 d.nm; the position of this peak varies with nanoparticle size. The Surface Plasmon Resonance is the phenomena which gives rise to this peak. Electrons are confined to the surface of the gold nanoparticles which occur at the interface of the gold and the suspension. The electrons in the conduction band interact with the photons of polarized light, a wave like oscillation is induced, which causes a reduction in the reflected light intensity. AuNPs absorb light in the green and reflect in the red which denotes the color of the solution, the relationship of the visible light region of the electromagnetic spectrum is illustrated in Figure 3-7. When the light hits the electron cloud, the electrons begin to oscillate resulting in some polarization, the electrons begin to bounce back and forth between the now positive and negative charges and therefore resonate with the frequency of visible light.

In order to determine the absorbance two measurements are taken, first the measurement of I_0 is taken by running a blank scan, with distilled water in the reference and sample holders. This is then followed by the measurement of I by taking a measurement of the sample in the sample holder. [235]

UV/Vis measurements were taken by a Perkin Elmer Lambda 35 Spectrometer; this machine consists of a holographic concave grating found in the monochromator. The optical system is coated in silica and is illustrated in Figure 3-8. There are two

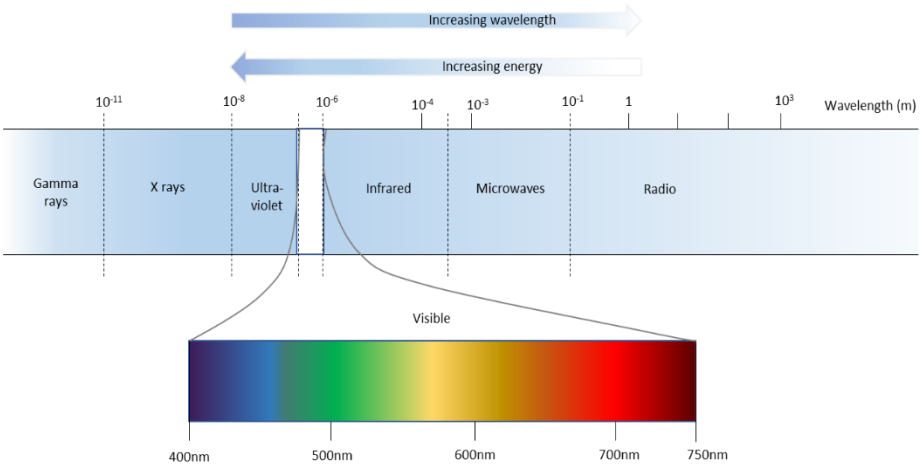

Figure 3-7 Schematic representing the electromagnetic spectrum highlighting the visible region

sources of radiation, a deuterium lamp and a halogen lamp. When operating in the visible range of the spectrum the mirror labelled M1 reflects the radiation from the halogen lamp, onto the mirror M2 meanwhile blocking the radiation from the deuterium lamp which is used for the ultra violet (UV) region of the electromagnetic spectrum. When analyzing in the UV range the M1 mirror is raised to allow the radiation from the deuterium lamp to seek the source mirror M2. Radiation is then reflected through an optical filter on the filter wheel which is driven in synchronization with the monochromator. An appropriate filter (dependent on the wavelength used) is then selected in the beam path to pre filter the radiation before it enters the monochromator. [235] The radiation leaves the optical filter and passes through slit 1 of the monochromator, it is then dispersed at the grating which produces a spectrum, a segment is selected from this spectrum and reflected through slit 2 to the mirror M3. The function of the exit slit is to restrict the spectrum until it is a near monochromatic beam; this beam is then reflected onto the beam splitter which divides the beam by allowing 50 % of the radiation to pass onto the plane mirror M4 while reflecting 50 % of the radiation onto the plane mirror M5. M4 focuses the beam into the sample cell while mirror M5 focuses the radiation through the reference cell. Both beams are then picked up by a convex lens and focused onto the photodiode detector. [235]

For UV/Vis spectroscopy, 1.4 ml of each of the sample is aliquoted out into a quartz cuvette. Unless otherwise stated the samples were analyzed in the range of 600-400 nm with a 0.1 nm step and 240 scanning speed using the Perkin Elmer Lambda 35 Spectrometer. The technique is used to measure the standard absorbance of AuNPs which is usually in the range of 510-540 nm; by monitoring the peak and the absorbance of the peak it is possible to confirm the colloidal stability in the presence of PBS and NaCl (chapters 4 & 6) and colloidal stability and agglomeration in a range of pH buffers (chapter 5) and the attachment of any ligands which is monitored throughout this Thesis.

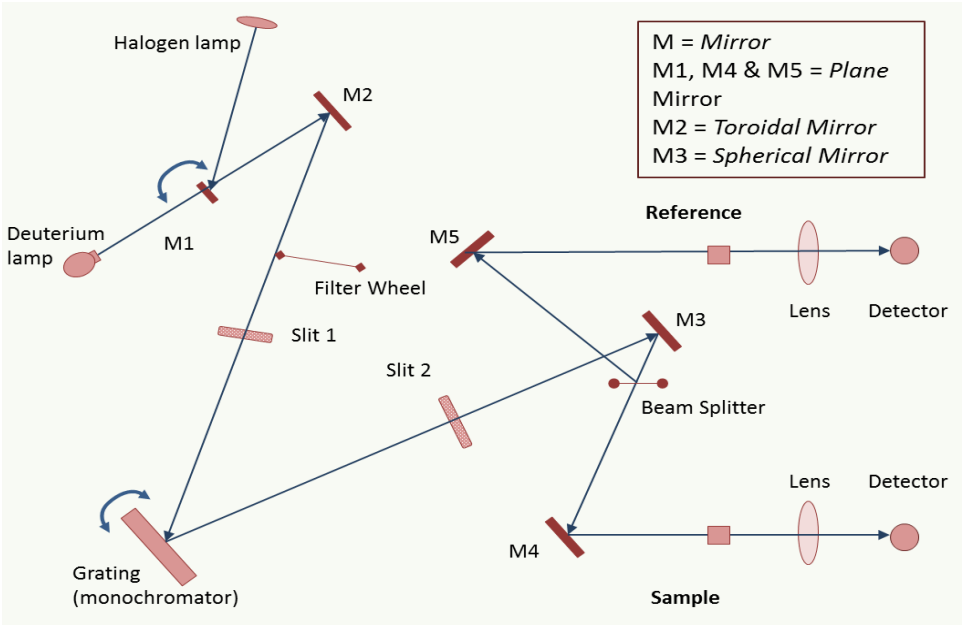

Figure 3-8 Illustration of the optical system of a Perkin Elmer Lambda 35

3.5.4 Transmission Electron Microscopy

Transmission Electron Microscopy (TEM) is an electron microscopy imaging technique. TEM uses electrons as a light source typically from a Tungsten or lanthanum hexaboride filament and due to their low wavelength compared to visible light, they allow a much higher resolution to be obtained in the image. Materials can be studied at an atomic level, cells can be examined in minute details and objects can be studies to the order of a few angstroms (0.1 nm).

The electron source is found at the top of the microscope and emits electrons that travel down through a vacuum in the column of the microscope (which is illustrated in). Electromagnetic lenses focus these electrons into a narrow beam which transmits through the sample specimen, depending on the density of the sample some of the electrons scatter; some are blocked while the un-scattered electrons are gathered at the bottom of the microscope column. The sample needs to be very thin, typically < 100 nm. The objective lens is used to focus this beam. All the lenses in TEM are operated by either an electrostatic or magnetic field (for example, a magnetic coil), the first condenser lens controls the 'spot size' which is the size of the beam when it hits the sample; the second condenser lens controls the size the

beam appears on the sample from a pinpoint to wide dispersed beam, the condenser aperture removes high angle electrons from the beam. The objective aperture is used to enhance the contrast within the beam by blocking high angle electrons which have been scattered by the sample. This forms a shadow image which is in grey scale with different parts of the sample displayed in varied greys according to the density of the sample. Those un-scattered electrons which gather at the bottom of the column are passed through the intermediate and the projector lenses which enlarge the beam; they are then focused onto a fluorescent screen or a detector which converts the beam into a digital image for analysis.

The samples were dried on carbon coated copper grids and imaged using a JEOL 2100F Transmission Electron Microscope at 200 kV. TEM was used to analyze the shape, size, agglomeration and to image the uptake within the cell throughout this thesis. Image J was used for size analysis and the measure the number of nanoparticles with a minimum of 80 measurements taken per image.

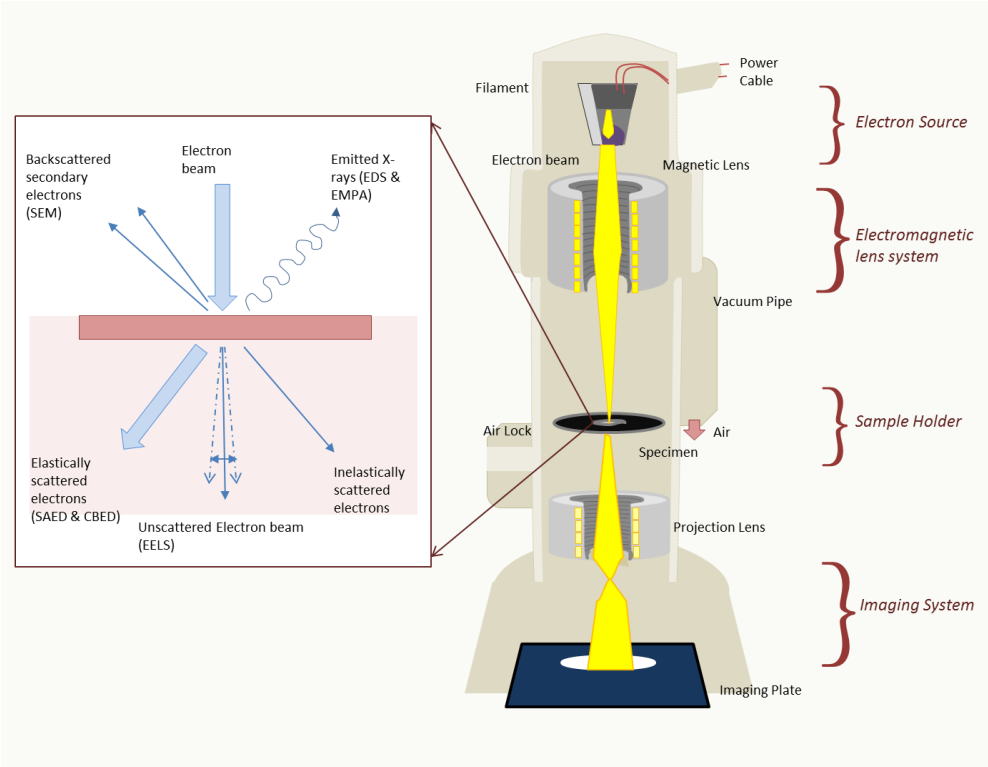

Figure 3-9 TEM cylinder Schematic

3.5.5 Fourier Transform – Infra Red Spectroscopy (FT-IR)

Infrared Spectroscopy (IR) is a powerful tool for the analysis of a sample; it is the study of interactions between infrared electromagnetic energy and matter and allows for qualitative and quantitative measurements. If the infrared light is absorbed by a sample it will result in the excitation of the samples molecular vibrations which cause the amplitude of bonds to change. This change is measured with FTIR.

FTIR can be used to measure all three states of matter, almost all compounds absorb variations of infrared light, and only chemical bonds that have a dipole moment that changes as a function of vibrations are capable of absorbing infrared light, only active IR bonds produce peaks. Every bind that absorbs IR light vibrates at a different, specific frequency, the small variations result in the peak position and is commonly referred to as the compounds fingerprint. It is commonly used to identify contaminants and in forensics as it can be used for hair and fiber analysis, or to identify compounds in unknown powders.

There are 4 sampling modes used in FTIR. Transmission, Reflectance, Diffuse Reflectance and Attenuated Total Reflectance. For this thesis, Diffuse Reflectance or DRIFTS was used, the sample was mixed with potassium Bromide (KBr), the water was evaporated off and the remaining pellet was ground and placed in the drifts cup.

During transmission FTIR spectroscopy IR radiation is passes through a sample, some of this radiation is absorbed by the sample while some if transmitted. The spectrum obtained represents a molecular fingerprint. In addition to identifying the unknown materials of a sample, FTIR can also determine the quality of a sample in conjunction with the amount of components within a mixture. [236] FTIR was initially invented to overcome the problems associated with a slow scanning process which was commonly found in all other dispersive instruments. The development of an interferometer overcame this, this is an optical device which produces a unique signal which has all of the infrared frequencies encoded into it, therefore the infrared frequencies could be measured simultaneously and not individually, thus reducing scanning time to mere seconds and not minutes.

A beam splitter divides the incoming infrared beam into two optical beams, one beam reflects off a fixed mirror while other reflects off a moving mirror. Both beams are re-joined, however due to the difference in paths due to the fixation and movement of the mirrors, the two beam now interfere with each other resulting in a signal known as the interferogram. The novelty of this interferogram is that each data point which makes up this signal contains information about every infrared frequency originating from the source. This interferogram signal must then be decoded for analysis via a technique known as the Fourier transformation.

The main components consist of a source, an interferometer, a sample, a detector and a computer. Before each sample analysis a background spectrum must be obtained as a reference point for a relative scale for the absorption intensity. The background is usually an empty cell, and then the percentage transmittance can be measured by comparing the measurement with a sample to the background scan. For this thesis, however the background is KBr. The background results in a spectrum with all the instrumental characteristics removed; therefore the data generated is solely a result of the sample. [236]

Samples were prepared by centrifuging 50 ml AuNP and removing 90 % of the supernatant. 1 ml of the now concentrated pellet was dropped via a plastic disposable pipette onto 1-2 g of KBr and dried in a Teflon flask at 40°C under vacuum. The remaining 4 ml were aliquoted onto the KBr powder over the course of 2-5 days as required* and the powder left to dry for a further 24 h.

*Due to the complexity of the AuNPs and the difficulty obtaining some spectra, the amount of KBr powder was tailored depending on the quality of the spectra obtained and the Absorbance value of the atmospheric peaks at 2000 – 2500 cm^{-1}.

For this Thesis, all spectra were obtained from a Varian 640-IR FTIR Spectrometer, the method used for AuNP analysis is more commonly referred to as DRIFTS. Diffuse Reflectance Infrared Fourier Transform Spectroscopy (DRIFTS-FTIR) analysis verifies the chemical and physical structures of materials. It analyses the sample by studying the surface chemistry of high surface area powders; it utilizes a controlled DRIFT cell by focusing the IR light onto the powder and collecting the scattered light. The DRIFTS cell used was a PIKE EasiDiff Diffuse Reflectance Infrared Fourier Transform Spectroscopy accessory. 4 scans per sample were obtained from 4000-400 cm^{-1} in absorbance mode at 4 cm^{-1} resolution.

3.5.6 Gel Electrophoresis

Agarose gel electrophoresis is a routinely used method for separating proteins, DNA or RNA. Nucleic acid molecules are size separated by the aid of an electric field where negatively charged molecules migrate toward anode (positive) pole.[237] For gold nanoparticles, gel electrophoresis is a useful tool as it will characterize the AuNPs based upon size and charge of the AuNPs. Like DLS, gl electrophoresis is sensitive to the organic coating of the AuNPs; larger AuNPs will have a slower migration profile than the smaller AuNPs. Therefore gel electrophoresis can be used in conjunction with DLS to confirm surface functionalization, as successful PEGylation and/or co-functionalization with peptides would result in a AuNP size increase and affect the migration profiles of the AuNP in relation to particle size. As well as size, gel electrophoresis is sensitive to charge, and the zeta potential of the AuNPs. Therefore a charge in zeta potential will affect which pole, and subsequent direction, which the AuNPs migrate to. Gel electrophoresis was carried out on 2 %

agarose eluted with 0.5 x TBE running buffer to confirm both conjugation and non-specific protein adsorption. 20 microliters of the AuNP samples containing 50 % sucrose solution were added to each gel well, and the gel was run at 100 V for 2 hours. Electrophoretic migration is dependent on the charge and size of the particles. [238] Gel electrophoresis was used in this thesis to confirm conjugation of both PEG and peptide as indicated by the migration profiles for each of the AuNP sample types, and to analyze the non-specific protein adsorption of the samples (chapter 6). [239]

3.5.7 Atomic Absorption Spectroscopy

Atomic Absorption Spectroscopy was performed by the collaborators in Queens University, Belfast, to measure the intracellular concentration of AuNPs. Initially 4.5 $x10^4$ cells were plated out and left to adhere for 24 hours then exposed to gold nanoparticles for 24 hours. The nanoparticles were then removed, the cells washed twice with phosphate-buffered saline (PBS), trypsinized and reconstituted in 0.5 ml 18 Ω deionized water to a total of 1 ml. 1 ml aqua regia was added (3:1 hydrochloric:nitric acid), left for 2 hours to digest and a further 3 ml 18 Ω deionized water added. Samples were then read using a flame atomizer AAS, AAnalyst 400 AA spectrometer (flame atomizer) from Perkin Elmer, and software Winlab 32 for AA. Atomic Absorption Spectroscopy (AAS) measures the concentrations of elements by measuring the wavelength of light absorbed by the element. Those wavelengths correspond to the amount of energy required to promote the electrons from one energy level to a higher energy level. Applications include pharmaceutical manufacturing to calculate residual catalysts, or in industry to examine raw materials and quantify toxic impurities. For this Thesis AAS was used to measure the concentration of the functionalized gold nanoparticles in solution and to quantify the mass of AuNPs endocytosed by cells after 24 h incubation with the various AuNP conjugates (chapter 5).

For AuNPs, a hollow cathode lamp, containing a tungsten anode and a cylindrical hollow cathode made of gold emits light from excited gold atoms to be absorbed by any gold atoms from the sample. These are sealed in a glass tube filled with an inert gas at a pressure between 1 Nm^{-2} and 5 Nm^{-2}. During AAS, the sample is atomized,

(converted into ground state free atoms in the vapor state). The atomizer can be aspiration or electro thermal atomization, which is the aspiration of a liquid into a flame or the placement of a sample droplet into a graphite tube to be electrically heated. The gaseous ions in the lamp bombard the cathode and eject gold atoms from the cathode (sputtering), some of these atoms are in an excited state and are emitted as a beam of electromagnetic radiation which is characteristic of gold and is passed through the vaporized sample. Some of the radiation is absorbed; the amount of radiation absorbed is dependent on the number of vaporized atoms. Therefore, the amount of light absorbed is proportional to the amount of gold atoms. The unknown sample is then compared against a calibration curve generated from running numerous known gold concentration samples under the same conditions. [240]

3.5.8 Photoluminescence

There are various forms of luminescence; these include chemiluminescence, incandescence, bioluminescence and photoluminescence. When an external energy supply is applied by either infra-red, ultraviolet or visible light, if the emitted light is of a different wavelength, the light is known as photoluminescence (pL). It is this light which undergoes fluorimetric analysis. When luminescence occurs, the system loses energy, therefore for continuous emission energy must be supplied from an external source. [241]

For this Thesis, the ultraviolet and visible regions of the electromagnetic spectrum are of most interest, which result in the excitation of outermost electrons of the molecule. All fluorescent tags had to be stored under tin foil, away from direct light as the energy associated with this radiation of this frequency is high which can be sufficient enough to break down the adsorbing tags resulting in fading.

The adsorption of light results in the formation of excited molecules which in turn dissipate their energy in other ways, for instance, our tags adsorbed energy in the ultraviolet and emitted light in the visible. The efficiency of this process is known as the quantum efficacy and is defined by Equation 3-14.

Equation 3-14

$$\Phi E = \frac{einsteins\ emitted}{einsteins\ absorbed}$$

ΦE – Quantum efficiency

Photoluminescence was performed using an Agilent Technologies, Cary Eclipse Fluorescence Spectrophotometer, model G9800a. The fluorescent tags which were added are as follows:

Texas Red:	excitation @ 595 nm,	Emission max @ 615 nm
FITC:	excitation @ 494 nm,	Emission @ 520 nm

The required amount was calculated based on Equation 3-1 and dissolved in an appropriate solvent and added to the AuNP solution which was stirring under ambient conditions wrapped in tinfoil.

3.5.9 ICP-MS

ICP-MS was performed by the collaborators in Queens University, Belfast, to measure the intracellular concentration of AuNPs. $2x10^5$ cells were plated in 6 well plates (Nunc, UK) with 2 ml of complete media and allowed to adhere overnight. The cells were then treated with the samples to be tested at a concentration of 50 μg/ml for 24 h. AuNPs were removed, cells washed three times in PBS, trypsinized and diluted 1:1 with PBS before being counted using a coulter counter at a dilution of 1:200 (Beckman-Coulter, ROI). Cells were then dissolved in 1 ml of aqua regia for 30 min. Samples were then made up to 5 ml with distilled water. Analysis of the samples was carried out using inductively coupled mass spectrometry (ICP-MS) Thermo Scientific iCap Q ICP-MS, which was connected to a CETAC ASX-520 auto-sampler. The ICP-MS operating conditions were: Standard (STD) mode: forward RF power 1550 W, nebuliser gas flow was ~1 L/min and the nebuliser liquid

sample flow rate was ~0.35 ml/min. A PFA mirco-flow nebuliser was used in a cyclonic quartz glass spray chamber, chilled to a constant 2.6 oC Collision cell (KED) mode: all aforementioned parameters were employed with the addition of helium as a collision cell gas at a flow rate of ~4.0 ml/min.

Gold 197Au mono-isotope was selected and analysis was performed in both STD and KED modes, using 6 replicates of 30 seconds per sample, giving a total of 3 minutes acquisition per sample. A linear series of Au only calibrations standards were prepared at 0, 1, 10 and 100 ppb made up in 1% HNO3/1%HCl (by volume). Samples were analysed by comparison to the standards previously mentioned. A quality control standard QC, was analysed every tenth sample and results are only reported given a suitably precise calibration and acceptable QC recoveries. Both STD and KED modes returned comparable results and the STD mode results were reported.

Intracellular concentrations of AuNPs were then calculated by dividing the ICP-MS reading by the cell number and multiplying up to calculate pg of Au.

4. The Synthesis of Co-functionalized AuNPs using a Bifunctional Linker

As discussed in the Literature Review, two methodologies are commonly used to co-functionalize the AuNP surface, both of which are illustrated in Figure 4-1. The first involves the synthesis of a mixed monolayer, for example, by attaching both a stabilizing ligand and a peptide or targeting ligand directly to the AuNP surface using thiol chemistries (Figure 4-1a). [12,158,184,203–206] The second method uses a hetero-bifunctional linker such as thiol-PEG-succinimidyl glutaramide which has a thiol at one end for attachment to the AuNP surface, and an NHS ester group at the other, which can react with the nucleophilic primary amine groups which exist at the N-Terminus of each peptide, thus acting as a linker (Figure 4-1b). While there are various *in vitro* and *in vivo* studies using both functionalization methodologies, there is no consensus within the published literature regarding the influence of attachment method on colloidal stability and biological response. [59–63,153,211]

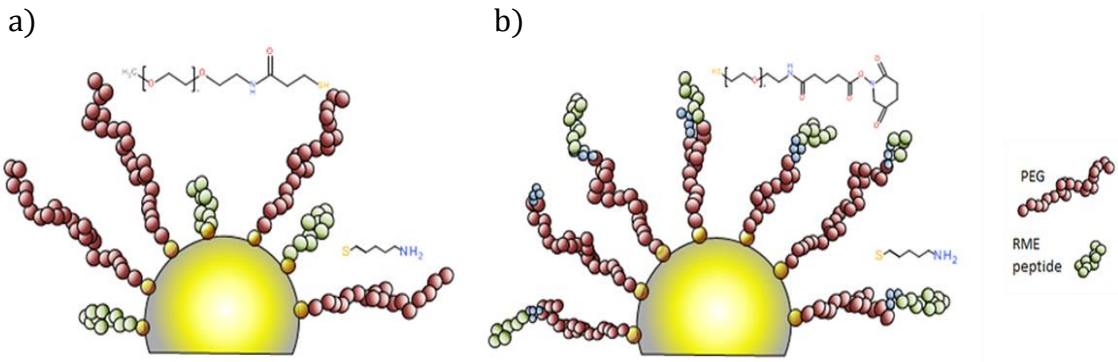

Figure 4-1 Schematic representing a) the synthesis of a mixed monolayer and b) co-functionalization using PEG as a thiol linker.

Chapter 2 discussed the various methods to functionalize the AuNP with peptides. The method of chemically conjugating a peptide onto the AuNP surface does not just vary with the physical interaction between the Au and S or N atoms (ionic attraction, hydrophobic attraction) or through the chemical interactions between the ligand and

the surface (chemisorption via thiol derivatives, bifunctional linkers etc.) but can also vary via the physical process of conjugation, these processes are known as either sequential or parallel loading. [242–245]

Sequential loading is the process of adding the stabilizing agent, followed by the desired biologically active ligand in sequence, as described in the section 3.4.2. Parallel loading, involves the subsequent reaction of two or more ligands separate to the AuNP suspension, then adding the pre-conjugated ligand to the nanoparticle surface (Figure 4-2). [157]

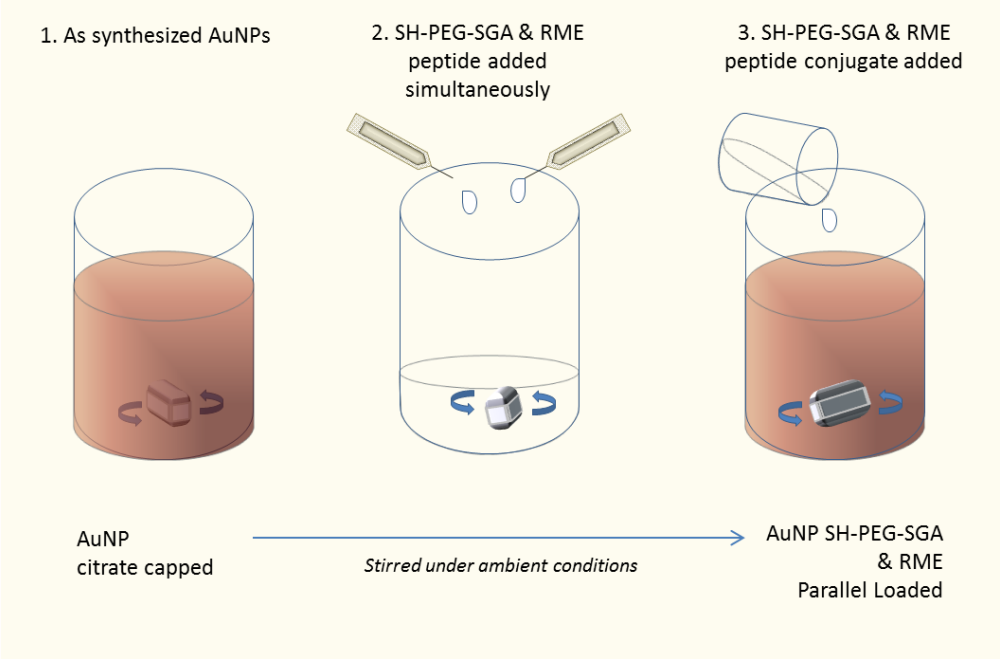

Figure 4-2 Illustration of the parallel loading method

An example of this is the reaction of lysine with the succinimide ester in parallel to form a BSA and MBS (3-maleimido benzoic acid N-hydroxysuccinimide ester) linker; this was the first of three steps to synthesize a BSA-peptide conjugate complexed to 20 nm diameter citrate-stabilized gold particles. A cysteine terminated peptide was then conjugated to the remaining exposed maleimido group and then washed via dialysis before being conjugated to AuNPs. While peptide concentrations were estimated via a mobility shift assay coupled with isoelectric focusing electrophoresis and the addition of fluorescein labels, the arrangement on the surface was confirmed by an increase in size by DLS, however DLS revealed that BSA-

peptide conjugates added < 2 nm to the radius of the nanoparticle complex. From this study, it was observed that the thiol in the cysteine residue was used to react to the maleimido group and not the gold leaving the C-terminus to bind to the gold surface using weak amine bonds. [157] It is possible that the chemical conjugating occurred through the amine groups found on the C-terminus and/or a combination of the C-terminus and the other amines present on the side chains of the remaining 583 amino residues which compose BSA. [157]

Otsuka *et al.* studied the conversion of acetal groups to aldehydes on immobilized block co-polymers before incorporating the process into the synthesis of a heterobifunctional PEG on an AuNP surface. The PEG acetal terminal group was converted to aldehyde by gentle acid treatment, followed by the reaction with sugar derivatives followed as a function of time through optical changes in the surface plasmon band in the UV–Vis spectrum. [217,246] Other examples utilized the shaking of a linker with AuNPs for surface functionalization, followed by centrifugal washing and tethering of platinum via amine-carboxylic acid reactions. PEGylated nanoparticles were characterized by electron probe microanalysis (EPMA) to confirm that both gold and platinum were present through their elemental peaks at 2.12 and 2.05 keV, respectively. [149] Amide linkage to Carboxylic (COOH) groups has also been identified in the literature through EDC (1-ethyl-3-(3-dimethylaminopropyl) carbodiimide hydrochloride) and NHS (D-hydroxysulfosuccinimide sodium salt) two-step coupling activation mechanism of the carboxylic group of the PEG derivative for conjugation to antibodies. [203] This process was carried out in THF (tetrahydrofuran). None of the methods outlined above attempt the synthesis of a linker with a cysteine containing ligand.

From analysis of the table in chapter 2, it is apparent that other methods to achieve a linker include the parallel loading of RNA to thiolated OEG. It is also observed that most linker formations were synthesized as a whole, prior to addition to the gold surface. [218,219] The techniques used to confirm the surface arrangement also vary, by the addition of coumarin dye, Shenoy *et al.* were able to prove the synthesis of linker via nucleophillic addition and the successful functionalization to gold via fluorescence. [157,218,219]

It is therefore of important note that most of the linkers previously discussed either involved the complete synthesis of the ligands in in a pre-linked formation via bottom up approaches, or was achieved via parallel loading. Sequential loading was only successfully observed from the literature in chapter 2 via the implementation of an EDC coupling reaction, and even then, this is usually not carried out in the presence of a thiol group on the additional ligand. [218]

Therefore, this chapter will outline the synthesis and co-functionalization of gold nanoparticles in a mixed monolayer arrangement using mono-functional (SH-PEG), and using a PEG hetero bifunctional linker (SH-PEG-SGA) – via both sequential and parallel loading – covalently attaching a peptide either to initiate receptor mediated endocytosis (RME) or a peptide to elicit endosomal escape (H5WYG). The chosen RME peptide is a 17-amino acid residue peptide (sequence CKKKKKKSEDEYPYVPN) terminated with a thiolated cysteine unit at the N terminus. This peptide can form a mixed monolayer arrangement when used in conjunction with mono-functional PEG by the strong thiolate bonds formed with the AuNP surface. The free amine group found on the cysteine could also potentially be used to form a bifunctional linker in the presence of the NHS ester found on the hetero bifunctional PEG. As illustrated in Figure 4-3 for a linker surface arrangement to be successful, the NHS ester reagent would react with the primary amine on the protein or peptide to form a stable amide bond with an NHS by product.

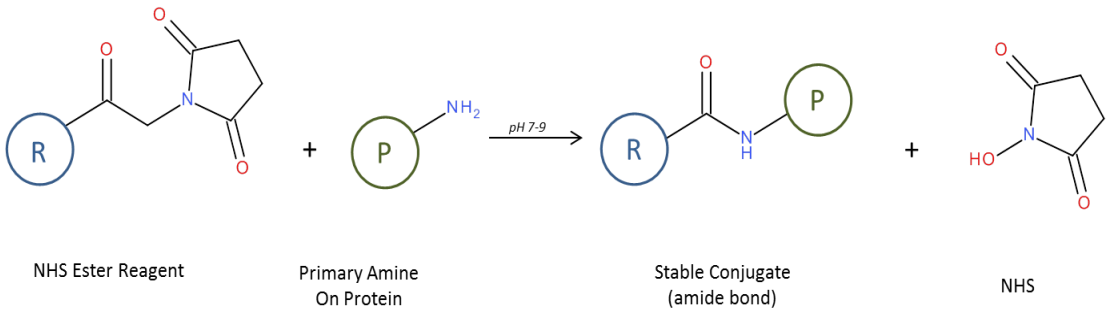

Figure 4-3 The reaction of an NHS ester with a Primary amine and the formation of the amide bond

Literature has identified that H5WYG (H5) can be used for successful endosomal escape both with and without a thiol group present. Therefore H5WYG was purchased from BIOMATIK with the following sequences (GCLFHAIAHFIHGGWHGLIHGWYG)& (GLFHAIAHFIHGGWHGLIHGWYG).

Both RME and H5WYG peptide were chosen due to the results obtained from the collaboration with Queens University Belfast, Pharmacy. Previous collaborative studies have shown marked differences between the endocytotic potential of various cell lines following 24 h incubation with 25 µg/ml AuNPs. Intracellular AuNP concentrations of between 7-8 pg/cell in MCF-10A, MDA-MB-231 and MCF-7 cells, reducing to 1.34 pg/cell in ZR-75-1 cells were observed. It was observed that the addition of PEG severely impaired AuNP uptake, with a 98-100 % reduction in all cases. Functionalization with the cell penetrating RME peptide helped to restore internalization in all cases generating a significant increase in AuNP uptake in MDA-MB-231 cells, MCF-7 and ZR75-1. [156,247]

Interestingly, however, AuNPs conjugated with the endosomal escape peptide H5WYG demonstrated an increased volume of intracellular Au content (but was not found to be statistically significant). [247] This is most likely a result of the net positive charge of these peptides conferred through the five histidine ligands. This peptide has previously been shown to initiate membrane disruption of the endosome

once internalized by the cell, subsequently allowing the release of the nanoparticles into the intracellular environment. [178] This also facilitates an increased AuNP surface area for electron emission. Endosomal escape provided by H5WYG and homogeneity from PEG help facilitate a larger therapeutic surface area, thereby promoting electron emission from the nanoparticle surface and subsequently a greater efficacy. [156]

The potential of endosomal release caused by H5WYG functionalized AuNPs could allow for an increased intracellular distribution and therapeutic surface area of nanoparticles, this combined with the ability to cause internalization translates into the potential for improved efficacy. The results from a previous publication from this research group have shown (Nicol *et al*.) the radio sensitizing potential of the various functional groups. [247] The annotated sensitizer enhancement ratio's (SER) within these graphs (resuts not shown - (Nicol *et al*.)) represent the RME, H5WYG and DP functionalized AuNPs respectively. Sensitizer enhancement ratio's (SER) document the enhancement at specific radiation doses of the nanoparticle preparations. Normal breast cells MCF-10A showed that the addition of H5WYG resulted in a 31% increase in radio sensitivity respectively as indicated by the SERs (results not shown). [247] MDA-MB-231 cells show a more significant impact following conjugation of the peptides producing SERs of 1.57, 1.84 with RME and H5WYG respectively. [247]

Two considerations must be considered for the successful synthesis of a linked ester and amine group. The first consideration is whether a peptide which contains a thiol residue can be successfully linked using a pre-synthesized NHS ester for reaction to the amine groups during AuNPs functionalization due to a thiols higher binding affinity to gold; and likeliness to be chemisorbed on Au via strong thiolate – Au bonds (40-50 kcal/ mol^{-1}). Review of the literature identified that many research groups facilitate the synthesis of a linker prior to conjugation to the AuNP surface and as such, to the authors best knowledge, the co-functionalization using a pre-synthesized NHS ester as demonstrated with the Thesis, is quite novel. Therefore, it can be postulated that one of the main challenges presented for bifunctional linker formulation is controlling the addition of peptides when one or more ligands are thiol-containing molecules. [248] It is therefore hypothesized that conjugation of

ligands (thiol or not thiolated) in parallel could facilitate reaction with a pre-synthesized NHS ester reaction and thus when added to the gold, the ‘pre-linked’ ligand could bind conveniently to the gold via the thiol found on the PEG, while retaining enhanced colloidal stability and potentially being able to elicit a positive biological response, in comparison to a mixed monolayer counterpart.

To test this first hypothesis, AuNPs will be functionalized with both mono-functional and bi functional PEG, then co-functionalized with RME (sequentially) and directly compared to identify how each peptide has bound to the AuNP surface. An equivalent sample will be synthesized concurrently for both arrangements in parallel to compare to the sequentially loaded samples to identify if the physical conjugation steps may play an important role in AuNP functionalization.

The second consideration is the solvent used for the dissolution of the NHS ester and the peptide. Solvents for the peptide must be carefully chosen due to the polarity of the peptide. Hydrophobic amino acids are usually buried within the core of the peptide structure, while charged residues are exposed to the solvent to a much higher degree, allowing the potential formation of hydrogen bonds. The H5WYG sequence consists of the following 32 residues: GLFHAIAHFIHGGWHGLIHGWYG. Glycine, Leucine, Phenylalanine, Alanine & Isoleucine are all uncharged hydrophobic residues, while Histidine (+1), Tyrosine & Tryptophan are polar. Based on the low propensity of the side chains to be in contact with a polar solvent like water, it was concluded that based on the Hydro-2 hydrophobicity parameter, the percentage of hydrophobic residues for this peptide is approximately 61% hydrophobic and as such should be dissolved in small amounts of organic solvents such as DMSO, DMF, Acetic acid or methanol. [249]

The solvent used for the dissolution of the PEG must also be carefully considered. As previously described; the simplest and most versatile technique for functionalizing AuNPs with proteins involves the utilization of chemical groups such as an NHS ester which can react with the nucleophilic primary amine groups which exist at the N-Terminus of each peptide. To the best of the author’s knowledge, this approach is novel as most literature involves the conversion of a carboxylic group to an ester using carbodiimides such as EDC coupling reactions. The approach in this

Thesis uses a bifunctional PEG with a ready-made NHS ester for functionalization, thus improving efficiency. The reaction of NHS esters with amines is strongly pH dependent, at a lower pH the amino group is protonated, at a higher than optimal pH hydrolysis is quick. [250]

NHS esters hydrolyze and glutaramide succinimidyl esters like the one used for this bifunctional PEG, have a half-life of only 15-20 minutes in water, this rate of hydrolysis increases with pH. As well as the potential hydrolysis of the ester, the solubility also varies with the buffer, and is dependent on the structure. Non-sulphonated forms of the NHS ester are water insoluble and ThermoFisher recommends organic solvents such as DMF or DMSO in 0.5-10% of the final volume, elsewhere it is recommended to PEGylate proteins or nanoparticles in a large excess of the PEG NHS esters due to the competitive hydrolysis reaction in an aqueous solution. [251] Based on these observations from the literature, it can be hypothesized that when using water, the synthesis of a linker will compete with the hydrolyzation of the ester, and therefore it is possible that a pre-linked ester may be completely dependent on the solvent it is suspended in. To investigate if the synthesis of a linker is dependent on the presence- or lack there of - of a thiolor if it will be dependent on the solvent, the two H5WYG peptides both with an without the cysteine residue will be testing – sequentially and via parallel loading – to idenfity which parameters are mandatory to synthesize a linker using a ‘ready-made’ NHS ester for amine reaction.

This chapter will outline the steps required for the successful synthesis of functionalized AuNPs using a PEG linker, and the characterization of each nanoparticle vector. The chapter will then directly compare the two surface arrangements in regards to colloidal stability, non-specific protein adsorption, internalization, cell viability and radio sensitization to determine if one arrangement results in more favorable biological result in comparison to its counterpart.

4.1 Results and Discussion

4.1.1 Sequentially loaded RME peptide

AuNPs were synthesized using the Turkevich method outlined in the Materials and Methods section of this Thesis. To prepare the mixed monolayer PEG capped AuNPs, 10.68 μg/ml of free SH-PEG was dissolved in 1 ml of distilled water and added to the citrate capped AuNPs. As described in chapter 3, this level of PEG addition yields approximately 50% of potential surface saturation with this ligand. [184] Therefore, to prepare the PEG linker samples, 20 μg/ml of free SH-PEG-SGA was dissolved in 1 ml of distilled water and added to the 'as synthesized' AuNPs to fully cap the nanoparticles with PEG Linker. [184] A PEG Linker sample was co-functionalized with both 4.45 μg/ml of RME, and 10 μg/ml RME to provide 50% coverage and complete saturation as calculated via Equation 3-1 in chapter 3 for comparative purposes.

The nanoparticles were characterized at various points during synthesis, including post synthesis, post PEGylation, post centrifugation and after co-functionalization with RME peptide. The characterization techniques employed for this chapter include DLS, TEM, UV/Vis, FTIR, Gel Electrophoresis and AAS. As synthesized AuNPs will be referred to as AuNP citrate capped. AuNP with mono functional PEG is AuNP SH-PEG, AuNP with bifunctional PEG is AuNP SH-PEG-SGA and the RME peptide co-functionalized counterparts will be referred to as AuNP SH-PEG & RME and AuNP SH-PEG-SGA & RME, with 4.45 μg/ml RME coverage being addressed as 50% and 10 μg/ml RME referred to as 100% for ease of report.

DLS size measurements were gathered by 9 runs per sample, with 15 measurements per one run, these were averaged and used to calculate the standard deviation highlighted in Table 4-1.

Table 4-1 DLS size and zeta measurements for functionalized AuNPs

Sample name	Size (d. nm)	PDI	Zeta (mV)
AuNP Citrate capped	17.4 ± 1.15	0.22	-30.65 ± 3.11
AuNP SH-PEG	37.29 ± 0.43	0.22	-6.74 ± 2.43
AuNP SH-PEG-SGA	34.84 ± 4.31	0.28	-28.8 ± 1.10
AuNP SH-PEG RME 50%	38.23 ± 1.54	0.32	-4.41 ± 0.29
AuNP SH-PEG-SGA RME 50%	34.87 ± 2.76	0.26	-13.8 ± 1.8
AuNP SH-PEG-SGA RME 100%	35.23 ± 0.30	0.28	-12.53 ± 1.18

This variation in nanoparticle length as a result of PEGylation is proposed to be a consequence of the different molecular weights of the PEG. Upon co-functionalization with SH-PEG & RME, the hydrodynamic diameter increased slightly to 38 d.nm. If we refer to Figure 4-1 the mixed monolayer arrangement is obtained by both the peptide and PEG attaching directly to the nanoparticle surface. Therefore, a large increase is size was not expected as the PEG chains are longer than those of the peptide. Any slight increases in size are hypothesized to be a result of 'straightening' of the polymer chain as a result of surface saturation by the peptide. Co-functionalizing the bifunctional AuNP SH-PEG-SGA with either 50% of 100% RME resulted in average AuNP diameters of 35 d.nm respectively, and therefore does not indicate the synthesis of a linker with the NHS ester.

The zeta potential showed an increase in surface charge from approximately -29 mV to -14 and -13 mV for the 50% and 100% RME co-functionalized samples respectively. Therefore, the DLS size measurements are concluded to be a result of the conformation of the peptide in solution. With slight changes in sizes increasing with the amount of PEG attached a result of straightening of possible coils of RME peptide suspended in distilled water.

Transmission electron microscopy (TEM) images for citrate capped showed an average particle size of 13.3 ± 4.2 nm. The PEG functionalized and RME peptide co-functionalized samples do not show any increase in size, which was expected as the acceleration voltage used is not sensitive to the organic coating. However from the images obtained in Harrison *et al.* it is apparent that functionalization minimizes the

degree of aggregation to some extent in comparisons to the citrate capped AuNPs, and – to some degree - the level of AuNPs overlapping for both the mono-functional and bifunctional PEGylated counterparts. [12,185]

AuNPs are subject to the quantum size effects, which gives rise to the unique properties known as the Surface Plasmon Resonance (SPR), which renders gold nanoparticles a ruby red color. Because of this SPR, which is the oscillation of electrons in the conduction band of AuNPs in resonance with a specific wavelength of light, AuNPs result in strong absorbance bands in the visible region [252,253]

Severe aggregation (referred to as instability throughout this Thesis), or a particle size increase towards the bulk limit reflects light in the infra-red portion of the electromagnetic spectrum and therefore most visible wavelengths are reflected, resulting in a clear solution. It is the unique property of the SPR which is of major clinical interest, as the SPR can be tailored by size and shape to enhance different applications. [254]

A study was conducted to determine the colloidal stability of AuNPs with varying amounts of PEG attached. This was an important study as to be able to functionalize the AuNPs with an array of ligands for various applications, the AuNP must be primarily functionalized with PEG for enhanced stability, if the AuNP remains stable with minimal amounts of PEG attached it potentially enables to AuNP to have minimal stabilizing agent and consequently a larger amount of ligand or payload for a biological consequence. Figure 4-4 displays the absorbance spectra for AuNPs functionalized with increasing amounts of SH-PEG. The characteristic peak at 520 nm is clearly visible for all AuNP samples in Figure 4-4, [183,252,255,256] and as such, all the AuNPs remained colloidally stable regardless of the amount of PEG attached, this state remained true for the bifunctional PEG, illustrated in Figure 4-5. Citrate capped AuNPs are stable due to the repulsions caused by like charges between particles, PEG offers a steric barrier, therefore partially covering the AuNPs may have resulted in aggregation due to slight changes in the surface charges (Table 4-1) while not offering sufficient steric barriers to prevent aggregation, whereas both the AuNP SH-PEG and the AuNP SH-PEG-SGA were stable irrespective of the amount of PEG attached.

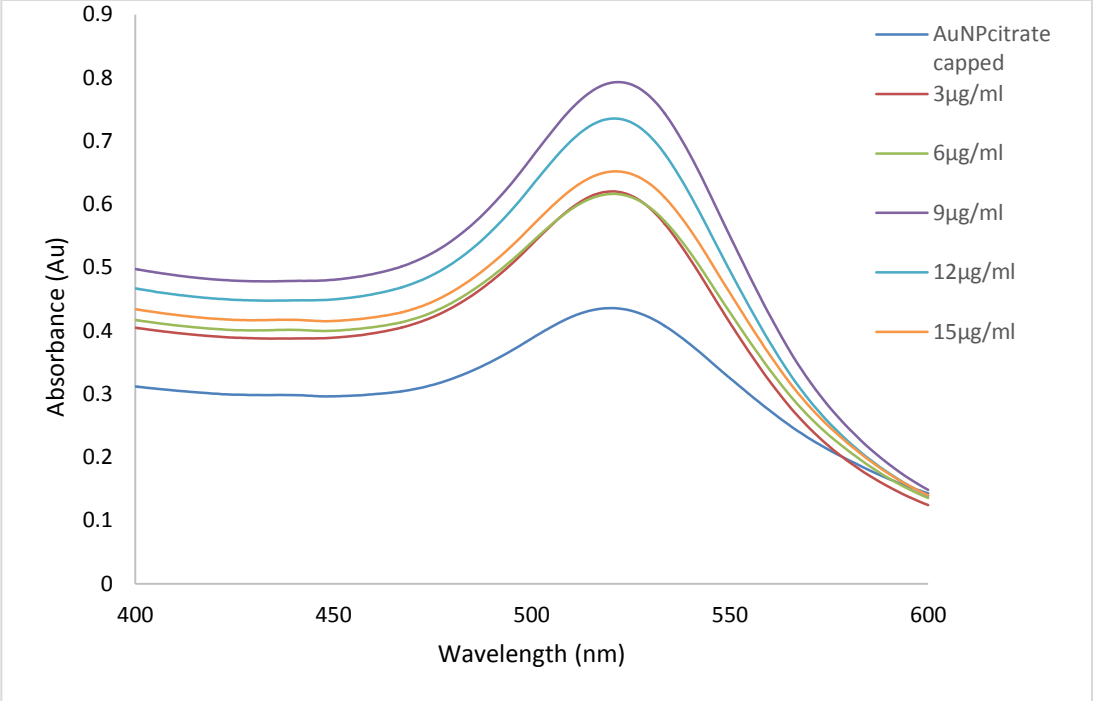

Figure 4-4 UV/Vis absorbance spectra for AuNP functionalized with increasing amounts of SH-PEG

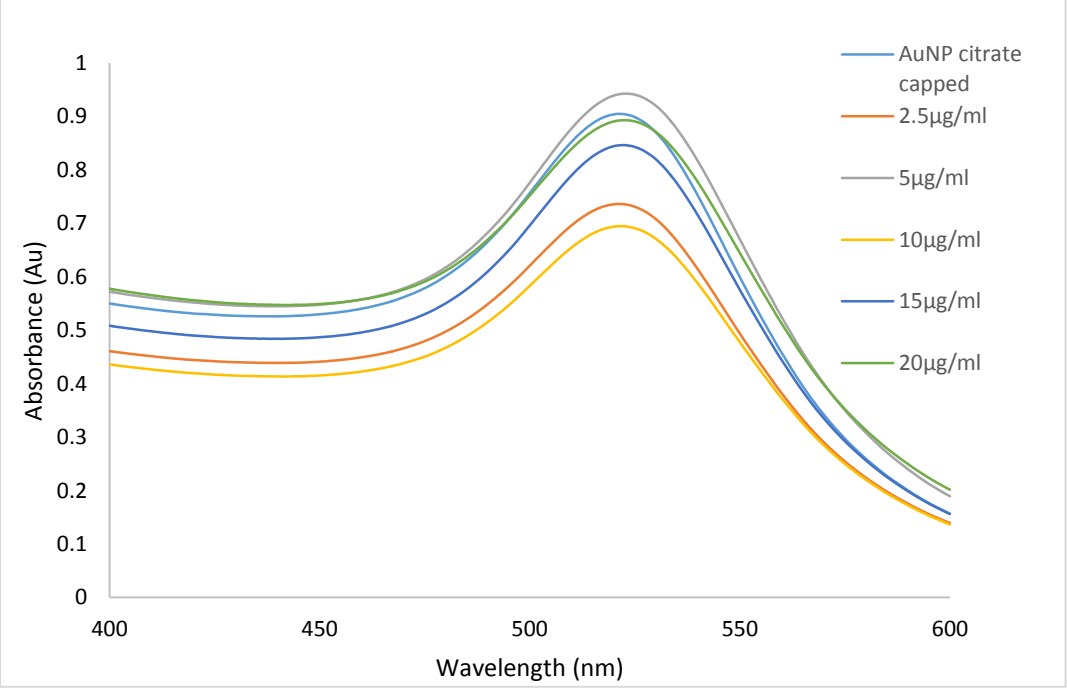

Figure 4-5 UV/Vis absorbance spectra for AuNP functionalized with increasing amounts of SH-PEG-SGA

UV/Vis measurements were then conducted on the AuNP samples co-functionalized with RME (AuNP SH-PEG & RME and AuNP SH-PEG-SGA & RME). The results showed in the previous publication that the colloidal solutions have maintained a high degree of colloidal stability following centrifugal washing and dispersion for the PEGylated colloidal gold and the co-functionalized RME samples. The colloidal stability of the co-functionalized samples was investigated by comparing each sample to the PEGylated counterpart prior to the peptide addition, dispersed in distilled water as a control. The mixed monolayer and linker spectra's exhibit a distinctive absorption peak at ~521 nm with small shifts apparent from 519.9 nm to approximately 521 nm as a result of the complex conjugation of AuNP citrate capped to PEG and peptide functionalized AuNPs. The results do not indicate any differences between the two surface arrangements in terms of length in relation to the successful synthesis of a linker.

To further investigate the influence of a hetero bifunctional linker on AuNP stability, AuNPs were functionalized with 50% or 100% coverage of SH-PEG-SGA, a pre-caluculated amount of PBS tablet was crushed and added to the AuNP samples and vortexed for 1 minute. The PEGylated samples were then monitored over a period of

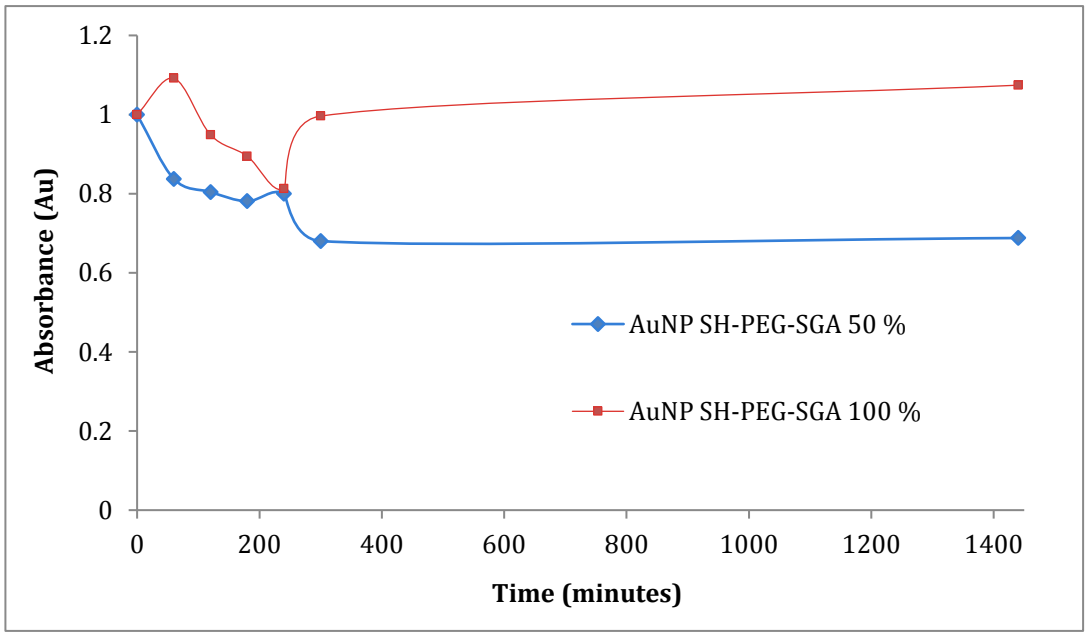

Figure 4-6 PBS colloidal stability study displayed the UV/Vis relative absorbance of AuNP functionalized with either 50% or 100% SH-PEG-SGA over 24h

24 h to determine if aggregation occurred from monitoring the absorbance maxima of the SPR peak for AuNPs. PBS is commonly used to elicit physiological conditions of cells, these include a pH value within the range of 7 ~ 7.6, and often set to be 7.4 as the pH of blood nears 7.4, a value referred to as the physiological pH in biology and medicine. In addition to maintaining a constant pH, PBS in general has an osmolality that matches those of the human body (isotonic) and is non-toxic to the cells. [257] PBS has a molarity of 137 mM NaCl, when salt is added to gold nanoparticles the surface charge of the AuNPs neutralize, and without the like negative charges induced via the citrate, the particles aggregate. It was found that both samples retained their colloidal stability irrespective of the amount of bifunctional PEG added. This relationship is outlined in Figure 4-6.

Fourier Transform Infrared Spectroscopy was performed on the AuNP samples. FTIR serves to confirm the attachment of the ligands on the nanoparticle surface. A lot of complications can arise with FTIR analysis, especially with PEG and peptide attachment due to the similarities between the structures. As illustrated in Figure 4-3 for a linker surface arrangement to be successful, the NHS ester reagent would react with the primary amine on the protein or peptide to form a stable amide bond with an NHS by product. FTIR was therefore conducted on the samples to determine the formation of S-Au bonds and/or the loss of an NHS ester group.

Figure 4-7 displays the FTIR absorbance spectrum obtained for citrate capped AuNPs, the bands recorded can be ascribed to the internal frequencies of the citrate ion. 2923 cm^{-1}, 2956 cm^{-1} and 2854 cm^{-1} can be attributed to the out f phase and in phase CH and CH_2 vibrations. Bonds present at 1589 cm^{-1} and 1403 cm^{-1} are due to the CH_2 – O deformation and C=O stretching of the citrate ligand with the peak at 1644 cm^{-1} due to O-H-O bending modes. The peaks evident between 1500 cm^{-1} – 1630 cm^{-1} and 1305 cm^{-1} – 1415 cm^{-1} are due to the carboxylate group exhibiting. an asymmetric COO^- stretching vibration and with reference to Parry et al. the bands between 1111 cm^{-1} and 1137 cm^{-1} are resultant of trisodium citrate. [258]The bonds between the 1041 cm^{-1} and 1093 cm^{-1} have been scribed to the oscillations of the C-OH group.

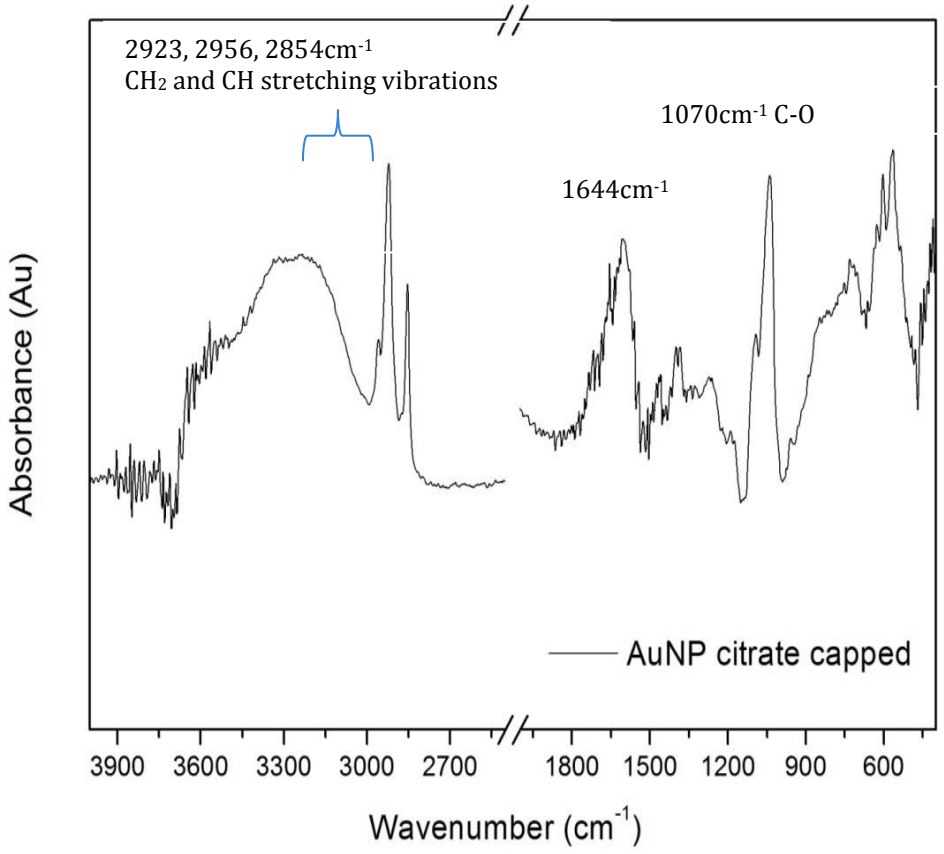

Figure 4-7 FTIR absorbance spectra for AuNP citrate capped

Prominent differences are visible in Figure 4-8 for the SH-PEG capped AuNP spectrum compared to that for the citrate capped AuNPs. Surface functionalization was confirmed by a decrease in the peaks corresponding to citrate capping aforementioned. Figure 4-8 displays the citrate capped AuNP, AuNP SH-PEG and 'free' SH-PEG. AuNP citrate capped (black) displays a peak at 1033 cm^{-1} corresponding to alkoxy C-O bonding. The decrease in this peak signifies a loss of the citrate ion from the surface.

The presence of the characteristic vibrations found in ethylene glycol ligands are expressed at 1106 cm^{-1} (C-O-C stretching), the acyl C-O groups (1300 cm^{-1}) and the phenol C-O groups (1245 cm^{-1}). The presence of the mono-functional thiol PEG (SH-PEG) on the AuNP-PEG is confirmed by an increase in the relative intensity of the peaks associated with C=O stretching (1,660 cm^{-1}) and bending (1,380 cm^{-1}) and

the presence of additional peaks relating to N-H bending and N-H wagging (600-900 cm^{-1}). [184,202,258–261]

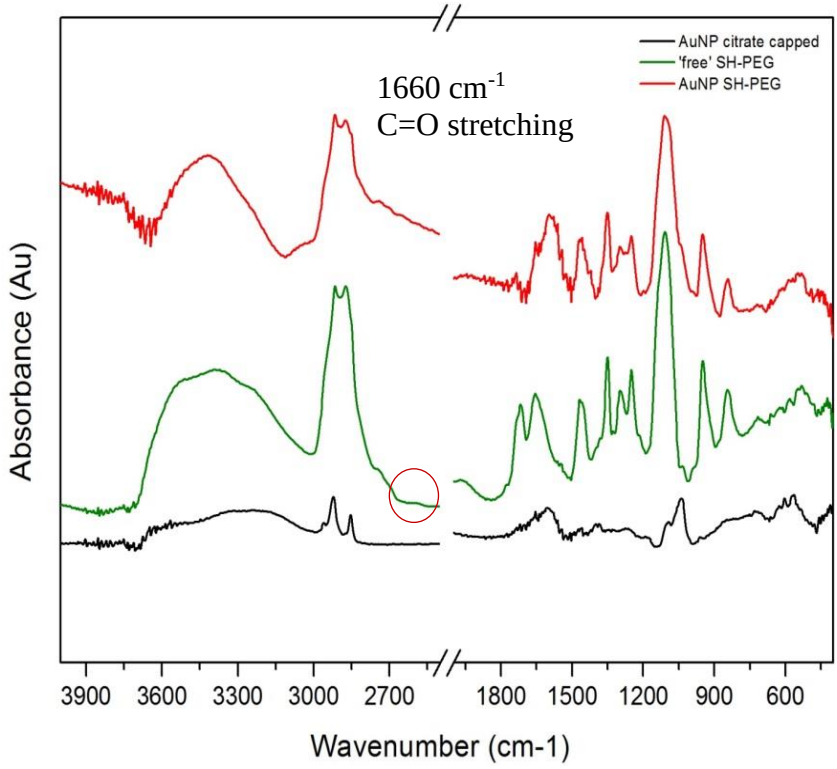

Figure 4-8 FTIR Spectra for AuNP citrate capped (black), 'free' SH-PEG (green) and AuNP SH-PEG (red)

For this area of research, the focus of the FTIR analysis was to determine surface arrangement, therefore it is important to note that the weak S-H vibrational stretch found at approximately 2550-2620 cm^{-1} on the 'free' SH-PEG was no longer observed on the AuNP SH-PEG conjugate as the thiol groups had reacted with gold to form S-Au covalent bonding.

The FTIR spectrum obtained after functionalization with the NHS ester containing SH-PEG-SGA corroborated with the loss of an S-H bond as seen in Figure 4-8 (circled in red). Figure 4-9 displays the FTIR spectra for citrate capped, 'free' SH-PEG-SGA and AuNP SH-PEG-SGA. Highlighted in blue are the bonds which are found on the AuNP SH-PEG-SGA conjugate but are not on the AuNP SH-PEG. Five bonds were found to be unique to the SGA containing PEG compared to the mono-functional PEG described previously. These bonds included asymmetric nitro at 1551 cm^{-1}; symmetric nitro or C-H bend at 1387 cm^{1} and an alkene C-H bend at 992 cm^{-1}. The peak at 1781 cm^{-1} on the 'free' SH-PEG-SGA is ascribed to the carbonyl stretch made in COO^{-} NHS ester ligand from the succinimide group, while the peak at 1735 cm^{-1} is ascribed to the saturated ester.[259,262]

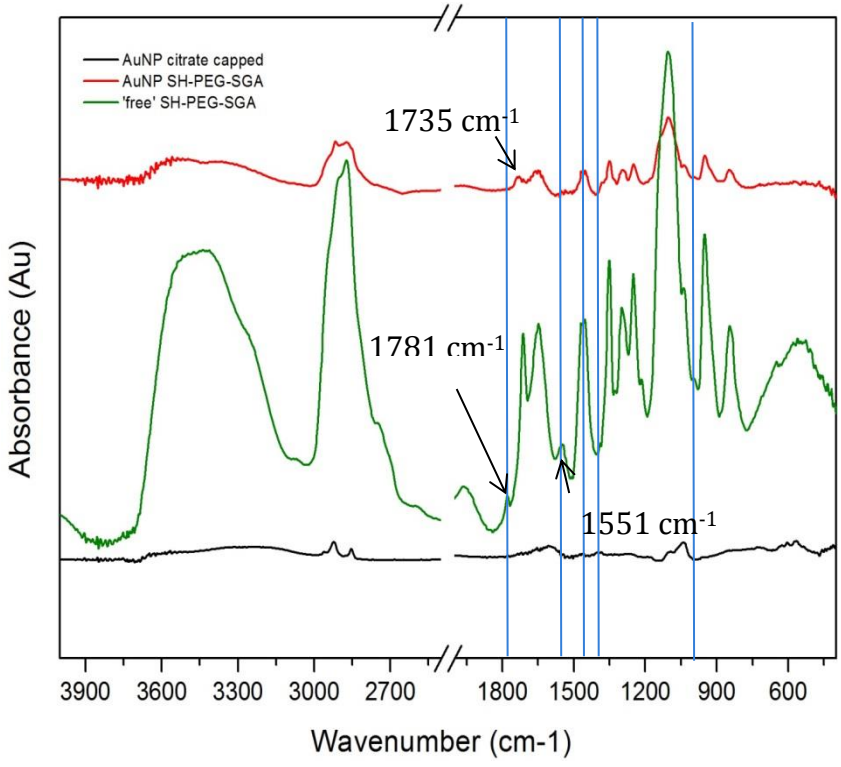

Figure 4-9 FTIR spectra for AuNP citrate capped (black), 'free' SH-PEG-SGA (green) and AuNP SH-PEG-SGA (red)

The solid-phase FTIR spectrum of the C=O stretch of the ester obtained by Tan *et al. (2006)* was given as 1787 cm^{-1}. [263] a peak is observed on the AuNP SH-PEG-SGA sample which plateaus between 1720-1740 cm^{-1}, peaks at 1720-1735 cm^{-1} belong to an aromatic ester and/or saturated ester while literature describes peaks at 1740 cm^{-1} to belong to an NHS ester as illustrated in Figure 4-9, the synthesis of a linker would involve the loss of the NHS ester, therefore the presence of this saturated ester on the AuNP surface confirms conjugation directly to the surface. [264,265]

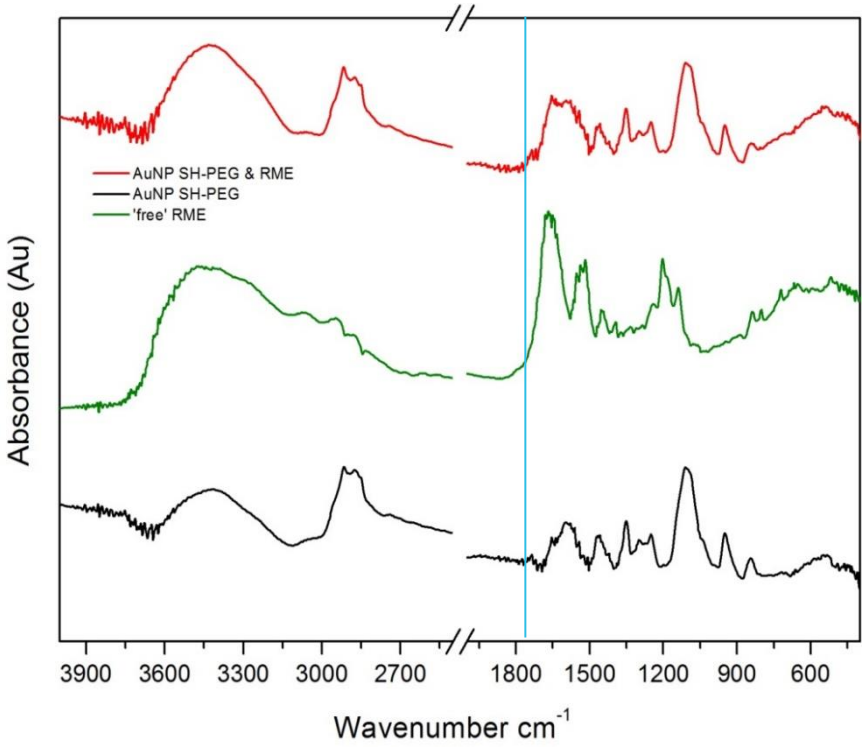

Figure 4-10 FTIR spectra for 'free' RME (green), AuNP SH-PEG (black) and AuNP SH-PEG RME (red)

Thiol bonds are present on the ‘free’ RME sample between 1550-1620 cm^{-1} in Figure 4-10. They are not present on either the AuNP SH-PEG or the AuNP SH-PEG RME sample. Thus, confirming conjugation via the S-H found on the cysteine unit. S-Au bonds are expected to appear at 1777 or 1545 cm^{-1}. Both conjugates present a minor peak at 1750 (highlighted in blue). While the shift may indicate the

presence of Au-S bonds it cannot be confirmed, however, the relative intensity has increased for the AuNP SH-PEG RME sample in comparison to the AuNP SH-PEG conjugate.

This suggests an increase in the number of Au-S bonds formed at this wavenumber via the attachment of the RME peptide. The presence of RME on the nanoparticle surface is further confirmed through the formation of amide bonds and N-H wagging ($600cm^{-1}$ – $900cm^{-1}$) on the RME conjugated sample. [266,267]

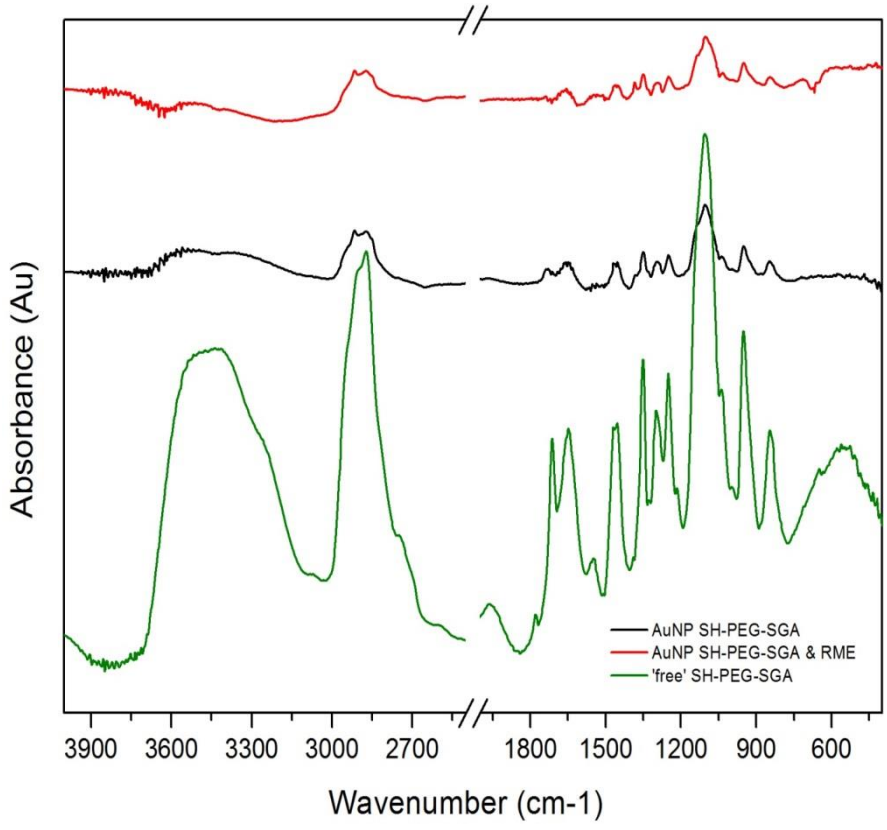

Figure 4-11 FTIR spectra for 'free' SH-PEG-SGA' (green), AuNP SH-PEG-SGA (black) and AuNP SH-PEG-SGA & RME (red)

Figure 4-11 compares the 'free' SH-PEG-SGA to the AuNP SH-PEG-SGA & RME conjugate to look for the disappearance of a NHS ester group; saturated esters are present at 1735 cm^{-1}. Figure 4-12 compares the AuNP SH-PEG-SGA & RME

conjugate to ‘free’ RME to identify the loss of a thiol group or the formation of the N-Au bond.

AuNP SH-PEG-SGA as described previously the successful conjugation of RME to the nanoparticle surface was confirmed by the appearance of new amide bonds around 1670 $cm^{-1}$and 1550 $cm^{-1}$for amide I and II respectively. The NHS ester groups which would react to form the linker with the amine group on the N Terminus of the RME cannot be confidently identified. However the peaks observed for symmetric nitro (1551 cm^{-1}), C-H bend (1387cm^{-1}), C-H alkene bend (992 cm^{-1}), saturated ester (1735 cm^{-1}) and the C=O stretched of the succinimide in the AuNP SH-PEG-SGA sample previously are still evident.

The peaks present at 1735 cm^{-1} corresponding to the saturated ester found on the SH-PEG-SGA are still present post co-functionalization with the RME peptide. However, the peak ascribed to the succinimide group has decreased in intensity post functionalization with RME, while this could signify the synthesis of a linker by the loss of the ester group, it cannot be confidently concluded. Therefore, it leads to the

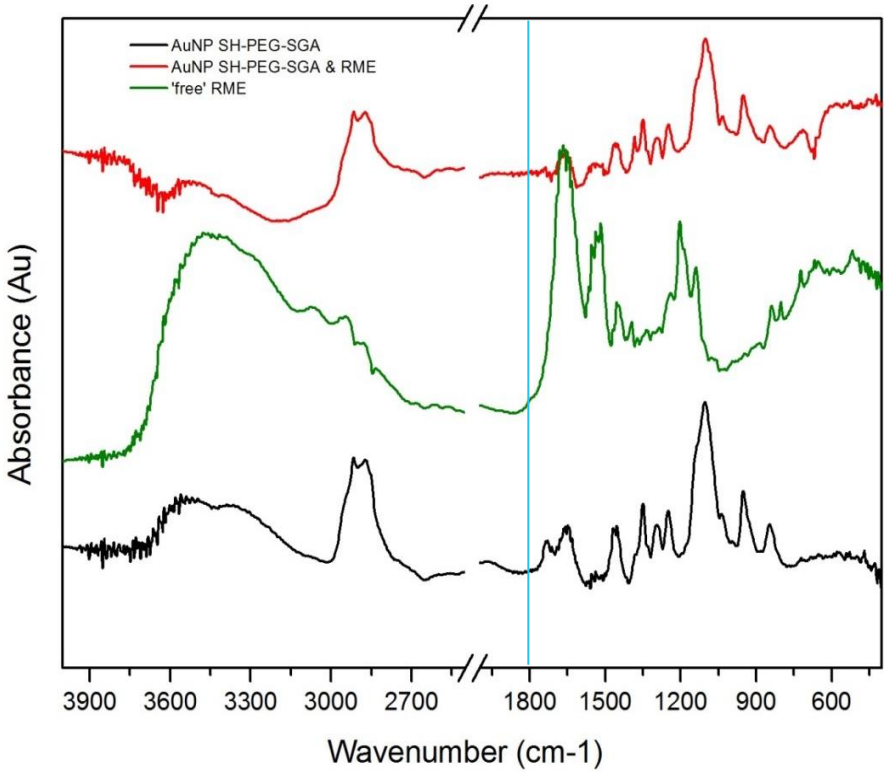

Figure 4-12 FTIR spectra for 'free' RME (green), AuNP SH-PEG-SGA (black) and AuNP SH-PEG-SGA RME (red)

likely conclusion that the RME peptide has not reacted with the SH-PEG-SGA.

From Figure 4-12 the conjugation of RME is evident from the increase in the relative intensity of the amide bonds. However, while the formation of Au-N from the free amine group on the N-terminus is unlikely, due to the likeliness of a mixed monolayer formation through the cysteine due to the high affinity of gold for thiols, the presence of Au-N cannot be confirmed. Au-N should peak in the far Infrared region at IR at 391cm^{-1}, 474 cm^{-1}, 368 cm^{-1}, 476 cm^{-1}, 375 cm^{-1} and 415 cm^{-1}. The commonly used region for infrared absorption spectroscopy is 4000 ~ 400 cm^{-1} because the absorption radiation of most organic compounds and inorganic ions is within this region. Therefore due to the expected peak position, the peaks are not characteristic enough for identification.

The presence of Au-S cannot be confirmed on either the AuNP SH-PEG-SGA or the AuNP –SH-PEG-SGA RME samples. The frequency of the S-Au bond is expected to be low due to the concentration of thiol groups present in the entirety of the sample therefore it is suggested that the signal has been quenched due to the ratio of the bonding found within the other ligands. There is an increase in noise present at 1777 cm^{-1} for the RME conjugated sample in comparison to the PEGylated sample, and there is no noise around that bond for the 'free' RME, however because of this, the synthesis of the S-Au covalent bond is inconclusive, however it is noted that there is no thiol group present on the conjugates.

In addition to the FTIR results, the literature supports the idea that the RME peptide bound directly to the gold and not to the PEG via the amine group as required to synthesize the desired linker. Sulphur atoms are better soft donor atoms than Nitrogen, Park *et al.* functionalized three bifunctional ligands, 2-pyridylphophines, thioamides and 1,1-dicyanoethylene-2,2-dithiolate to the gold through the P and S atoms due to the higher affinity that Sulphur and Phosphorous have for gold. [268,269] Therefore, it was generally assumed that gold (I) will not effectively coordinate to a donor nitrogen atom. [268,269]

As a further secondary technique to conclude that the RME peptide is not creating a linker with the SH-PEG-SGA, gel electrophoresis was employed to analyze the chare and migration profiles of each of the AuNP samples. Gel electrophoresis is an analytical technique normally employed for separating macromolecules or particles based upon size and charge, due to the unique red color of gold, gel electrophoresis enables direct observation of the particles migration profiles. As seen from the zeta results in Table 4-1, altering the AuNP surface with ligands results in a difference in zeta potential on the particle surface, which can be observed by variations in the migration pattern (Figure 4-13). In conjunction with that, there is an increase in size caused by the surface functionalization. Like DLS, gel electrophoresis is sensitive to the organic coating on the nanoparticles, therefore differences in the electrophoretic speed indicates differences in size and surface charge as a result of particle modification.

Gel electrophoresis confirmed conjugation of both PEG and peptide as indicated by the migration profiles for each of the AuNP sample types (Figure 4-13). [239]

However, for the linker samples, AuNPs were functionalized with both 10.68 µg/ml and 20 µg/ml of SH-PEG-SGA, and then co-functionalized with RME peptide in the hope to synthesize an NHS ester - amine linker as illustrated previously Figure 4-3. However it is likely that the faster migration decay SH-PEG-SGA is a result of the hydrolysis of the ester, as the ester hydrolysis competes with the primary amine reaction, the ester appears to be hydrolyzing and splitting into carboxylic acids, which accounts for the change in charge, and the differences in zeta potential previously observed in Table 4-1. [153]

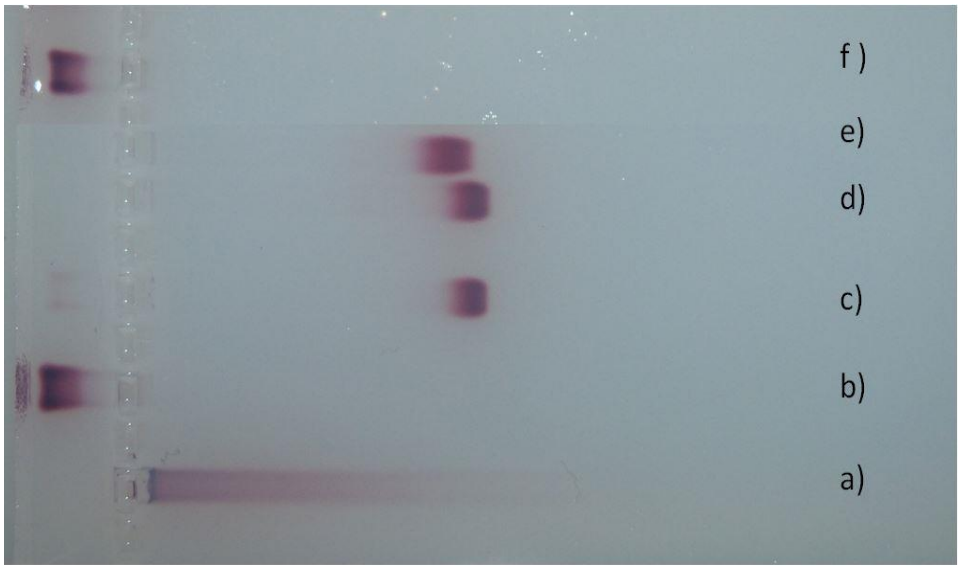

Figure 4-13 Gel electrophoresis for a) citrate capped, b) AuNP 10.68 µg/ml SH-PEG c) AuNP 10.68 µg/ml SH-PEG-SGA, d) AuNP 20 µg/ml SH-PEG-SGA, e) AuNP 20 µg/ml SH-PEG-SGA 4.45µg/ml RME, f) AuNP 10.68 µg/ml SH-PEG 4.45 µg/ml RME.

The characterization techniques have so far indicated that RME peptide has successfully attached to the AuNP conjugate for both the AuNP SH-PEG and AuNP SH-PEG-SGA functionalized particles, however that the co-functionalization with RME has produced a mixed monolayer in both approaches. Photoluminescence was carried out on both AuNP SH-PEG & RME and AuNP SH-PEG-SGA & RME to confirm this.

Texas Red C_2 Maleimide is a thiol reactive bright red fluorescent bio conjugate with excitation/emission maxima ~595/615 nm. If a thiol group is present in solution, Texas Red will bind to the S-H and fluoresce when excited ~595 nm. Figure 4-14 illustrates the chemical structure of Texas Red, the required amount was calculated using the Molecular Weight by the methods previously described in chapter 3.

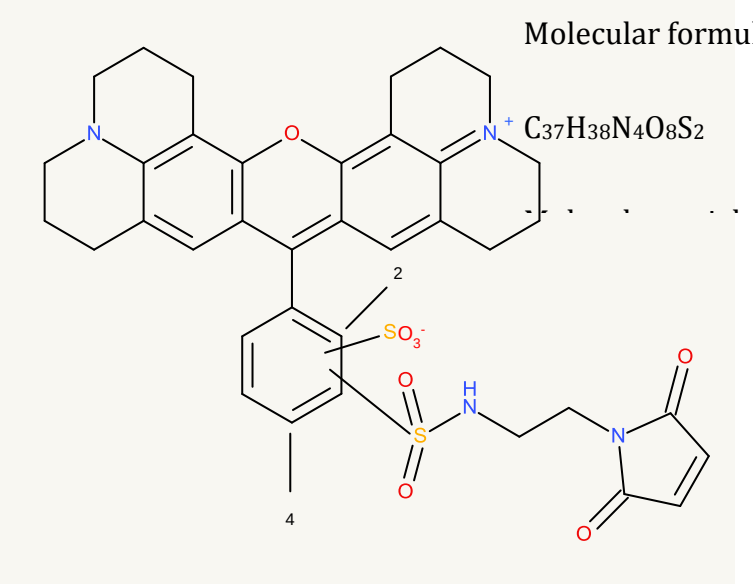

Figure 4-14 Chemical structure for the thiol reactive Texas Red C2 Maleimide bio conjugate

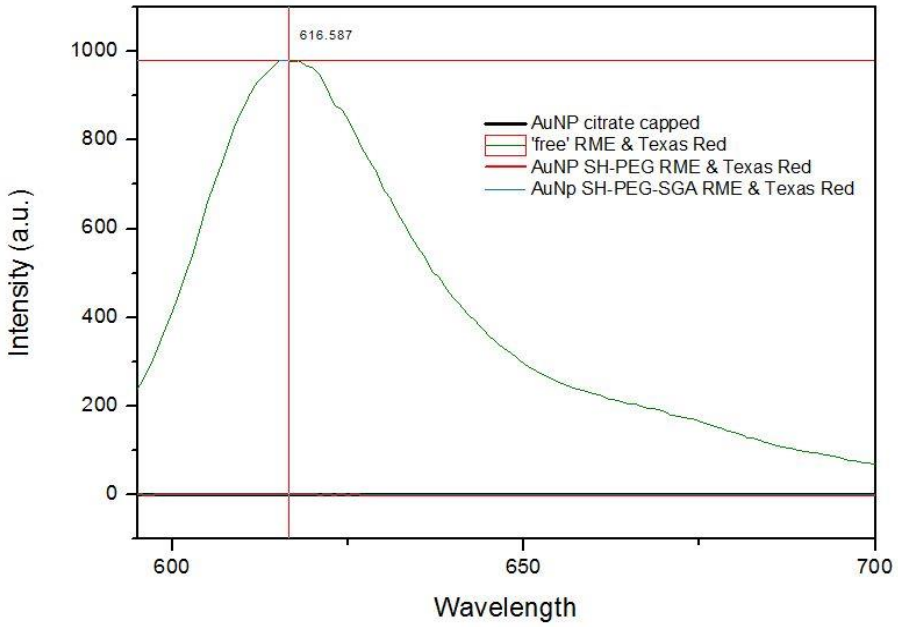

Figure 4-15 Emission spectra for the Texas Red displaying the intensity for the thiols for the citrate capped gold (negative control), 'free' RME (positive control), mixed monolayer (AuNP SH-PEG & RME) and the linker (AuNP SH-PEG-SGA & RME)

The excitation at 595 nm resulted in the subsequent emission at 617 nm for the 'free' RME sample confirming the presence of free thiol in solution. As expected, no excitation peak was present for the mixed monolayer confirming the attachment of the RME peptide to the gold via the thiol found on the cysteine residue. The Texas Red results for the linker arrangement corroborated with the conclusions drawn from the previous results. There was no excitation peak corresponding to a thiol group presents for the linker arrangement confirming that the RME bound to the gold surface via the thiol group and not via the NHS ester group as previously predicted.

This result corroborates with previous literature which involved the analysis of pepsin composed of one lysine and five cysteine residues.[270] While it is known that amine functional groups from primary amines bind to colloidal gold through weak covalent interactions, [271] it was concluded that the pepsin-Au conjugate enzyme molecules bound to the colloidal surface via thiolate linkages through the cysteine residues as well. [272]

4.1 Parallel Loading

It is apparent that various methods have been employed to characterize nanoparticles post functionalization with various ligands and/or ligands. While most involve the utilization of DLS as a fundamental basis for conjugation based on an increase in particle size, [157] many research groups facilitate the synthesis of a linker prior to conjugation to the AuNP surface. This process, known as parallel loading, involves the subsequent reaction of two or more ligands and the characterization of that solution prior to addition to the nanoparticle surface. [157]

AuNPs were synthesized using the Turkevich method outlined in the Materials and Methods chapter of this Thesis. To investigate the initial method of loading, 20 μg/ml of free SH-PEG-SGA was dissolved in 1 ml of distilled water and added 1 ml of dissolved RME peptide in water as illustrated in Figure 4-2. The solution was stirred overnight under ambient conditions and then added to the gold nanoparticles as described in the Materials and Methods. The parallel loaded samples were

compared to the mixed monolayer and bifunctional linker samples synthesized and co-functionalized as described previously. [184]

DLS of the AuNP SH-PEG-SGA & RME parallel loaded sample showed an average number measurement of 29.85 ± 1.9 with an average PDI of 0.2. This in comparison to the number mean measured previously for the sequentially loaded AuNP SH-PEG-SGA & RME shows a significant decreased in particle size decreasing from ~ 35 d.nm for PEGylated gold and between 25 – 37 d.nm for sequentially loaded RME. The decrease in particle size could be a result of unsuccessful conjugation of the parallel loaded sample to the gold or only partial saturation caused by the reaction of the thiol groups found on the cysteine on both the PEG and the RME peptide.

Fourier Transform Infrared Spectroscopy was performed on the AuNP samples dried in Potassium Bromide. Figure 4-16 & Figure 4-17 displays the absorbance spectra for the AuNP SH-PEG-SGA for both parallel and sequential loading.

Significant differences were evident between the two spectra. Extra peaks were present on the parallel loaded sample at 917 cm^{-1}, 980 cm^{-1}, 1394 cm^{-1} & 1569 cm^{-1}. Extra peaks were found on the sequential loaded sample at 950 cm^{-1}, 1543 cm^{-1}, 1595 cm^{-1} & 1738 cm^{-1}. The presence of RME on the co-functionalized sample was previously confirmed by the presence of additional peaks assigned as follows; amide band I at 1515 cm^{-1}, amide band II at 1710 cm^{-1} and N-H wagging between 600-900 cm^{-1}. [185,259] Bands ranging between approximately 1320 - 1400 cm^{-1} are generally ascribed to the sp3 C-H bend, while changes in the amide bonds are likely due to structural changes caused by binding with the NHS ester. The most notable change in peak is the peak present between 1730 - 1740 cm^{-1}; it is likely that this peak belongs to an unsaturated ester, which is present on the sequentially loaded sample but not the parallel loaded sample. This peak which would suggest that the reaction was successful by the NHS ester for the parallel loaded sample. However, the FTIR results combined with the DLS results indicate that while the synthesis of a linker in parallel may have been successful, the conjugation to gold is likely to be occurring via both the thiol found on the PEG, and the free thiol on the N terminus of the RME peptide. [265]

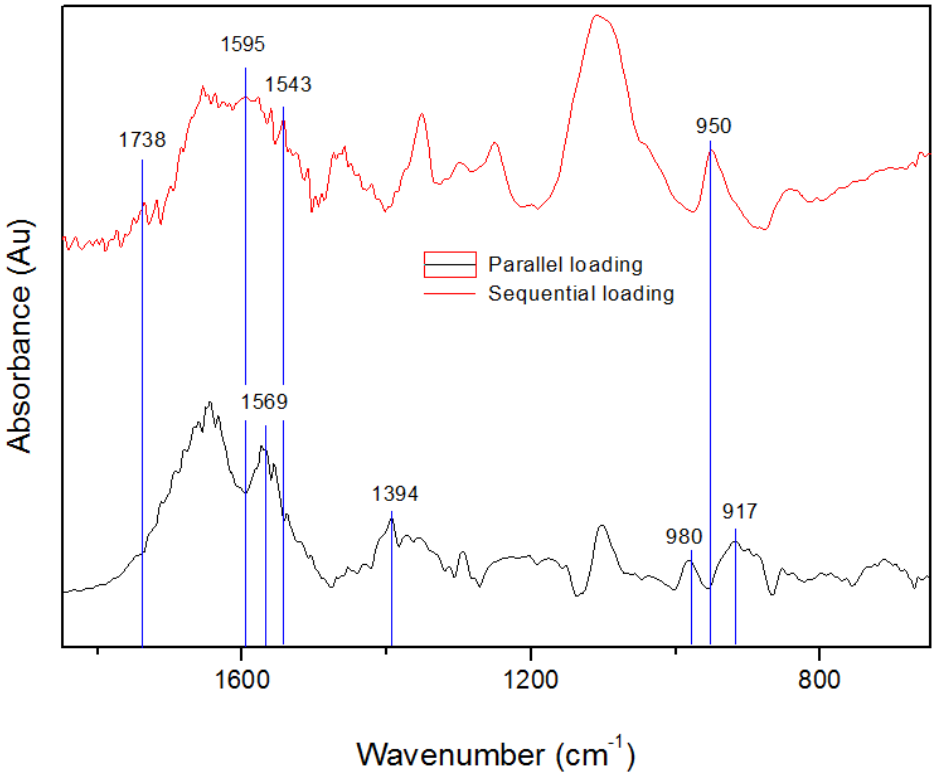

Figure 4-16 FTIR absorbance spectra for RME peptide both sequentially (red) and parallel loaded (black)

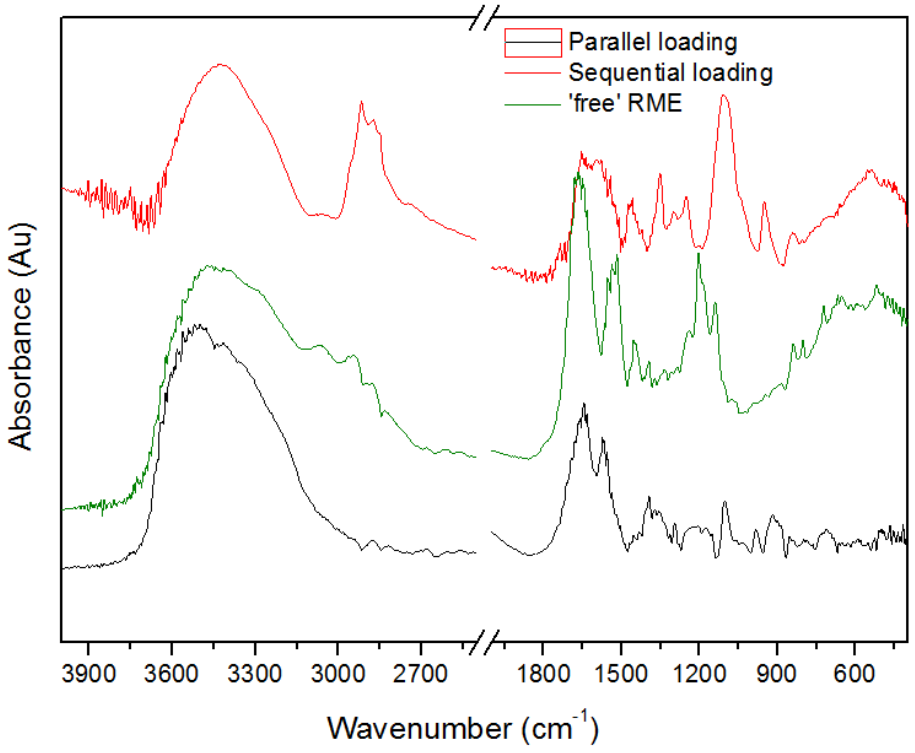

Figure 4-17 FTIR absorbance spectra for RME peptide both sequentially (red) and parallel loaded (black) compared to 'free' RME peptide (green)

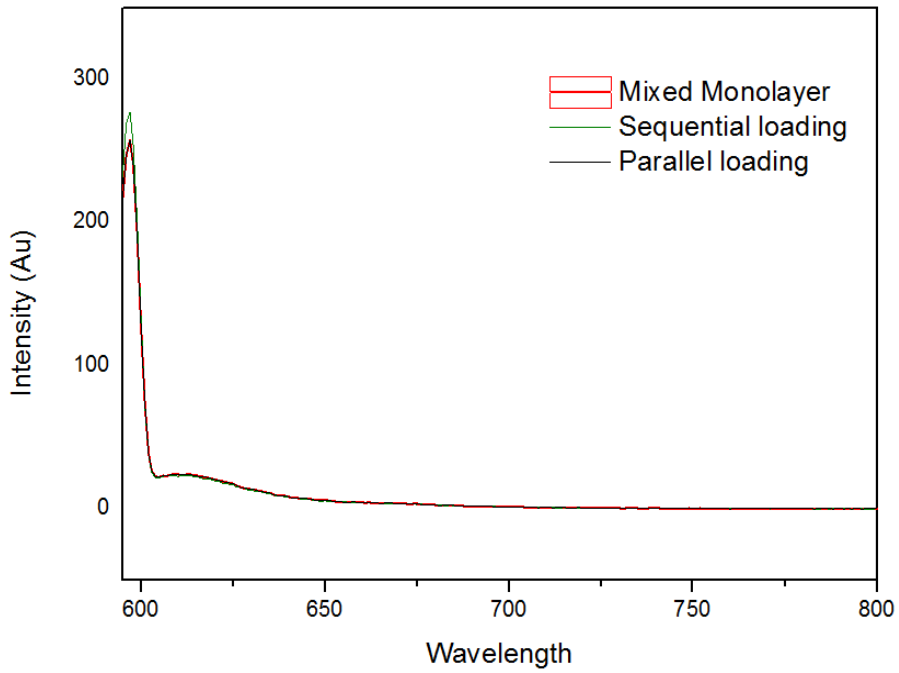

Figure 4-18 Emission spectrum for Texas Red showing the excitation and lack of emission for all the samples tested

The Texas Red thiol fluorescent probe previously employed was re-applied for the mixed monolayer, sequentially loaded and parallel loaded samples. The required amount was calculated using the Molecular Weight by the methods previously described in chapter 3.

The excitation at 595 nm did not result in any emission for any of the samples tested. The Texas Red results for the parallel loaded sample corroborates with the conclusions drawn from the FTIR and DLS. It can be concluded by the lack of an excitation peak corresponding to thiols, that the parallel loaded AuNP conjugate bound to the colloidal surface via thiolate bonds through the cysteine residues found on the SH-PEG-SGA and the RME peptide. [248,272]

4.1.1 Cysteine binding theory – H5

The results so far in this chapter have thus indicated that the samples functionalized with RME peptide have not successfully synthesized a linker for comparison to the mixed monolayer counterpart. Due to the affinity of thiol to gold it is hypothesized that the conjugation of peptide in the form of a linker may not be possible when a thiol is present. Literature has identified that H5WYG can be used for successful endosomal escape both with and without a thiol group present. Therefore H5WYG was purchased from BIOMATIK with the following sequence (GLFHAIAHFIHGGWHGLIHGWYG) and functionalized both sequentially and in parallel and compared to the thiol containing H5 co-functionalized using an SH-PEG in a mixed monolayer arrangement. [156]

To investigate the cysteine binding theory, 1 L of citrate capped AuNPs were synthesized, characterized and PEGylated with bifunctional SH-PEG-SGA. DLS particle size analysis was repeated and the AuNP SH-PEG-SGA was split in to 10 batches of 200 ml. each pair of individual batches were then co-functionalized by either parallel loading or sequential loading (as detailed previously) with H5 both with and without the thiolated cysteine residue.

Dynamic light scattering was applied to measure the hydrodynamic diameter of nanoparticles, which is sensitive to the organic coating associated with the functionalized AuNP. DLS is predominantly used in this chapter to evaluate the conjugation of ligands to the AuNP surface and to assess the level of aggregation. DLS size measurements were gathered by measuring and averaging each pair of the same sample, 9 runs per sample, with 15 measurements per run. AuNP citrate capped reported an average hydrodynamic diameter of 16.19 d. nm, the SH-PEG-SGA reported an increased to approximately 34.6 d.nm. Upon co-functionalization, the bifunctional AuNP SH-PEG-SGA & H5 without the cysteine residue resulted in average AuNP diameters of 35.79 and 29.89 d.nm for the sequential and parallel loaded samples respectively (Table 4-2). The bifunctional AuNP SH-PEG-SGA & H5 with the cysteine residue resulted in a hydrodynamic diameter of 36.5 and 36.7 d.nm for the sequential and parallel loaded samples respectively. The thiol terminated H5WYG follows the previosu observations with the RME peptide,

indicating that another mixed monolayer may have formed. While unexpected, the Number averages for the thiol free H5WYG peptide also mimics this trend when added sequentially, the results show a slight increase in size (while not statistically different), with a large decrease in size when added in parallel. Due to the amine chemistry, it is possible that when added sequentially, that the initial thiol terminated PEGylation allows some degree of colloidal stability and anchors the PEG in place. Whereas when added in parallel the NHS ester forms the amide bond with the H5WYG, but when added to the gold, several of the amine groups found on the sidechains of the peptide residues along with the thiolate cysteine my potentially cause multiple bonds to the gold positioned at various amino residues (Figure 4-19). It is also possible that the strength of the Au amine affinity outweighs that of the NHS ester bond, resulting in dissociation, causing several overlapping of the peptide on the AuNP surface. However, these results are inconclusive; nevertheless, it is of note that the largest error was identified for those samples with parallel loading, Dunnett's Post Test was carried out with 95% confidence limits using GraphPad Prism against AuNP SH-PEG-SGA as the control and no significant difference was found for any of the samples investigated ($P < 0.05$).

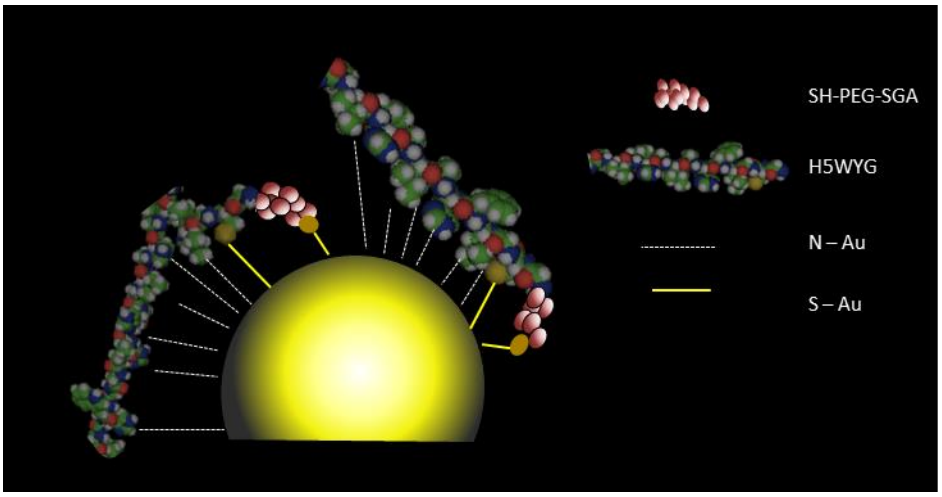

Figure 4-19 Scheme of the multiple bonding sites available to the AuNP surface and potential conjugation through utilization of all the available functional groups

Table 4-2 Table of nanoparticle size measurements for AuNP SH-PEG-SGA co-functionalized with H5 (with and without the cysteine unit)

Sample	Zeta (mV)	Size (d.nm)	PDI
AuNP citrate capped	-33.76 ± 1.1	16.19 ± 1.5	0.10
Sequential loading			
AuNP SH-PEG-SGA	-31.38 ± 1.1	34.60 ± 1.6	0.13
AuNP SH-PEG-SGA & H5 with C	-15.42 ± 3.6	36.50 ± 2.3	0.42
AuNP SH-PEG-SGA & H5 without C	-28.45 ± 5.7	35.79 ± 2.9	0.34
Parallel loading			
AuNP SH-PEG-SGA & H5 with C	-12.61 ± 0.3	36.72 ± 8.9	0.38
AuNP SH-PEG-SGA & H5 without C	-20.72 ± 0.6	29.89 ± 7.5	0.26

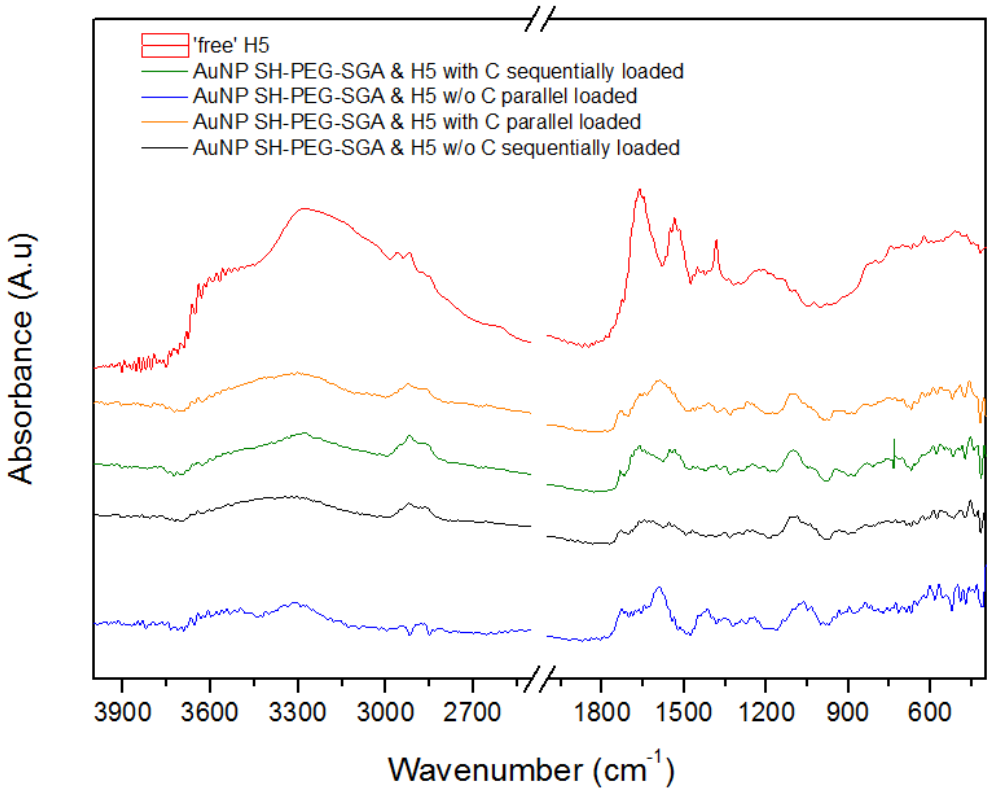

Figure 4-20 FTIR absorbance spectra for AuNP functionalized with bifunctional PEG and H5WYG both with and without the cysteine residue, and both in parallel and sequentially

The FTIR spectra for the co-functionalized samples are illustrated in Figure 4-20; all 4 functionalized samples display similar spectra. While the presence of H5WYG peptide can be observed by the addition of peaks corresponding to peaks evident from the H5WYG spectrum, the saturated NHS ester peak at 1735 cm^{-1} remains present for all spectra regardless of the type of loading and/or if there is a thiol present, this leads to the conclusion that a linker has not yet been successfully formed.

4.1.2 Solvent theory

Hydrophobic amino acids are usually buried within the core of the peptide structure, while charged residues are exposed to the solvent to a much higher degree, allowing the potential formation of hydrogen bonds. The H5WYG sequence consists of the following 32 residues: GLFHAIAHFIHGGWHGLIHGWYG. Glycine, Leucine, Phenylalanine, Alanine & Isoleucine are all uncharged hydrophobic residues, while Histidine (+1), Tyrosine & Tryptophan are polar. Based on the low propensity of the side chains to be in contact with a polar solvent like water, it was concluded that based on the Hydro-2 hydrophobicity parameter, the percentage of hydrophobic residues for this peptide is approximately 61% hydrophobic and as such should be dissolved in small amounts of organic solvents such as DMSO, DMF, Acetic acid or methanol. [249] As previously described; the simplest and most versatile technique for functionalizing AuNPs with proteins involves the utilization of chemical groups such as an NHS ester which can react with the nucleophilic primary amine groups which exist at the N-Terminus of each peptide.

To the best of the authors knowledge, this approach is novel as most literature involves the conversion of a carboxylic group to an ester using carbodiimides such as EDC coupling reactions. The approach in this Thesis uses a bifunctional PEG with a ready-made NHS ester for functionalization, thus improving efficiency. The reaction of NHS esters with amines is strongly pH dependent, at a lower pH the amino group is protonated, at a higher than optimal pH hydrolysis is quick. [250] NHS ester hydrolyze and Glutaramide Succinimidyl esters like the one used for this bifunctional PEG, have a half-life of only 15-20 minutes in water, this rate of hydrolysis increases with pH. As well as the potential hydrolysis of the ester, the

solubility also varies with the buffer, and is dependent on the structure. Non-sulphonated forms of the NHS ester are water insoluble and ThermoFisher recommends organic solvents such as DMF or DMSO in 0.5-10 % of the final volume, elsewhere it is recommended to PEGylate proteins or nanoparticles in a large excess of the PEG NHS esters due to the competitive hydrolysis reaction in an aqueous solution. [251] Based on these observations from the literature, it can be concluded that the synthesis of the linker using the methods employed in chapters 4 & 6 was not achievable due to the hydrolysis of the NHS ester combined with the lack of solubility; consequently, it is possible that the ester hydrolyzed meaning the remaining functional end of the bifunctional linker was no longer available for conjugation, resulting in the RME & H5WYG peptide binding directly to the gold.

To test this theory, 2 L of AuNP citrate capped were synthesized and characterized, then split into batches for co-functionalization to reduce any batch to batch variability. An array of solvents in a range of functionalization methods were tested, these included organic solvents such as amine-free, anhydrous dimethylformamide (DMF) and dimethyl sulfoxide (DMSO), methanol, acetonitrile and pH 8 buffer solution, using both sequential and parallel loading.

Citrate capped AuNPs were centrifuged and re-dispersed in pH 8 buffer solutions, the resultant solution was highly unstable and have visually fallen out of solution, the same was apparent for the methanol and acetonitrile solubilized samples, as a result DLS was not measured. Mono functional thiol PEG proved to be the most stable of the PEGylated samples in chapter 4, citrate capped AuNPs were functionalized with SH-PEG following the protocols in chapter 3 to achieve 50% coverage and were centrifuged and re-suspended in pH 8. To this mixture, an aliquot of 1 ml of SH-PEG-SGA & H5WYG (without cysteine) which had been stirred for 24 h under ambient conditions in DMSO was added and stirred for another 24 h. The nanoparticles showed an DLS number average of approximately 32 d.nm ± 7 (PDI 0.33) for both AuNP SH-PEG & the co-functionalized counterpart indicting no increase in size as a result of a linker formation (results not shown). Table 4-3 outlines the remaining samples and the solvents in which they were suspended. The H5WYG peptide used for this part of the research did not contain a cysteine residue.

Table 4-3 Table of nanoparticle size measurements for AuNP SH-PEG-SGA co-functionalized with H5 without the cysteine unit in various solvents

Sample	*Size (d.nm)*	*PDI*
AuNP citrate capped	***16.19 ± 1.5***	***0.10***
Sequential loading		
AuNP SH-PEG-SGA in DMSO	***34.41 ± 2.1***	***0.19***
AuNP SH-PEG-SGA & H5 in DMSO	***47.11 ± 5.1***	***0.21***
Parallel loading		
AuNP SH-PEG-SGA in pH8 & H5 in DMF	***28.94 ± 5.4***	***0.32***
AuNP SH-PEG-SGA & H5 in DSMO	***36.84 ± 12.3***	***0.19***

From the results outlined in Table 4-3 it is evident that adding the SH-PEG-SGA in DMSO did not adversely affect the PEG in relation to AuNP size when compared to the AuNP SH-PEG-SGA in water from the previous samples ($P > 0.05$). Dissolving the SH-PEG-SGA in a pH buffer solution of pH 8 and adding H5WYG dissolved in DMF resulted in a decrease in AuNP size showing colloidal instability however was not statistically significant ($P > 0.05$). Both parallel and sequentially loaded samples showed an increase in nanoparticle hydrodynamic diameter when functionalized in DMSO. Although the parallel loaded sample suggested large instabilities via the large variance experienced when measuring DLS size. Sequential loading however resulted in the largest increase in particle size with narrow error bars and was the only statistically significant increase when compared to all the solvents tested via a One way Anova with Tukey's post-test ($P = 0.001$).

UV/Vis analysis was applied for the above samples to monitor the red shift of the SPR peak in relation to conjugation. From the UV/Vis spectra illustrated in Figure 4-21 and outlined in Table 6-4 it is evident that a great loss in absorption occurred for the citrate capped re-suspended in pH 8 and the AuNP SH-PEG & parallel loaded SH-PEG-SGA & H5WYG complex confirming a degree of aggregation for those samples and a loss of AuNP colloidal stability. When dissolved in DMF, the H5WYG sample did not have peak shift, this combined with the decrease in AuNP

size indicated that the DMF had resulted in an adverse effect for the SH-PEG-SGA and/or the H5WYG peptide.

The remaining samples, both parallel and sequentially loaded DMSO samples, showed a significant peak shift to approx. 524 nm as a result of co-functionalization complementing the results obtained from the DLS previously.

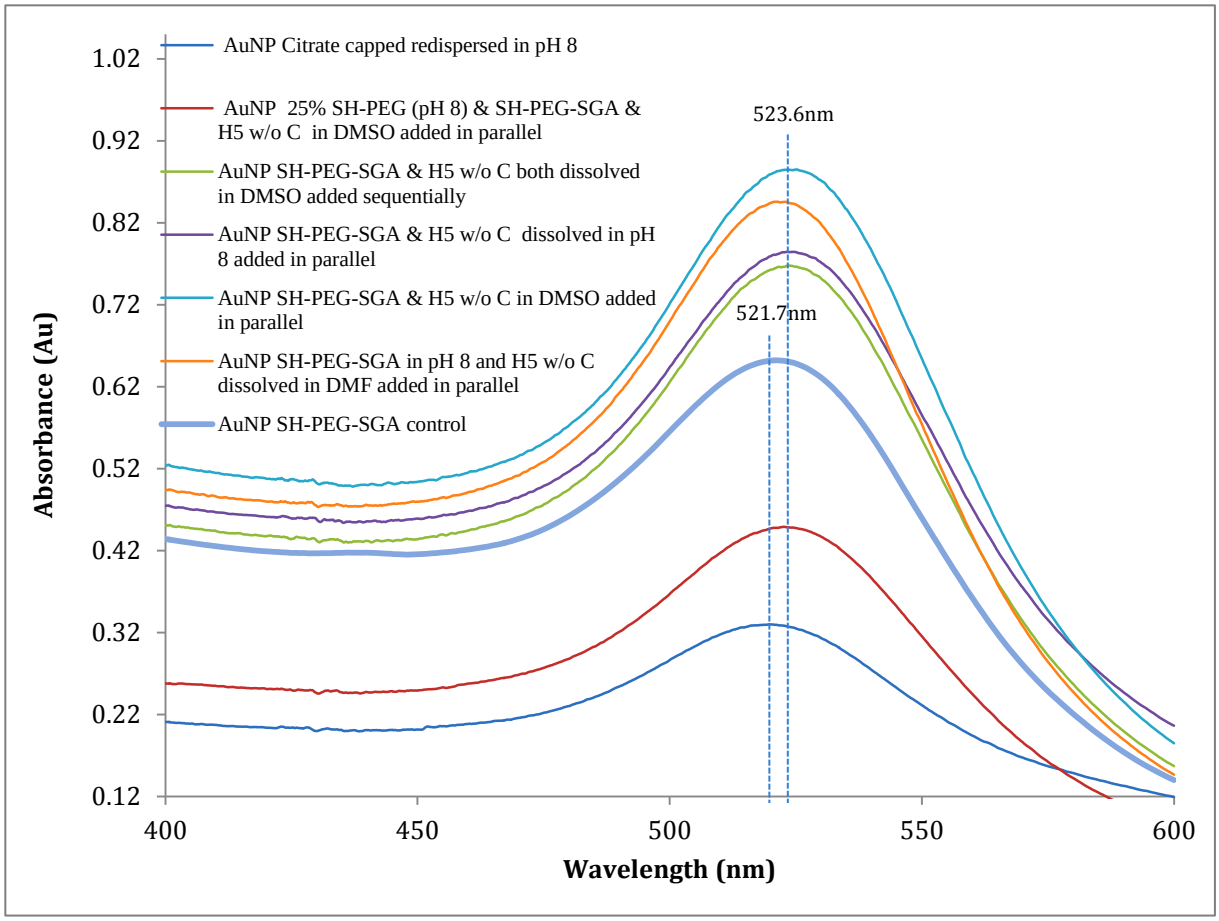

Figure 4-21 UV/Vis spectra for the H5 co-functionalized AuNPs in a range of solvents both added sequentially and in parallel

Table 4-4 UV/Vis SPR peak shifts for the AuNPs co-functionalized in a range of solvents both via sequential and parallel loading

Sample	Wavelength (nm)	Absorbance (Au)	Peak Shift from control
AuNP SH-PEG-SGA control	521.3	0.65	N/A
AuNP Citrate capped re-dispersed in pH 8 buffer	519.8	0.33	-1.5
AuNP 25% SH-PEG (pH 8) & SH-PEG-SGA & H5 in DMSO (Parallel loaded)	522.7	0.449	+1.4
AuNP SH-PEG-SGA & H5 w/o C both dissolved in DMSO added Sequentially	523.6	0.77	+2.3
AuNP SH-PEG-SGA & H5 dissolved in pH 8 added in Parallel	524.6	0.78	+3.3
AuNP SH-PEG-SGA & H5 in DMSO added in Parallel	525.2	0.89	+3.9
AuNP SH-PEG-SGA in pH 8 and H5 dissolved in DMF added in Parallel	521.4	0.85	+0.1

FTIR analysis demonstrated a clear peak at 1735 cm^{-1} for both the samples added in pH 8 buffer solutions and DMF (Results not shown). This peak corresponds to an unsaturated ester and therefore indicates that the NHS ester reaction has been unsuccessful. For the parallel loaded H5WYG peptide in water, the presence of the peak at 1735 cm^{-1} is still observed, indicating the lack of a reaction with the NHS ester; however the complete loss of the saturated ester for the sequentially loaded sample in DMSO indicates that a linker can be successfully synthesized when suspended in DMSO (Figure 4-22). This is an important finding fundamental to the context of this Thesis. The FTIR analysis combined with the DLS & UV/Vis strongly indicate the successful synthesis if the linker arrangement when added via sequential loading using DMSO. However extra peaks are present on the spectra at 3000, 2900, 1200-1240, 1000-1080, 960 & 690 cm^{-1}, these arise from the DMSO spectra as illustrated in Figure 4-23 taken from the NIST Chemistry WebBook, NIST Standard Reference Database Number 69, as it is very difficult to remove all traces of DMSO. [273]

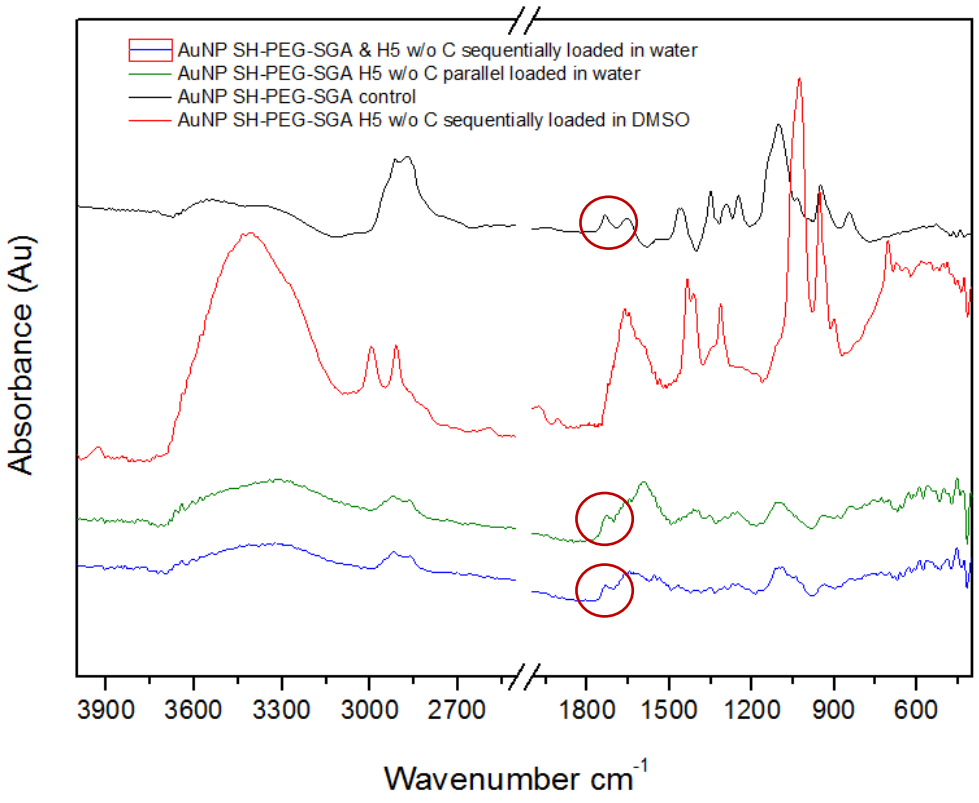

Figure 4-22 FTIR absorbance spectra comparing the parallel (green) and sequentially loaded (blue) AuNPs in water to the sequentially loaded sample in DMSO (red)

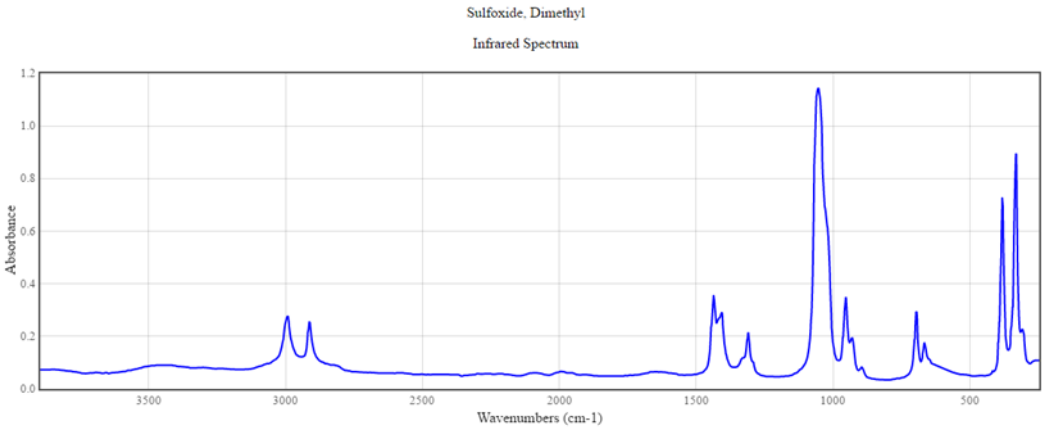

Figure 4-23 FTIR absorbance spectra for pure DMSO taken from the NIST Chemistry WebBook, NIST Standard Reference Database Number 69 [273]

Therefore, it could be argued that the lack of the ester peak is a result of signal quenching and not the loss of the ester as a by-product. Therefore, the results remain inconclusive.

Therefore, to confidently conclude the successful synthesis of a linker; citrate capped AuNPs were functionalized with bifunctional PEG dissolved in 1 ml DMSO and stirred overnight under ambient conditions. The PEGylated sample was then co-functionalized with H5WYG peptide containing a thiolated cysteine residue (GCLFHAIAHFIHGGWHGLIHGWYG). The sample was then centrifuged three times and measured by FTIR. The FTIR spectra obtained was very like that of the H5 peptide without the thiol, although peaks were present at approximately 2550-2600 cm^{-1} which corresponds to an unreacted thiol group, indicating further the binding via the primary amine and not the cysteine. The remaining pellet was then mixed with the required amount of Texas Red thiol sensitive dye and left to stir over night. The sample was then centrifuged 3 times and 1 ml of the sample was retained after each centrifugation for analysis in triplicate via a fluorescent plate reader. As evident in Table 4-5 the fluorescent found that after the first centrifugation, a plateau was reached indicating that no more peptide was washed away from the AuNP. The Texas Red result concluded definitively that even in the presence of a cysteine residue that a linker could be achieved when synthesized sequentially in DMSO. Figure 4-24 shows the fluorescent spectra for the Texas Red with the mixed monolayer acting as a negative control. it can be observed that an emission spectra

occurred for the bifunctional linker samples synthesized in DMSO but not for the sampled conjugated in water, indicating that the thiol has remained free in solution, that combined with all the previous results which confirm the presence of the peptide on the AuNP surface conclude the successful synthesis if a bifunctional linker.

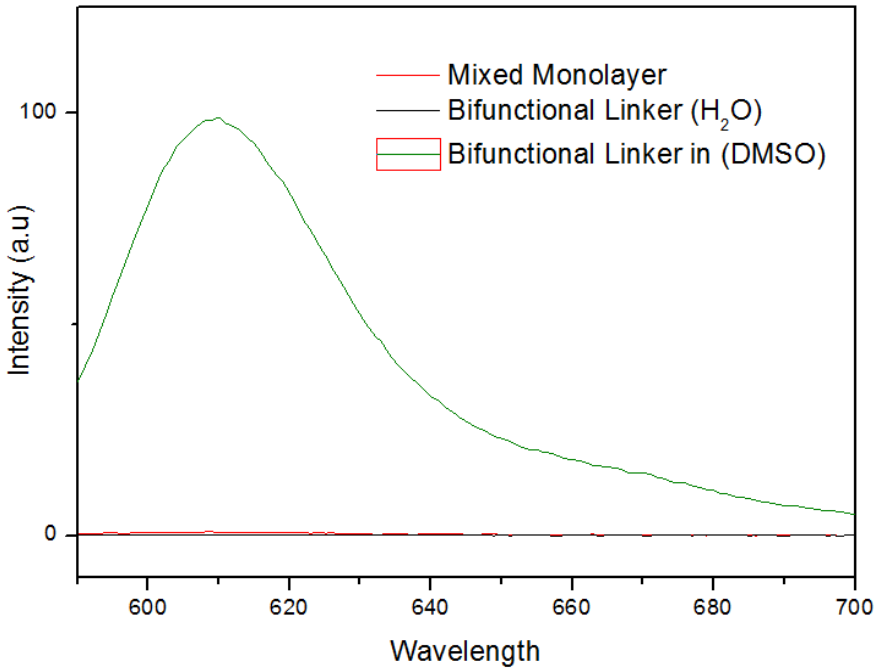

Figure 4-24 Texas Red thiol sensitive fluorescent spectra illustrating the emission for the mixed monolayer (red), bifunctional linker in water (black) and the bifunctional linker synthesized in DMSO (green)

Table 4-5 displaying the OD measured following centrifugation via a plate reader

# of times centrifuged	**OD**		**Average**
	Rep 1	Rep 2	
1	23520	23520	23520
2	23806	23806	23806
3	24383	24383	24383

4.1.3 Solubility Study

Dimethyl Sulfoxide (DMSO) is a polar aprotic, organosulfur compound which dissolves both polar and non-polar entities and is miscible in water. The methyl groups on DMSO ($(CH_3)^2SO$) are mildly acidic with a pK = 35. [274,275] As such it can be successfully employed to solubilize a wide variety of molecules, and has been commonly used in the literature to solubilize hydrophobic compounds in cell biology experiments and poorly soluble drugs in permeation assays such as that using Caco2 enterocyte-like cells. This coupled with its apparent low toxicity at concentrations < 10% has led to its ubiquitous use and application in biology. [276,277] Nevertheless the cytotoxic effect of DMSO has recently become controversial in the literature. Several studies have been identified to evaluate the toxic effect of DMSO in cell viability assays, however the results are diverse. Caco2/TC7 cells were cultured for 21 d on 96-well plates and incubated with DMSO solutions (0-100%) in Hank's balanced salt solution containing HEPES (biological buffer (25 mM)), pH 7.4. DMSO 10% did not induce any significant increase in lactate dehydrogenase (LDH) release whereas a significant increase in LDH activity (ANOVA, $p < 0.05$) occurred at a DMSO concentration of 20 to 50%. NR incorporation in viable cells was statistically reduced by 27 to 36% at DMSO concentration of 20% up to 100% (ANOVA, $p > 0.05$). No statistical difference ($p < 0.05$) was observed between the control and 10% DMSO groups. [276] Comparable results were obtained following exposure of HeLa cell lines to DMSO for periods of 30, 60, 90 & 120 minutes. At concentrations below 15% there seemed to be no significant difference following exposure as measured by confluency of cultures at the end of 96 h. [278] In direct contradiction with these results, studies have since shown that exposure of astrocyte cultures to 1% DMSO for 24 h did not significantly affect cell survival, but decreased cell viability and at concentrations of 5% significantly inhibited cell variability and promoted apoptosis of astrocytes, accompanied with more severe mitochondrial damage. [279] Elsewhere toxicity was confirmed *in vitro* in a retinal neuronal cell line, at DMSO concentrations >1% (v/v), using annexin V, terminal deoxynucleotidyl transferase dUTP nick end labelling (TUNEL), 3-(4,5-dimethylthiazol-2-yl)-2,5-diphenyltetrazolium bromide (MTT), and AlamarBlue cell viability assays. Low concentrations (2-4% DMSO) induce caspase-3 independent neuronal death that involves apoptosis-inducing factor (AIF) translocation from

mitochondria to the nucleus and poly-(ADP-ribose)-polymerase (PARP) activation. [280]

As there is such diversity present, and the subsequent effect of DMSO on prostate cancer cell lines is still ambiguous, a solubility study was performed to identify the lowest concentration of DMSO possible to still elicit the successful solubilization and subsequent synthesis of a bifunctional linker. The synthesis of a linker with a cysteine residue in DMSO as seen from the Texas Red results in Figure 4-24 became highly unstable after just 72 h, with the gold visibly 'falling out' of solution. Therefore, all the following linker samples were conjugated via sequential loading using the SH-PEG-SGA & H5WYG without the cysteine residue in DMSO.

The purpose of this study is to identify if neat DMSO is required to synthesize a stable AuNP linker conjugate. A stock batch of 1.5 L citrate capped AuNPs was synthesized, and split into 5 x 100 ml batches. Each batch was functionalized with SH-PEG-SGA in increasing amounts of DMSO and left to stir under ambient conditions then characterized using DLS & UV/Vis. From the results obtained in Table 4-6 & Table 7-7 an obvious trend was observed with increasing zeta potential correlating to an increase in % DMSO. The PDI remained consistent for all samples indicting that there was no increase in polydispersity because of the varying % of DMSO, however the largest (and most consistent size in relation to all the AuNP SH-PEG-SGA batches synthesized throughout this Thesis) belongs to the neat DMSO. The UV/Vis spectra (Figure 4-25) displays the characteristic peak at approximately 520 nm with all peak positions appearing at approximately 524 nm. Based on these results 100% DMSO was chosen to continue with co-functionalization, the remaining 1 L of the stock AuNP citrate capped was then functionalized with SH-PEG-SGA dissolved in 100% DMSO and added, 1 ml in 1 L yields 0.1% DMSO while still offering the NHS ester for co-functionalization while preventing ester hydrolysis.

Table 4-6 Table displaying the DLS size and zeta potential measurements for the AuNP SH-PEG-SGA samples synthesized using increasing concentrations of DMSO

Sample (% of DMSO)	Size (d.nm)	PDI	Zeta (mV)
AuNP SH-PEG-SGA (20%)	25.36 ± 2.3	0.26	-32.59 ± 3.1
AuNP SH-PEG-SGA (40%)	26.58 ± 3.0	0.29	-32.62 ± 2.1
AuNP SH-PEG-SGA (60%)	26.33 ± 5.6	0.23	-37.74 ± 1.6
AuNP SH-PEG-SGA (80%)	31.86 ± 3.1	0.22	-20.32 ± 3.1
AuNP SH-PEG-SGA (100%)	33.72 ± 2.4	0.23	-19.82 ± 4.0

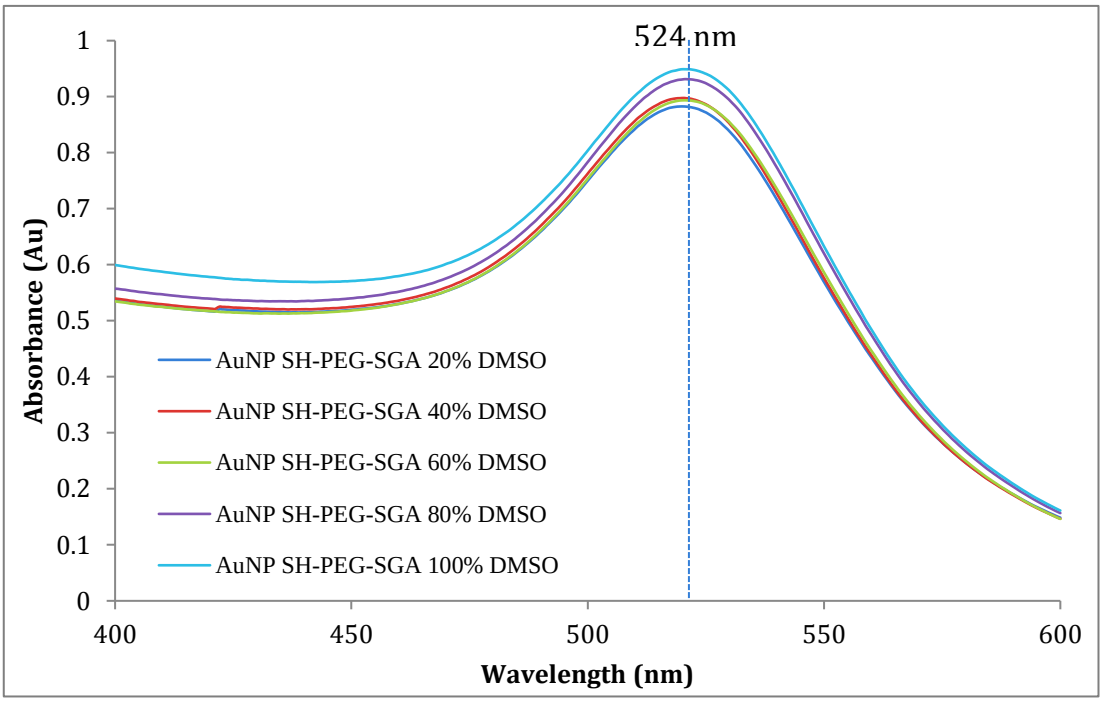

Figure 4-25 UV/Vis absorbance spectra for AuNP SH-PEG-SGA in increasing concentrations of DMSO varying from 20 % (dark blue), 40 % (red), 60 % (green), 80 % (purple) and 100 % (light blue) n = 3

After stirring under ambient conditions overnight, the now 1 L AuNP SH-PEG-SGA stock batch was split in to 5 x 200 ml batches and co-functionalized with H5WYG peptide dissolved in increasing amounts of DMSO (20-100%). After stirring for 24 hours the samples were then characterized via DLS and UV/Vis. Table 7-7 identifies a similar trend as Table 4-6 with increasing zeta potential being a direct result of increasing % of DMSO. This is expected due to the lightly acidic nature of the DMSO with protonating possibly occurring at the methyl groups. While a One way Anova identified no statistical significance between the hydrodynamic diameter, the PDI showed an inversely proportional relationship with the % DMSO, decreasing as the concentration of DMSO increased. Visual observation observed varying degrees of aggregation for the H5 the lower the amount of DMSO, the more aggregation observed. This trend can also be observed via the UV/Vis in Figure 4-26. Although slight, the absorbance value decreased with the lower amounts of DMSO, while the highest absorbance value was observed for the H5WYG peptide added with 100% DMSO.

Table 4-7 Table displaying the DLS size and zeta potential measurements for the AuNP SH-PEG-SGA & H5 peptide functionalized samples synthesized using increasing concentrations of DMSO

Sample (% of DMSO)	Size (d.nm)	PDI	Zeta (mV)
AuNP SH-PEG-SGA & H5 (20%)	38.89 ± 1.3	0.58	-38.08 ± 4.3
AuNP SH-PEG-SGA & H5 (40%)	37.45 ± 5.4	0.47	-38.08 ± 3.1
AuNP SH-PEG-SGA & H5 (60%)	36.97 ± 3.3	0.48	-29.24 ± 1.4
AuNP SH-PEG-SGA & H5 (80%)	40.56 ± 2.6	0.39	-22.38 ± 2.8
AuNP SH-PEG-SGA & H5 (100%)	41.80 ± 1.2	0.24	-0.14 ± 0.3

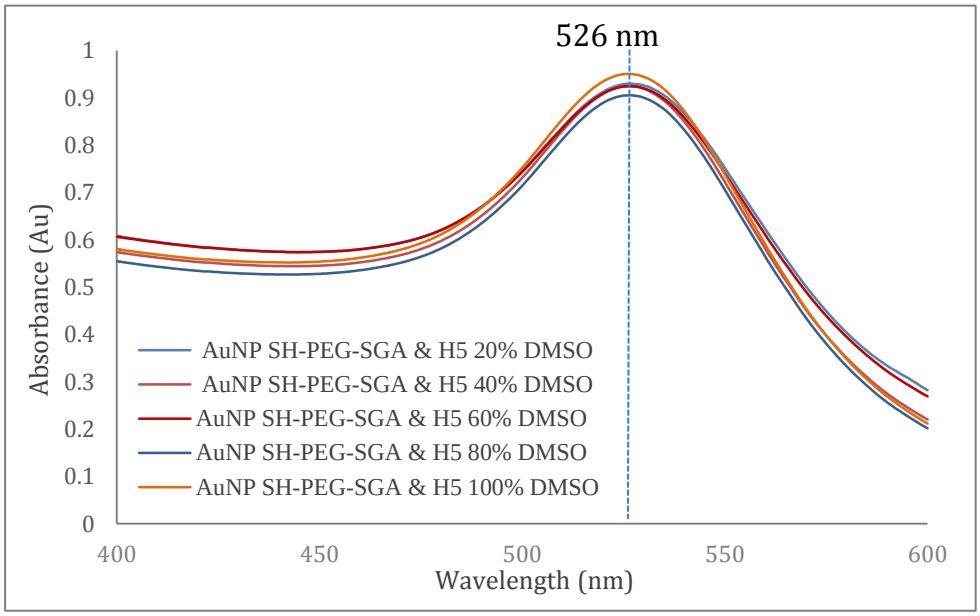

Figure 4-26 UV/Vis absorbance spectra for AuNP SH-PEG-SGA (100% DMSO) & H5WYG peptide at increasing concentrations of DMSO ranging from 20 % (light blue), 40 % (pink), 60 % (red), 80 % (dark blue) and 100 % (orange), n = 3

To determine the binding efficiency of the H5WYG in varying % of DMSO, a Micro bicinchoninic acid (Micro-BCA) assay was performed to determine the exact quantity of peptide present on the surface of the AuNP. The total amount of peptide loaded onto the surface of the NPs was calculated in percentages, and the final concentration of peptide was obtained in µg/ml (Table 4-8). Each AuNP batch was centrifuged and the supernatant decanted, then mixed back to the original volume. Both the centrifuged sample and the corresponding supernatant were quantified using the Micro BCA. It was concluded that 100% DMSO would be used to synthesize the linker. For the remaining studies 2 L of citrate capped AuNPs were synthesized, 400 ml was retained for analysis and the remaining AuNP was split into 2 x 800 ml batches to synthesize the mixed monolayer and the bifunctional linker samples for subsequent analysis thus reducing lot to lot variability. 2 ml of DMSO would eventually be added in total to 400 ml of AuNPs suspended in water yielding a total DMSO % of 0.5% which is below the recommended % identified from the literature. Once synthesized the samples were centrifuged and washed 3 times and re-dispersed in sterile PBS under cell culture conditions.

Table 4-8 Table displaying the concentrations obtained through utilization of a Micro BCA assay on both the sample and its corresponding supernatant

Sample	**Centrifuged x1**		**Supernatant**	
% DMSO	concentration (µg/ml)	%	concentration (µg/ml)	%
20%	19.93	64.79%	10.83	35.21
40%	19.57	61.83%	12.08	38.17
60%	20.37	64.63%	11.15	35.37
80%	19.08	63.33%	11.05	36.67
100%	18.79	60.46%	12.29	39.54%

4.2 Conclusions

The successful synthesis of AuNPs functionalized with both PEG and/or the H5WYG or RME peptide using either a mixed monolayer surface arrangement or the incorporation of a hetero bifunctional PEG linker was confirmed via FTIR, DLS and through the use of the Texas Red thiol marker. Results from sequentially loading RME peptide dissolved in water to AuNPs functionalized with SH-PEG-SGA demonstrated no significant differences in size or UV/Vis peak position in comparison to the mixed monolayer counterpart. This was expected, as the RME peptide sequence encompasses a thiol containing cysteine residue with a binding affinity of 40-50 kcal/mol^{-1} to gold. The subsequent hypothesis was that loading the SH-PEG-SGA in parallel with the RME peptide would allow the successful synthesis of the linker and the RME peptide, which could then be loaded unto the AuNP surface. However results observed no significant difference in the DLS Number average measurements, and it was concluded that a linker was not formed due to the potential hydrolysis of the ester, and the potential that even if the linker was successfully synthesized, the thiol found on the cysteine residue could still be potentially binding to the gold (Figure 4-19). To determine if it was the competing hydrolysis reaction or the thiol bond preventing the successful synthesis of an AuNP conjugate using a linker, H5WYG peptide (both with and without a cysteine residue)

was dissolved in either water or DMSO and co-functionalized to the AuNP surface. FTIR and Texas Red concluded that it is necessary to use a solvent such as DMSO, to prevent hydrolysis of the NHS ester of the bifunctional PEG – to successfully synthesis a gold nanoparticle using a bifunctional linker, even in the presence of a thiol group (Figure 4-24). A linker was successfully synthesized when in the presence of a cysteine residue (H5WYG peptide) and confirmed via Texas Red, however became quickly unstable and visibly 'fell' out of solution. Therefore, while changing the solvent overcomes the competition of hydrolysis, it is still unadvised to synthesize a linker using a pre-ready NHS ester in the presence of a thiol due to the instabilities presented from the results in this These. As such it is recommended that investigations comparing a mixed monolayer directly to a peptide conjugated using a PEG linker should be synthesized in DMSO using a thiol free peptide. Therefore the next chapter will encompass the H5 peptide sequences GCLFHAIAHFIHGGWHGLIHGWYG & GLFHAIAHFIHGGWHGLIHGWYG to synthesize the mixed monolayer and linker respectively, allowing the cysteine residue to be available for binding to the AuNP surface when synthesizing a mixed monolayer, and the absence of the thiol when synthesizing a linker sequentially using DMSO. Further investigations are required to compare the arrangements and address the inconsistencies identified in the literature surrounding the 'anti-PEG' effect predicted, and to determine is using one method of attachment can offer a more desirable response for stability, the ability to resist non-specific protein adsorption, internalization and enhanced radiosensitivity than the respective arrangement.

5. MIXED MONOLAYER ARRANGEMENT VS. THE USE OF A HETERO BIFUNCTIONAL LINKER

It has been hypothesized in this Thesis that the use of a linker would allow for direct cell contact between the internalization peptide and the prostate cancer cell, and that the use a mono-functional PEG would hinder the peptide interaction to a degree. Inconsistencies in the literature include the effect on colloidal stability, the resulting opsonization and the effect each arrangement has on cellular internalization. Currently there is little consensus regarding which approach should be applied in a situation. However the literature has displayed great promise for mixed monolayer arrangements, such as that reported by Paciotti *et al.* [59–63]

One of the largest inconsistencies from the literature is the role of peptide length in relation to biological availability. It is plausible that having peptides which exceed the length of the PEG could have an 'anti-PEG' effect, and allow for the recognition as foreign, making the AuNP susceptible to non-specific protein attachment and potential removal by the immune system. [131,153,222]

Chapter 4 investigated the conditions required to synthesize a linker to co-functionalize AuNPs. A benefit of using a bifunctional linker would be to allow the AuNP surface to be completely saturated with PEG and the remaining active end groups could then to be used to anchor a biologically active group. This would have a two-fold benefit as firstly, it would allow direct contact with the receptors on the tumor cell, and secondly it would allow more of the required therapeutic, targeting or other payloads to be attached in comparison to a mixed monolayer arrangement.

The results indicated that the synthesis of a stable bifunctional linker cannot be achieved in the presence of a thiol group or when using an NHS ester suspended in water, as such the research effort has identified DMSO as the most suitable solvent out of those tested. Therefore, this chapter serves to address whether having a bifunctional linker would result in a loss of colloidal stability due to an 'anti-PEG' effect, or if the bifunctional linker would enable the conjugated peptide to overcome

any potential steric hindrance caused by the stabilizing agent in a mixed monolayer arrangement. [217,222]

5.1 Results and Discussion

AuNPs were synthesized using the Turkevich method outlined in the Materials and Methods section of this Thesis. To prepare the mixed monolayer PEG capped AuNPs, 10.68 μg/ml of free SH-PEG was dissolved in 1 ml of distilled water and added to the citrate capped AuNPs. As described in chapter 3, this level of PEG addition yields approximately 50% of potential surface saturation with this ligand. 5.56 μg/ml of H5 peptide was measured and dissolved in water and aspirated vigorously until dissolved, then added to the stirring AuNP SH-PEG under ambient conditions and left over night. [184] 20 μg/ml of free SH-PEG-SGA was dissolved in 1 ml of DMSO and aspirated, then added to the 'as synthesized' AuNPs to fully cap the nanoparticles with PEG linker. [184] 5.56 μg/ml of H5 was measured and dissolved in 1 ml of DMSO and aspirated until dissolved, then added to stirring AuNP SH-PEG-SGA under ambient conditions and left over night. The co-functionalized samples were collected and decanted into 50 ml centrifuge tubes, and centrifuged at 10,000 RPM for 90 minutes. The supernatant was decanted off and the pellet was re-suspended in sterile water (for the mixed monolayer) or sterile PBS (for the linker). This process was repeated in triplicate to further nullify any potential toxicity experienced by the DMSO.

The nanoparticles were characterized at various points during synthesis, including post synthesis, post PEGylation, post centrifugation and after co-functionalization with H5WYG peptide. The characterization techniques employed for this chapter include DLS, UV/Vis, FTIR, ICP-MS, cell culture and Clonogenic survival assays.

Unless otherwise specified, samples synthesized from this point on include AuNP citrate capped, AuNP SH-PEG, AuNP SH-PEG and H5WYG peptide (AuNP SH-PEG & H5 (mixed monolayer)), AuNP SH-PEG-SGA dissolved in DMSO (AuNP SH-PEG-SGA) and AuNP SH-PEG-SGA & H5WYG peptide (AuNP SH-PEG-SGA & H5 (bifunctional linker)) dissolved in DMSO. For the mixed monolayer arrangement, a cysteine terminated H5WYG peptide

(GCLFHAIAHFIHGGWHGLIHGWYG) was used, while for the bifunctional linker arrangement, the thiol free H5WYG peptide (GLFHAIAHFIHGGWHGLIHGWYG) was employed.

5.2 Dynamic Light Scattering

DLS is predominantly used to confirm the conjugation of ligands to the AuNP surface and is also employed to assess the level of aggregation of the nanoparticles, particularly after co-functionalization. AuNP citrate capped reported an average hydrodynamic diameter of 16.18 d. nm, the mono-functional SH-PEG saw an increase to approximately 35.35 d. nm and the bifunctional SH-PEG-SGA reported an increased to approximately 34.31 d.nm which when compared to the AuNP SH-PEG-SGA re-suspended in DMSO, identified no significant ($P > 0.05$) and a diameter of 34.78 (Figure 5-1). Upon co-functionalization, SH-PEG & H5 increased slightly to 34.5 d.nm which is not unexpected as the H5WYG peptide is shorter than the length of the SH-PEG. Co-functionalizing the bifunctional AuNP SH-PEG-SGA with H5 resulted in an average AuNP diameter of 39.26, when re-suspended in PBS this increased slightly to and 41.25 d.nm, which was again statistically insignificant. The change however between the AuNP SH-PEG-SGA both in DMSO and PBS is statistically significant when compared to the AuNP SH-PEG-SGA & H5 counterparts. This contrasts to the results obtained for the ‘linker’ in chapter 4, as a large enough increase in diameter to cause a statistical difference did not occur. The PDI for each of the samples outlined in Table 6-1suggests that the samples remained relatedly mono disperse, and there were no large variances observed via the error bars.

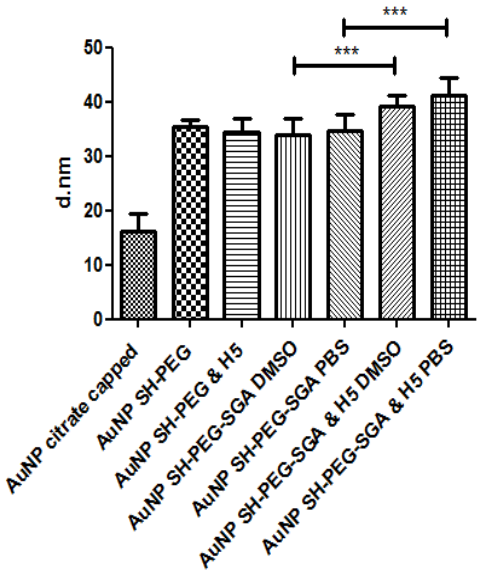

Figure 5-1 DLS Number average results graphically comparing the nanoparticle hydrodynamic diameters for AuNP co-functionalized samples in DMSO & PBS showing no significant difference between the same samples re-dispersed in either PBS or DMSO, but significant difference between the PEGylated and co-functionalized counterparts (P>0.05)

Table 5-1 DLS Number average results for the samples synthesized for the mixed monolayer and linker biological studies showing the AuNP SH-PEG-SGA and AuNP SH-PEG-SGA & H5 samples in both DMSO and PBS

Conjugate	DLS Number average	PDI
AuNP citrate capped	16.18 ± 3.3	0.22
AuNP SH-PEG	35.35 ± 1.2	0.17
AuNP SH-PEG & H5	34.5 ± 2.5	0.19
AuNP SH-PEG-SGA DMSO	34.01 ± 2.8	0.19
AuNP SH-PEG-SGA PBS	34.78 ± 2.9	0.29
AuNP SH-PEG-SGA & H5 DMSO	39.26 ± 1.9	0.41
AuNP SH-PEG-SGA & H5 PBS	41.25 ± 3.1	0.42

5.2.1 Colloidal stability Studies

As synthesized AuNPs aggregate instantly under physiological conditions, PEGylation overcomes this by shielding the AuNP surface by the conjugated polymer. Literature identifies inconstancies when discussing the colloidal stability of linkers. It is generically believed that using a bifunctional linker may result in an 'anti-PEG' effect. While there is already some literature available with has successfully utilized linker formation both *in vitro* and *in vivo*, as outlined in chapter 2 this study was conducted to directly compare the two surface arrangements to see if one enhances colloidal stability in comparison to the other. As previously mentioned, aggregated AuNPs are accompanied by a red shift in the electromagnetic spectrum, combined with broadening of peaks and a decrease in peak intensities. Aggregated nanoparticles are also visibly detectable by an obvious change in solution color from ruby red to blue/purple. Therefore UV/Vis provides a simple and effective method to assess the colloidal stability of each of the samples *in vitro* under both increasing NaCl concentration and in PBS over an extended periods. [281]

AuNPs which are not coated with PEG or an alternative stabilizing agent aggregate *in vivo* at physiological salt concentrations. Aggregated AuNPs will change color from ruby red to blue, or to clear with particulates visible in solution. This change can be monitored via a loss of absorbance and a red shift from UV/Vis analysis. [217,222]

To investigate the effect of functionalization on AuNP colloidal stability the samples were centrifuged and re-suspended in PBS. The suspension medium for the linker samples have since been changed to PBS to overcome any toxicity prevalent from the DMSO, therefore a CCC study was conducted on all samples with increasing molarity to 1 M NaCl. The samples were then left at 1 M NaCl for 7 days and re-analyzed using UV/Vis. The results of both studies are illustrated in Figure 5-2 & Figure 5-3 respectively.

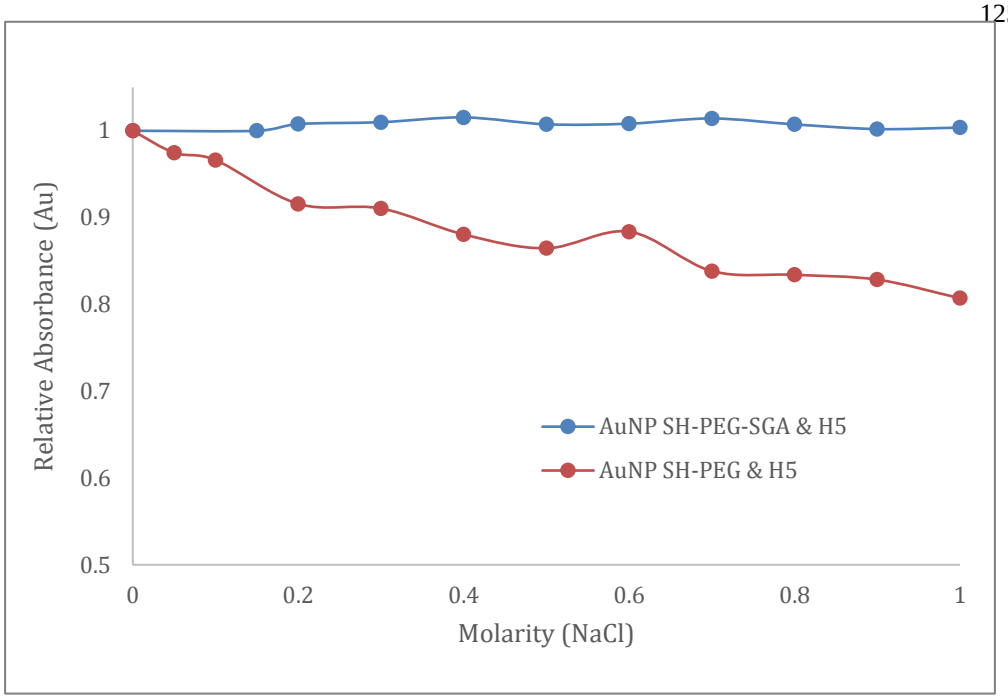

Figure 5-2 CCC study comparing the relative absorbance for the mixed monolayer (red) and the linker (blue) at increasing NaCl molarities up to and including 1 M NaCl, n=3

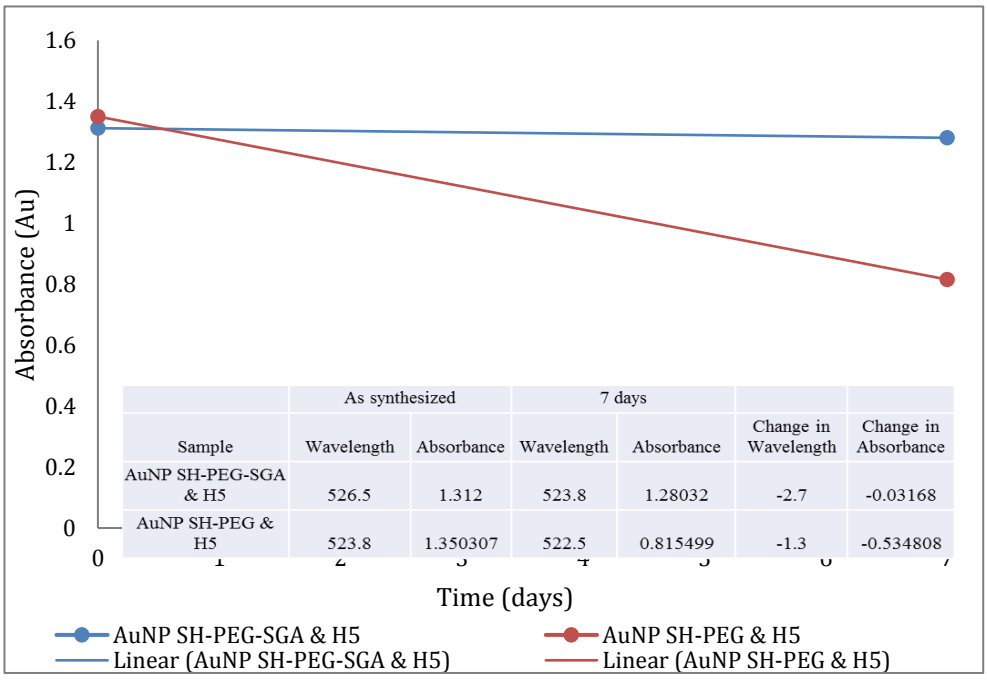

	As synthesized		7 days			
Sample	Wavelength	Absorbance	Wavelength	Absorbance	Change in Wavelength	Change in Absorbance
AuNP SH-PEG-SGA & H5	526.5	1.312	523.8	1.28032	-2.7	-0.03168
AuNP SH-PEG & H5	523.8	1.350307	522.5	0.815499	-1.3	-0.534808

Figure 5-3 UV/Vis CCC time study monitoring the relative absorbance SPR pattern for both the mixed monolayer (red) and the linker (blue) samples at 1 M NaCl over a period of 7 days, n=3

Figure 5-2 & Figure 5-3 depicts the results of the critical coagulation concentration study (CCC) which represents the UV-Vis peak height for each of the samples under increasing concentrations of NaCl. The results observed in both Figure 5-2 & Figure 5-3 contradict the literature, it has been previously reported that the use of a linker arrangement would have an 'anti-PEG'- effect, and as such, will decrease AuNP stability. [131] It is apparent from the UV/Vis that there was no loss of colloidal stability for the bifunctional linker samples up to 1 M NaCl for a period of 1 week, with the relative absorbance remaining at 1 for the CCC study and the absorbance dropping by only 0.03 (Au) after 7 days, however a peak shift of -2.7 nm was observed with the peak position shifting from 526.5nm to 523.8 nm. A drop in peak position could be argued to indicate a decrease in nanoparticle size, potentially due to the peptide 'falling off' over time. The results from the SPR pattern however, when combined with the previous characterization data, do not indicate a loss of functionalization and/or colloidal stability as a result of co-functionalization with DMSO. A decrease in peak position is also evident for the mixed monolayer arrangement, with a peak shift from 523.8 nm – 522.5. The SPR pattern from the CCC study indicated increasing aggregation because of increasing molarity, with the relative absorbance dropping from 1 to 0.81 Au at 1 M NaCl. The SPR pattern then continued to decrease over the 7-day period, plateauing at 0.815 Au showing a significant absorbance decrease of 0.53 Au in comparison to day 1.

Therefore, it is concluded that at the conditions studied, the use of a hetero-bifunctional linker did not adversely affect colloidal stability; however, the mixed monolayer approach displayed significant aggregation when exposed to high NaCl concentrations over extended periods. While this is true for the H5WYG studied in this chapter, based on the previous chapters utilizing a mixed monolayer with RME, H5WYG and RGD peptides, it is likely that this occurrence is a result of the peptide investigated and not the arrangement. It is possible that the reduced colloidal stability observed with the H5WYG peptide may be because of the lower net charge of +0.4 compared to 2.9 for the RME peptide. In addition, the H5WYG peptide contains a higher proportion of hydrophobic residues (namely A, F, I, L W &Y) than RME rendering the peptide less water soluble.

5.2.2 Non-Specific Protein Adsorption

As well as colloidal stability being an essential attribute of AuNPs, the ability to resist protein adsorption is crucial in determining the biological fate of the AuNP. Non-specific protein attachment can occur *in vivo* with a corona of protein adhering to the nanoparticle surface. The biological fate of the AuNP is largely determined by these nonspecific proteins. Regarding the literature, there is a consensus that using a hetero-bifunctional linker will have an 'anti-PEG' effect. It has also been reported that the PEG length has to exceed that of the peptide to shield the nanoparticle from opsonization for maximum circulation. [217,222]

The DLS results outlined in Table 5-2 indicate that both methodologies (mixed monolayer and PEG linker) are effective at inhibiting non-specific protein attachment when incubated in DMEM FCS 10%. A highly significant increase in in size is evident for the citrate capped AuNP after incubation with FCS from approximately 19.97 d.nm - 60.44 d.nm (P value of < 0.0001) indicating the presence of protein on the AuNP surface, while the remaining PEG capped and PEG & H5 co-functionalized samples indicate no such increase in size. This data (Figure 5-4) therefore concludes that synthesizing a linker does not initiate an 'anti-PEG' effect. [131,153,222]

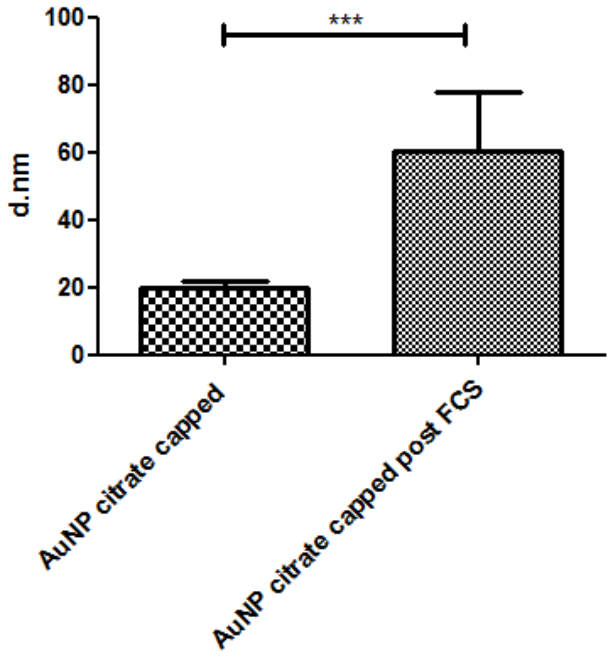

Figure 5-4 Statistical comparison for average diameter of citrate capped AuNPs before and after incubation with 10% FCS in DMEM

Table 5-2 Table displaying the non-specific protein adsorption results for the mixed monolayer and linker samples made using H5 peptide both prior to and following incubation with FCS in DMEM media

Conjugate	**DLS volume average**	**DLS volume average post DMEM FCS10%**
AuNP citrate capped	19.97 ± 1.6	60.44 ± 17.5
AuNP SH-PEG	35.29 ± 2.7	35.14 ± 6.2
AuNP SH-PEG-SGA	35.64 ± 3.3	33.58 ± 3.8
AuNP SH-PEG & H5	36.18 ± 2.76	34.03 ± 4.6
AuNP SH-PEG-SGA & H5	38.74 ± 3.4	36.18 ± 2.3

5.2.3 Cell Viability

The cytotoxicity of AuNPs and the correlation of cytotoxicity and/or the production of reactive oxygen species (ROS) as a result of nanoparticle size, shape, hydrophobicity and charge have been studied in many research papers. The hydrophobicity and charge also determine the binding sites for receptors and influence the dispersion and aggregation. Surface charge is often linked to hydrophobicity, whereas some studies have found that by using oleic acid coated nickel ferrite and stearic acid coated TiO_2 (titanium oxide) at the same surface charge, that toxicity is due to the surface coating. [282] Cytotoxicity can also be a factor caused by contamination, solubility or toxic payloads; however it can also be linked to biological parameters such as the cell line investigated, exposure time and/or temperature. Recent results demonstrating the potential toxic impact of AuNPs have generated controversy. There is vast diversity in the toxic responses reported, Raman-active AuNPs (PEG-R-AuNPs) cause minimal toxicity in both HeLa and HepG2 cells in an acute setting, [283] Soderstjerna *et al.* reported toxicity was only encountered in concentrations above 20 nM, whereas in osteoblastic cells, AuNPs have been reported to enhance differentiation. [284,285] The data therefore indicates that cytotoxicity may depend on the type of cell and could vary greatly across different cell lines. [286]

Nanoparticle toxicity was investigated for both surface arrangements by an MTT cell viability assay. The aim of this study was to address the literature and determine whether a longer PEG length will reduce toxicity as experienced with AuNPs functionalized with both tiopronin and a long-chain mercaptoundecyl-tetraethylene glycol (MUAPEG); or will utilizing a linker arrangement induce a toxic effect due to the loss of PEG shielding. [222] It also serves to investigate the effect of charge on toxicity.

2 cell lines were investigated for this study, PC3 and DU145 at three time points (days 3, 5 & 7). PC3 and DU145 cells are an epithelial cell line from a homosapien prostate. PC3 is derived from a metastatic bone of grade IV, adenocarcinoma, whereas DU145 is derived from a metastatic carcinoma brain site. Both lines were chosen based on the abundance of cellular studies in the literature. The results for the

The aim of the cell viability study is 3-fold; to investigate the toxicity induced as a result of surface arrangement, increasing nanoparticle concentrations and to confirm whether nanoparticle toxicity is a potential result caused by any unreacted species (supernatant). Initial observations indicated obvious aggregation for citrate capped nanoparticles (see chapter 6), which increased drastically with increasing concentrations. However, from the results obtained, it is apparent that loss in viability is inversely proportional to the degree of AuNPs aggregation. This relationship has also been previously observed in HeLa cell lines. [287]

(AuNP SH-PEG & H5) mixed monolayer arrangement are outlined in Figure 5-5 and the (AuNP SH-PEG-SGA & H5) bifunctional linker results are outlined in Figure 5-6. Statistical analysis was performed using a one-way ANOVA and Tukey post-test using Graphpad Prism software, with a P number <0.05 indicating statistical significance.

The cytotoxicity of nanoparticles has been studied in an abundance of literature, however initial conclusions seem that toxicity is dependent on the cell line and the concentration of the AuNPs. [284–286] From the results (Appendix 2 and Appendix 3) toxicity was dependent upon increasing concentrations with over 100 µg/ml exhibiting some degree of toxicity for all samples tested, and that the degree of toxicity exhibited was directly dependent on the level of functionalization that the AuNPs had undergone. [287] The aim of the previous study was to address the literature and determine whether a longer PEG length would reduce toxicity as experienced with AuNPs functionalized with both tiopronin and a long-chain mercaptoundecyl-tetraethylene glycol (MUAPEG); or will utilizing a linker arrangement induce a toxic effect due to the loss of PEG shielding. [222] It was concluded that that loss in viability is inversely proportional to the degree of AuNPs aggregation, a decrease in % survival is evident as the sample concentration increases, the supernatant studies have demonstrated that there is no reduced viability as a result of any unreacted species and that an increase in AuNP functionality, irrespective of the surface arrangement used, results in an increase in nanoparticle toxicity. A cell viability assay is essential for this part of the research due to the implementation of DMSO as the solubilizing solvent. The most standardized and validated test to estimate the cytotoxicity of compounds towards

cells is MTT test. This assay is dependent on the ability of live but not dead cells to reduce significant amounts of water-soluble yellow MTT dye to insoluble violet formazan crystals, which can be measured by a colorimetric method.

The data indicates that the rate of cell viability decreased significantly ($P < 0.05$) with increasing concentrations of all examined AuNP samples compared to those of the negative control group and cytotoxicity increase was surface functionality dependent, Figure 5-5 & Figure 5-6 illustrates the cytotoxicity results at Day 7 for the individual AuNP samples with increasing concentrations (25, 100 & 200 µg/ml) for both PC3 and DU145 cell lines. Citrate capped AuNPs demonstrated toxicity for both cell lines at 100 & 200 µg/ml increasing from 92, 81 to 77 % survivals for 25 100 & 200 µg/ml respectively in DU145 cell lines.

Aggregation was in abundance at the higher concentrations for the citrate capped AuNPs, however was not visible for the remaining samples (see Figure 5-7), this indicated that there was no toxicity as a direct result of aggregation as not all samples exhibited aggregation but yet all samples displayed similar toxicities. While this result may contradict earlier literatures, the results obtained conveys the conclusions drawn by Cui *et al. (2012),* who studied the influence of aggregation on HeLa cell lines. [288] They found that when AuNPs are endocytosed and aggregate, they result in cytotoxicity, however when the aggregates become too large and instead adhere to the cell surface, the growth rate of the HeLa cells increases. A similar trend is seen with the DU145 cells lines, at D7 the % survival was calculated to be 92 %, which subsequently increased to 96 % by D14 (see appendix 1) showing proliferation. When cross referenced with the image displayed in Figure 5-7 it is observed that a large degree of aggregation is present, and while some appears to be internalized, a large amount appears to be surrounding and obscuring the cells from observation. [288]

There was no statistically significant cytotoxicity evident in the DU145 cell lines for all working concentrations apart from the SH-PEG & H5 which displayed an 89.77 % survival at 25 µg/ml which decreased steadily to 71 % at 200 µg/ml which was similar to SH-PEG with 70.53% toxicity (200 µg/ml). While the AuNP SH-PEG-SGA was non-toxic at 25 µg/ml with 96% survival, it dropped quickly to 69.48 %

and 59.8 % with increasing AuNP concentration which is almost 20% below the AuNP citrate capped for DU145. While the linker samples retained viability with 92 % survival for 25 µg/ml, the survival rate dropped and plateaued at 70% for both 100 and 200 µg/ml. Similar trends were observed for PC3 cell lines however an increased % survival was noted for the AuNP SH-PEG-SGA samples retaining 74 % survival at 200 µg/ml and 72 % when co-functionalized with H5.

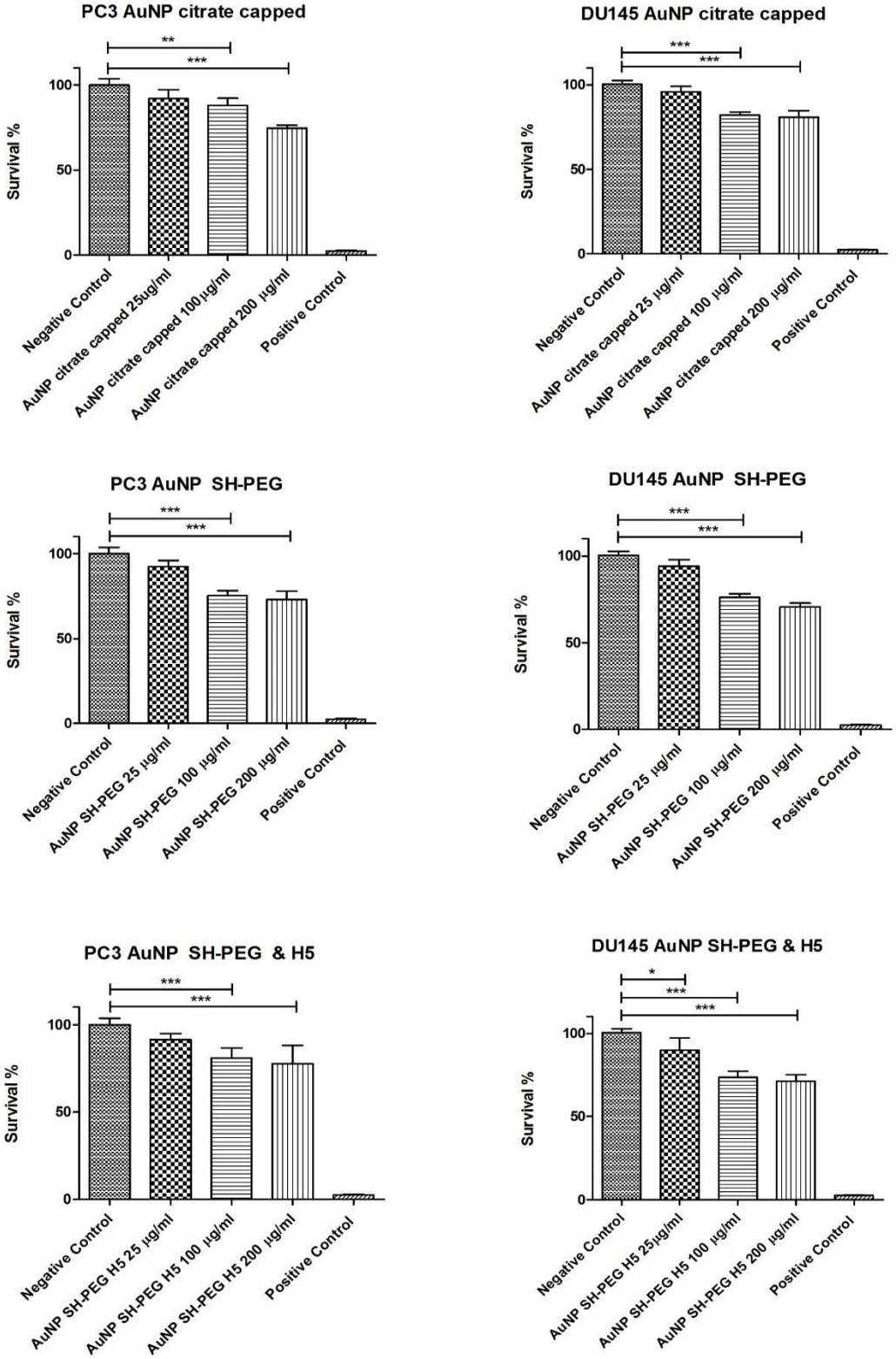

Figure 5-5 Cell viability results displaying the survival % for mixed monolayer AuNPs at each stage of functionalization for both PC3 (left) and DU145 (right) at Day 7

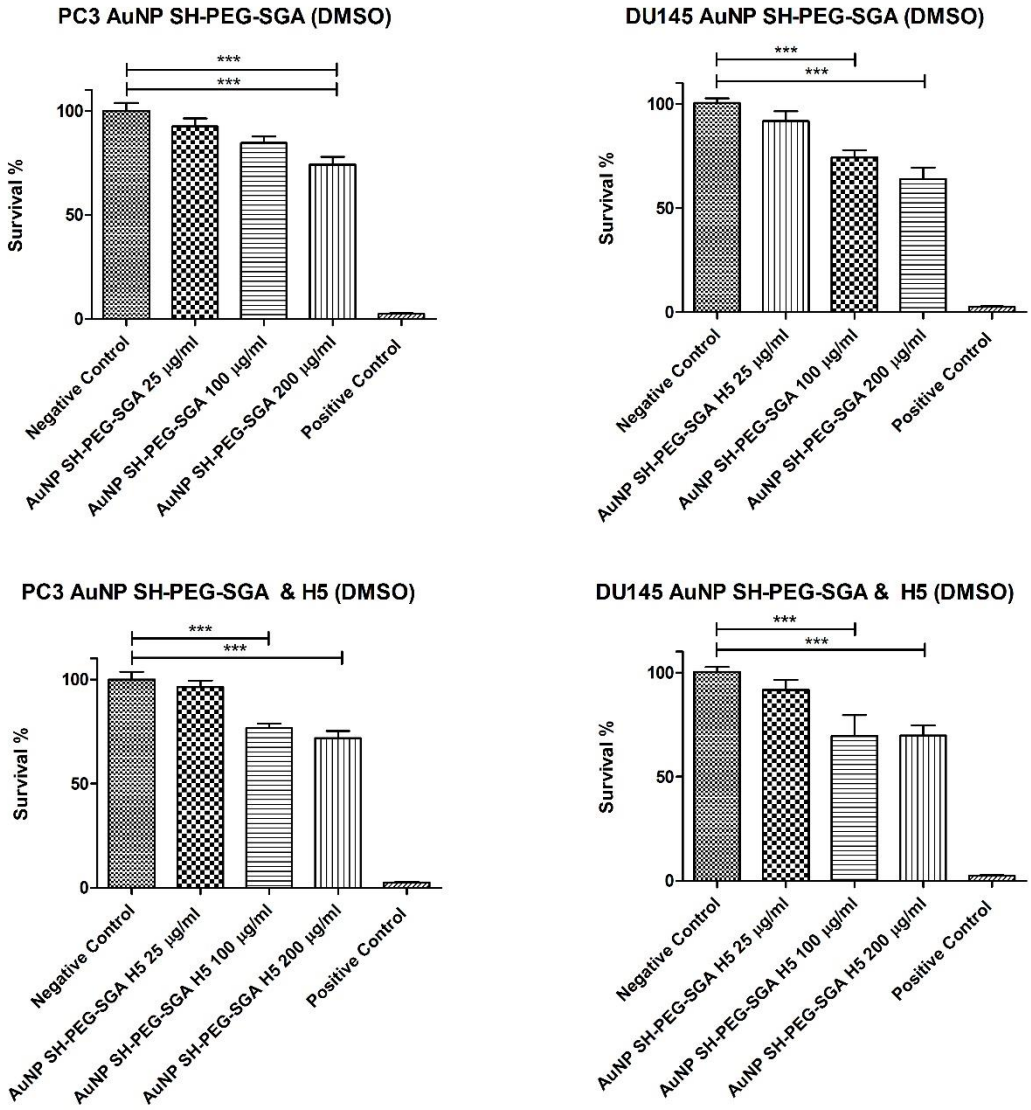

Figure 5-6 Cell viability results displaying the survival % for bifunctional linker AuNPs at each stage of functionalization for both PC3 (left) and DU145 (right) at Day 7

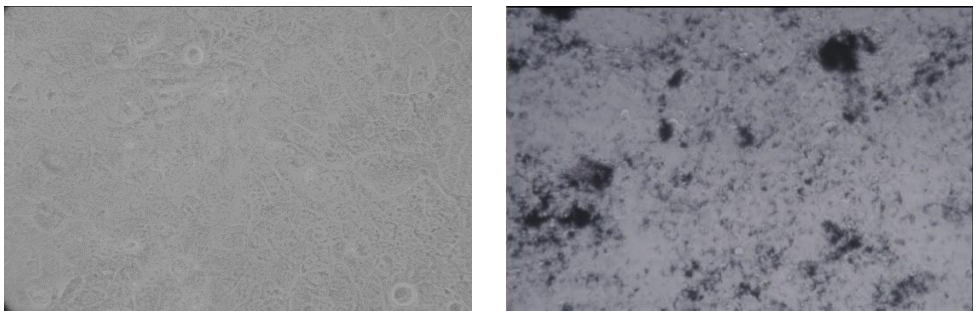

Figure 5-7 optical images of DU145 cells treated with AuNP SH-PEG-SGA & H5 (left) and citrate capped AuNPs (right)

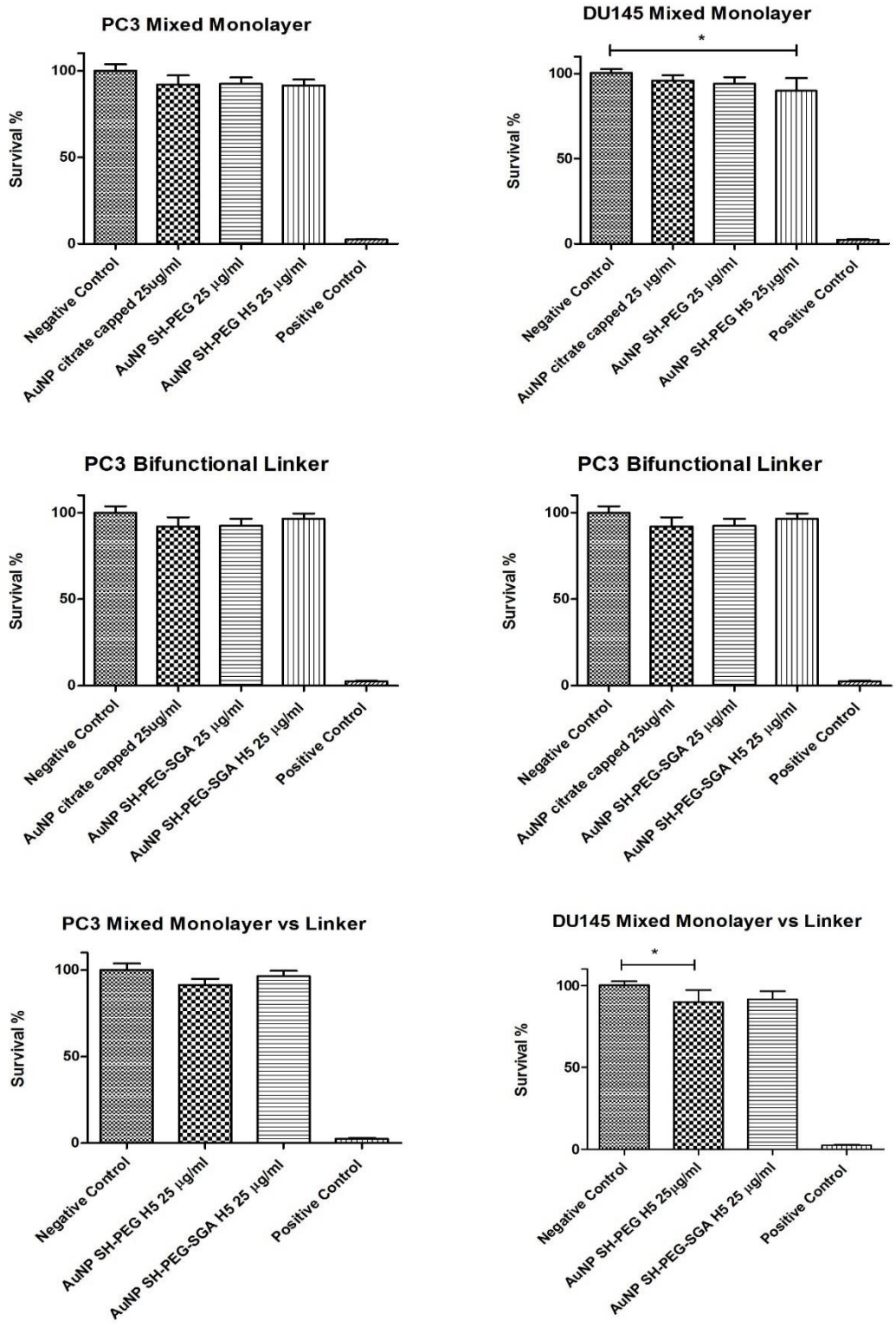

Figure 5-8 Cell viability results displaying the survival % for the mixed monolayer arrangement (top) and the bifunctional linker arrangement (middle) with direct comparisons of each (bottom) across both cell lines (PC3: left, DU145: right), n=4

Linker samples appear to have less toxic effects than the mixed monolayer arrangement, this is unexpected, with significant differences being found between the mixed monolayer and the negative control ($P < 0.05$). This is theorized to be a combination of the influence of the PBS. PBS is an important buffer solution commonly used in biological research. It is a water-based salt solution containing disodium hydrogen phosphate, sodium chloride and, in some formulations, potassium chloride and potassium dihydrogen phosphate. Literature has also reported it to act as an antioxidant in cells, it helps to neutralize (ROS) such as free radicals. [147] The increase in cytotoxicity evident by an increase in concentration could be a result of the production of Reactive Oxygen Species (ROS), ROS are by products of cellular oxidative metabolism, most of which occur in the mitochondria. In the mitochondria, ATP is synthesized by the reduction of molecular oxygen to water through processes of coupled proton and electron transfer reactions. During this process, a small percentage of the oxygen is not completed reduced, which results in the formation of superoxide anion radicals and other oxygen containing radicals. [289] The overproduction of ROS can induce oxidative stress which results in cells failing to maintain normal physiological redox-regulated functions. Generation of ROS induced by nanomaterials is one of several mechanisms leading to nano-toxicity. The level of ROS production is determined by the chemical properties which arise as a result of their small size, high surface area and high surface reactivity which differs greatly from the bulk-size counterpart. The physical and chemical properties which contribute to the production of ROS include their size and shape and surface bound ligands including coatings, solubility and degree of aggregation. [289]

It is also predicted that the toxicity from the linker may decrease due to the removal of the second active functional group by co-functionalization, as the RME linker showed only a 55% survival after 7days at 200 µg/ml with working concentrations dropping from 92% viability for the linker and 90% for the AuNP SH-PEG-SGA. As a trend, the viability seems to be generally lower with the RME peptide. This could be a result of the peptide. Overall the general toxicity has decreased with the H5WYG peptide with only the mixed monolayer displaying toxicity in comparison to the negative control at 25 µg/ml. The cell viability results after 14 days (results not shown – see appendix 2, 3 & 4) observed an average % survival of 96% for the

citrate capped AuNPs exhibiting that as synthesized AuNPs are not cytotoxic after prolonged exposure (up to 14 days). From the DU145 results at day 14, it is observed that the mixed monolayer arrangement is increasingly more toxic as the level of functionalization increases, with significant difference evident between the AuNP SH-PEG (96.6%) and the AuNP SH-PEG & H5 (90.7%). For the linker arrangement, while there is significant difference in viability apparent for both the PEGylated and linker samples, the degree does not significantly increase with surface functionalization remaining at 95% and 96% respectively. However, when directly comparing the mixed monolayer to linker the mixed monolayer is significantly more toxic than the linker (P number 0.0025), which was not observed at D7.

Overall, the mixed monolayer displayed the lowest % survival across all samples types for both cell lines with only 71% survival for DU145 and 68.4 % for PC3 in comparison to the bifunctional linker (81.7% PC3 & 80.8 % DU145). Therefore, it is concluded that the initial hypothesizes identified from the literature surrounding the effect of a linker on cytotoxicity is void. [222] In effect, from the samples studied in this piece of research, it can be concluded that the bifunctional linker has demonstrated higher degrees of both colloidal stability and cell viability, which is in direct contrast to arguments from the literature regarding an 'anti-PEG' effect. [217,222] Another result of note includes the little cytotoxicity experienced from the samples functionalized using DMSO which corroborates with the literature which has reported a cell viability rate of more than 90% observed at 0.1% DMSO. However in contrast to that, literature has previous identified toxicity to dramatically increase at DMSO concentrations of 0.5%, which was not seen for the AuNP SH-PEG-SGA & H5 across any cell lines at either time points. [277]

5.2.4 Internalization

The stability and cell viability studies have so far identified significant differences between the mixed monolayer and bifunctional linker arrangements when co-functionalized with H5WYG peptide, this contrasts significantly to the results previously obtained in chapter 4. Some literature suggests that vectors should carry ligands of a similar length to enable accessibility to the relevant receptors. [157,158,212–

[215,220] Cell internalization studies were investigated to see of the linker ligand would elicit an even greater biological response due to direct cell contact. H5WYG peptide has previously shown successful internalization in a mixed monolayer arrangement through the collaboration with Queen University Belfast, Pharmacy. This area of research was implemented to identify if statistically significant cellular result would be obtained due to AuNP surface arrangement. Figure 5-9 illustrates the ICP-MS results of intracellular AuNP concentration for both mixed monolayer and bifunctional linker arrangements following incubation for 24h. It is observed from Figure 5-9 that the uptake for the bifunctional PEGylated AuNPs is minimal, this corroborates with the literature, as PEG is commonly reported to hinder uptake. However unusually, the AuNP SH-PEG samples have displayed a degree of uptake, approximately 0.18pg. For both the PC3 and DU145 cell lines a significant increase is evident for the AuNP SH-PEG-SGA & H5 (Bifunctional linker) samples in comparison to the PEGylated counterpart (P value of 0.0329 and 0.003 for the PC3 and the DU145 cell lines respectively) offering an almost 30-fold increase in internalization for the DU145 cell lines and a 14-fold increase for the PC3 cell lines. The level of uptake for the DU145 linker samples is similar to the level previously experienced via the RME peptide peaking at approximately 0.7pg. The DU145 cell lines indicate a statistical difference for internalization between the mixed monolayer, indicating that the linker has elicited a higher internalization response for both cell lines with an overall F value of 181.8 and a P value of 0.0095 ($P < 0.05$) for the DU145 cell lines resulting in over 3 times the amount of gold within the cells. Overall the level of internalization is extremely low in comparison to the citrate capped AuNPs (approximate average of 10 pg – results not shown), however it should be noted that the H5WYG peptide is not an internalization peptide, and therefore while the results may not recover the internalization to the level experienced by the citrate capped AuNPs, it is still a positive result identifying significant difference between the mixed monolayer vs. linker arrangement and consequently identifies a niche to be explored potentially utilizing an array of targeting peptides and/or internalization ligands. Statistical analysis was performed using a one-way ANOVA and Tukey post-test using Graphpad Prism software, with a P number <0.05 indicating statistical significance.

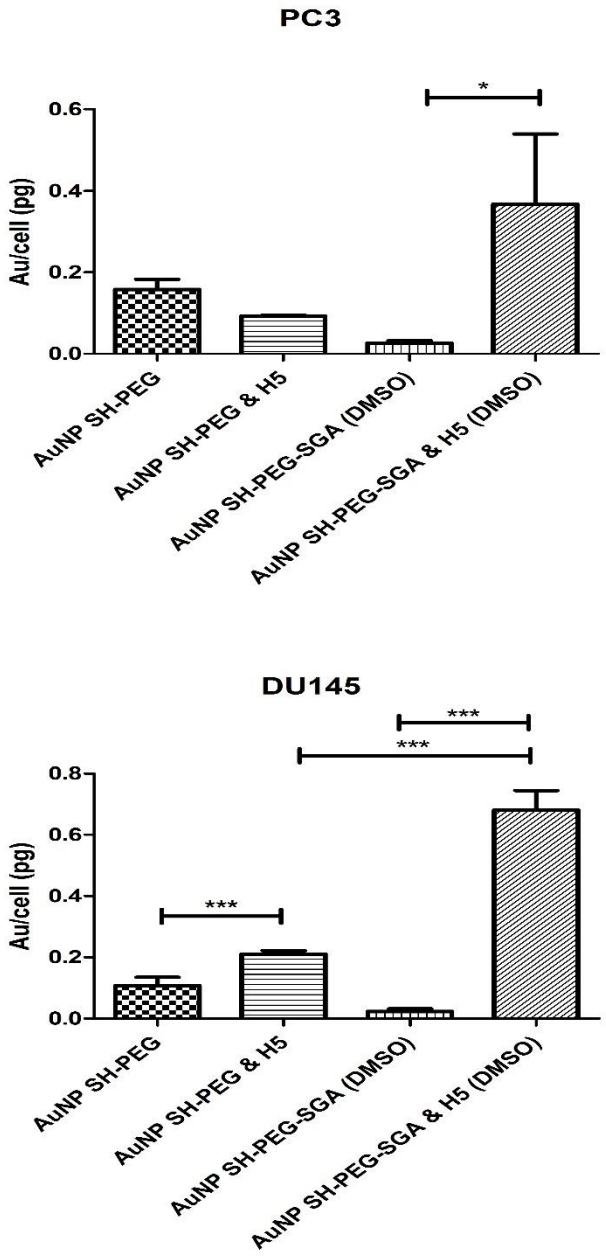

Figure 5-9 ICP-MS was used to quantify intracellular gold content per cell following exposure to a range of modified nanoparticles at 25 µg/ml for 24 h in PC3 and DU145 cells. Statistical analysis performed using a one-way Anova found significant increase evident for the linker samples in comparison to the PEGylated counterpart (P value of 0.0329 and 0.003 for the PC3 and the DU145 cell lines respectively) (n = 4).

5.2.5 Clonogenic Survival Assay

Based on the biocompatibility and elevated uptake apparent, DU145 cell lines were chosen to take forward in determining radiosensitivity of both the mixed monolayer and bifunctional linker samples. DU145 cells were incubated with 50 μg/ml of both AuNP conjugate types for a 24 h period, then removed and cells irradiated with 0-6 Gy. Figure 5-10 shows the survival fraction of irradiated cells for the clonogenic survival assay. The area under the curve (AUC), which represents the mean inactivation dose (MID), was calculated using Prism 6.0 (GraphPad software) and the sensitizer enhancement ratio (SER) calculated by dividing the MID of untreated cells with AuNP conjugate treated cells. The MID is an important measurement as it estimates overall radiosensitivity and incorporates all data points, whereas survival fraction provides information of a specific dose point on the survival curve which can be correlated to clinical tumor.

The results from the clonogenics demonstrate that 'as synthesized' AuNPs resulted in a modest 6 % increase in radio sensitivity (SERS 1.06) in comparison to the untreated control (P value = 0.04). The functionalization with SH-PEG-SGA and SH-PEG-SGA & H5 peptide resulted in SERS of 1.07 and 1.21, demonstrating an 7% and 21% increase in radiosensitivity respectively, with the Survival fraction of the linker at 4 Gy being 48% lower for the linker than the mixed monolayer arrangement. The results have indicated that the synthesis of a linker using a H5 peptide has resulted in a significant increase in the effectiveness of radiotherapy when compared to the control. (P value = 0.01). The mixed monolayer results illustrated a 9% decrease in radiosensitivity as the result of irradiation in comparison to the negative control. These results correlate to the higher internalization quantities previously measured in Figure 5-9 for the linker samples, however the inverse relationship between increasing concentrations within the DU145 cells between AuNP SH-PEG & AuNP SH-PEG & H5 and decreasing radiosensitivities displayed for the mixed monolayer samples indicate that internalization does not necessarily automatically correlate to enhanced radiosensitization, and that optimized radiosensitization may have been achieved through the linker methodology as a result of the enhanced accessibility resultant of the linker arrangement.

To ensure radiosensitization at 50 μg/ml was not an effect of long term toxicity resultant of the nanoparticles in the absence of radiation, clonogenic controls were calculated (± 20 μg/ml AuNP) were and plotted (see appendix 5), showing no significant decrease in the ability of the AuNP treated cells to form colonies, and thus they don't affect the cells ability to re-populate and as such are non-toxic.

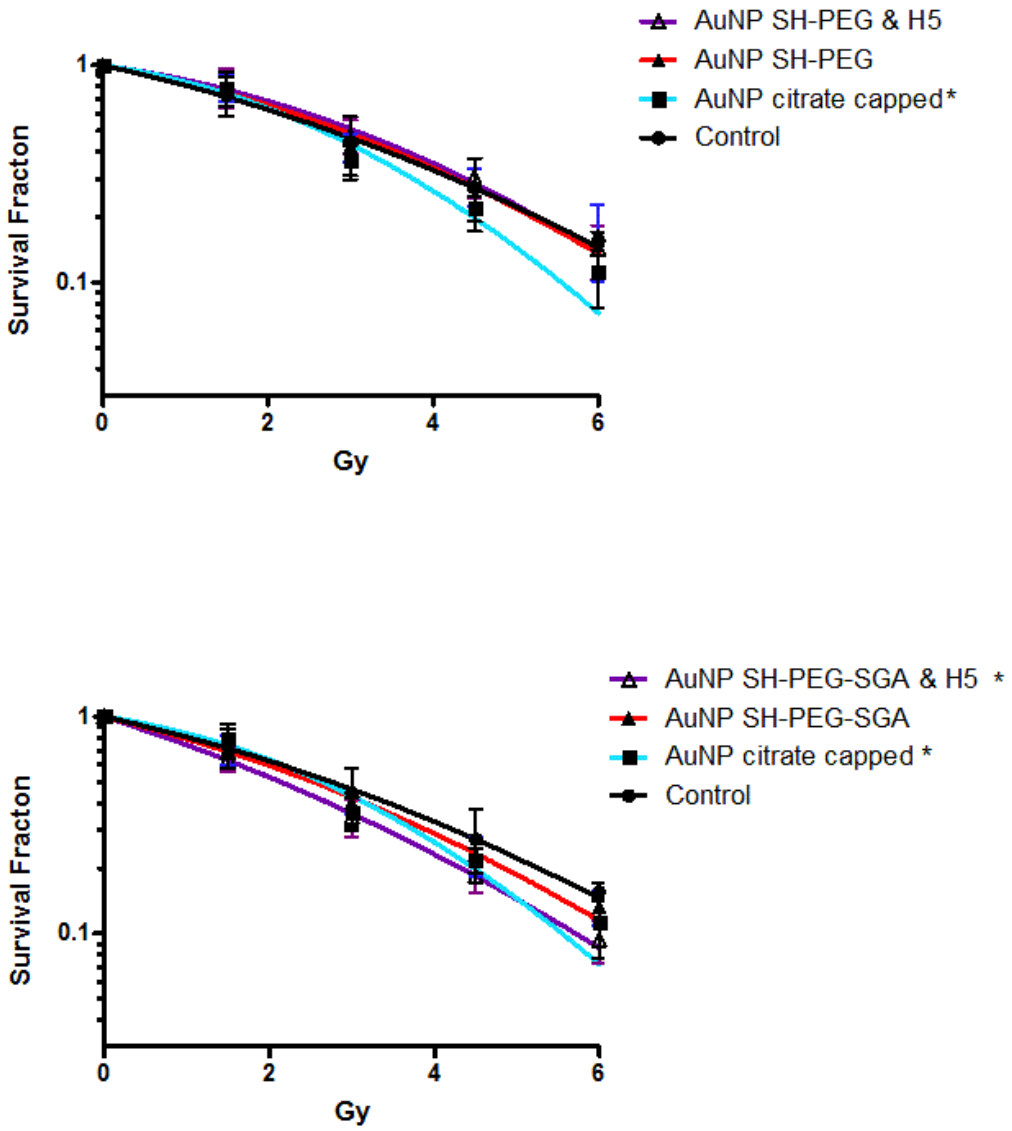

Figure 5-10 Clonogenic survival assay was used to assess the radio sensitizing potential of 50 µg/ml AuNPs following a 24 h incubation using DU145 cell lines, followed with 0-6 Gy using 160 kVp x-rays. Error bars represent the SEM (n = 4).

5.3 Conclusion

This research has found that despite it being reported that using a PEG linker methodology to synthesize an AuNP-BSA-peptide conjugate resulted in frequent instabilities; that there is no loss in colloidal stability due to the synthesis of a bifunctional linker. [157,212–215] The results observed in this chapter dispute the initial hypothesis outlined above.

Many researchers have successfully employed AuNPs functionalized using mixed monolayers; for example, Kumar *et al.* successfully utilized a mixed monolayer structure to allow for the controlled release of a thiol bound fluorescent dye (as a model drug payload) over a period of 2 hours. These authors found that the addition of PEG inhibited the initial burst release of the payload as well as preventing particle aggregation. [153,182] In 2006 significant progress was made by constructing a novel nanomedicine, CYT-6091 by assembling recombinant human tumor necrosis factor alpha (rhTNF) to the surface of a 26nm AuNP with thiol PEG in the form of a mixed monolayer. A 7-10-fold increase was seen in the amount of tumor necrosis factor (TNF) that was delivered to the tumor compared to the injection of native TNF. It was also found that a 7.5 µg/ml injection of CYT-6091 was as effective as 15 µg/ml of native TNF, and that the 15 µg-native TNF resulted in a 60% survival rate, compared to the 100% survival after treatment with 15 µg of CYT-6091. Thus, the formulation is undergoing clinical trial. A Phase I study commenced in 2005, where 29 patients with solid tumors demonstrated no dose-limiting toxicity up to 600 µg m^{-2}. The main side effect was reported as controllable grade II fever. One partial response and three stable disease states were observed, demonstrating a positive outcome in 14% of patients. [59–63,290]

The results from the internalization study concur with some aspects of the literature which concluded that PEG length does not impede peptide function when used in a mixed monolayer arrangement. Investigations were previously undertaken to determine whether longer PEG molecules would hinder the efficiency of the targeting peptides, interestingly, after experiments utilizing three thiol modified PEGs of various molecular weights (900MW, 1500MW, 5000MW) it was found that the number of PEG5000/RME conjugates in HeLa cell lines were nearly a factor 4

larger than that of PEG900/RME conjugates, thus indicating that PEG length did not sterically hinder the function of the peptide. [153] This finding has been supported by other studies which have observed excellent performance for mixed monolayer functionalized AuNPs. [56,61,63,223]

This chapter has demonstrated that the co-functionalization of AuNPs with RME peptide using a NHS ester has resulted a mixed monolayer arrangement due to the availability of the cysteine as evident from the PyMol drawing in chapter 5. The presence of the ligands along with the method of arrangement of those peptides on the AuNP surface has been confirmed by a combination of FTIR, DLS and Texas Red. It can also be concluded that while a pre-synthesized NHS ester could offer a more efficient means to synthesized a linker, it is heavily dependent on the solvent used to synthesize the linker. Changing the solvents gave a wide range of results with the parallel loaded and sequentially loaded samples without the cysteine showing the successful synthesis of a linker. It was concluded that the NHS ester was hydrolyzing and due to the hydrophobicity coupled with the net charge of the H5, that it was highly unstable in water.

Once a linker had been successfully synthesized, a range of mixed monolayer vs. linker studies contracted the initial hypothesis both in this Thesis and in the literature. It was found that for the H5 peptide that colloidal stability, cell viability and internalization were enhanced via the utilization of a bifunctional linker. Therefore, having peptide chains longer then the stabilization agent does not have a negative effect on colloidal stability or opsonization, and using a linker does enable easier accessibility for the peptide to have direct with the cell to elicit a higher biological response, with both the PC3 and DU145 cell lines a significant increase evident in internalization for the AuNP SH-PEG-SGA & H5 (bifunctional linker) samples in comparison to the PEGylated counterpart (P value of 0.03 and 0.003 for the PC3 and the DU145 cell lines respectively). The DU145 cell lines indicated a statistical difference for internalization between the mixed monolayer ($P < 0.05$).

The clonogenic survival assay has also identified significant difference between the untreated control and the linker with a P value of 0.02 whereas there was no significant difference present for mixed monolayer.

Therefore, in spite of recent progress, defining the rules that control the surface functionalization of AuNPs with molecular linkers is still a challenge, and while clonogenic survival assays observed a significant increase in radio sensitization as a result of a linker, future work should re-visit internalization ligands in a linker formation as well as the inclusion of a targeting ligand such as RGD peptide. From this study, it is now clear that the binding affinity of the conjugating groups should be carefully considered prior to functionalization and further characterization methods should be employed when utilizing a linker to confirm the co-functionalization of the ligand on the surface.

6. OPTIMIZING ATTACHMENT

6.1 Introduction

AuNP synthesis via the Turkevich method produces 10–80 nm diameter, citrate capped particles with a zeta potential of approximately -20 to -40 mV. [183] Co-functionalization is commonly achieved via electrostatic charge attachment, specific affinity immobilization and/or covalent bonding typically by means of thiol, or less frequently, amine groups. [290,291] While it has been observed that pH plays an important role in controlling ligand attachment, it is not currently possible to predict an optimum pH for attaching a particular peptide. Optimizing the ligand attachment by altering the pH may have the benefit of being able to maximize the binding efficiency with the nanoparticle. [21,185,186,290]

It is predicted that slightly acidic buffer solutions will elicit a positive charge of the peptides and therefore elicit a higher binding affinity towards the negatively charged gold nanoparticle. Therefore, this study will focus on tailoring the pH of the AuNP solution in relation to the isoelectric point (pI) values of a range of peptides to investigate if there is an optimum pH for peptide attachment, and if this varies depending upon the peptide characteristics. The attachment of the peptides (RME, H5WYG and RGD) to partially PEG capped AuNPs were studied in a range of pH buffers above, below and at the isoelectric points of the peptides. The peptides used were the receptor mediated endocytosis (RME) sequence CKKKKKKSEDEYPYVPN which has an overall net charge of +2.9 and a pI of 9.6 at a neutral pH. The buffers used for investigation of RME peptide were pH 8, 9, 9.2, 9.4, 9.6, 9.8, 10 & 11. An endosomal escape pathway H5WYG peptide sequence GCGLFHAIAHFIHGGWHGLIHGWYG with a net charge of +0.4 and a pI of 7.75 (at a pH of 7) was also studied. The buffers used for investigation of H5WYG peptide were pH 6, 7, 7.25, 7.5, 7.75, 8, 9, 10 & 12. Finally, the Nrp-1 targeting peptide (RGD) labelled with FITC (FITC-Ahx-CRGDK) was investigated which has a net charge of +1 and a pI of 8.6 at a neutral pH. The buffers used for investigation of the RGD peptide were pH 6, 7, 8, 8.6, 9, & 10. RME & RGD peptides are both terminated with a cysteine residue at the N-terminus for functionalization with the

AuNP surface via the thiol, while H5WYG is terminated with a Glycine residue alongside the secondary Cysteine residue, which offers the potential attachment via the free amine group found on both the N-terminus and C-Terminus.

All three peptides have been modeled using PyMol, as illustrated in Figure 6-1, wherein the yellow spheres indicate the thiol group in each sequence and highlights the availability of the cysteine residues for surface interaction. The dissociation constant (Pk) values for the remaining 'free' reactive groups found on the amino acids for the three chosen peptides were calculated as follows:

RME pI = 8.7

H5WYG pI = 6.7

RGD pI = 7

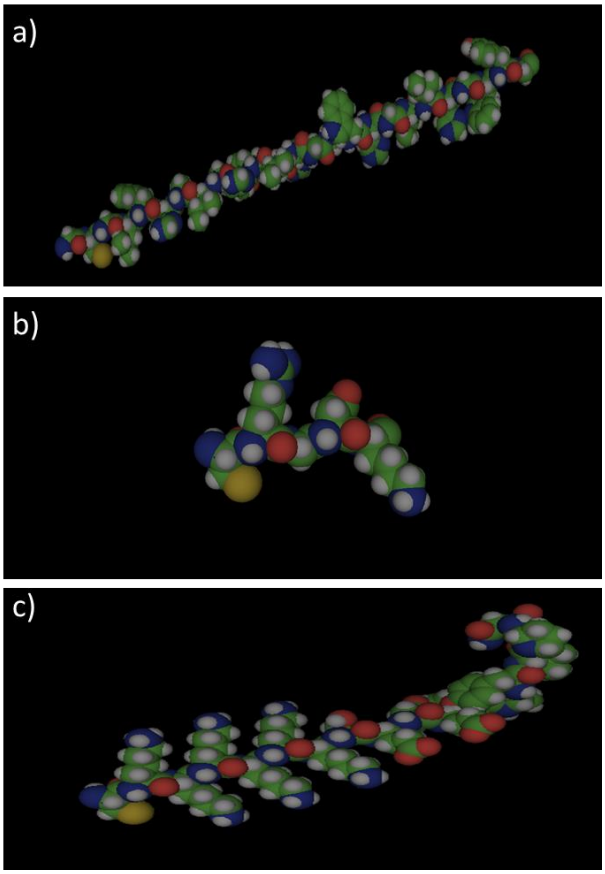

Figure 6-1 PyMol Modelling of the a) H5 peptide, b) RGD targeting peptide and c&d) the RME peptide taken from Harrison et al. 2017 [308]

6.2 Results and Discussion

The samples synthesized for this chapter are the ‘as synthesized’ AuNPs which will be referred to as AuNPs citrate capped, AuNPs functionalized with monofunctional (SH-PEG) Polyethylene glycol which will be referred to as AuNP SH-PEG. And PEGylated AuNPs co-functionalized with either the receptor mediated endocytosis peptide, an endosomal escape pathway (H5WYG) or and Nrp-1 targeting ligand (RGD) peptide which will be referred to as AuNP SH-PEG & RME, AuNP SH-PEG & H5, AuNP SH-PEG & RGD respectively.

AuNPs were synthesized using the Turkevich method described in chapter 3, the synthesized citrate capped AuNPs and PEGylated AuNPs were characterized using TEM and FTIR as described in chapter 3. The citrate capped AuNPs showed an average particle size of 13.21nm ± 1.31 by TEM (results not shown). The PEG functionalized and co-functionalized samples do not show a significant increase in size, as discussed harrison *et al.* [185]

The nanoparticles were characterized post synthesis; post PEGylation, post re-dispersion with the relevant buffer and after co-functionalization with the various peptides. The characterization techniques employed for this chapter include FTIR, UV/Vis, DLS, Zeta, Photoluminescence and Micro BCA. As synthesized AuNPs will be referred to as AuNP citrate capped. AuNP with mono functional PEG is AuNP SH-PEG

6.2.1 FTIR

Fourier Transform Infrared Spectroscopy (FTIR) spectra of the washed and dried AuNPs, AuNP SH-PEG, AuNP SH-PEG RME, AuNP SH-PEG H5WYG and AuNP SH-PEG RGD are shown in Figure 6-2. Prominent differences are visible in the spectra for the PEG capped AuNP spectrum compared to that for the citrate capped AuNP. The presence of the mono-functional thiol PEG (SH-PEG) on the AuNP SH-PEG is confirmed by the peaks associated with C=O stretching (1,660 cm^{-1}) and bending (1,380 cm^{-1}) and the presence of additional peaks relating to N-H bending (1,660 cm^{-1}) and N-H wagging (600-900 cm^{-1}). [185] The characteristic vibrations found in ethylene glycol ligands are observed at 1106 cm^{-1} (C-O-C stretching) and a narrowing of the CH_2 stretching mode (2850 cm^{-1}). [61,182,184,202,258] S-Au bonds are expected to appear at 1777 or 1545 cm^{-1}. All conjugates present noise at approximately 1777 cm^{-1}. While the noise may indicate the presence of Au-S bonds

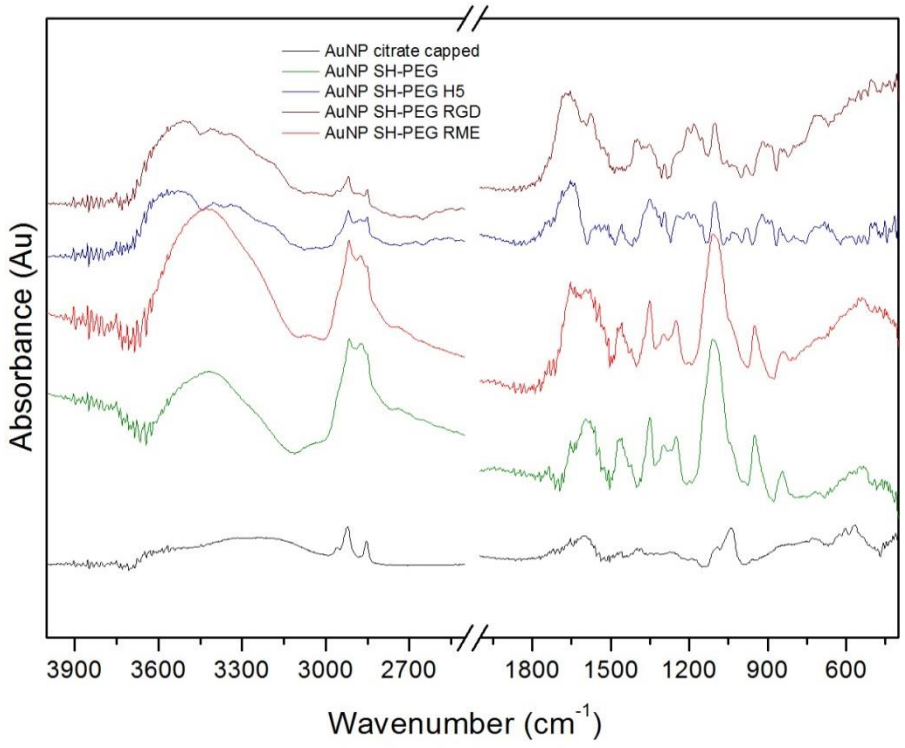

Figure 6-2 FTIR Spectra of the washed and dried AuNP citrate capped (black), AuNP SH-PEG (green), AuNP SH-PEG RME (red), AuNP SH-PEG H5WYG ((H5)blue) and AuNP SH-PEG RGD (wine red)

it cannot be confirmed. The successful conjugation of all three peptides to the nanoparticle surface was confirmed by the appearance of new amide bonds around 1670 $cm^{-1}$and 1550 cm^{-1} for amide I and II respectively. Amide I bands are mainly associated with the C=O stretching vibration relating to the backbone conformation, while Amide II bands result from N-H bending and C-N stretching. Co-functionalization was further confirmed through the observation of N-H wagging peaks (600cm^{-1} – 900cm^{-1}) on the peptide functionalized samples, with a C-H bend at approximately 1376 - 1387 cm^{-1} and the C-H alkene bend (992 cm^{-1}). [184,259–261,292–294] Amide III bonds found on the co-functionalized samples (approximately 1400 – 1300 cm^{-1} region) are complex bands resulting from a mixture of several coordinate displacements. Successful attachment of the PEG was further confirmed by an increase in hydrodynamic area, by DLS after co-functionalization, from a size of 17.5 nm to approximately 35.4 nm.

FTIR confirmed the successful attachment of each of the peptides in distilled water, therefore to investigate the effect on pH the citrate capped AuNPs were PEGylated with SH-PEG, and the AuNP-PEG solutions were then collected and aliquoted evenly into 50 ml centrifuge tubes and centrifuged for 90 min at 13,500 RCF. 95% of the supernatant was then decanted and discarded leaving the remaining 5% of the AuNP as a pellet in the bottom of the centrifuge tube. Each individual centrifuge tube was then refilled to the initial volume using the required pH buffer and then vortexed to re-disperse.

Co-functionalization was achieved by continually stirring the re-dispersed AuNP-PEG samples, 4.45 μg/ml of free RME peptide, 5.86 μg/ml of free H5WYG peptide or 2.31 μg/ml of free FITC labelled RGD peptide (dissolved in 1 ml of the relevant buffer) were added to the PEGylated AuNPs (see chapter 3). [184]

6.2.2 UV/Vis

For this chapter nanoparticle colloidal stability is defined as the ability to resist aggregation as detected by UV/Vis. UV/Vis is commonly used to investigate the aggregation states of colloidal gold. The unique optical properties of metal nanoparticles, which result from the surface plasmon resonance effect, offers a simple means to study size, functionalization and aggregation states with high sensitivity. [252,253] AuNP aggregation is accompanied by a red-shift in the plasmon peak, as well as broadening of the adsorption peak, and a decrease in absorbance which can be easily monitored by UV/Vis spectroscopy. [295] An increase in size resulting from aggregation is also evident visually with a change in color of the solution from red to blue/purple. [296] Complete aggregation and settling out of the AuNP will result in a loss of color and diminution of the characteristic peak in UV/Vis. Each sample was measured after synthesis; following PEGylation, after re-dispersion in the various pH buffer solutions, and after peptide co-functionalization. We used the intensity and peak location (λmax) of the plasmon peak in the UV-vis spectra as indicators of AuNP aggregation state. Each sample was measured after synthesis; following PEGylation, co-functionalization and post re-dispersion in the various pH buffer solutions. Intensity, peak width, and peak location (λmax) of the Plasmon peak in the UV-Vis spectra was used as an indicator of the AuNP stability.

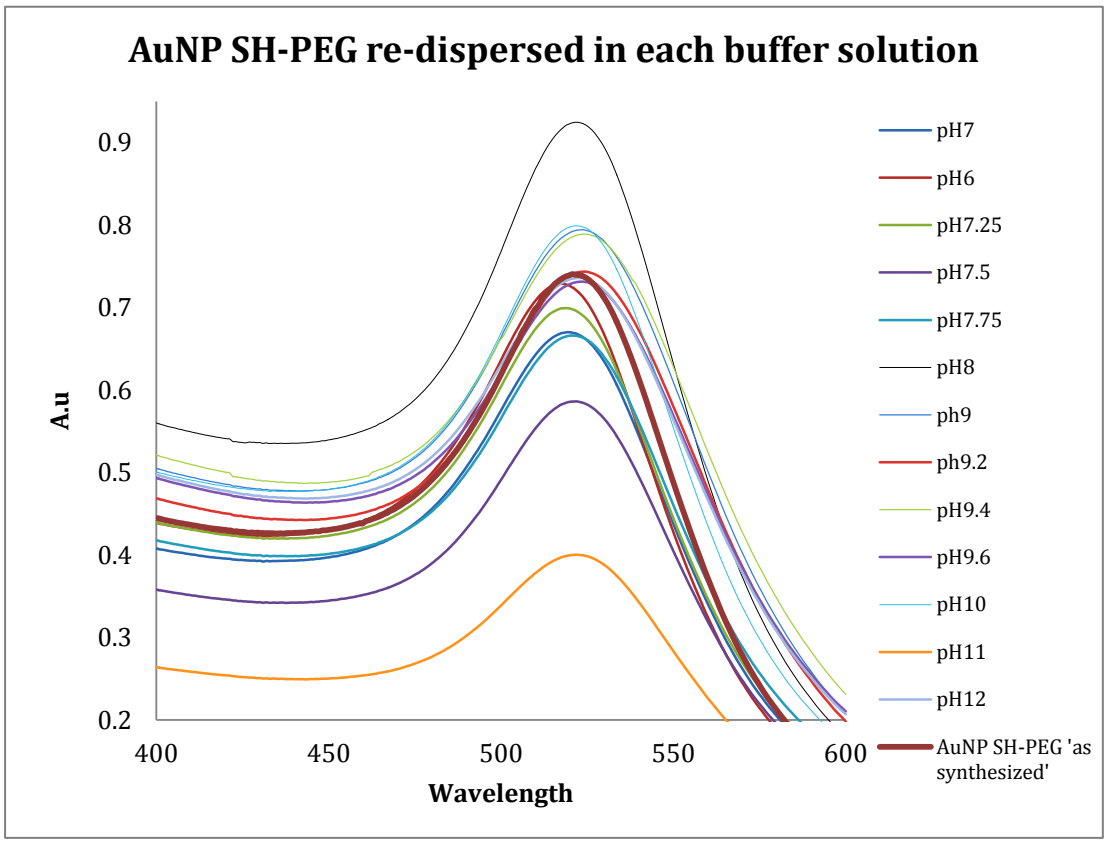

Figure 6-4 UV/Vis absorbance spectra for AuNP SH-PEG re-suspended in each pH buffer solution, n=4

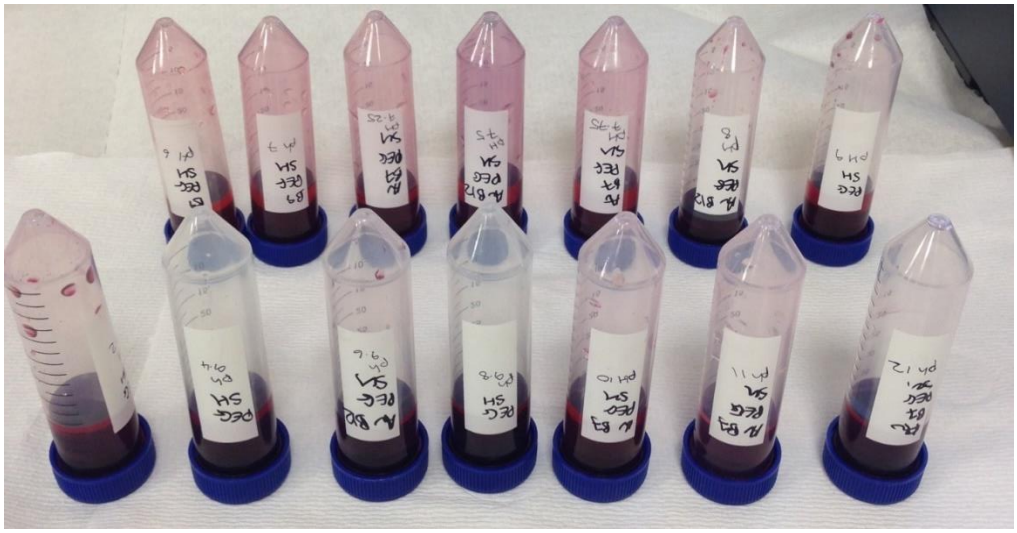

Figure 6-3 AuNP SH-PEG in buffer solution prior to peptide attachment visually displaying the discoloration of the originally transparent centrifuge tube, stained red in varying degrees dependent on the pH buffer solution

AuNPs were re-dispersed in the appropriate buffer to obtained the desired solution pH. The buffers used were citric acid/sodium hydroxide buffer solution pH 6 borax/sodium hydroxide buffer solution pH 8 and 10, di-sodium hydrogen phosphate/sodium hydroxide buffer solution pH 12. All of these buffer solutions were then altered with sodium hydroxide or hydrochloric acid to produce the intermediates.

Figure 6-4 displays the UV/Vis spectra for AuNP SH-PEG which has been re-suspended in the various buffer solutions compared to the AuNP SH-PEG control. No change was found for the peak position and absorbance profiles for the surface plasmon band of the sample before modification as a function of pH which displayed a wavelength of 520.8 nm with an absorbance value of 0.74. The absorbance values for the AuNP SH-PEG in a range of pH is indicative of the surface reactions. Each pH change results in a different surface reaction which changes the surface potential, this change can result in varying degrees of a loss of stability, which is evident through a significant decrease in absorbance intensity as a result of a change in pH. It is evident from Figure 6-4 that pH 11 and 9.6 have the greatest loss in absorbance intensity. Figure 6-3 observes a change in the color of the centrifuge tube for the AuNP SH-PEG samples in each pH buffer solution. From Figure 6-4 it is clear that pH 6, 7, 7.25, 7.5, 7.75, 9.2 and11 all discolor the transparent centrifuge tube to varying degrees of red. This corroborates with the UV/Vis spectrum in Figure 5-3, as each of these samples decrease in Absorbance. The functional groups present on the AuNP are pH reactive, and as their buffer changes the pKa of the functional groups on the AuNP surface, they ionize to different degrees which affects the colloidal and chemical stability in solution. In agreement with a number of publications the characteristic peak at 520 nm is clearly visible for all the AuNP samples illustrating a degree of stability across the pH range tested. [183,252,255,256] The results show that the PEGylated colloidal AuNP solutions have maintained a high degree of colloidal stability following centrifugal washing and re-dispersion in the buffer solutions. Extremely acidic pH were not measured, as Das *et al. (2012)* observed that the SPR band remained stable except at extreme acidic pH conditions. It was reported that at a pH of 1, the characteristic SPR peak was shifted to 537 nm from 527 nm and an extra peak at 649.80 nm was observed. [281] Investigations into the colloidal stability of nanoparticles in a range of pH buffers also identified a stable range application for

each buffer solution used. Those ranges would show clear plasmonic peaks whereas outside of the ranges the nanoparticles would display considerable decreased absorbance's or significant peak shifts. [297]

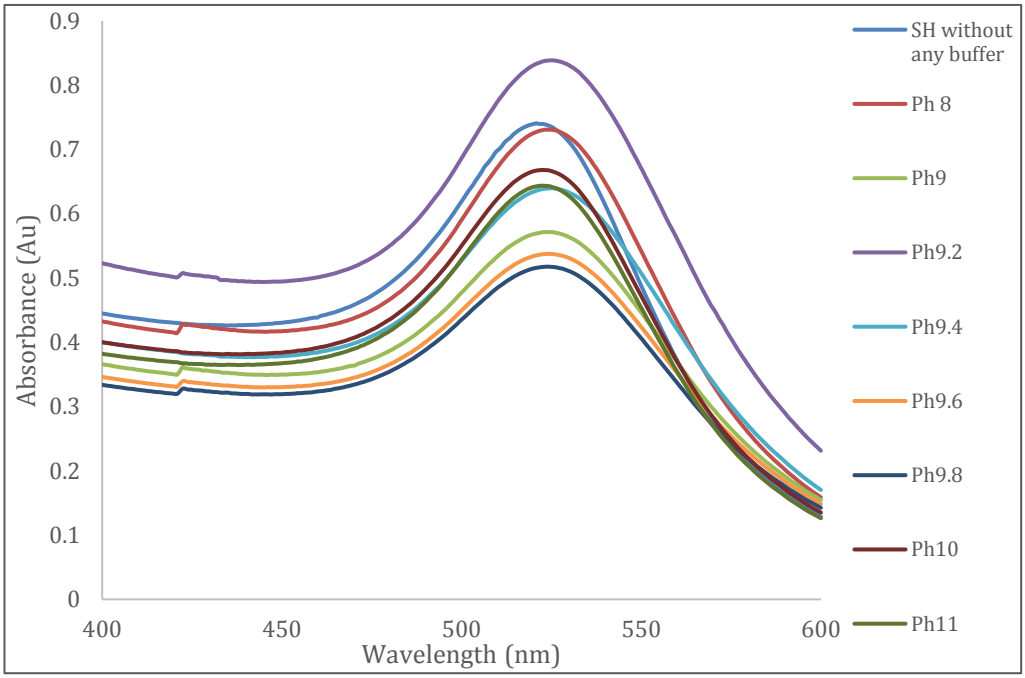

Figure 6-5 UV/Vis Absorbance spectra for AuNP SH-PEG mixed monolayer & RME after 24h in each buffer solution

Table 6-1 Changes in UV/Vis Absorbance Maxima for AuNP SH-PEG and RME at each pH

	SH-PEG & Buffer		SH-PEG, Buffer & RME		
pH	Wavelength	Absorbance	Wavelength	Absorbance	Change in Absorbance
8	522	0.92	523.6	0.73	-0.19
9	523.6	0.79	523.2	0.57	-0.21
9.2	524.4	0.74	524.8	0.83	+0.10
9.4	524	0.79	524.8	0.63	-0.15
9.6	523.6	0.73	524	0.53	-0.19
9.8	523.7	0.85	524	0.51	-0.33
10	521.8	0.80	522.4	0.66	-0.13
11	521.9	0.40	522.4	0.64	+0.24

Figure 6-5 & Figure 6-6 displays the UV/Vis spectra for AuNPs co-functionalized with PEG and RME peptide in various buffers 24 h after functionalization or at hourly intervals across a 24 h period respectively. Table 5-1 shows the results in tabular form listing the peak positions and absorbance values of the samples, both before and after co-functionalization with RME peptide.

The conjugation of these samples was investigated by comparing the UV/Vis spectra of each sample to the PEGylated AuNP prior to the peptide addition. Upon successful binding of ligands to the gold nanoparticle surface, the SPR spectra will red-shift by a few nanometers. This shift is a result of an increase in the local refractive index at the gold nanoparticle surface, and is consistent with peptide attachment. A very large upshift in peak position and a reduction in absorbance, or complete loss of the plasmon peak are indicative of AuNP aggregation (loss of colloidal stability). From Figure 6-5 and Table 5-1, it is apparent from the maintenance of a significant peak, that RME co-functionalized AuNPs demonstrated significant stability at all pH levels tested. Optimum co-functionalization was indicated via a characteristic shift in peak position occurring at a pH of 8, accompanied by a modest reduction in absorbance.

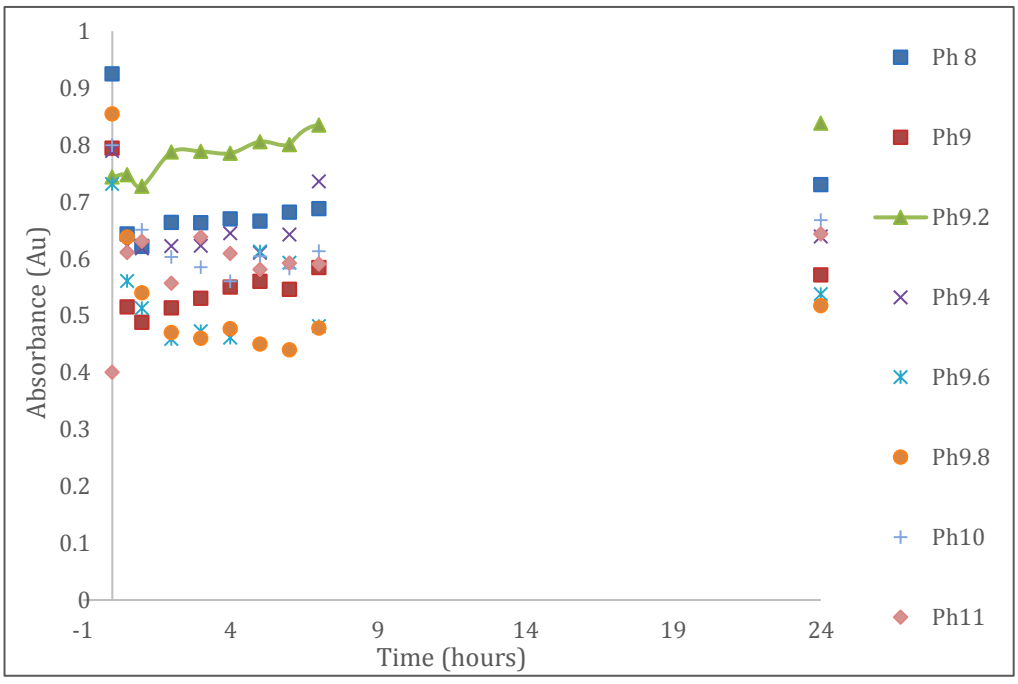

Figure 6-6 AuNP SH-PEG mixed monolayer & RME peptide monitored for 24 h using UV/Vis to identify absorbance maxima at each time point for each pH

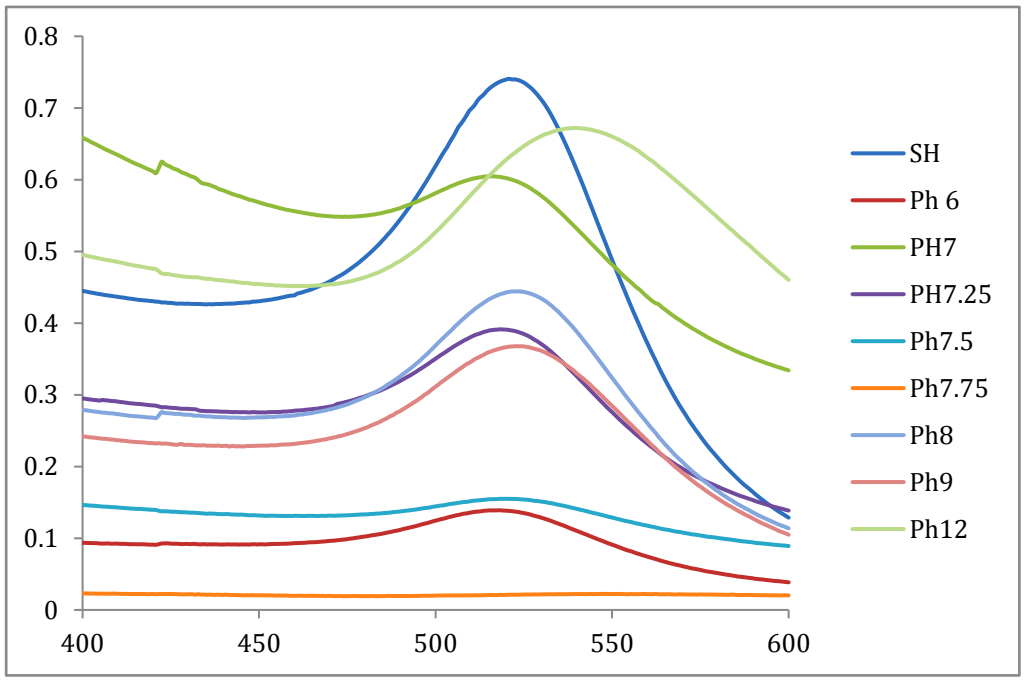

Figure 6-7 AuNP SH-PEG mixed monolayer & H5 peptide monitored for 24 h using UV/Vis to identify absorbance maxima at each time point for each pH

Table 6-2 Changes in UV/Vis maximum peak position and Absorbance for AuNP SH-PEG & H5 at each pH

	PEG & Buffer		PEG, Buffer & H5WYG		
pH	Wavelength	Absorbance	Wavelength	Absorbance	Change in Absorbance
6	517.7	0.73	518.4	0.13	-0.59
7	519.3	0.67	515.2	0.60	-0.01
7.25	518.7	0.70	518.4	0.39	-0.31
7.5	521.7	0.59	520	0.15	-0.55
7.75	520.6	0.67	548	0.02	-0.64
8	522	0.92	523.2	0.44	-0.47
9	523.6	0.79	523.2	0.36	-0.42
12	522.2	0.74	540	0.67	-0.7

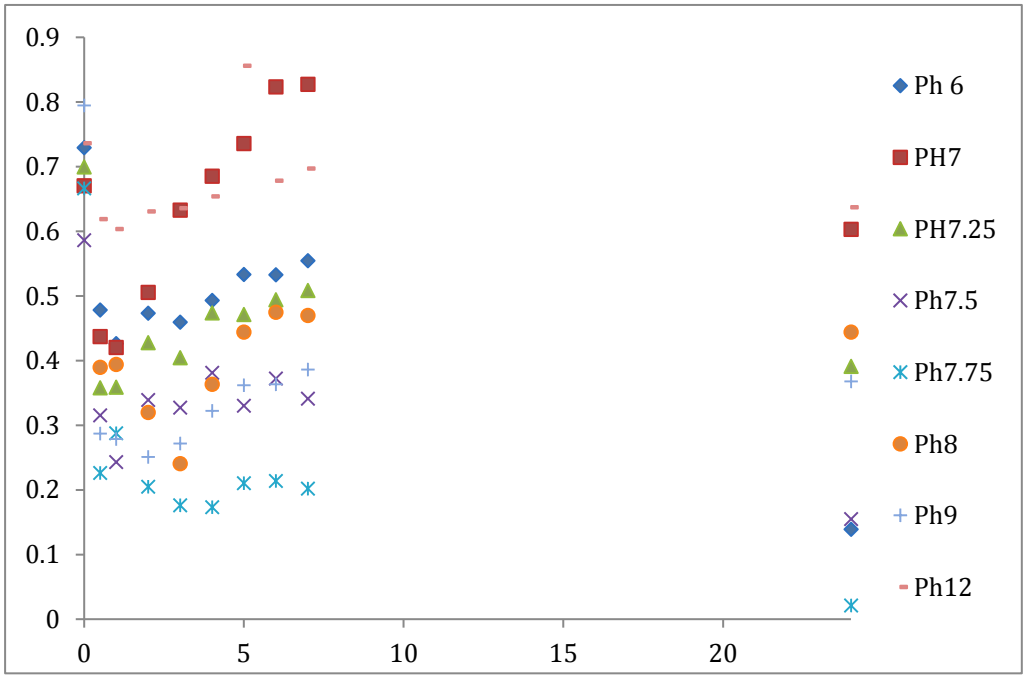

Figure 6-8 UV/Vis Absorbance Maxima for AuNP SH-PEG mixed monolayer & H5 monitored over 24h for each buffer solution

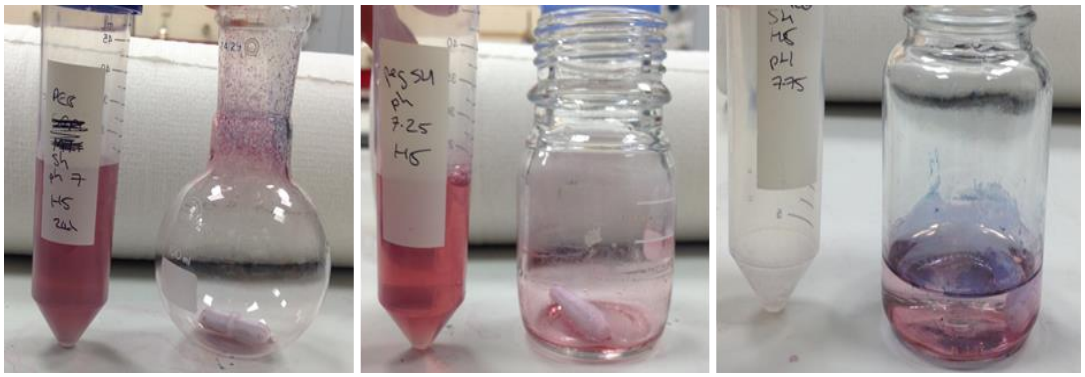

Figure 6-9 Images for AuNP SH-PEG & H5 co-functionalized AuNPs a) pH 7 b) pH 7.25 & c) pH 7.75

Figure 6-7 & Figure 6-8 display the UV/Vis absorbance spectra for AuNP SH-PEG & H5WYG at 24h and over a period of 24 h respectively. In the case of the H5WYG peptide, it can be seen that many of the buffers tested resulted in a very significant or complete loss of the plasmon peak, or a large upshift in peak position indicating aggregation. This slight broadening in the long wavelength region as a result of surface modification may suggest that a large change of surface charge caused by a change in pH affects the surface plasmon oscillation. The lack of a trend is not unexpected, as this is a multi-variable interaction, in which some constituents of the buffer solutions are not consistent across all the experiments performed and vary in a non-linear manner across pH. The constituents of the different pH buffers change dramatically with pH in comparison to chemical constituents in a neutral pH. Citric is present in the pH 6 buffer solution which may interact with the AuNP surface conjugates making a specific change to amount of citrate bound whereas the absence of citric in the borax buffer will have a different effect on the remaining AuNP surface citrate coverage. These combinations along with the differing pKas make it difficult to predict what information can be gathers about surface species and binding as multiple parameters are varying between each solution, however does serve to test if the AuNP formulation is stable from an impical point of view.

Figure 6-9 visually represents the aggregation evident from the complete loss of the SPR when re-suspended in pH 7.75 (Figure 6-9 b) and also highlights further the instabilities noticed during co-functionalization for pH 7 & 7.25 which isn't clearly evident from Figure 6-7. Interestingly the 24 h study displayed in Figure 6-8 identify a gradual decrease in absorbance for pH 7 corroborating with the discoloration evident in Figure 6-9, along with a loss of absorbance in relation to time for pH 6, 7.25, 7.5 & 7.75. Only the samples functionalized at pH 6 and 8 displayed a small (~2-3 nm) upshift in peak position; however, pH 6 was accompanied via a large change in absorbance while pH 8 maintained significant absorbance consistent with successful functionalization and colloidal stability. The sample prepared at pH 12 showed only a small drop in absorbance after peptide addition, but the upshift in peak position from 521.6 to 540 suggests a significant degree of aggregation. For both peptides, a pH of 8 (see Table 5-1 & 5-2) was concluded to be the optimum pH for successful cysteine conjugation of peptides to the nanoparticle surface. The reduced colloidal stability observed with the H5WYG peptide may be as a result of

the lower net charge of +0.4 compared to 2.9 for the RME peptide. As the AuNPs are slightly negatively charged (-5 mV) after PEGylation the higher positive charge on the RME will result in more electrostatic attraction between the RME and PEGylated AuNPs. The H5WYG will also be less stable in solution as there will be little repulsion between the peptide chains due to their low net charge. In addition, the H5WYG peptide contains a higher proportion of hydrophobic residues (namely A, F, I, L W &Y) than RME rendering the peptide less water soluble.

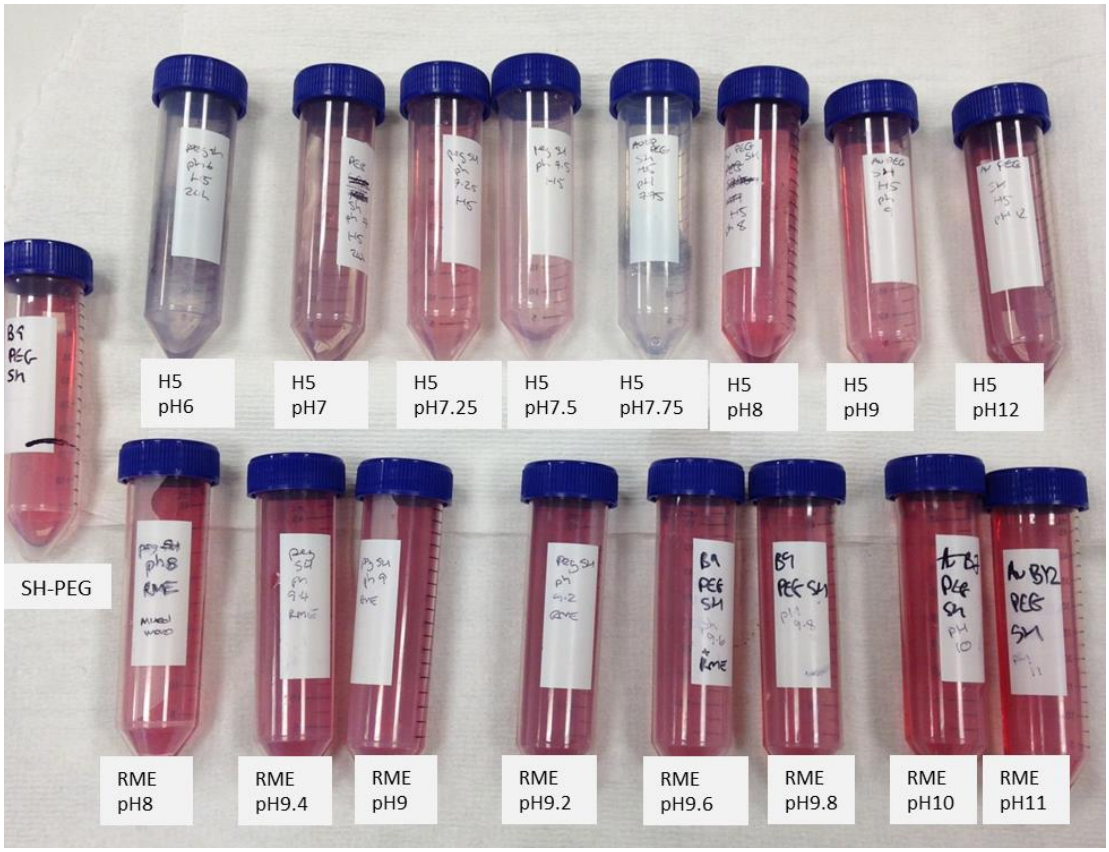

Figure 6-10 AuNP SH-PEG RME and AuNP SH-PEG H5WYG co-functionalized AuNPs in each buffer solution

Figure 6-10 shows the various RME and H5WYG (labelled H5) co-functionalized samples, visually confirming the findings from the UV/Vis analysis. Another trend observed from the addition of peptides is that there were higher levels of aggregation evident from a reduction in absorbance around the isoelectric point (pI) of the H5WYG peptide. The more highly charged nature of the RME peptide may explain the colloidal stability of the peptide at the isoelectric point. While the peptide has no

net charge at the isoelectric point, individual units will still be charged offering a degree of electrostatic repulsion. This is to be expected given Zwitterions, such as the proteins used in this study, have minimum solubility at their isoelectric point (a feature that can aid isolation via precipitation at the pI). Figure 6-10 displays this phenomenon visually with the sample functionalized with H5WYG at the isoelectric point (pH 7.75) showing a shift from red to purple and an almost complete loss of color intensity. Figure 6-10 shows the optical images of the co-functionalized AuNPs in their respective buffer solutions. Wide range colloidal stability identifies the range at which the color will not alter as a result of pH, whereas short range pH stability is indicative of a blueish taint once an adjustment has been made to outside of the pH range. The images agree with the observations made by UV/Vis.

6.2.3 DLS

All samples were characterized using DLS post synthesis and post functionalization. Table 6-3 displays the results obtained for the nanoparticle size for PEG prior and post RME addition. PEGylation was confirmed for AuNP SH-PEG via the increase in nanoparticle diameter from 17.5 d.nm to approximately 35.4 d.nm respectively which complements the results observed in chapter 4. After washing and dispersion in each buffer solution the nanoparticle diameter measurement was repeated. There was no significant difference found between nanoparticle size for AuNP SH-PEG prior to buffer and post buffer for all the samples apart from pH 11. The variations observed in particle size could be theorized to the use of a normal buffer solution. [298] Takashima *et al.* investigated the approach of surface potential estimation by altering the pH of gold nanoparticle solutions using hydrochloric acid and sodium hydroxide. The rationale of this approach was to control the potential objective ion species by limiting the possibilities to H+, Na+, OH- and Cl-. Limiting the potential ionic species minimizes the effect of ion adsorption on the particle surface which may disturb the surface charge and avoids inter-ion interaction in bulk solution. [298]

From Table 6-3 only pH 8, 9, 9.6, 9.8, 10 and 11 displayed an increase in nanoparticle size following the addition of RME peptide. Out of those pH, only pH 8, 9 & 9.6 retained a hydrodynamic diameter close to the AuNP SH-PEG control whereas pH 9.6 showed a decrease in particle size in relation to the control. Post co-

functionalization with RME peptide indicated the most significant increase in size for pH 8 in relation to the addition of RME without showing signs of loss of colloidal stability by large error bars and/or an unusual decrease in size.

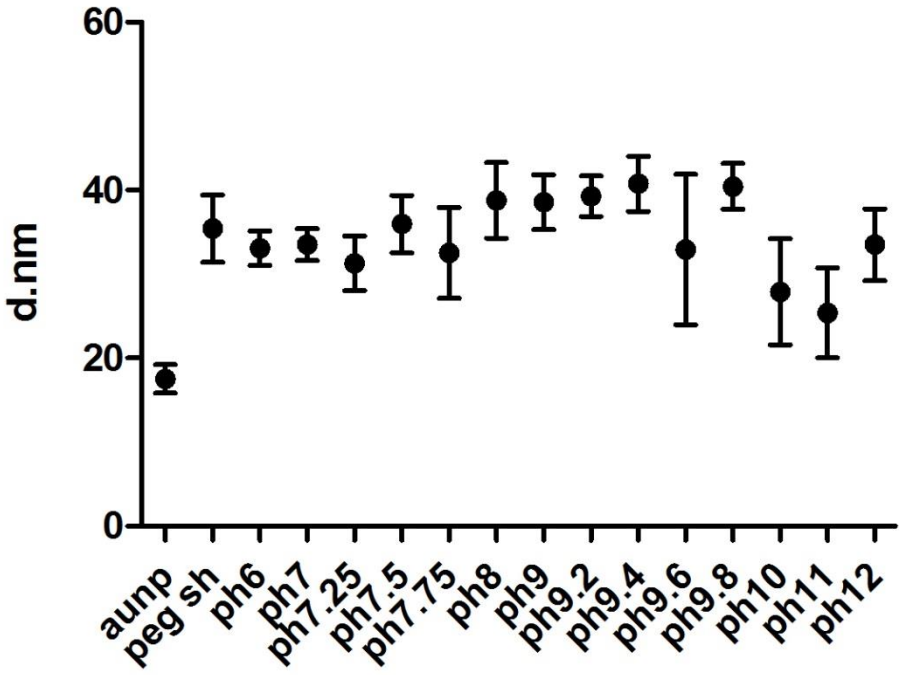

Figure 6-11 SH-PEG DLS Number average and standard error prior to peptide addition suspended in each buffer solution (n=9)

Table 6-3 DLS Number average diameter sizes for AuNP SH-PEG with RME

	prior to buffer	in buffer	with RME
Citrate capped	17.5 ± 1.7		
SH-PEG	35.41 ± 4		
pH 8		38.77 ± 4.2	43.33 ± 2.0
pH 9		38.58 ± 3.2	37.23 ± 7.8
pH 9.2		39.27 ± 2.4	36.76 ± 13.4
pH 9.4		40.76 ± 3.2	40.08 ± 2.9
pH 9.6		32.93± 9	37.6 ± 6.1
pH 9.8		40.44 ± 2.7	41.06 ± 3.5
pH 10		27.89 ± 6.3	36.78 ± 14
pH 11		24.61 ± 5.5	41.07 ± 7.7

Table 6-4 DLS Number average diameter sizes for AuNP SH-PEG with H5

	prior to buffer	in buffer	with H5
Citrate capped	17.5 ± 1.7		
SH-PEG	35.41 ± 4		
pH 6		33.07 ± 2	55.58 ± 29.7
pH 7		33.53 ± 1.9	70.33 ± 26.4
pH 7.25		31.27 ± 3.2	32 ± 13.4
pH 7.5		35.96 ± 3.4	42.3 ± 18.7
pH 7.75		32.53± 5.4	44.7 ± 13.3
pH 8		38.77 ± 4.5	39.1 ± 2.8
pH 9		38.58 ± 3.2	36.5 ± 5.6
pH 12		33.51 ± 4.2	62.7 ± 10.8

From Table 6-4 all the samples apart from pH 9 displayed an increase in nanoparticle size following the addition of H5WYG peptide. Out of those pH, only pH 7.25 & 8, displayed a moderate increase in hydrodynamic diameter however pH 7.25 showed a high degree of variability in the error bars. pH 6, 7, and 12 indicated aggregation by a large increase in hydrodynamic diameter. This aggregation was highlighted previously in Figure 6-8 and by a decrease in absorbance evident for pH 6, a decrease in wavelength for pH 7 coupled with a decrease in absorbance over time and a large peak shift to approximately 540nm for pH 12 coupled with a loss of absorbance (Figure 6-7).

6.2.4 Zeta

In solution, if pH < pK then the protonated form of an amino acid side chain predominates. This is based upon the Henderson-Hasselbalch equation. If the pH > pK then the deprotonated form of the amino acid side chain predominates. This relationship however cannot be directly applied as each peptide is bound to a negatively charged gold nanoparticle. Instead zeta potential measurements were applied to help determine colloidal stability. Ahmed *et al.* investigated the relationship between zeta potential and long term stability when suspended in solution. It was found that the zeta potential is predictive of its long-term stability and resistance to aggregation at different pH values. [297] AuNPs with a lower repulsive potential thus failing to counterbalance Van der Waals attraction, are more prone to aggregation; whereas zeta potentials of around -36.1 mV proved to show the greatest colloidal stability over a period of time. [297] Investigations into the colloidal stability of nanoparticles in a range of pH buffers also identified a stable range application for each buffer solution used. Those ranges would show clear plasmonic peaks whereas outside of the ranges the nanoparticles would display considerable decreased absorbance's or significant peak shifts. [297]

Therefore Table 5-1 & 5-2 when cross referenced with Figure 6-5 & Figure 6-7 identifies the stable ranges for the AuNPs in buffer solutions to be between a pH 8 – 12 with pH below 8 displaying a decrease in wavelength in comparison to the control and pH 7.5 displaying a drastic drop in absorbance. Once co-functionalized with RME peptide, there were no drastic changes in wavelength and/or absorbance,

illustrating that RME peptide seems to have good chemical stability in a range of buffer solutions. The results for H5WYG however indicate large peptide instability, with only pH 8 & 6 having a shift towards the red and pH 6, 7.25, 7.5 & 7.75 having drastic decreases in absorbance.

These observations then cross referenced with Table 6-5 & Table 6-6 are in agreement with the relationships investigated by Ahmed *et al.* [297] with the exception of pH 9.8.

Table 6-5 Zeta potential of AuNP SH-PEG mixed monolayer with RME

	Prior to peptide attachment		Mixed monolayer with RME		Change in Zeta
	Average	Standard Deviation	Average	Standard Deviation	
SH-PEG	-13.45	0.99			
pH 8	-17.71	10.26	-21.81	1.84	-4.11
pH 9	-14.46	2.45	-18.31	1.67	-3.86
pH 9.2	-2.54	3.46	-30.44	7.22	-27.90
pH 9.4	-9.64	2.24	-27.24	4.61	-17.61
pH 9.6	-12.99	3.00	-22.08	4.29	-9.08
pH 9.8	-15.54	3.20	-8.22	0.80	7.32
pH 10	-13.03	1.56	-21.27	3.19	-8.23
pH 11	-14.71	1.92	-32.87	3.87	-18.16

Table 6-6 Zeta Potential of AuNP SH-PEG mixed monolayer with H5

	Prior to peptide attachment		Mixed monolayer with H5		Change in Zeta
	Average	Standard Deviation	Average	Standard Deviation	
SH-PEG	-13.45	0.99			
pH 6	-7.14	1.29	-6.81	1.39	0.33
pH 7	-6.63	0.83	-3.71	1.82	-17.08
pH 7.25	-4.72	0.38	-4.02	0.40	0.70
pH 7.5	-2.38	1.69	-7.22	1.05	3.16
pH 7.75	-2.56	0.33	-7.49	1.45	-4.93
pH 8	-17.70	10.25	-19.3	3.50	-1.59
pH 9	-14.45	2.44	-10.49	3.16	3.97
pH 12	-11.19	1.33	1.59	0.95	12.79

Zeta changes displayed for the RME peptide identify all samples apart from pH 9.8 to become more negative in surface charge, this coordinates with the literature and the UV/Vis spectra for the RME co-functionalized AuNPs which displayed the largest drop in absorbance and is the most positive pH explored for this peptide. When functionalized with H5WYG, pH 8 and 9 have the most negatively zeta potential, with all the remaining pH buffers resulting in more positive zeta with pH 12 becoming +1.59 mV. Based on the conclusions drawn from the literature, this would indicate instability, which is in agreement with the conclusions observed from UV/Vis data, with the most drastic change in wavelength via UV/Vis being a result of pH 12. Therefore, for both peptides, pH 8 resulted in a more negative zeta potential indicating long term colloidal stability.

6.2.5 Fluorescence

To confirm the optimum pH for peptide attachment being approximately pH 8; a third peptide was investigated. The RGD Nrp-1 targeting peptide (CRGDK) was modified with the fluorescent ligand FITC. The AuNP SH-PEG & RGD sample was analyzed via UV/Vis in triplicate and the spectra obtained are plotted in Figure 6-12.

The UV/Vis spectra for pH 7, 8 & 8.6 display a peak at 495nm corresponding to the FITC and the characteristic peak at ~520 – 525 nm, for AuNP. For the remaining buffer solutions, due to poor colloidal stability under other pH conditions, the FITC peak dominates the spectra. [299,300]

In previous literature pure FITC has showed a wide absorption band at 480 nm and a characteristic emission peak between 495 and 650nm when excited. [299,300] For pH ranging between 7- 8.6 a weak peak corresponding to the gold nanoparticles at approximately 520 nm is clearly visible, and an adsorption band at approximately 495 nm corresponding to the FITC, with the pH 8 maintaining the highest absorption profile with respect to both AuNP and FITC. For the remaining pH (6, 9-12) there is an AuNP shoulder present, however this signal is being almost entirely masked by the FITC, overall there is a gradual decrease in the fluorescent intensity of the FITC signal observed as the pH drops towards 6.

Fluorescein has a pKa of 6.4, when the AuNP solution pH is below the pKa of the fluorescein, the protonated forms predominate and the proportion of the fluorescein molecules bound to AuNP increases. [301]

The fluorescent strength of some fluorescents appear to be different in alkaline and acidic solutions. Fluorescein is almost non-fluorescent at neutral pH and fluoresces brightly in acidic environments.[301,302] The fluorescence output per fluorophore is proportional to the product of the extinction coefficient and the quantum yield. The most important effect on the fluorescent response of fluorescein is the pH, as structurally, pH causes a reconfiguration of the fluorophores π-electron system that occurs upon protonation. Literature has shown that a change in pH of 7 to 6 can result in a 10 % drop in the relative fluorescence response pf fluorescein. [301] In acidic environments (< pH 6) the fluorescent response drops to almost 40 %. However, there are contradictions in the literature surrounding the effect on fluorescein intensity in pH solutions about ph 7. Zhu *et al.* demonstrated that the fluorescent intensity increased as the pH value increased from 6.86 to 8.43, and concluded that the stable solution pH range should be 8.43 or higher as fluorescent intensity became nearly constant when pH value was 9.10 or greater, whereas absorbance studies by Peterson in 2009 have shown that above a pH of 7.5, there

was no significant increase in absorbance for increasing pH compared to a neutral pH. [301] Diehl *et al.* found similar results, the UV/Vis absorbance maxima first fell rapidly as the pH rises from 0.15, reaching a minimum at pH 3.63, then increases to a maximum at pH 5.3, and finally falls to steady value at pH > 8.0.[303]

Initially, pH 7, 8 & 8.6 maintains the highest absorption profile with respect to both AuNP and FITC. For pH values of 6 & 9-12 there is no AuNP signal present, overall there is a gradual decrease in the fluorescent intensity due to the absorbed FITC as the pH drops towards 6. However, after 24 h the absorption profile for pH 7 greatly diminishes with only the sample prepared at a pH of 8 retaining the characteristic profile of AuNP at 520 nm. For the remaining samples only the absorption peak at approximately 495nm is apparent.

Therefore, while it can be postulated that the increase in the FITC signal when conjugated to AuNPs as the pH drops to pH 6 is due to the unsuccessfully conjugated FITC outweighing the absorption signal from the AuNPs, it must be considered that this is a direct response of the FITC to the slightly acidic pH. However contrary to this, due to the evidence that a of pH 7+ does not adversely affect the fluorescent signal from the FITC, it can be concluded that the masked signals for pH 9-12 are a result of conjugation to the AuNP surface, and the highest absorption profile for the FITC at pH 8 is most likely due to the enhanced binding efficiency of the RGD peptide to the AuNP surface (i.e. resulting in more FITC present on the AuNP surface), and not a decrease in quantum efficiency (Equation 3-14).

It is also noteworthy that a loss of colloidal stability was not observed at the isoelectric point of 8.6. This may be due to the high solubility of the peptide. Short peptides are inherently highly water soluble and the sequence containing a high proportion of hydrophilic residues and no hydrophobic residues. The addition of the water soluble FITC tag may also have increased the colloidal stability of the peptide at the pI.

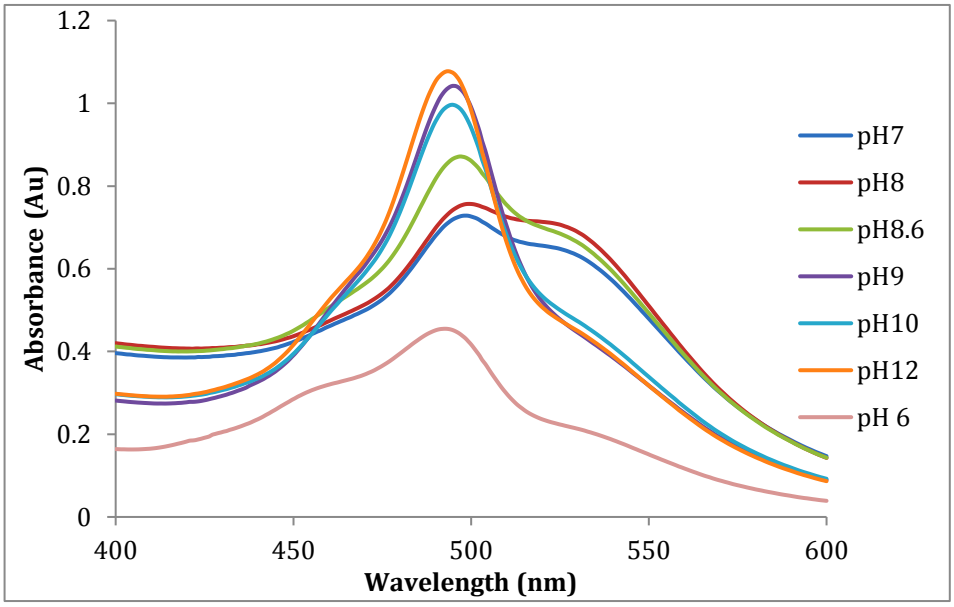

Figure 6-12 – UV/Vis absorbance spectra of the FITC tag on the AuNP SH-PEG & RGD peptide in a range of buffer solutions, pH 6 (pink), pH 7 (dark blue), pH 8 (red), pH 8.6 (green), pH 9 (purple), pH 10 (light blue), and pH 12 (orange) after 1 hour

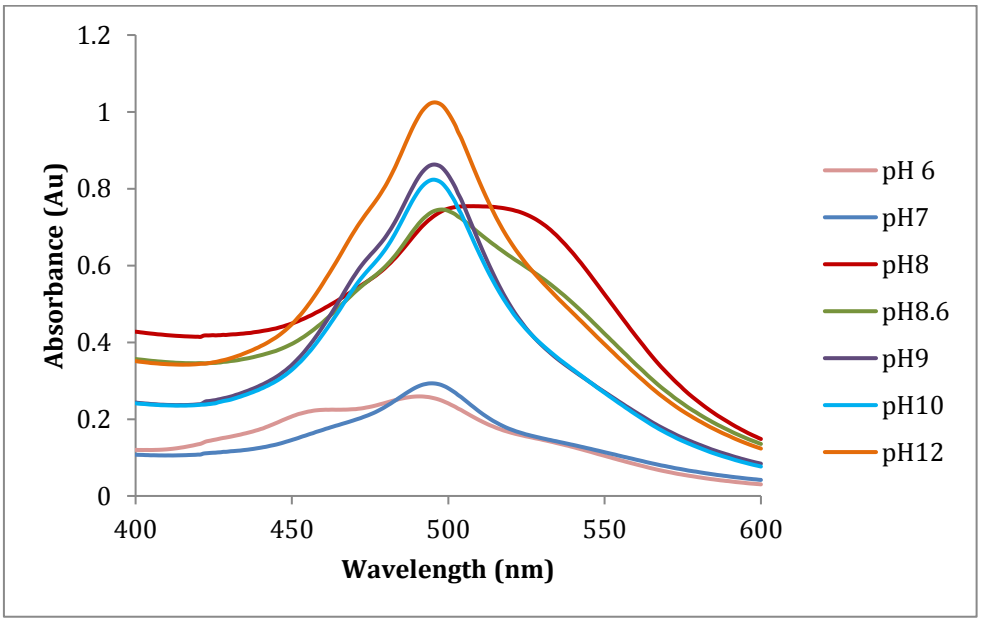

Figure 6-13 UV/Vis absorbance spectra of the FITC tag on the AuNP SH-PEG & RGD peptide in a range of buffer solutions, pH 6 (pink), pH 7 (dark blue), pH 8 (red), pH 8.6 (green), pH 9 (purple), pH 10 (light blue), and pH 12 (orange) at 24 hours after addition

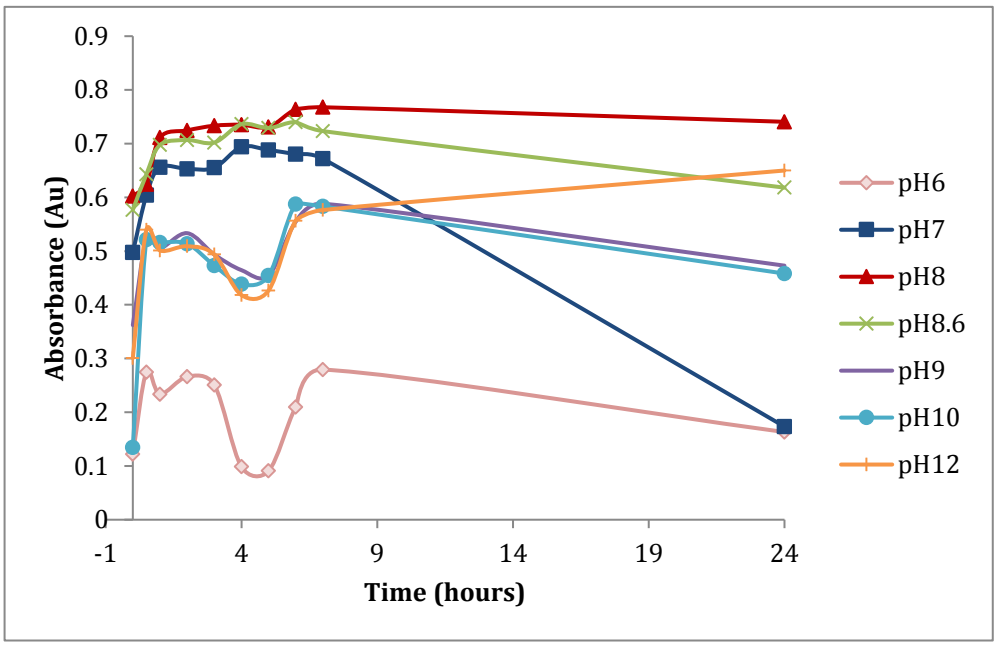

Figure 6-14 UV/Vis absorbance spectra of the FITC tag on the AuNP SH-PEG & RGD peptide in a range of buffer solutions, pH 6 (pink), pH 7 (dark blue), pH 8 (red), pH 8.6 (green), pH 9 (purple), pH 10 (light blue), and pH 12 (orange) tracking the SPR maximum over 24 h

Table 6-7 Changes in UV/Vis Absorbance Maxima peak position and Absorbance for each pH for RGD peptide

	PEG & Buffer		PEG, Buffer & H5			
pH	Wavelength	Absorbance	Wavelength	Absorbance	Peak shift	Change in Absorbance
6	520.8	0.12	490.4	0.26	-30.40	0.14
7	520.00	0.50	494.4	0.29	-25.60	-0.20
8	522.40	0.60	508	0.75	-14.40	0.15
8.6	520.80	0.58	498.4	0.75	-22.40	0.17
9	521.6	0.36	495.2	0.86	-26.40	0.50
10	522.4	0.13	495.2	0.82	-27.20	0.69
12	520.8	0.30	496	1.02	-24.80	0.72

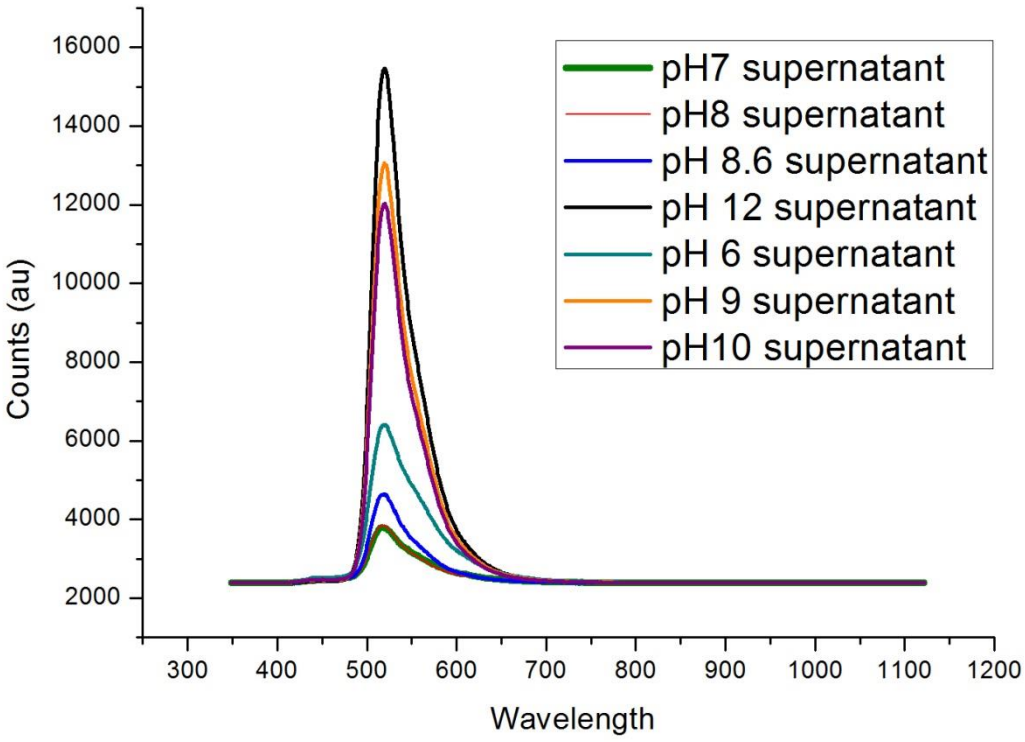

Figure 6-15 Fluorescent emission spectra for the AuNP SH-PEG & RGD (FITC tagged) supernatant

Figure 6-15 shows the fluorescence spectra of the supernatants after centrifugal removal of the FITC labelled RGD and SH-PEG capped AuNPs. After co-functionalization with the RGD peptide in a range of buffer solutions, the samples were centrifuged in 1.5 ml eppendorf's at 10,000 RPM for 30min, to remove the co-functionalized AuNPs. [296] The amount of unbound free FITC labeled RGD peptide following centrifugation was determined from the fluorescent intensity of FITC left in the supernatant. A clear emission peak was noted around 520nm for all sample types. This is typical for green fluorescein FITC. [299,300] At pH 9-12 there were high intensities of fluorescing FITC found in the supernatant, consequently indicating large amounts of unbound peptide. Whereas pH 6 - 8.6 had significantly lower intensities, with pH 7 and 8 having the lowest intensity. These results confirm optimal attachment at pH values of 7 & 8 reaffirming the result observed with the RME and H5WYG peptides, however due to the instabilities identified previously, of the buffers tested, pH 8 has been identified as being the most effective for attaching the peptide.

6.2.6 Protein Concentrations

Photoluminescence could not be used to confirm binding for the remaining two peptides due to the lack of a fluorescent tag, therefore to confirm optimized binding efficiency at pH 8; protein estimation was carried out using a Micro BCA Protein Assay Kit for the RME and H5WYG peptides at a pH range of 6, 8 & 10. Although biuret based protein assays are theoretically applicable to peptide measurement, there is a high level of inter-peptide variation, determined largely by peptide hydrophobicity. This variation in peptide reactivity can be significantly reduced by heat-denaturation of peptides at 95 °C for 5 min in the presence of 0.1M NaOH containing 1% (w/v) SDS, therefore prior to incubation with BCA, each peptide was denatured at 90°C. [304]

1 ml of each sample was retained for analysis, each sample was aliquoted into 1.5 ml Eppendorf tubes and centrifuged at 10,000 RPM for 30minutes. 900µl of the supernatant was then removed and labelled as the supernatant counterpart to be measured. The remaining pellet was re-dispersed. 100µl of each peptide 'as synthesized', after centrifugation, and their respective supernatant, were pipetted into

a 96 well plate in quadruplicate. After incubating the assays for the time specified in the kit; the absorbance was measured at 562 nm and the OD was converted to concentration (µg/ml) using the standard curve generated from BSA. The results for both peptides are displayed in Table 6-8.

Table 6-8 Protein estimation via BCA for H5 and RME peptide at pH 6, 8 & 10

H5			
pH	Before (µg/ml)	Supernatant (µg/ml)	% in supernatant
6	5.75	1.11	19%
8	5.82	0.58	10%
10	5.62	1.03	18%
RME			
6	5.59	1.6	29%
8	6.6	1.5	23%
10	6.57	1.99	30%

The average amount of H5 peptide added was calculated to be ~ 5.73 µg/ml. Approximately 19 and 18 % of the peptide added was measured in the supernatant for the samples functionalized at a pH of 6 & 10 respectively; whereas only 10% of the overall peptide added was found to be present in the supernatant for pH 8. Thus, indicating that the remaining 5.24 µg/ml had successfully attached to the AuNPs in comparison to the 4.64 µg/ml and 4.59 µg/ml for pH 6 and 10 respectively. A similar trend was observed for the RME peptide. Lower attachment percentages were observed in general for RME peptide in comparison to the H5WYG, however it was still apparent that the most efficient attachment occurred at a pH of 8. This confirms that for the pH levels tested, a pH of 8 results in the most efficient attachment for all three peptides.

6.2.7 Long Term Colloidal Stability

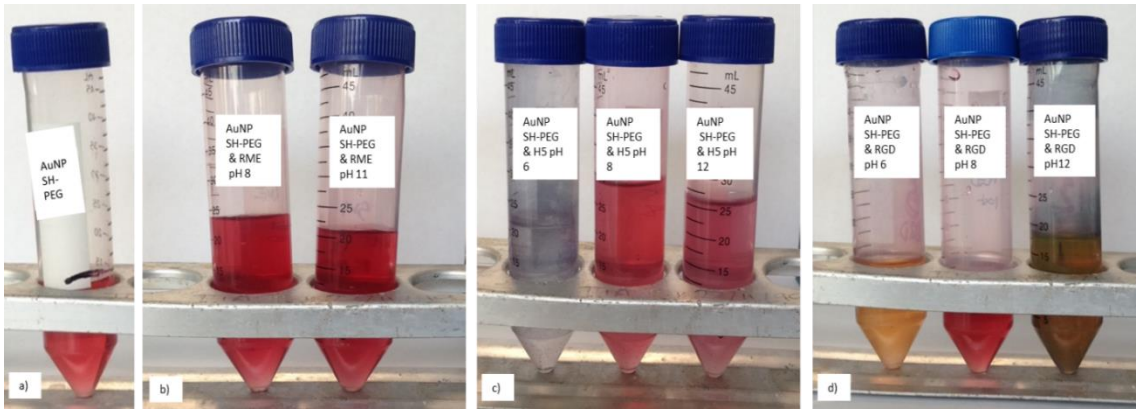

Figure 6-16 Images of AuNP SH-PEG (a), AuNP SH-PEG & RME (b), AuNP SH-PEG & H5 (c) and AuNP SH-PEG & RGD (d) all at pH 6, 8 and 10 (left to right)

After a period of 28 days under dark ambient conditions Figure 6-16, the AuNP solutions were imaged to monitor long term stability, with changes in solution color indicative of aggregation. When compared to the AuNP SH-PEG control with varying degrees of aggregation observed at pH values distant from this optimal pH across the three peptide types of RME, H5WYG and RGD. It is evident that AuNPs co-functionalized at a pH of 8 showed minimal changes in color, consistent with other previous measurements investigating initial surface functionalization

6.3 Discussion

This chapter investigated the effect of pH on binding efficiency of three peptides to SH-PEG functionalized AuNPs using either citric acid/sodium hydroxide buffer solution (pH 6), a borax/sodium hydroxide buffer solution (pH 8 or pH 10) and/or a di-sodium hydrogen phosphate/sodium hydroxide buffer solution (pH 12). All of these buffer solutions were then altered with sodium hydroxide or hydrochloric acid to obtain the desired intermediate pH ranges.

The peptides chosen all contain thiol groups and amine groups for functionalization to the AuNP surface, however it is expected that the chosen peptides will all coordinate to the AuNP surface through the thiol due to the much higher binding

affinity of thiol groups to Au (40 – 50 kcal/mol^{-1}), than amine groups to gold (8 kcal/mol^{-1}). [305,306]

The binding efficiency of a ligand to the AuNP surface is dependent on AuNP size, the length of the ligands, the rotational flexibility of the bond, steric effects as well as the type of bonding used in the coupling chemistry. [296,298] As previously reported there are several strategies for conjugation of peptides and proteins to AuNPs resulting in distinct types of binding. Van der Waal forces and hydrogen bridges result in weak binding forces between the conjugate and nanoparticle (NP), whereas covalent bonding produces stronger conjugation. [296,298] For any of these binding modes to occur, repulsion between the AuNP and ligand should be minimized in a manner that maintains repulsion between the individual particles – which is essential to minimize aggregation. pH may play an important role in this, altering the pH can alter the surface charge, therefore by producing a positively charged ligand, opposite surface charges will be induced between the ligand and the negative surface potential of the citrate capped AuNP (- 30 mV), thus enhancing the binding efficiency.

When altering the pH, consideration must be given to the isoelectric point (pI) of the peptide. Peptides are composed of a sequence of up to 100 amino residues, all of which contain amine groups and carboxyls and some of which contain unique side chains. All of these functional groups have the potential to interact with the AuNP surface in some form. Therefore the dissociation constant (pK) of the various functional groups in each amino acid sequence should be considered. The total pK values for the remaining 'free' reactive groups found on the amino acids vary between 6.7 – 8.7, however the pK values for the individual cysteine residues are 1.71, 8.33 and 10.78 for the carboxyl, ammonium and thiol group respectively. While Glycine has pK values of 2.34 and 9.6 and for the carboxyl and amine groups respectively. [269,307]

The results from the UV/Vis analysis identified optimum co-functionalization for both RME and H5WYG peptides at a pH of 8 via a characteristic shift in peak position occurring, accompanied by a modest reduction in absorbance. UV/Vis analysis of the H5WYG peptide demonstrated that many of the buffers tested

resulted in a significant or complete loss of the plasmon peak, or a large upshift in peak position indicating aggregation. This slight broadening in the long wavelength region as a result of surface modification may suggest that a large change of surface zeta potential caused by a change in pH affects the surface plasmon oscillation. DLS number averages demonstrated that suspension in pH 8 buffer solutions resulted in the largest increase in hydrodynamic diameter in relation to co-functionalization with either RME or H5 peptide without showing signs of loss of colloidal stability by large error bars, and zeta potential measurements for both peptides resulted in a more negative zeta potential at a pH of 8, indicating long term colloidal stability. Fluorescent spectra of the supernatants following centrifugal removal of the FITC labelled RGD peptide demonstrated the intensity of unbound free FITC A clear emission peak was noted around 520nm for all sample types. This is typical for green fluorescein FITC. [299,300] Of the buffer solutions testing, a pH of 7 and 8 having the lowest intensity. The correlates to the least amount of FITC present in the supernatant due to the optimum binding resultant of the pH in comparison to the remaining samples. While some onsidratio has to be givent o the effect of h on the quantum yield of the FITC fluorescent, literature has agreed that fluorescein concentration increased with increasing pH, and there was not a significant increase in absorbance above pH 7.5, and as such these results confirm optimal attachment at pH values of 7 & 8 reaffirming the result observed with the RME and H5WYG peptides, however due to the colloidal and chemical instabilities identified previously, of the buffers tested, pH 8 has been identified as being the most effective for attaching the three peptides chosen for this Thesis. [301,302] [303]

6.4 Conclusions

pH plays a critical role in controlling peptide binding and subsequent protein modified AuNPs colloidal stability; PEG capped AuNPs are stable between pH values of ~6 - 12. Citrate capped AuNPs have a zeta potential of approximately -30 mV, therefore to initiate binding between Au and the ligand required it must be oppositely charged. This can be obtained by shifting the solution pH by a buffer to a pH value above the pKa value of the gold nanoparticle (6.3 is the pKa of the AuNP

functionalized surface with citrate dominating the pKa) but below the pKa value of the chosen peptide. Adjusting the pH to ~8 optimizes cysteine binding, but care should be taken to avoid the pI of the peptide as this may lead to colloidal instability. This method of peptide attachment can be used to synthesize AuNPs capped with PEG and one or more peptides, allowing the synthesis of stable AuNPs with the desired biological activity. However, it may not always be possible to synthesize stable peptide modified AuNPs by selecting a pH in the region of 8. If this pH is close to the pI value of the peptide used for surface modification the material may show limited colloidal stability under such conditions. The net charge and water solubility of the peptide used in surface modification are also crucial factors contributing to protein functionalized AuNP stability.

This chapter therefore suggests that the cysteine – AuNP binding efficiency is optimized at a pH of 8 for these three peptides. This chapter builds upon the results obtained through chapter 4 that careful consideration must be given to the method of binding when using a peptide containing a thiol due to the strength of the thiol bond.

7. CONCLUSIONS & RECOMMENDATIONS FOR FUTURE WORK

7.1 Conclusion

This Thesis has focused on the methods and characterization techniques which must be employed to facilitate and confirm the successful synthesis of a AuNP therapeutic system utilizing a bifunctional linker. This Thesis also served to address the uncertainty in the literature surrounding surface functionalization, on whether a chosen surface arrangement could elicit a more favorable biological response, in the form of improved colloidal in-vitro stability, potential toxicity, and if one method of co-functionalizing a AuNP could result in an enhanced peptide response (improved internalization and/or enhanced radiosensitivity).

In a previous publication, the author attempted to directly compare the mixed monolayer arrangement to utilizing a PEG linker. In this aforementioned paper, AuNPs were functionalized with either mono-functional SH-PEG, or bifunctional SH-PEG-SGA, and co-functionalized with RME peptide which had been dissolved in distilled water. The resultant nanoparticles were then compared directly to investigate the effects on stability, non-specific protein adsorption and cellular uptake (emma material science). In this previous publication little differences were observed between the two approaches, with both offering similar levels of stability, non-specific protein absorption and cellular uptake. However, new analysis which is described throughout this Thesis has shown that in the case of the samples synthesized using a PEG linker, the thiol containing RME peptide had bound directly onto the AuNP surface rather than onto the end of the bifunctional PEG linker. Such binding of the peptide directly to the gold surface would lead to the synthesis of another mixed monolayer arrangement rather than the utilization of the intended PEG linker. As described in chapter 4, it was discovered that the NHS ester end of the bifunctional PEG had hydrolyzed in water, and was therefore unavailable for peptide attachment. This issue was overcome with the use of DMSO and the H5WYG peptide, leading to the successful preparation of functionalized AuNPs

using the bifunctional PEG linker, the published results have since been challenged with the recent submission of a paper which addresses the difficulties encountered when synthesizing an AuNP using a linker.

The research reported here has sought to investigate the role of surface functionalization and to identify peptides which can be utilized to initiate a biological response (internalization, radiosensitivity, enhanced stability *in vitro*, ability to resist non-specific protein adsorption) and to challenge to hypothesis identified in the literature, the using a linker could potentially result in an 'anti-PEG' effect. To conclude if one method of AuNP sample preparation would elicit a more desirable biological response than the other, AuNPs were capped with either the mono-functional SH-PEG or the bifunctional SH-PEG-SGA, and co-functionalized sequentially using the endosomal escape peptide, H5WYG ((H5), (GLFHAIAHFIHGGWHGLIHGWYG. FTIR, DLS and UV/Vis were the central characterization techniques used throughout this Thesis for confirming gold nanoparticle functionalization. Thiol sensitive probes became paramount in confirming the surface arrangement.

Colloidal stability was investigated by mimicking physiological salt concentrations and the biological effect was determined using cell viability assays, cellular internalization and clonogenic survival assays to measure the radiosensitizing response as a result of AuNP functionalization. The initial 'anti-PEG' hypothesis was disproved when both the linker and mixed monolayer formation showed nanoparticle stability in high ionic strengths; the mixed monolayer was surprisingly more prone to non-specific protein adsorption in comparison to using a linker.

Cell internalization studies indicated that for both the PC3 and DU145 cell lines a significant increase is evident for the AuNP SH-PEG-SGA & H5 (Bifunctional linker) samples in comparison to the PEGylated counterpart (P value of 0.0329 and 0.003 for the PC3 and the DU145 cell lines respectively). This increase offered an almost 30-fold increase in internalization for the DU145 cell lines and a 14-fold increase for the PC3 cell lines. The level of uptake for the DU145 linker samples is similar to the level previously experienced via the RME peptide in the

aforementioned publication, peaking at approximately 0.7pg. The DU145 cell lines indicate a statistical difference for internalization between the mixed monolayer, indicating that the linker has elicited a higher internalization response for both cell lines with an overall F value of 181.8 and a P value of 0.0095 ($P < 0.05$) for the DU145 cell lines resulting in over 3 times the amount of gold within the cells, identifying significant difference between the mixed monolayer versus linker arrangement.

The results from the clonogenic survival assays demonstrated that functionalization with SH-PEG-SGA and SH-PEG-SGA & H5 peptide resulted in SERS of 1.07 and 1.21, demonstrating an 7% and 21% increase in radiosensitivity respectively, with the Survival fraction of the linker at 4 Gy being 48% lower for the linker than the mixed monolayer arrangement. The results have indicated that the synthesis of a linker using a H5 peptide has resulted in a significant increase in the effectiveness of radiotherapy when compared to the control. (P value = 0.01).

Due to the necessity to dissolve the SH-PEG-SGA and peptide in DMSO to facilitate the synthesis of a linker, the mixed monolayer arrangement was brought forward to investigate the last phase of this Thesis, which was investigating if there was an optimum pH which would improve peptide binding efficiency. pH plays an important role in controlling ligand attachment; however it was not possible to predict an optimum pH for attaching a particular peptide. The ability to optimize the ligand attachment by altering the pH may have the benefit of being able to maximize the binding efficiency with the nanoparticle. Functionalization is commonly achieved via electrostatic charge attachment, gold has a zeta potential of approximately -30 mV therefore an opposite charge is required to initiate binding between the Au and the desired ligand. This desired difference in charge was hypothesized to be obtained by shifting the solution pH by a buffer to a pH value above the pKa value of citrate capped gold (6.3) but below the pKa value of the chosen peptide. It was hypothesized that a slightly acidic buffer solution would elicit a positive charge of the peptides and therefore synthesize a higher binding affinity towards the negatively charged gold nanoparticle.

It was concluded that adjusting the pH to ~8 optimizes cysteine binding, but care should be taken to avoid the pI of the peptide as this may lead to colloidal instability. This method of peptide attachment can be used to synthesize AuNPs capped with PEG and one or more peptides, allowing the synthesis of stable AuNPs with the desired biological activity.

In terms of a definitive conclusion being drawn as to one surface arrangement over another, the data presented in this Thesis has highlighted the difficulty of synthesizing an AuNP system using a linker, and the need for an in-depth characterization portfolio. The mixed monolayer arrangement offers equal colloidal stability to the linker; however the studies in this Thesis have indicated that the bifunctional linker resulted in enhanced internalization and radiosensitivity. As such it can be concluded that a linker should be used going forward as it offers enhanced bioavailability and accessibility to cellular receptors while providing stability equivalent to that of the mixed monolayer, and improved resistance to non-specific protein adsorption. Optimizing peptide attachment is heavily dependent on the peptides chosen, while it has been shown that a pH of 8 satisfies the three cysteine containing peptides outlined in this body of work, if an efficient linker methodology is to be adopted, then careful thought must be applied to the solvent in which the AuNP is to be suspended in.

7.2 Future work

From the results presented in this Thesis, it is hypothesized that future challenges when utilizing the synthesis of a linker will revolve around the addition of peptides when one or more ligands are thiol-containing molecules. One of the main choices for the use of gold nanoparticles is their ease of functionality; therefore any aversion to the utilization of thiols moving forward is not ideal. As such it is the recommendation that future work will focus on synthesizing a sample like the H5 sample explored, containing the cysteine residue, but one which is stable in water. It is also recommended that a linker methodology be employed using an internalization peptide (thiol free) for a better determination of the effect of direct cell contact, as while the H5 peptide investigated adversely results in internalization, it’s primary

function is for endosomal escape, and as such does not give a concrete conclusion on the efficiency of uptake by using a linker.

Other means to synthesize a linker are recommended, such as the using of biotin and avidin (or Neutravidin) coupling systems, it is proposed by the author of this Thesis that a complex of two targeting mechanisms, primarily the RGD peptide identified within this work which targets Nrp-1 receptors found on cancerous cells, and PSMA 617, a prostate specific membrane antigen when combined, will allow effective active targeting. Or as illustrated in Figure 7-1 a complex of a photosensitizer and targeting mechanism, as the internalization data throughout this body of work does not indicate that internalization correlates to enhanced radiotherapy.

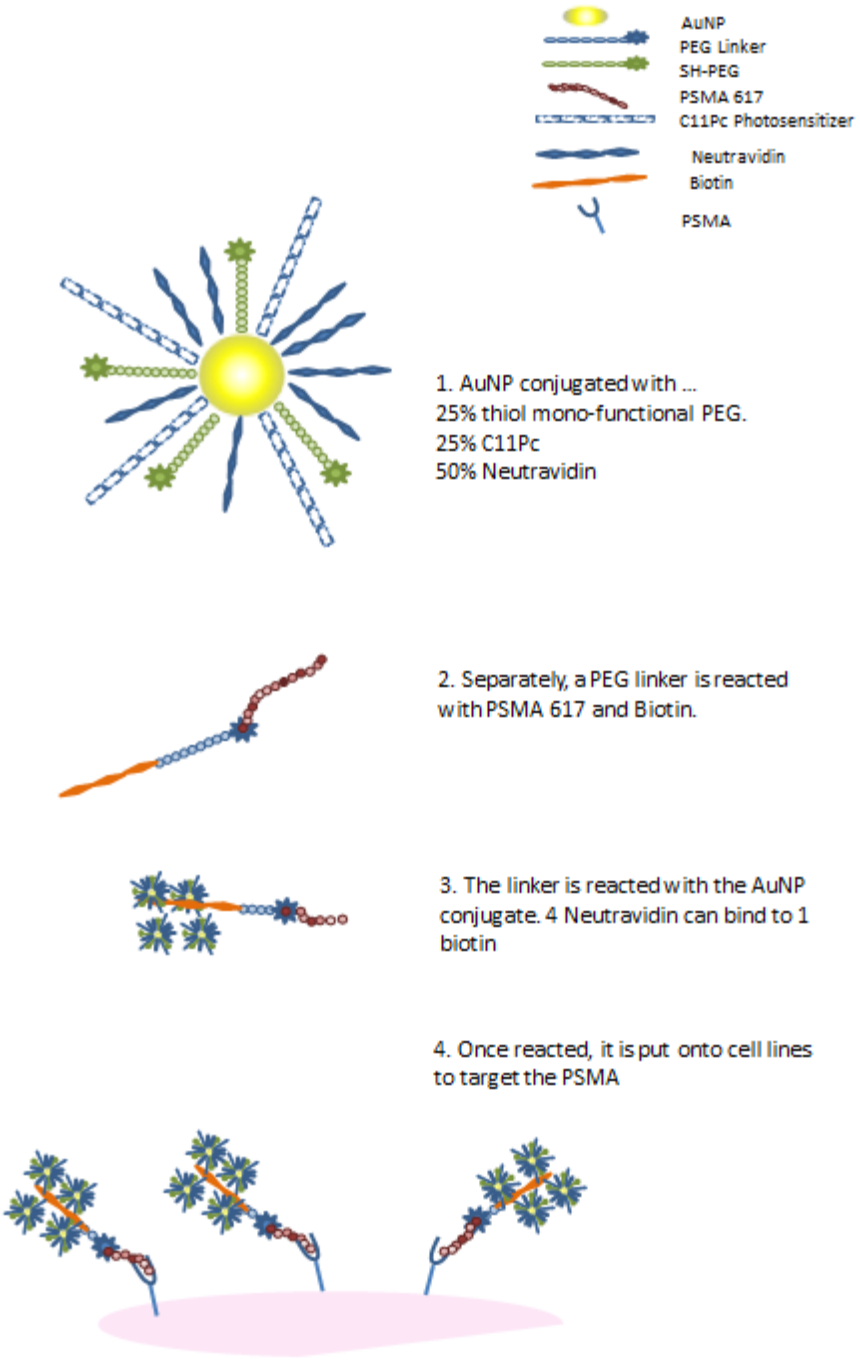

Figure 7-1 Illustration of a AuNP active targeting and photosensitizing AuNP complex for potential future work

8. REFERENCES

[1] D. Pissuwan, T. Niidome, M. B. Cortie, *J. Control. Release* **2011**, *149*, 65.

[2] S. Rosa, C. Connolly, G. Schettino, K. T. Butterworth, K. M. Prise, *Cancer Nanotechnol.* **2017**, *8*, 2.

[3] NIST, "X-Ray Mass Attenuation Coefficients," can be found under https://www.nist.gov/pml/x-ray-mass-attenuation-coefficients, **2012**.

[4] Yugang Sun, and Brian T. Mayers, Y. Xia*, **2002**, DOI 10.1021/NL025531V.

[5] Yu-Ying Yu, Ser-Sing Chang, and Chien-Liang Lee, C. R. C. Wang*, **1997**, DOI 10.1021/JP971656Q.

[6] N. R. Jana, L. Gearheart, C. J. Murphy, *Adv. Mater.* **2001**, *13*, 1389.

[7] B. N. and, M. A. El-Sayed*, **2003**, DOI 10.1021/CM020732L.

[8] C. Loo, A. Lin, L. Hirsch, M.-H. Lee, J. Barton, N. Halas, J. West, R. Drezek, *Technol. Cancer Res. Treat.* **2004**, *3*, 33.

[9] X. Huang, S. Neretina, M. A. El-Sayed, *Adv. Mater.* **2009**, *21*, 4880.

[10] M. Hu, J. Chen, Z.-Y. Li, L. Au, G. V. Hartland, X. Li, M. Marquez, Y. Xia, *Chem. Soc. Rev.* **2006**, *35*, 1084.

[11] S. . Oldenburg, R. . Averitt, S. . Westcott, N. . Halas, *Chem. Phys. Lett.* **1998**, *288*, 243.

[12] D. Kumar, Meenan, Dixon, *Int. J. Nanomedicine* **2012**, *7*, 4007.

[13] R. Hong, G. Han, J. M. Fernández, B. Kim, N. S. Forbes, V. M. Rotello, *J. Am. Chem. Soc.* **2006**, *128*, 1078.

[14] S. Barua, S. Mitragotri, *Nano Today* **2014**, *9*, 223.

[15] "What Is Cancer? - National Cancer Institute," can be found under http://www.cancer.gov/cancertopics/cancerlibrary/what-is-cancer, **n.d.**

[16] "Prostate Cancer - National Cancer Institute," can be found under http://www.cancer.gov/cancertopics/types/prostate, **n.d.**

[17] "Cancer of the Prostate - SEER Stat Fact Sheets," can be found under http://seer.cancer.gov/statfacts/html/prost.html, **n.d.**

[18] K. Miller, R. Siegel, A. Jemal, *Cancer Treatment & Survivorship Facts & Figures 2016*, **2016**.

[19] N. Ahmed, H. Fessi, A. Elaissari, *Drug Discov. Today* **2012**, *17*, 928.

[20] Q. a Pankhurst, J. Connolly, S. K. Jones, J. Dobson, *J. Phys. D. Appl. Phys.* **2003**, *36*, R167.

[21] E. Harrison, J. A. Coulter, D. Dixon, *Nanomedicine* **2016**, *11*, 851.

[22] K. Y. Lin, E. J. Kwon, J. H. Lo, S. N. Bhatia, *Nano Today* **2014**, *9*, 550.

[23] E. Pérez-Herrero, A. Fernández-Medarde, *Eur. J. Pharm. Biopharm.* **2015**, *93*, 52.

[24] N. T. K. Thanh, L. A. W. Green, *Nano Today* **2010**, *5*, 213.

[25] C. A. S. Batista, R. G. Larson, N. A. Kotov, *Science* **2015**, *350*, 1242477.

[26] S. Avvakumova, Gold Nanoconjugates : Preparation , Characterisation and Biological Applications Svetlana Avvakumova, Università degli Studi di Milano, **2012**.

[27] W. Cai, X. Chen, *Small* **2007**, *3*, 1840.

[28] A. M. Alkilany, C. J. Murphy, *J. Nanoparticle Res.* **2010**, *12*, 2313.

[29] McGraw-Hill, *McGraw-Hill Dict. Sci. Tech. Terms, 6E.* **2003**, *6E*.

[30] P. Zhao, N. Li, D. Astruc, *Coord. Chem. Rev.* **2013**, *257*, 638.

[31] W. H. Weber, G. W. Ford, *Opt. Lett.* **1981**, *6*, 122.

[32] V. Mondes, E. Antonsson, J. Plenge, C. Raschpichler, I. Halfpap, A. Menski, C. Graf, M. F. Kling, E. Rühl, *Appl. Phys. B* **2016**, *122*, 155.

[33] F. S. Rosarin, S. Mirunalini, *J. Bioanal. Biomed.* **2011**, *3*, 85.

[34] L. Zhang, F. Gu, J. Chan, A. Wang, R. Langer, O. Farokhzad, *Clin. Pharmacol. Ther.* **2008**, *83*, 761.

[35] C. H. J. Choi, C. A. Alabi, P. Webster, M. E. Davis, *Proc. Natl. Acad. Sci.* **2010**, *107*, 1235.

[36] R. Duncan, *Nat. Rev. Drug Discov.* **2003**, *2*, 347.

[37] R. Duncan, *Nat. Rev. Cancer* **2006**, *6*, 688.

[38] L. Bildstein, C. Dubernet, P. Couvreur, *Adv. Drug Deliv. Rev.* **2011**, *63*, 3.

[39] N. Goodarzi, R. Varshochian, G. Kamalinia, F. Atyabi, R. Dinarvand, *Carbohydr. Polym.* **2013**, *92*, 1280.

[40] Y. Malam, M. Loizidou, A. M. Seifalian, *Trends Pharmacol. Sci.* **2009**, *30*, 592.

[41] E. Blanco, A. Hsiao, A. P. Mann, M. G. Landry, F. Meric-Bernstam, M. Ferrari, *Cancer Sci.* **2011**, *102*, 1247.

[42] H. Nagai, Y. Okazaki, S. H. Chew, N. Misawa, Y. Yamashita, S. Akatsuka, T.

Ishihara, K. Yamashita, Y. Yoshikawa, H. Yasui, L. Jiang, H. Ohara, T. Takahashi, G. Ichihara, K. Kostarelos, Y. Miyata, H. Shinohara, S. Toyokuni, *Proc. Natl. Acad. Sci. U. S. A.* **2011**, *108*, E1330.

[43] N. Sinha, J. T.-W. Yeow, *IEEE Trans. Nanobioscience* **2005**, *4*, 180.

[44] W. Wu, R. Li, X. Bian, Z. Zhu, D. Ding, X. Li, Z. Jia, X. Jiang, Y. Hu, *ACS Nano* **2009**, *3*, 2740.

[45] K. Ajima, T. Murakami, Y. Mizoguchi, K. Tsuchida, T. Ichihashi, S. Iijima, M. Yudasaka, *ACS Nano* **2008**, *2*, 2057.

[46] B. K. Nanjwade, H. M. Bechra, G. K. Derkar, F. V. Manvi, V. K. Nanjwade, *Eur. J. Pharm. Sci.* **2009**, *38*, 185.

[47] J. B. Wolinsky, M. W. Grinstaff, *Adv. Drug Deliv. Rev.* **2008**, *60*, 1037.

[48] M. K. Khan, S. S. Nigavekar, L. D. Minc, M. S. T. Kariapper, B. M. Nair, W. G. Lesniak, L. P. Balogh, *Technol. Cancer Res. Treat.* **2005**, *4*, 603.

[49] N. Malik, R. Wiwattanapatapee, R. Klopsch, K. Lorenz, H. Frey, J. . Weener, E. . Meijer, W. Paulus, R. Duncan, *J. Control. Release* **2000**, *65*, 133.

[50] R. Duncan, L. Izzo, *Adv. Drug Deliv. Rev.* **2005**, *57*, 2215.

[51] S. Seton-Rogers, *Nat. Rev. Drug Discov.* **2014**, *13*, 176.

[52] C. K. Kim, P. Ghosh, C. Pagliuca, Z.-J. Zhu, S. Menichetti, V. M. Rotello, *J. Am. Chem. Soc.* **2009**, *131*, 1360.

[53] D. K. Chatterjee, T. Wolfe, J. Lee, A. P. Brown, P. K. Singh, S. R. Bhattarai, P. Diagaradjane, S. Krishnan, *Transl. Cancer Res.* **2013**, *2*, 256.

[54] J. F. Hainfeld, D. N. Slatkin, H. M. Smilowitz, *Phys. Med. Biol.* **2004**, *49*, N309.

[55] M.-Y. Chang, A.-L. Shiau, Y.-H. Chen, C.-J. Chang, H. H.-W. Chen, C.-L. Wu, *Cancer Sci.* **2008**, *99*, 1479.

[56] T. Wolfe, D. Chatterjee, J. Lee, J. D. Grant, S. Bhattarai, R. Tailor, G. Goodrich, P. Nicolucci, S. Krishnan, *Nanomedicine Nanotechnology, Biol. Med.* **2015**, *11*, 1277.

[57] A. Mesbahi, F. Jamali, N. Garehaghaji, *Bioimpacts* **2013**, *3*, 29.

[58] X. Huang, P. K. Jain, I. H. El-Sayed, M. a El-Sayed, *Nanomedicine* **2007**, *2*, 681.

[59] G. F. Paciotti, D. G. I. Kingston, L. Tamarkin, *J. Clin. Psychiatry* **1993**, *54*, 10.

[60] S. D. Perrault, C. Walkey, T. Jennings, H. C. Fischer, W. C. W. Chan, *Nano Lett.* **2009**, *9*, 1909.

[61] G. F. Paciotti, L. Myer, D. Weinreich, D. Goia, N. Pavel, R. E. McLaughlin, L. Tamarkin, *Drug Deliv.* **2004**, *11*, 169.

[62] J. Lipka, M. Semmler-Behnke, R. A. Sperling, A. Wenk, S. Takenaka, C. Schleh, T. Kissel, W. J. Parak, W. G. Kreyling, *Biomaterials* **2010**, *31*, 6574.

[63] S. K. Libutti, G. F. Paciotti, A. A. Byrnes, H. R. Alexander, W. E. Gannon, M. Walker, G. D. Seidel, N. Yuldasheva, L. Tamarkin, *Clin. Cancer Res.* **2010**, *16*, 6139.

[64] A. N. Kharlamov, A. E. Tyurnina, V. S. Veselova, O. P. Kovtun, V. Y. Shur, J. L. Gabinsky, *Nanoscale* **2015**, *7*, 8003.

[65] P. Pedrosa, R. Vinhas, A. Fernandes, P. Baptista, *Nanomaterials* **2015**, *5*, 1853.

[66] S. Ruan, Q. He, H. Gao, *Nanoscale* **2015**, *7*, 9487.

[67] B. Feng, Z. Xu, F. Zhou, H. Yu, Q. Sun, D. Wang, Z. Tang, H. Yu, Q. Yin, Z. Zhang, Y. Li, *Nanoscale* **2015**, *7*, 14854.

[68] S. V Sambasivarao, **2013**, *18*, 1199.

[69] M. M. Yallapu, M. Jaggi, S. C. Chauhan, *Drug Discov. Today* **2012**, *17*, 71.

[70] H. Chen, X. Zhang, S. Dai, Y. Ma, S. Cui, S. Achilefu, Y. Gu, *Theranostics* **2013**, *3*, 633.

[71] W. Cai, T. Gao, H. Hong, J. Sun, *Nanotechnol. Sci. Appl.* **2008**, *Volume 1*, 17.

[72] O. Bar-Ilan, R. M. Albrecht, V. E. Fako, D. Y. Furgeson, *Small* **2009**, *5*, 1897.

[73] Arnida, A. Malugin, H. Ghandehari, *J. Appl. Toxicol.* **2010**, *30*, 212.

[74] A. D. Ostrowski, T. Martin, J. Conti, I. Hurt, B. H. Harthorn, *J. Nanoparticle Res.* **2009**, *11*, 251.

[75] C. J. Murphy, A. M. Gole, J. W. Stone, P. N. Sisco, A. M. Alkilany, E. C. Goldsmith, S. C. Baxter, *Acc. Chem. Res.* **2008**, *41*, 1721.

[76] Y.-S. Chen, Y.-C. Hung, I. Liau, G. S. Huang, *Nanoscale Res. Lett.* **2009**, *4*, 858.

[77] T. Mironava, M. Hadjiargyrou, M. Simon, V. Jurukovski, M. H. Rafailovich, *Nanotoxicology* **2010**, *4*, 120.

[78] Y. Pan, S. Neuss, A. Leifert, M. Fischler, F. Wen, U. Simon, G. Schmid, W. Brandau, W. Jahnen-Dechent, *Small* **2007**, *3*, 1941.

[79] W.-S. Cho, M. Cho, J. Jeong, M. Choi, H.-Y. Cho, B. S. Han, S. H. Kim, H. O. Kim, Y. T. Lim, B. H. Chung, J. Jeong, *Toxicol. Appl. Pharmacol.* **2009**, *236*, 16.

[80] C. M. Goodman, C. D. McCusker, T. Yilmaz, V. M. Rotello, *Bioconjug. Chem.* **2004**, *15*, 897.

[81] A. M. Alkilany, P. K. Nagaria, C. R. Hexel, T. J. Shaw, C. J. Murphy, M. D. Wyatt, *Small* **2009**, *5*, 701.

[82] T. Niidome, M. Yamagata, Y. Okamoto, Y. Akiyama, H. Takahashi, T. Kawano, Y. Katayama, Y. Niidome, *J. Control. Release* **2006**, *114*, 343.

[83] N. Chanda, P. Kan, L. D. Watkinson, R. Shukla, A. Zambre, T. L. Carmack, H. Engelbrecht, J. R. Lever, K. Katti, G. M. Fent, S. W. Casteel, C. J. Smith, W. H. Miller, S. Jurisson, E. Boote, J. D. Robertson, C. Cutler, M. Dobrovolskaia, R. Kannan, K. V. Katti, *Nanomedicine Nanotechnology, Biol. Med.* **2010**, *6*, 201.

[84] N. Li, P. Zhao, D. Astruc, *Angew. Chem. Int. Ed. Engl.* **2014**, *53*, 1756.

[85] A. Gerber, M. Bundschuh, D. Klingelhofer, D. A. Groneberg, *J. Occup. Med. Toxicol.* **2013**, *8*, 32.

[86] M. Faraday, *Philos. Trans. R. Soc. London* **1857**, *147*, 145.

[87] M. C. Daniel, D. Astruc, *Chem. Rev.* **2004**, *104*, 293.

[88] M. Wuithschick, A. Birnbaum, S. Witte, M. Sztucki, U. Vainio, N. Pinna, K. Rademann, F. Emmerling, R. Kraehnert, J. Polte, *ACS Nano* **2015**, *9*, 7052.

[89] E. A. HAUSER, J. E. LYNN, *EXPERIMENTS IN COLLOID CHEMISTRY*, McGraw Hill Book Company, INC. , New York and London, **1940**.

[90] G. Frens, *Nat. Phys. Sci.* **1973**, *241*, 20.

[91] J. Kimling, M. Maier, B. Okenve, V. Kotaidis, H. Ballot, A. Plech, *J. Phys. Chem. B* **2006**, *110*, 15700.

[92] R. Jin, *Nanoscale* **2010**, *2*, 343.

[93] Yuan Gao, Yangwei Liu, Ying Li, Oksana Zaluzhna, Y. J. Tong, *Functional Nanometer-Sized Clusters of Transition Metals*, Royal Society Of Chemistry, Cambridge, **2014**.

[94] F. Vitale, I. Fratoddi, C. Battocchio, E. Piscopiello, L. Tapfer, M. V. Russo, G. Polzonetti, C. Giannini, *Nanoscale Res. Lett.* **2011**, *6*, 103.

[95] C. LOUIS, O. PLUCHERY, in *Gold Nanoparticles Physics, Chem. Biol.*,

IMPERIAL COLLEGE PRESS, Université Pierre et Marie Curie, France, **2012**, pp. i–ix.

[96] D. Baranov, E. N. Kadnikova, *J. Mater. Chem.* **2011**, *21*, 6152.

[97] V. Miguel, L.-L. Ángela, *Gold Nanoparticles in Analytical Chemistry*, Elsevier Science, University of Córdoba, **2014**.

[98] K. R. Brown, M. J. Natan, *Langmuir* **1998**, *14*, 726.

[99] K. R. Brown, D. G. Walter, M. J. Natan, *Chem. Mater.* **2000**, *12*, 306.

[100] E. J. Guidelli, A. P. Ramos, M. E. D. Zaniquelli, P. Nicolucci, O. Baffa, *Radiat. Phys. Chem.* **2012**, *81*, 301.

[101] V. K. LaMer, A. S. Kenyon, *J. Colloid Sci.* **1947**, *2*, 257.

[102] M. K. Chow, C. F. Zukoski, *J. Colloid Interface Sci.* **1994**, *165*, 97.

[103] L. Pei, K. Mori, M. Adachi, *Langmuir* **2004**, *20*, 7837.

[104] † Boon-Kin Pong, ‡ Hendry I. Elim, § Jian-Xiong Chong, ‡ Wei Ji, †,⊥ and Bernhardt L. Trout, †,§ Jim-Yang Lee*, **2007**, DOI 10.1021/JP068666O.

[105] X. Ji, X. Song, J. Li, Y. Bai, W. Yang, X. Peng, *J. Am. Chem. Soc.* **2007**, *129*, 13939.

[106] L. Zhao, D. Jiang, Y. Cai, X. Ji, R. Xie, W. Yang, *Nanoscale* **2012**, *4*, 5071.

[107] E. E. Finney, R. G. Finke, *J. Colloid Interface Sci.* **2008**, *317*, 351.

[108] S. Kumar, K. S. Gandhi, R. Kumar, *Ind. Eng. Chem. Res.* **2007**, *46*, 3128.

[109] Y. Mikhlin, A. Karacharov, M. Likhatski, T. Podlipskaya, Y. Zubavichus, A. Veligzhanin, V. Zaikovski, *J. Colloid Interface Sci.* **2011**, *362*, 330.

[110] J. Polte, T. T. Ahner, F. Delissen, S. Sokolov, F. Emmerling, A. F. Thünemann, R. Kraehnert, *J. Am. Chem. Soc.* **2010**, *132*, 1296.

[111] J. Polte, R. Erler, A. F. Thünemann, F. Emmerling, R. Kraehnert, *Chem. Commun.* **2010**, *46*, 9209.

[112] J. W. Park, J. S. Shumaker-Parry, *ACS Nano* **2015**, *9*, 1665.

[113] T. Luo, P. Huang, G. Gao, G. Shen, S. Fu, D. Cui, C. Zhou, Q. Ren, *Opt. Express* **2011**, *19*, 17030.

[114] C. a Mirkin, **2014**, *49*, 3280.

[115] S. Jain, D. G. Hirst, J. M. O'Sullivan, *Br. J. Radiol.* **2012**, *85*, 101.

[116] R. R. Seeley, T. D. Stephens, P. Tate, *Anatomy And Physiology*, Mc Graw Hill, **2008**.

[117] T. A. Larson, P. P. Joshi, K. Sokolov, *ACS Nano* **2012**, *6*, 9182.

[118] C. D. Walkey, J. B. Olsen, H. Guo, A. Emili, W. C. W. Chan, *J. Am. Chem. Soc.* **2012**, *134*, 2139.

[119] L. R. Hirsch, R. J. Stafford, J. A. Bankson, S. R. Sershen, B. Rivera, R. E. Price, J. D. Hazle, N. J. Halas, J. L. West, *Proc. Natl. Acad. Sci. U. S. A.* **2003**, *100*, 13549.

[120] C. R. C. R. Patra, R. Bhattacharya, D. Mukhopadhyay, P. Mukherjee, *Adv. Drug Deliv. Rev.* **2010**, *62*, 346.

[121] W. Jiang, B. Y. S. Kim, J. T. Rutka, W. C. W. Chan, *Nat. Nanotechnol.* **2008**, *3*, 145.

[122] J. M. Stern, J. Stanfield, Y. Lotan, S. Park, J.-T. Hsieh, J. A. Cadeddu, *J. Endourol.* **2007**, *21*, 939.

[123] G. Han, N. S. Chari, A. Verma, R. Hong, C. T. Martin, V. M. Rotello, *Bioconjug. Chem.* **2005**, *16*, 1356.

[124] M. Thomas, A. M. Klibanov, *Proc. Natl. Acad. Sci. U. S. A.* **2003**, *100*, 9138.

[125] V. Dixit, J. Van den Bossche, D. M. Sherman, D. H. Thompson, R. P. Andres, *Bioconjug. Chem.* **2006**, *17*, 603.

[126] K. Cho, X. Wang, S. Nie, Z. G. Chen, D. M. Shin, *Clin. Cancer Res.* **2008**, *14*, 1310.

[127] B. D. Chithrani, A. a. Ghazani, W. C. W. Chan, *Nano Lett.* **2006**, *6*, 662.

[128] H. Maeda, J. Wu, T. Sawa, Y. Matsumura, K. Hori, *J. Control. Release* **2000**, *65*, 271.

[129] Y. Noguchi, J. Wu, R. Duncan, J. Strohalm, K. Ulbrich, T. Akaike, H. Maeda, *Jpn. J. Cancer Res.* **1998**, *89*, 307.

[130] M. Suzuki, K. Hori, I. Abe, S. Saito, H. Sato, *J. Natl. Cancer Inst.* **1981**, *67*, 663.

[131] G. Nanocrystals, X. Huang, X. Peng, Y. Wang, Y. Wang, D. M. Shin, M. a El, S. Nie, *ACS Nano* **2010**, *4*, 5887.

[132] C. H. J. Choi, C. a Alabi, P. Webster, M. E. Davis, *Proc. Natl. Acad. Sci. U. S. A.* **2010**, *107*, 1235.

[133] D. W. Bartlett, H. Su, I. J. Hildebrandt, W. A. Weber, M. E. Davis, *Proc. Natl. Acad. Sci. U. S. A.* **2007**, *104*, 15549.

[134] D. B. Kirpotin, D. C. Drummond, Y. Shao, M. R. Shalaby, K. Hong, U. B. Nielsen, J. D. Marks, C. C. Benz, J. W. Park, *Cancer Res.* **2006**, *66*, 6732.

[135] K. F. Pirollo, E. H. Chang, *Trends Biotechnol.* **2008**, *26*, 552.

[136] E. Garanger, D. Boturyn, P. Dumy, *Anticancer. Agents Med. Chem.* **2007**, *7*, 552.

[137] T. R. Daniels, T. Delgado, J. A. Rodriguez, G. Helguera, M. L. Penichet, *Clin. Immunol.* **2006**, *121*, 144.

[138] C. R. Dass, P. F. M. Choong, *J. Control. Release* **2006**, *113*, 155.

[139] L. Xu, K. F. Pirollo, W. H. Tang, a Rait, E. H. Chang, *Hum. Gene Ther.* **1999**, *10*, 2941.

[140] A. R. Hilgenbrink, P. S. Low, *J. Pharm. Sci.* **2005**, *94*, 2135.

[141] K. de Bruin, N. Ruthardt, K. von Gersdorff, R. Bausinger, E. Wagner, M. Ogris, C. Bräuchle, *Mol. Ther.* **2007**, *15*, 1297.

[142] B. B. Kasten, T. Liu, J. R. Nedrow-Byers, P. D. Benny, C. E. Berkman, *Bioorganic Med. Chem. Lett.* **2013**, *23*, 565.

[143] T. Liu, J. R. Nedrow-Byers, M. R. Hopkins, L. Y. Wu, J. Lee, P. T. a Reilly, C. E. Berkman, *Bioorganic Med. Chem. Lett.* **2012**, *22*, 3931.

[144] G. Jianjun Chenga, Benjamin A. Teplya, Ines Sherifia, Josephine Sunga, C. Luthera, Frank X. Gua, Etgar Levy-Nissenbauma, Aleksandar F. Radovic-Morenob, D. Robert Langera, b, c, and Omid C. Farokhzadb, **2007**, *28*, 869.

[145] S. S. Chang, D. S. O'Keefe, D. J. Bacich, V. E. Reuter, W. D. Heston, P. B. Gaudin, *Clin. Cancer Res.* **1999**, *5*, 2674.

[146] K. D. Godeiro, A. C. de A. Frota, E. Antecka, A. N. Odashiro, S. Maloney, B. Fernandes, M. N. Burnier, *J. Carcinog.* **2006**, *5*, 21.

[147] A. Kumar, S. Huo, X. Zhang, J. Liu, A. Tan, S. Li, S. Jin, X. Xue, Y. Zhao, T. Ji, L. Han, H. Liu, X. Zhang, J. Zhang, G. Zou, T. Wang, S. Tang, X.-J. Liang, *ACS Nano* **2014**, *8*, 4205.

[148] S. Payton, *Nat. Rev. Urol.* **2012**, *9*, 544.

[149] S. D. Brown, P. Nativo, J. A. Smith, D. Stirling, P. R. Edwards, B. Venugopal, D. J. Flint, J. a. Plumb, D. Graham, N. J. Wheate, *J. Am. Chem. Soc.* **2010**, *132*, 4678.

[150] H. Hess, Y. Tseng, *ACS Nano* **2007**, *1*, 390.

[151] M. A. Dobrovolskaia, S. E. McNeil, *Nat. Nanotechnol.* **2007**, *2*, 469.

[152] S. D. Conner, S. L. Schmid, *Nature* **2003**, *422*, 37.

[153] Y. Liu, M. K. Shipton, J. Ryan, E. D. Kaufman, S. Franzen, D. L. Feldheim,

Anal. Chem. **2007**, *79*, 2221.

[154] Y. Liu, M. K. Shipton, J. Ryan, E. D. Kaufman, S. Franzen, D. L. Feldheim, *Anal. Chem.* **2007**, *79*, 2221.

[155] C. Foerg, U. Ziegler, J. Fernandez-Carneado, E. Giralt, R. Rennert, A. G. Beck-Sickinger, H. P. Merkle, *Biochemistry* **2005**, *44*, 72.

[156] J. R. Nicol, Radiation Dose Enhancement : The Development and Application of Radiosensitising Gold Nanoparticles, Queens University Belfast, **2012**.

[157] A. G. Tkachenko, H. Xie, D. Coleman, W. Glomm, J. Ryan, M. F. Anderson, S. Franzen, D. L. Feldheim, N. Carolina, S. Uni, **2003**, 4700.

[158] D. Mandal, A. Maran, M. J. Yaszemski, M. E. Bolander, G. Sarkar, *J. Mater. Sci. Mater. Med.* **2009**, *20*, 347.

[159] C. Yang, D. Yohan, D. B. Chithrani, *Colloids Interface Sci. Commun.* **2014**, *1*, 54.

[160] C. Plank, B. Oberhauser, K. Mechtler, C. Koch, E. Wagner, *J. Biol. Chem.* **1994**, *269*, 12918.

[161] J. D. Lear, W. F. DeGrado, *J. Biol. Chem.* **1987**, *262*, 6500.

[162] A. Subramanian, H. Ma, K. N. Dahl, J. Zhu, S. L. Diamond, *J. Gene Med.* **2002**, *4*, 75.

[163] S. OLIVEIRA, I. VANROOY, O. KRANENBURG, G. STORM, R. SCHIFFELERS, *Int. J. Pharm.* **2007**, *331*, 211.

[164] E. Mastrobattista, G. A. Koning, L. van Bloois, A. C. S. Filipe, W. Jiskoot, G. Storm, *J. Biol. Chem.* **2002**, *277*, 27135.

[165] A. M. Funhoff, C. F. van Nostrum, A. P. C. A. Janssen, M. H. A. M. Fens, D. J. A. Crommelin, W. E. Hennink, *Pharm. Res.* **2004**, *21*, 170.

[166] A. M. Funhoff, C. F. van Nostrum, M. C. Lok, M. M. Fretz, D. J. A. Crommelin, W. E. Hennink, *Bioconjug. Chem.* **2004**, *15*, 1212.

[167] X. Jiang, M. C. Lok, W. E. Hennink, *Bioconjug. Chem.* **2007**, *18*, 2077.

[168] R. Weissleder, M. Lewin, N. Carlesso, C.-H. Tung, X.-W. Tang, D. Cory, D. T. Scadden, *Nat. Biotechnol.* **2000**, *18*, 410.

[169] A. M. J. Beerens, A. F. Y. Al Hadithy, M. G. Rots, H. J. Haisma, *Curr. Gene Ther.* **2003**, *3*, 486.

[170] V. P. Torchilin, T. S. Levchenko, R. Rammohan, N. Volodina, B. Papahadjopoulos-Sternberg, G. G. M. D'Souza, *Proc. Natl. Acad. Sci.* **2003**,

100, 1972.

[171] S. L. Lo, S. Wang, *Biomaterials* **2008**, *29*, 2408.

[172] N. Kämper, P. M. Day, T. Nowak, H.-C. Selinka, L. Florin, J. Bolscher, L. Hilbig, J. T. Schiller, M. Sapp, *J. Virol.* **2006**, *80*, 759.

[173] K. A. Browne, E. Blink, V. R. Sutton, C. J. Froelich, D. A. Jans, J. A. Trapani, **1999**, *19*, 8604.

[174] S.-H. Min, D. C. Lee, M. J. Lim, H. S. Park, D. M. Kim, C. W. Cho, D. Y. Yoon, Y. Il Yeom, *J. Gene Med.* **2006**, *8*, 1425.

[175] M. Magzoub, A. Pramanik, A. Gräslund, *Biochemistry* **2005**, *44*, 14890.

[176] M. Magzoub, S. Sandgren, P. Lundberg, K. Oglęcka, J. Lilja, A. Wittrup, L. E. Göran Eriksson, Ü. Langel, M. Belting, A. Gräslund, *Biochem. Biophys. Res. Commun.* **2006**, *348*, 379.

[177] J. Fernández-Carneado, M. J. Kogan, S. Castel, E. Giralt, *Angew. Chemie Int. Ed.* **2004**, *43*, 1811.

[178] T. F. Martens, K. Remaut, J. Demeester, S. C. De Smedt, K. Braeckmans, *Nano Today* **2014**, *9*, 344.

[179] J. Behr, *Int. J. Chem.* **1997**, *2*, 34.

[180] P. Midoux, A. Kichler, V. Boutin, J. C. Maurizot, M. Monsigny, *Bioconjug. Chem.* **1998**, *9*, 260.

[181] A. Mocanu, I. Cernica, G. Tomoaia, L. D. Bobos, O. Horovitz, M. Tomoaia-Cotisel, *Colloids Surfaces A Physicochem. Eng. Asp.* **2009**, *338*, 93.

[182] D. Kumar, Meenan, Dixon, *Int. J. Nanomedicine* **2012**, *7*, 4007.

[183] D. Kumar, B. J. Meenan, I. Mutreja, R. D'Sa, D. Dixon, *Int. J. Nanosci.* **2012**, *11*, 1250023.

[184] J. Manson, D. Kumar, B. J. Meenan, D. Dixon, *Gold Bull.* **2011**, *44*, 99.

[185] E. Harrison, J. R. Nicol, M. Macias-Montero, G. A. Burke, J. A. Coulter, B. J. Meenan, D. Dixon, *Mater. Sci. Eng. C* **2016**, *62*, 710.

[186] R. A. Sperling, W. J. Parak, R. Soc, *Philos. Trans. A. Math. Phys. Eng. Sci.* **2010**, *368*, 1333.

[187] W. Wang, Q. Q. Wei, J. Wang, B. C. Wang, S. H. Zhang, Z. Yuan, *J. Colloid Interface Sci.* **2013**, *404*, 223.

[188] A. Anne, C. Demaille, J. Moiroux, *Macromolecules* **2002**, *35*, 5578.

[189] G. Hager, A. G. Brolo, *J. Electroanal. Chem.* **2003**, *550–551*, 291.

[190] A. Ulman, *Chem. Rev.* **1996**, *96*, 1533.

[191] C. D. Bain, H. A. Biebuyck, G. M. Whitesides, *Langmuir* **1989**, *5*, 723.

[192] G. Dodero, L. De Michieli, O. Cavalleri, R. Rolandi, L. Oliveri, A. Daccà, R. Parodi, *Colloids Surfaces A Physicochem. Eng. Asp.* **2000**, *175*, 121.

[193] A. S. Dakkouri, D. M. Kolb, R. Edelstein-Shima, D. Mandler, *Langmuir* **1996**, *12*, 2849.

[194] C. S. Weisbecker, M. V Merritt, G. M. Whitesides, *Langmuir* **1996**, *12*, 3763.

[195] H. Ron, I. Rubinstein, *J. Am. Chem. Soc.* **1998**, *120*, 13444.

[196] A. Gole, C. Dash, V. Ramakrishnan, S. R. Sainkar, A. B. Mandale, M. Rao, M. Sastry, *Langmuir* **2001**, *17*, 1674.

[197] E. R. Goldman, E. D. Balighian, H. Mattoussi, M. K. Kuno, J. M. Mauro, P. T. Tran, G. P. Anderson, *J. Am. Chem. Soc.* **2002**, *124*, 6378.

[198] H. Mattoussi, J. Matthew Mauro, E. R. Goldman, G. P. Anderson, V. C. Sundar, F. V. Mikulec, M. G. Bawendi, *J. Am. Chem. Soc.* **2000**, *122*, 12142.

[199] H. Mattoussi, J. M. Mauro, E. R. Goldman, T. M. Green, G. P. Anderson, V. C. Sundar, M. G. Bawendi, *Phys. status solidi* **2001**, *224*, 277.

[200] M. R. Ivanov, AuNP57-Covalently Functionalized Gold Nanoparticles : Synthesis , Characterization , and Integration into Capillary Electrophoresis, The University of Iowa, **2011**.

[201] Z. Lin, X. Su, Y. Wan, H. Zhang, Y. Mu, B. Yang, Q. Jin, *Russ. Chem. Bull.* **2004**, *53*, 2690.

[202] W. Shi, Y. Sahoo, M. T. Swihart, *Colloids Surfaces A Physicochem. Eng. Asp.* **2004**, *246*, 109.

[203] T. Stuchinskaya, M. Moreno, M. J. Cook, D. R. Edwards, D. a Russell, *Photochem. Photobiol. Sci.* **2011**, *10*, 822.

[204] A. M. Fales, H. Yuan, T. Vo-Dinh, *Mol. Pharm.* **2013**, *10*, 2291.

[205] S. Xu, S. J. N. Cruchon-Dupeyrat, J. C. Garno, G.-Y. Liu, G. Kane Jennings, T.-H. Yong, P. E. Laibinis, *J. Chem. Phys.* **1998**, *108*, 5002.

[206] C. Vericat, G. a Benitez, D. E. Grumelli, M. E. Vela, R. C. Salvarezza, *J. Phys. Condens. Matter* **2008**, *20*, 184004.

[207] F. Frederix, J.-M. Friedt, K.-H. Choi, W. Laureyn, A. Campitelli, D. Mondelaers, G. Maes, G. Borghs, *Anal. Chem.* **2003**, *75*, 6894.

[208] M. De, C. C. You, S. Srivastava, V. M. Rotello, *J. Am. Chem. Soc.* **2007**, *129*,

10747.

[209] R. GhoshMoulick, J. Bhattacharya, C. K. Mitra, S. Basak, A. K. Dasgupta, *Nanomedicine Nanotechnology, Biol. Med.* **2007**, *3*, 208.

[210] Ž. Krpetić, S. Saleemi, I. a. Prior, V. Sée, R. Qureshi, M. Brust, *ACS Nano* **2011**, *5*, 5195.

[211] H. Yuan, A. M. Fales, T. Vo-Dinh, *J. Am. Chem. Soc.* **2012**, *134*, 11358.

[212] C. M. Feldherr, D. Akin, *J. Cell Biol.* **1990**, *111*, 1.

[213] C. M. Feldherr, R. E. Lanford, D. Akin, *Proc. Natl. Acad. Sci. U. S. A.* **1992**, *89*, 11002.

[214] C. M. Feldherr, D. Akin, *Exp. Cell Res.* **1993**, *205*, 179.

[215] C. M. Feldherr, D. Akin, *Exp. Cell Res.* **1994**, *215*, 206.

[216] M. Iijima, Y. Nagasaki, T. Okada, M. Kato, K. Kataoka, *Macromolecules* **1999**, *32*, 1140.

[217] H. Otsuka, Y. Nagasaki, K. Kataoka, *Adv. Drug Deliv. Rev.* **2012**, *64*, 246.

[218] W. Fu, D. Shenoy, J. Li, C. Crasto, G. Jones, C. Dimarzio, S. Sridhar, M. Amiji, *MRS Proc.* **2004**, *845*, DOI 10.1557/PROC-845-AA5.4.

[219] D. A. Giljohann, D. S. Seferos, A. E. Prigodich, P. C. Patel, C. A. Mirkin, *Anal. Chem.* **2009**, *81*, 8715.

[220] A. K. Oyelere, C. P. C, X. Huang, I. H. El-Sayed, M. a El-Sayed, *Bioconjug. Chem.* **2006**, *18 VN-r*, 1490.

[221] P. C. Chen, S. C. Mwakwari, A. K. Oyelere, *Nanotechnol. Sci. Appl.* **2008**, *1*, 45.

[222] R. Blood, C. Counts, C. a Simpson, A. C. Agrawal, A. Balinski, K. M. Harkness, D. E. Cliffel, S. E. T. Al, **2011**, 3577.

[223] M. Eghtedari, M. Eghtedari, A. V Liopo, A. V Liopo, J. a Copland, J. a Copland, A. a Oraevsky, A. a Oraevsky, M. Motamedi, M. Motamedi, *Nano Lett.* **2009**, *9*, 287.

[224] L. D. Unsworth, H. Sheardown, J. L. Brash, *Biomaterials* **2005**, *26*, 5927.

[225] V. Sanz, J. Conde, Y. Hernández, P. V. Baptista, M. R. Ibarra, J. M. de la Fuente, *J. Nanoparticle Res.* **2012**, *14*, 917.

[226] W. P. Wuelfing, S. M. Gross, D. T. Miles, R. W. Murray, *J. Am. Chem. Soc.* **1998**, *120*, 12696.

[227] World Health Organization 2015, "Boil Water - Technical Brief," can be

found under http://www.who.int/water_sanitation_health/dwq/Boiling_water_01_15.pdf, **2015**.

[228] Radiologyinfo.org, "Definition: Radiation Units," can be found under https://www.radiologyinfo.org/en/glossary/glossary1.cfm?gid=369, **n.d.**

[229] Horiba, **2014**, 1.

[230] Malvern Instruments, *Http://Www.Malvern.Com/En/Products/Technology/Dynamic-Light-Scattering/* **2014**, 1.

[231] P. Elmer, *Series 200 UV / VIS Detector User ' S Manual*, Connecticut, **2003**.

[232] M. Akul, "Ultraviolet-Visible (UV-Vis) Spectroscopy | Analytical Chemistry | PharmaXChange.info," can be found under http://pharmaxchange.info/press/2011/12/ultraviolet-visible-uv-vis-spectroscopy-principle/, **2011**.

[233] J.-L. Bredas, *Mater. Horiz.* **2014**, *1*, 17.

[234] Andor, "ATR Spectroscopy - An introduction to ATR Spectroscopy," can be found under http://www.andor.com/learning-academy/absorption-transmission-reflection-spectroscopy-an-introduction-to-absorption-transmission-reflection-spectroscopy, **2016**.

[235] PerkinElmer Ltd, *Lambda 25, 35, 45 User's Guide*, Buckinghamshire, **2000**.

[236] T. Nicolet, C. All, *A Thermo Electron Bussines* **2001**, 1.

[237] *Publ. by InTech Janeza Trdine* **5100**, *9*.

[238] T. Pellegrino, R. a Sperling, a P. Alivisatos, W. J. Parak, *J. Biomed. Biotechnol.* **2007**, *2007*, 1.

[239] H. Mok, T. G. Park, *Biopolymers* **2008**, *89*, 881.

[240] T. Hadeishi, R. McLaughlin, *Zeeman Atomic Absorption Spectrometry*, Berkeley, CA, **1978**.

[241] PerkinElmer, *Microchem. J.* **2000**, *65*, 353.

[242] J. Ljungblad, Antibody-Conjugated Gold Nanoparticles Integrated in a Fluorescence Based Biochip, Linköping University, **2009**.

[243] M. H. Jazayeri, H. Amani, A. A. Pourfatollah, H. Pazoki-Toroudi, B. Sedighimoghaddam, *Sens. Bio-Sensing Res.* **2016**, *9*, 17.

[244] S. Kumar, J. Aaron, K. Sokolov, *Nat. Protoc.* **2008**, *3*, 314.

[245] G. T. Hermanson, *Bioconjugate Techniques*, Elsevier, London, **2013**.

[246] H. Otsuka, Y. Nagasaki, K. Kataoka, *Biomacromolecules* **2000**, *1*, 39.

[247] J. R. Nicol, E. Harrison, S. M. O'Neill, D. Dixon, H. O. McCarthy, J. A. Coulter, *Nanomedicine* **2017**, *14*, 439.

[248] R. Lévy, *ChemBioChem* **2006**, *7*, 1141.

[249] S. Al-Karadaghi, "Peptide Structure & Design," can be found under http://www.proteinstructures.com/About/about.html, **2016**.

[250] Lumiprobe, "NHS ester labeling of amino biomolecules," **2014**.

[251] ThermoFisher, Scientific, "Amine-Reactive Crosslinker Chemistry," can be found under https://www.thermofisher.com/uk/en/home/life-science/protein-biology/protein-biology-learning-center/protein-biology-resource-library/pierce-protein-methods/amine-reactive-crosslinker-chemistry.html, **2016**.

[252] Y. Wang, Y. Ni, *Talanta* **2014**, *119*, 320.

[253] J. Homola, M. Piliarik, **2006**, pp. 45–67.

[254] S. J. Oldenburg, "Silver Nanoparticles: Properties and Applications | Sigma-Aldrich," can be found under http://www.sigmaaldrich.com/technical-documents/articles/materials-science/nanomaterials/gold-nanoparticles.html, **2015**.

[255] S. F. Sweeney, G. H. Woehrle, J. E. Hutchison, *J. Am. Chem. Soc.* **2006**, *128*, 3190.

[256] W. Zhao, T. M. H. Lee, S. S. Y. Leung, I.-M. Hsing, *Langmuir* **2007**, *23*, 7143.

[257] R. DULBECCO, M. VOGT, *J. Exp. Med.* **1954**, *99*, 167.

[258] J.-W. Park, J. S. Shumaker-Parry, *J. Am. Chem. Soc.* **2014**, *136*, 1907.

[259] J. Kim, *Piketech.Com* **n.d.**, 11.

[260] H. Intramolecular, **2016**, *3645*, 2.

[261] R. Narain, *Engineered Carbohydrate-Based Materials for Biomedical Applications*, John Wiley & Sons, Inc., Hoboken, NJ, USA, **2011**.

[262] K. A. Kilian, T. Böcking, K. Gaus, J. J. Gooding, *Angew. Chemie Int. Ed.* **2008**, *47*, 2697.

[263] H. Tan, T. Zhan, W. Y. Fan, *J. Phys. Chem. B* **2006**, *110*, 21690.

[264] C. Wang, Q. Yan, H. B. Liu, X. H. Zhou, S. J. Xiao, *Langmuir* **2011**, *27*,

12058.

[265] S. D. Tables, *Spectroscopy* **2010**, *2620*, DOI 10.1016/j.ijmm.2014.11.005.

[266] B. A. Al-Maythalony, M. Monim-Ul-Mehboob, M. Altaf, M. I. M. Wazeer, A. A. Isab, S. Altuwaijri, A. Ahmed, V. Dhuna, G. Bhatia, K. Dhuna, S. S. Kamboj, *Spectrochim. Acta - Part A Mol. Biomol. Spectrosc.* **2013**, *115*, 641.

[267] A. a Isab, M. N. Shaikh, M. Monim-ul-Mehboob, B. a Al-Maythalony, M. I. M. Wazeer, S. Altuwaijri, *Spectrochim. Acta. A. Mol. Biomol. Spectrosc.* **2011**, *79*, 1196.

[268] H. H. Murray, *J. Am. Chem. Soc.* **2000**, *122*, 4534.

[269] H. E. Abdou, A. A. Mohamed, J. P. Fackler, in *Gold Chem.*, Wiley-VCH Verlag GmbH & Co. KGaA, Weinheim, Germany, **2009**, pp. 1–45.

[270] A. R. Sielecki, A. A. Fedorov, A. Boodhoo, N. S. Andreeva, M. N. G. James, *J. Mol. Biol.* **1990**, *214*, 143.

[271] D. V Leff, L. Brandt, J. R. Heath, *Langmuir* **1996**, *12*, 4723.

[272] A. Gole, C. Dash, V. Ramakrishnan, S. R. Sainkar, A. B. Mandale, M. Rao, M. Sastry, *Langmuir* **2001**, *17*, 1674.

[273] H. Y. Afeefy, J. F. Liebman, S. E. Stein, in *NIST Chem. WebBook, NIST Stand. Ref. Database Number 69*, **1997**, p. http://webbook.nist.gov, (abgerufen 03.04.2013).

[274] W. S. Matthews, J. E. Bares, J. E. Bartmess, F. G. Bordwell, F. J. Cornforth, G. E. Drucker, Z. Margolin, R. J. McCallum, G. J. McCollum, N. R. Vanier, *J. Am. Chem. Soc.* **1975**, *97*, 7006.

[275] R. Olin, *Drug Facts and Comparisons*, Wolters Kluwer, 2017, **2017**.

[276] G. Da Violante, N. Zerrouk, I. Richard, G. Provot, J. C. Chaumeil, P. Arnaud, *Biol. Pharm. Bull.* **2002**, *25*, 1600.

[277] L. Jamalzadeh, H. Ghafoori, R. Sariri, H. Rabuti, J. Nasirzade, H. Hasani, M. R. Aghamaali, *Avicenna J. Med. Biochem.* **2016**, *In press*, DOI 10.17795/ajmb-33453.

[278] T. I. Malinin, V. P. Perry, *Cryobiology* **1967**, *4*, 90.

[279] C. Yuan, J. Gao, J. Guo, L. Bai, C. Marshall, Z. Cai, L. Wang, M. Xiao, *PLoS One* **2014**, *9*, e107447.

[280] J. Galvao, B. Davis, M. Tilley, E. Normando, M. R. Duchen, M. F. Cordeiro, *FASEB J.* **2014**, *28*, 1317.

[281] S. Das, N. Debnath, S. Mitra, A. Datta, A. Goswami, "Comparative analysis of stability and toxicity profile of three differently capped gold nanoparticles for biomedical usage," **2012**.

[282] E. Fröhlich, *Int. J. Nanomedicine* **2012**, *7*, 5577.

[283] A. S. Thakor, R. Luong, R. Paulmurugan, F. I. Lin, P. Kempen, C. Zavaleta, P. Chu, T. F. Massoud, R. Sinclair, S. S. Gambhir, *Sci. Transl. Med.* **2011**, *3*.

[284] E. Söderstjerna, M. Zanardo-Gomes, E. Reynolds, *PLoS One* **2013**, *8*, e58211.

[285] K. S. Suh, Y. S. Lee, S. H. Seo, Y. S. Kim, E. M. Choi, *Biol. Trace Elem. Res.* **2013**, *153*, 428.

[286] P. J. Chueh, R.-Y. Liang, Y.-H. Lee, Z.-M. Zeng, S.-M. Chuang, *J. Hazard. Mater.* **2014**, *264*, 303.

[287] W. Cui, J. Li, Y. Zhang, H. Rong, W. Lu, L. Jiang, *Nanomedicine Nanotechnology, Biol. Med.* **2012**, *8*, 46.

[288] W. Cui, J. Li, Y. Zhang, H. Rong, W. Lu, L. Jiang, et al., *Nanomedicine* **2012**, *8*, 46.

[289] P. P. Fu, Q. Xia, H.-M. Hwang, P. C. Ray, H. Yu, *J. food drug Anal.* **2014**, *22*, 64.

[290] J. R. Nicol, D. Dixon, J. A. Coulter, *Nanomedicine (Lond).* **2015**, *10*, 1315.

[291] N. M. Sosibo, F. K. Keter, A. Skepu, R. T. Tshikhudo, N. Revaprasadu, *Nanomaterials* **2015**, *5*, 1211.

[292] W. Gallagher, *Biochemistry* **1997**, 662.

[293] B. Y. B. R. Lakshmanan, **1956**, 27.

[294] "FTIR and UV-Vis Accessories, ATR Specular and Diffuse Reflectance, Integrating Spheres, Microscopes and Transmission," can be found under http://www.piketech.com/dr-easidiff-tm.html, **n.d.**

[295] D. C. Hone, A. H. Haines, D. A. Russell, *Langmuir* **2003**, *19*, 7141.

[296] X. Wang, O. Ramström, M. Yan, *Anal. Chem.* **2010**, *82*, 9082.

[297] S. R. Ahmed, S. Oh, R. Baba, H. Zhou, S. Hwang, J. Lee, E. Y. Park, *Nanoscale Res. Lett.* **2016**, *11*, 65.

[298] K. Kimura, S. Takashima, H. Ohshima, *J. Phys. Chem. B* **2002**, *106*, 7260.

[299] S. Veeranarayanan, A. C. Poulose, S. Mohamed, A. Aravind, Y. Nagaoka, Y. Yoshida, T. Maekawa, D. S. Kumar, *J. Fluoresc.* **2012**, *22*, 537.

[300] K. Dave, N. M. R. N, M. Trinadh, B. A. Monisha, V. S. S. Annadanam, M.

Dhayal, *RSC Adv.* **2016**, *6*.

[301] C. Peterson, **n.d.**, DOI 10.1007/s11270-009-0215-5.

[302] H. Zhu, R. C. Derksen, C. R. Krause, R. D. Fox, R. D. Brazee, H. E. Ozkan, *Appl. Eng. Agric.* **n.d.**, *21*, 325.

[303] H. Diehl, N. Horchak-Morris, *Talanta* **1987**, *34*, 739.

[304] K. N. Kapoor, D. T. Barry, R. C. Rees, I. Anthony Dodi, S. E. B. McArdle, C. S. Creaser, P. L. R. Bonner, *Anal. Biochem.* **2009**, *393*, 138.

[305] E. Pensa, E. Cortés, G. Corthey, P. Carro, C. Vericat, M. H. Fonticelli, G. Benítez, A. A. Rubert, R. C. Salvarezza, *Acc. Chem. Res.* **2012**, *45*, 1183.

[306] F. Chen, X. Li, J. Hihath, Z. Huang, N. Tao, *J. Am. Chem. Soc.* **2006**, *128*, 15874.

[307] H. H. Murray, *J. Am. Chem. Soc.* **2000**, *122*, 4534.

[308] E. Harrison, J. W. J. Hamilton, M. Macias-Montero, D. Dixon, *Nanotechnology* **2017**, *28*, 295602.

APPENDIX 1

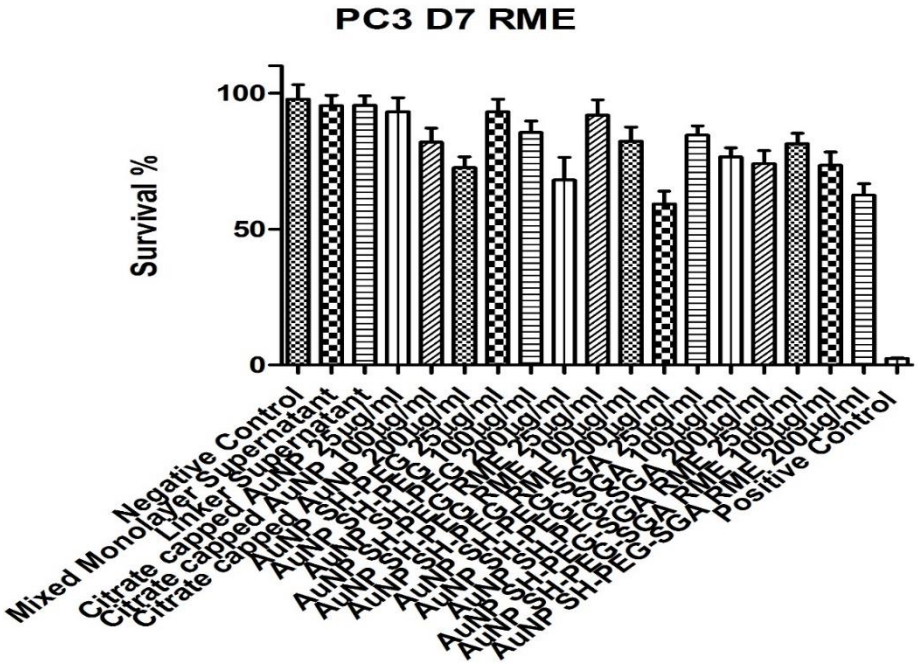
PC3 D7 RME
Survival %
100
50
0
Negative Control
Mixed Monolayer Supernatant
Linker Supernatant
Citrate capped AuNP 25µg/ml
Citrate capped AuNP 100µg/ml
Citrate capped AuNP 200µg/ml
AuNP SH-PEG 25µg/ml
AuNP SH-PEG 100µg/ml
AuNP SH-PEG 200µg/ml
AuNP SH-PEG-GGG RME 25µg/ml
AuNP SH-PEG-GGG RME 100µg/ml
AuNP SH-PEG-GGG RME 200µg/ml
AuNP SH-PEG-SGA RME 25µg/ml
AuNP SH-PEG-SGA RME 100µg/ml
AuNP SH-PEG-SGA RME 200µg/ml
Positive Control

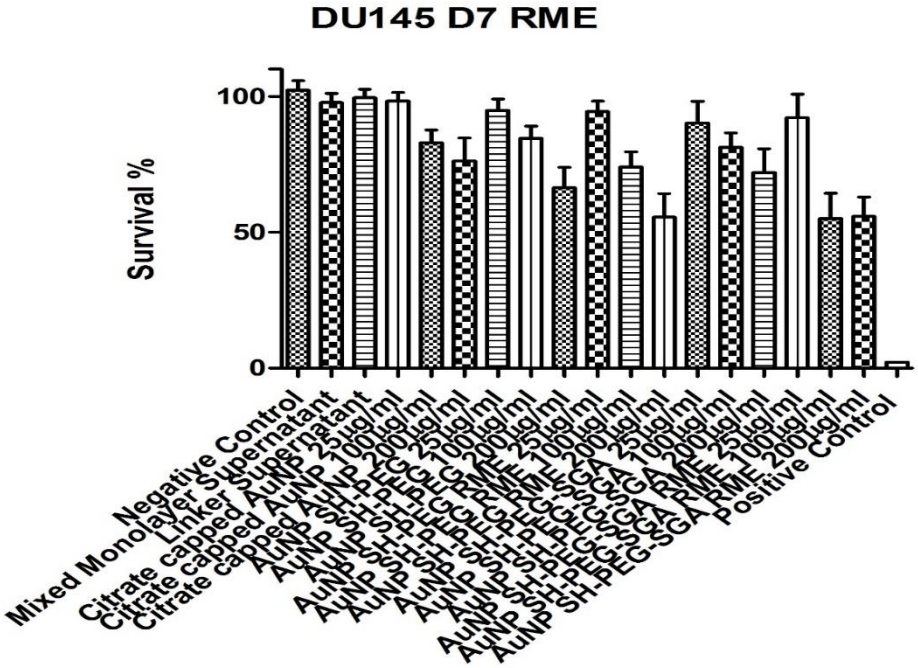
DU145 D7 RME
Survival %
100
50
0
Negative Control
Mixed Monolayer Supernatant
Linker Supernatant
Citrate capped AuNP 25µg/ml
Citrate capped AuNP 100µg/ml
Citrate capped AuNP 200µg/ml
AuNP SH-PEG 25µg/ml
AuNP SH-PEG 100µg/ml
AuNP SH-PEG 200µg/ml
AuNP SH-PEG-GGG RME 25µg/ml
AuNP SH-PEG-GGG RME 100µg/ml
AuNP SH-PEG-GGG RME 200µg/ml
AuNP SH-PEG-SGA RME 25µg/ml
AuNP SH-PEG-SGA RME 100µg/ml
AuNP SH-PEG-SGA RME 200µg/ml
Positive Control

APPENDIX 2

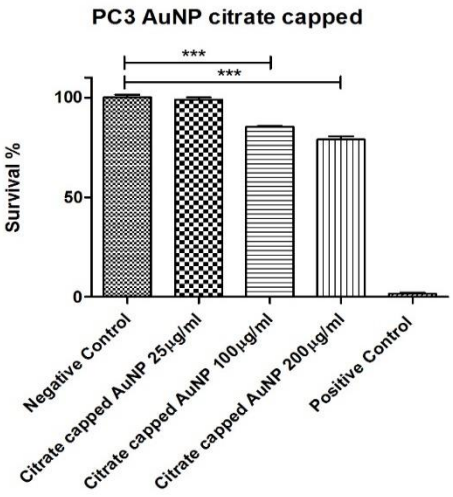
PC3 AuNP citrate capped
Survival %
100
50
0
***
***
Negative Control
Citrate capped AuNP 25µg/ml
Citrate capped AuNP 100µg/ml
Citrate capped AuNP 200µg/ml
Positive Control

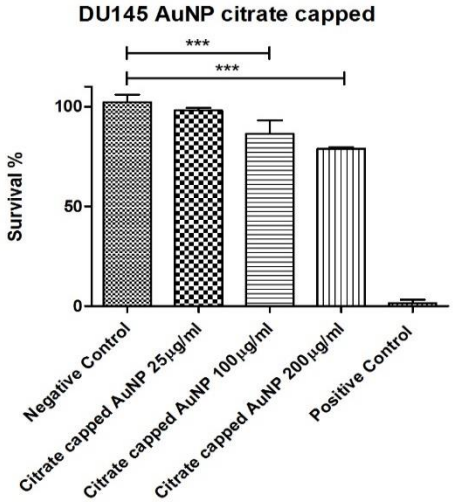
DU145 AuNP citrate capped
Survival %
100
50
0
***
***
Negative Control
Citrate capped AuNP 25µg/ml
Citrate capped AuNP 100µg/ml
Citrate capped AuNP 200µg/ml
Positive Control

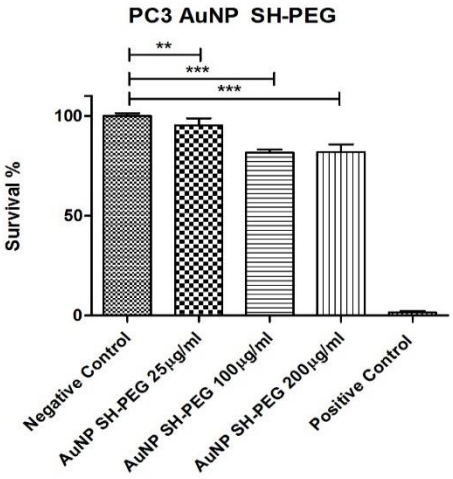
PC3 AuNP SH-PEG
Survival %
100
50
0
**
***
***
Negative Control
AuNP SH-PEG 25µg/ml
AuNP SH-PEG 100µg/ml
AuNP SH-PEG 200µg/ml
Positive Control

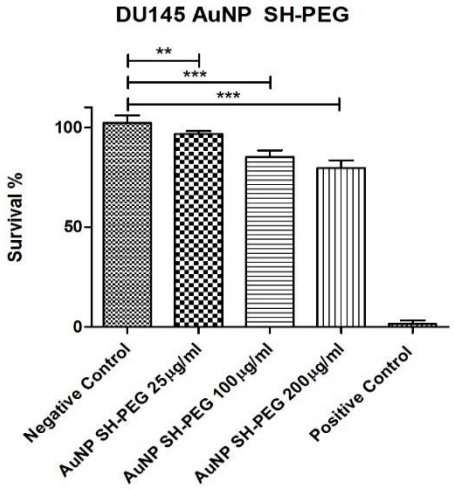
DU145 AuNP SH-PEG
Survival %
100
50
0
**
***
***
Negative Control
AuNP SH-PEG 25µg/ml
AuNP SH-PEG 100µg/ml
AuNP SH-PEG 200µg/ml
Positive Control

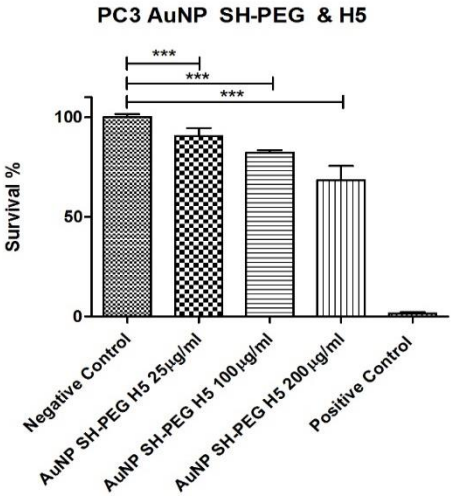
PC3 AuNP SH-PEG & H5
Survival %
100
50
0
***
***
***
Negative Control
AuNP SH-PEG H5 25µg/ml
AuNP SH-PEG H5 100µg/ml
AuNP SH-PEG H5 200µg/ml
Positive Control

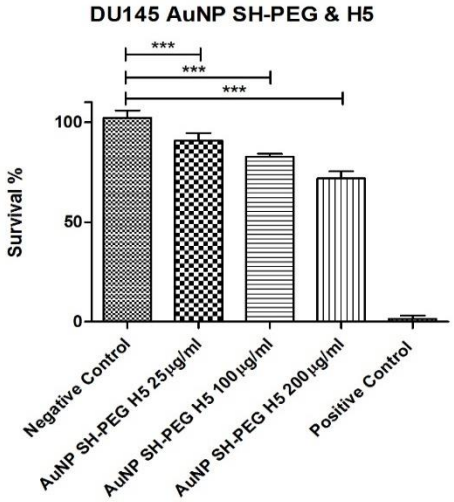
DU145 AuNP SH-PEG & H5
Survival %
100
50
0
***
***
***
Negative Control
AuNP SH-PEG H5 25µg/ml
AuNP SH-PEG H5 100µg/ml
AuNP SH-PEG H5 200µg/ml
Positive Control

APPENDIX3

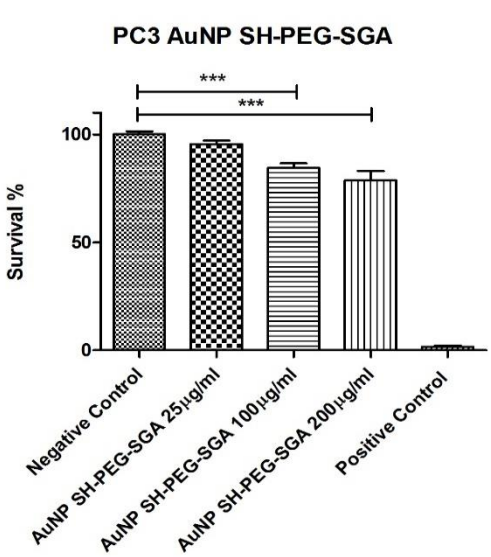
PC3 AuNP SH-PEG-SGA
***
***
Survival %
100
50
0
Negative Control
AuNP SH-PEG-SGA 25µg/ml
AuNP SH-PEG-SGA 100µg/ml
AuNP SH-PEG-SGA 200µg/ml
Positive Control

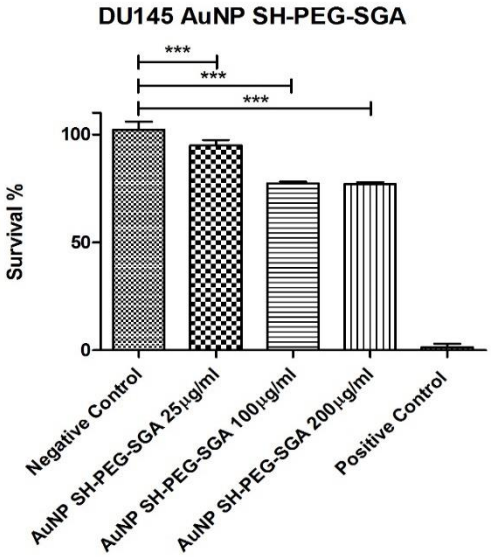
DU145 AuNP SH-PEG-SGA
***
***
***
Survival %
100
50
0
Negative Control
AuNP SH-PEG-SGA 25µg/ml
AuNP SH-PEG-SGA 100µg/ml
AuNP SH-PEG-SGA 200µg/ml
Positive Control

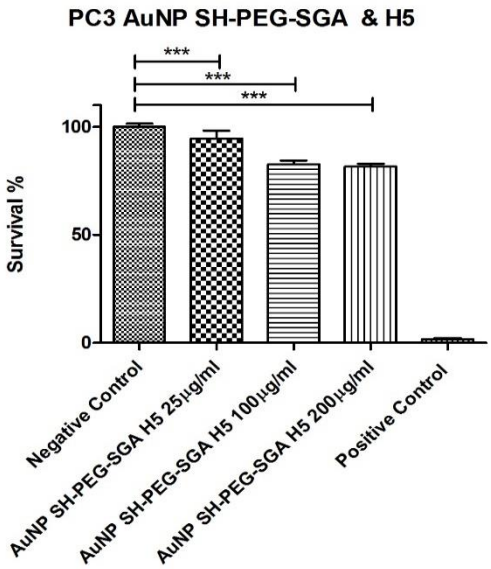
PC3 AuNP SH-PEG-SGA & H5
***
***
***
Survival %
100
50
0
Negative Control
AuNP SH-PEG-SGA H5 25µg/ml
AuNP SH-PEG-SGA H5 100µg/ml
AuNP SH-PEG-SGA H5 200µg/ml
Positive Control

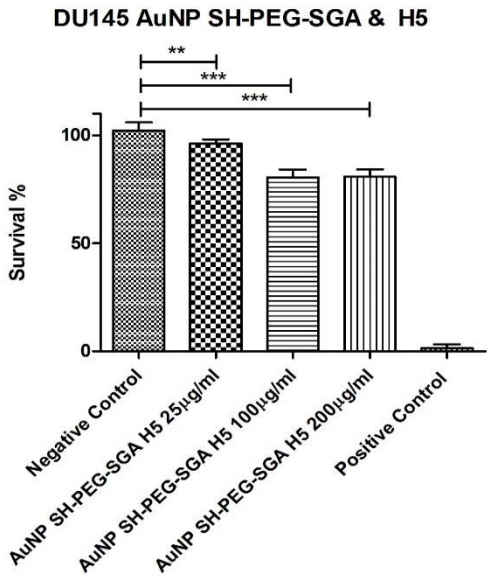
DU145 AuNP SH-PEG-SGA & H5
**
***
***
Survival %
100
50
0
Negative Control
AuNP SH-PEG-SGA H5 25µg/ml
AuNP SH-PEG-SGA H5 100µg/ml
AuNP SH-PEG-SGA H5 200µg/ml
Positive Control

APPENDIX 4

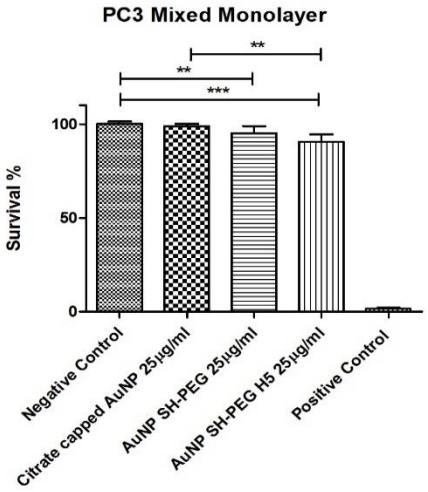
PC3 Mixed Monolayer
Survival %
100
50
0
**
**
***
Negative Control
Citrate capped AuNP 25µg/ml
AuNP SH-PEG 25µg/ml
AuNP SH-PEG H5 25µg/ml
Positive Control

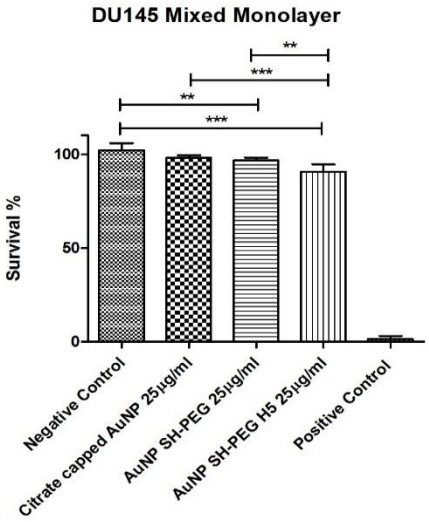
DU145 Mixed Monolayer
Survival %
100
50
0
**
***
**
***
Negative Control
Citrate capped AuNP 25µg/ml
AuNP SH-PEG 25µg/ml
AuNP SH-PEG H5 25µg/ml
Positive Control

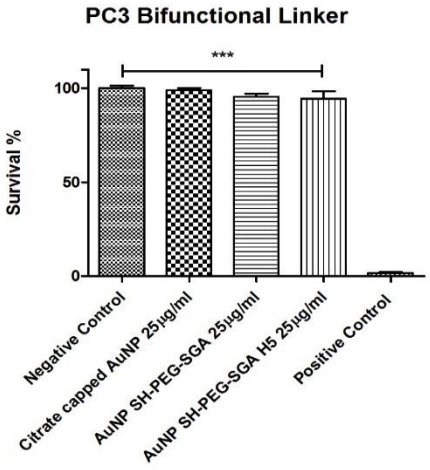
PC3 Bifunctional Linker
Survival %
100
50
0
***
Negative Control
Citrate capped AuNP 25µg/ml
AuNP SH-PEG-SGA 25µg/ml
AuNP SH-PEG-SGA H5 25µg/ml
Positive Control

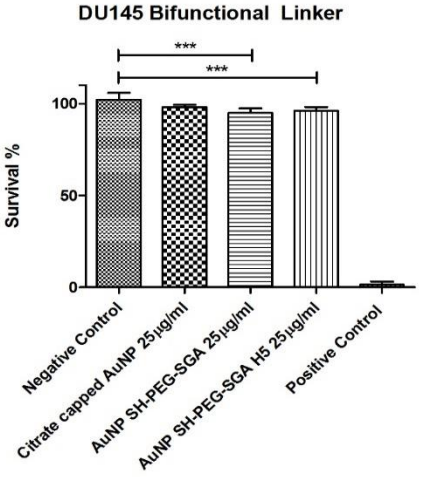
DU145 Bifunctional Linker
Survival %
100
50
0
***
***
Negative Control
Citrate capped AuNP 25µg/ml
AuNP SH-PEG-SGA 25µg/ml
AuNP SH-PEG-SGA H5 25µg/ml
Positive Control

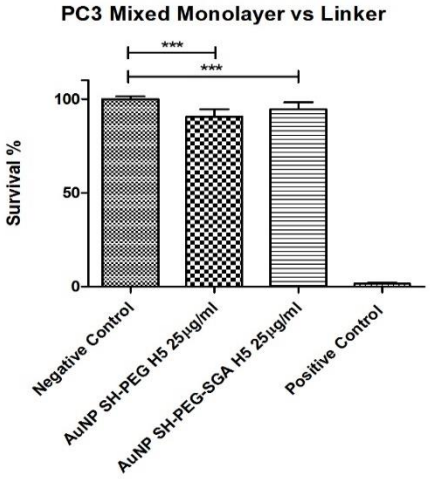
PC3 Mixed Monolayer vs Linker
Survival %
100
50
0
***
***
Negative Control
AuNP SH-PEG H5 25µg/ml
AuNP SH-PEG-SGA H5 25µg/ml
Positive Control

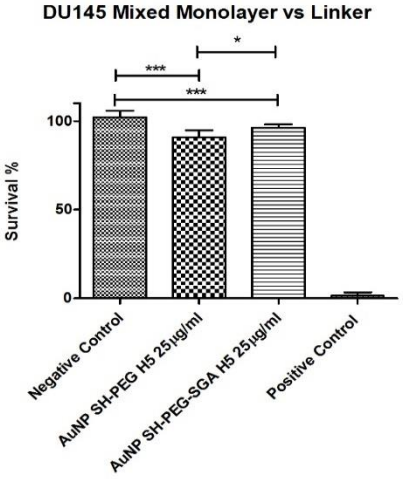
DU145 Mixed Monolayer vs Linker
Survival %
100
50
0
*
***
***
Negative Control
AuNP SH-PEG H5 25µg/ml
AuNP SH-PEG-SGA H5 25µg/ml
Positive Control

APPENDIX 5

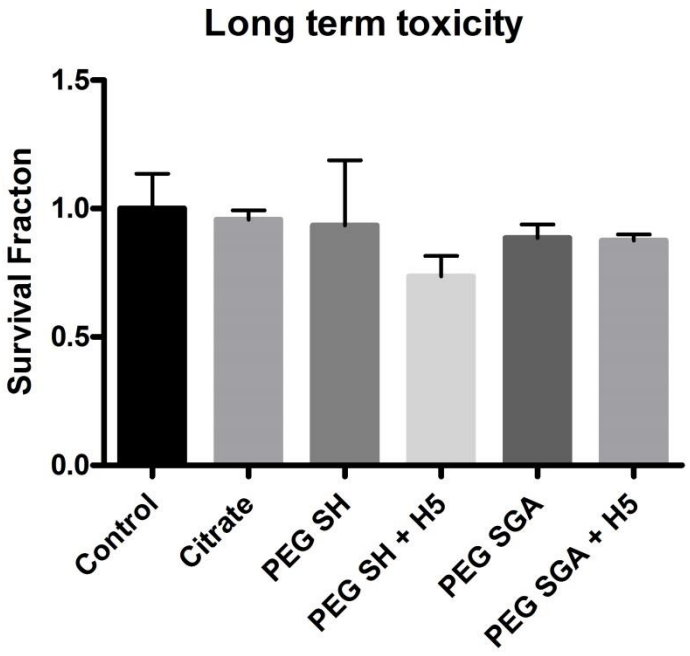
Long term toxicity
Survival Fracton
1.5
1.0
0.5
0.0
Control
Citrate
PEG SH
PEG SH + H5
PEG SGA
PEG SGA + H5